University of Alberta

Effect of Near-Wall Turbulence on Selective Removal of Particles from Sand Beds Deposited in Pipelines

by

Hossein Zeinali

A thesis submitted to the Faculty of Graduate Studies and Research
in partial fulfillment of the requirements for the degree of

Doctor of Philosophy
in
Petroleum Engineering

Department of Civil and Environmental Engineering

©Hossein Zeinali
Fall 2012
Edmonton, Alberta

Permission is hereby granted to the University of Alberta Libraries to reproduce single copies of this thesis and to lend or sell such copies for private, scholarly or scientific research purposes only. Where the thesis is converted to, or otherwise made available in digital form, the University of Alberta will advise potential users of the thesis of these terms.

The author reserves all other publication and other rights in association with the copyright in the thesis and, except as herein before provided, neither the thesis nor any substantial portion thereof may be printed or otherwise reproduced in any material form whatsoever without the author's prior written permission.

Dedication

This work is dedicated to everyone who has made some contribution to my life and occupies some special space in my universe.

Abstract

A large-scale experimental facility was designed, constructed, and operated to study multiphase flow of solid-liquid mixtures (i.e., slurry flow) in horizontal pipelines.

Trains of discrete lenticular deposits (LDs) and continuous beds were identified and studied in detail, representing two distinct forms of solids deposits occurring during horizontal pipeline flow of stratified slurries. The experimental results showed that LDs, which occur at relatively low flow velocities and solids concentrations, are identifiable and reproducible and are the stable pattern of slurry flow/transportation.

Experiments were conducted to examine how near-wall turbulent structures (i.e., turbulent burst and sweep activity) are influenced by the geometry of bed deposits. Particle image velocimetry (PIV) was used to measure the near-wall (interface) velocity and turbulent activity. Turbulence structure in the vicinity of LDs and the continuous bed were observed, measured, and compared to near-wall turbulent structures of a glass pipe containing water only.

It was found that naturally shaped LDs reduce the burst-sweep frequency and intensity compared to the continuous bed pattern, resulting in reduced production of turbulent kinetic energy.

Experiments were also conducted to study the effect of near-wall turbulent activity (burst-sweep) on selective (size-dependent) removal of particles from

beds with initially broad size distributions deposited in a 95-mm ID glass pipe. Deposit beds were formed using particles (i) predominantly smaller than 60 µm (Phillips domain), (ii) predominantly larger than 170 µm (Shields domain), (iii) intermediate in size between i and ii (intermediate domain), and (iv) of all sizes mixed together (poly-sized particles).

For a bed containing predominantly Phillips-domain particle sizes, larger particles are preferentially removed, mainly because inter-particle attraction forces (e.g., van der Waals forces) dominate in this range. The fine particles are retained in the bed. However, for a bed of predominately Shields-domain particle sizes, the smaller particles are removed.

In the intermediate region ($60 < dp < 170$ µm), particles are evenly exposed to the "updraft under a burst" force and are lifted into the bulk flow; therefore, the overall solids concentration decreases in this region.

Results from poly-sized (mixed) particle experiments confirm the results for the individual domains.

Acknowledgements

Dr. Ergun Kuru and Dr. Peter Toma have been supervising and mentoring my work throughout the course of my degree, and without their guidance, instruction, and contributions the work presented would not have been possible. I greatly appreciate their help and contributions.

Much thanks to my final doctoral exam committee members: Dr. Tayfun Babadagli and Dr. Japan Trivedi, from the U of A department of civil and environmental engineering; Dr. Zhenghe Xu, from the U of A department of chemical and materials engineering; and Dr. Mengjiao Yu, from the University of Tulsa petroleum engineering department. These individuals gave of their valuable time and each made unique and important contributions to my work.

Financial support from the Canada Foundation for Innovation (CFI) and the Natural Science and Engineering Research Council of Canada (NSERC), which made possible the construction of the multi-purpose experimental facilities, is gratefully acknowledged.

Amirkabir University of Technology (Tehran Polytechnic) financial scholarship support is so appreciated.

I would like to thank Dr. David Nobes from department of mechanical engineering for his valuable suggestions with the setup and operation of the PIV system. In addition, I would like to thank Dr. N. Raj Rajaratnam from the U of A department of civil and environmental engineering for many helpful discussions pertaining to this work. Special thanks are due to Dr. Carlos Lange from department of mechanical engineering for his excellent suggestion during my studies.

In particular, I would like to thank Dr. Vahid Rezania for his amazing help with Matlab and his dedicated support during my studies. Special recognition is extended to Dr. Mostafa Naghizadeh and Rhonda Kajner for their great suggestions and other help whenever it was needed.

Thanks are also due to Mr. Tao Guo for his valuable help during the experiments in the summer of 2010.

Special recognition is extended to Dr. J.J. Roger Cheng, professor and chair of the Department of Civil and Environmental Engineering for his leadership and excellence in organizational management.

I would like to express sincere gratitude to my friends and supporters and all those who provided any kind of help throughout the course of my degree.

Finally, the greatest thanks go to my parents and each of my family members, who have helped and supported me unconditionally over the years. They are the greatest gift of my life.

Table of Contents

1 Introduction and Background 1
1.1 Introduction 1
1.2 Statement of the Problem 8
1.3 Objectives of the Research 11
1.4 Methodology 12
1.5 Contributions of the Present Research 23
1.6 Structure of the Thesis 26
1.7 References 28

2 Description of Multiphase Flow Experimental Facility 31
2.1 Introduction 31
2.2 Safety Features 33
2.2.1 System Location 33
2.2.2 Piping and Bypass Line 34
2.2.3 Operating Procedures 35
2.3 Experimentation 36
2.3.1 Slurry Flow Loop Set-up 36
2.3.1.1 Preparation and circulation tank 37
2.3.1.2 Flow lines in the loop 39
2.3.1.3 Control valves at the flow lines 40
2.3.1.4 Slurry flow loop instrumentation 41
2.3.2 Particle Image Velocimetry (PIV) System 43
2.3.3 Slurry Flow Loop Pump and Control System 44
2.3.4 LabView for Data Acquisition and Instrument Control 46
2.3.5 Automated Image Analyzer for PSD Analysis 46
2.4 Slurry Flow Loop Operation and Project Accomplishments 48

3 Methodology of Particle Image Velocimetry (PIV) Data Acquisition and Analysis 51
3.1 Introduction 51
3.2 History and Milestones of PIV Measurement 52
3.3 Experimental Setup 56
3.3.1 Transparent Glass Pipeline 57
3.3.2 Light Sources (Particle Illumination) 57
3.3.3 Rectangular Box Around Convex Pipe Surface 57
3.3.4 High-Resolution PIV Camera 58
3.3.5 PIV System Specifications and Model 59
3.3.6 Tracer (Seeding) Particles 60
3.4 Measurement Technique 61

3.4.1 Principle of Measurements 61
3.4.2 PIV Recordings 61
3.4.3 Raw Images and Frequency Filter 63
3.4.4 Image Processing 63
3.4.5 Cross-Correlation Technique 66
3.5 PIV Data Validation 67
3.5.1 Particle Image Density for PIV Measurements 68
3.5.2 Correlation Map for the Specified IW 71
3.5.3 Histogram of the Particle Images 74
3.5.4 Velocity Vector Map from PIV Measurements 77
3.5.5 Comparison of Velocity Profile Data from PIV with the Universal Velocity Profile 81
3.6 Discussion and Conclusions 83
3.7 References 85

4 Reduction of Frictional Pressure Drop Associated with Formation of Natural Lenticular Deposits 88
4.1 Introduction 88
4.2 Background 89
4.3 Experimental Setup and Materials 99
4.3.1 General Observations of Slurry Flow Patterns 101
4.3.1.1 Effect of slurry concentration on the formation of LDs 106
4.3.1.2 Mechanisms and velocity of LD propagation movement 107
4.4 Effect of LD Formation on Frictional Pressure Drop 109
4.5 Burst-Sweep and TKE in the Near-Wall Region 119
4.5.1 PIV Experimental Setup and Test Conditions 121
4.5.2 Near-Wall Velocity Profiles Obtained from PIV Measurements . 124
4.5.3 Velocity Maps for LDs, Continuous Bed, and Water-Only Flow 130
4.5.4 Assessment of Near-Wall Coherent Structures 133
4.5.5 Comparisons of Frequencies of Turbulent Coherent Structures ... 135
4.5.6 Assessment of TKE 136
4.6 Conclusions 143
4.7 Appendix 4.A 144
4.7.1 Churchill's Equation: 144
4.8 Appendix 4.B 145
4.8.1 Criteria for Identifying Near-Wall Turbulent Coherent Structures 145
4.9 References 147

5 Effect of Near-Wall Turbulence on Selective Removal of Particles from Sand Beds Deposited in Pipelines 151

5.1 Introduction 151
5.2 Near – Wall Turbulent Activity (Burst – Sweep) 152
5.2.1 Assessment of Burst and Sweep Frequency 153
5.3 Selective Removal of Particles from Bed Deposits 156
5.3.1 Forces Involved in Removal of Particles from Bed Deposits 158
5.4 Experimental Program 163
5.4.1 Slurry Flow Loop and Operational Procedure 163
5.5 Results and Discussions 166
5.5.1 Evaluation of Burst Frequency Using PIV 166
5.5.2 Measurements of Selective Particle Removal (Grading) 169
5.6 Conclusions 173
5.7 Appendix 5.A Assessing Burst Frequency Activity with the Aid of PIV 174
5.8 References 177

6 Experimental Study of Shifting Particle Size Distribution and Selective Removal of Fines from a Pipeline Deposit 179
6.1 Introduction and Background 179
6.2 Balance of Forces Acting on Particles in Pipeline Flow 184
6.2.1 Forces Involved in Particle Entrainment 186
6.2.1.1 Attraction (van der Waals) force 186
6.2.1.2 Net weight force 187
6.2.1.3 Lift force (updraft due to turbulent burst) 187
6.2.1.4 Hydrodynamic drag 188
6.2.2 Force Balance for Effective Entrainment 188
6.2.2.1 Force balance for the experimental velocities 189
6.3 Experimental Program 195
6.3.1 Test Facilities 195
6.3.2 Experimental Methodology 203
6.4 Analysis of Results 207
6.4.1 Phillips Domain 207
6.4.2 Intermediate Domain 219
6.4.3 Shields Domain 231
6.4.4 Mixed Domain 239
6.5 Discussion: Experimental Results and Model Predictions 251
6.6 Conclusions 256
6.7 References 260

7 Contributions of this Thesis 263
7.1 Limitations of the Current Study and Recommendations for Future Work 266

List of Tables

1.1 Baseline experimental case studies 16
1.2 Extended experimental bed-slurry study 17
3.1 Summary of R&D on measurements by PIV 52
3.2 Interrogation window sizes for 27.5 mm x 20.8 mm measurement region 64
4.1 PSD of Sil 325 101
4.2 PSD of Sil 1 101
4.3 PSD of glass beads 2429 (A-soda lime glass) 101
4.4 LD propagation velocities for different median diameters and fluid velocities 108
4.5 Specifics of data management with PIV 122
4.6 Summaries of PIV experiments 124
5.A-1 Number of burst counts during 100 seconds of flow (after correction for evolvement angle and multiple-frames factor) 175
6.1 Summary of force balance models and coefficient values for different domains 188
6.2 PSD of glass beads and silica sands for the experiments 203
6.3 PSD shift summary for different domains and three experimental velocities 251

List of Figures

1.1 Particle size distribution for typical oil sand and tailings ponds resulting from processing the mined outcrop..... 3
1.2 Slurry flow categories based on patterns of Newitt et al. [1]..... 4
1.3 Illustration of the experimental methodology..... 15
1.4 Schematic of selective deposition-removal between the slurry bed and the bulk flow 18
1.5 Idealized description of laminar sublayer (LSL) and two-stages of intermittent inflow-outflow condition responsible for selective entrainment of bed particles into main turbulent flow (after Praturi and Brodkey [6]). 21

2.1 The side view of the frame module of the horizontal multiphase experimental facility..... 32
2.2 The top view of the frame module of the horizontal multiphase experimental facility. The module assembly consists of the frame and all the modules supporting the glass tubes 32
2.3 The photo of the experimental setup. The PIV measurement location is also shown..... 36
2.4 Slurry preparation and circulation tank with pneumatic agitator installed; (a) top view, (b) side view (dimensions are given) 38
2.5 Bottom extractor probe to sample deposits at the pipeline bottom..... 43
2.6 PIV system location approximately 5.5 m downstream the entrance..... 44
2.7 The pump performance curve which also provides information on pump efficiency. The pump operates at the intersection of the pump's performance curve and the system head curve..... 45
2.8 Leica automated image analyser for PSD analysis 47

3.1 PIV system setup used for the experiments 56
3.2 Rectangular box around the circular pipe filled with glycerol to minimize reflection and distortion..... 58
3.3 Digital PIV CCD camera – high resolution 59
3.4a Typical PIV image for water-only flow. Particles in the image are just impurities from the tap water and are not due to external seeding..... 69
3.4b Typical PIV image for continuous bed, no external seeding, 16 x 16 pixel grid size with available particles for cross-correlation..... 70
3.4c Typical PIV image for LD, no external seeding, 16 x 16 pixel grid size with available particles for cross-correlation 71
3.5 Typical 3D correlation maps of 16 x 16 cross-correlation IWs. (a) water-only flow, (b) continuous bed, and (c) LD..... 73

3.6a Histogram of particle distribution in water-only flow. Horizontal axis shows the number of particles and the vertical axis shows the number of pixels containing a specific number of particles. 75
3.6b Histogram of particle distribution in continuous-bed flow. Horizontal axis shows the number of particles and the vertical axis shows the number of pixels containing a specific number of particles. 76
3.6c Histogram of particle distribution in LD flow. Horizontal axis shows the number of particles and the vertical axis shows the number of pixels containing a specific number of particles. 77
3.7 Typical velocity vector map for water-only flow using normal lens, U_{avg}= 0.24 m/s, 32 x 32 pixel IW with 50% overlap, flow direction from right to left 78
3.8 Velocity vector map for water-only flow, U_{avg} = 0.24 m/s using micro lens. (a) Upper map is 32 x 32 pixel IW with 50% overlap, (b) Lower map is 16 x 16 pixel IW with 50% overlap 80
3.9 Data obtained from PIV for 16 x 16 pixel IW with 50% overlap in pipeline at U_{avg} = 0.24 m/s (Re = 24,379); green line for the near-wall profile of $y^+ < 5$; blue line for $y^+ \geq 5$; red line for the data from PIV 81

4.1 Slurry flow pattern for a broad range of solids concentrations and flow velocities (Newitt et al. [3]) 90
4.2 Friction gradient versus flow rate for different sand slurry concentrations and dunes in a 95-mm ID pipeline (particle mean diameter 685 µm) [20] 98
4.3 Flow loop setup for slurry experiments 100
4.4a The parabolic form of LDs 103
4.4b The barchan form of LDs 103
4.5 Detachment and re-attachment points as well as recirculation zone in an LD; the sidebar gives the magnitude of the velocity field in m/s 105
4.6a Bed form for slurry concentration greater than 1 vol% 106
4.6b Bed form for slurry concentration of 0.5 vol% 107
4.7 LD propagation velocities in pipe at different fluid velocities and particle sizes. The data in this study were compared with the data from Toma et al. [9] experiments 109
4.8 Base data for calibration of DP cells – measured versus calculated frictional pressure drop 110
4.9 Recorded pressure drop versus time during transitions from continuous bed to LDs 111
4.10 Measured and calculated frictional pressure drops due to flow over a continuous bed. Average flow velocity is 0.45 m/s 113
4.11 Effect of dune formation on frictional pressure drop. Average flow velocity is 0.41 m/s 114

4.12 Effect of dune formation on frictional pressure drop (normalized with respect to frictional pressure drop in water flow)..... 115
4.13 Frictional pressure drop due to flow over LDs. Average flow velocity is 0.37m/s 115
4.14 Effect of dune formation on frictional pressure drop (repeated experiment, U_{avg} = 0.41m/s)..... 116
4.15 Effect of dune formation on frictional pressure drop (normalized with respect to frictional pressure drop due to water flow, repeated experiment, U_{avg} = 0.41m/s)..... 117
4.16 PIV setup on the slurry flow loop 121
4.17 Horizontal and vertical divisions of the PIV investigation area and the number of columns and rows for the experimental measurement field .. 123
4.18 Velocity profile from PIV measurements for three cases: (a) water only, (b) continuous sand bed, and (c) LD for the average velocity of 0.24 m/s... 127
4.19 Mean velocity profiles for the model and experimental data from PIV for U_{avg} = 0.17 m/s (*Re* = 17,269) 128
4.20 Velocity profile over LD obtained from PIV measurement. Flow direction is from right to left. Smooth red lines are the model calculation, green lines are the experimental data for the water-only flow, and blue lines are the experimental data over different sections of the LD 130
4.21 Velocity map for full dune. Flow is from right to left with U_{avg} = 0.24 m/s. The dune profile is drawn manually for clarity 131
4.22 Velocity map for uniform bed equivalent to full dune area with U_{avg} = 0.24 m/s. The bed profile is drawn manually for clarity. Flow is from right to left..... 132
4.23 Contours of constant velocity for water-only flow equivalent to full dune investigation area (control volume). Flow is from right to left with U_{avg} = 0.24 m/s. 132
4.24 Quadrant technique for detection of near-wall coherent structures 133
4.25 LD breakdown into sections; the red broken line shows the wall margins along the LD. The flow is from right to left 134
4.26 Comparison of near-wall coherent structures – burst and sweep frequencies for the three cases at U_{avg} = 0.24 m/s in the y^+ = 0–10 zone 135
4.27 Differences in frequencies for LD and water-only flow cases. Water-only flow has a higher burst and sweep frequency than the LD at the given condition; U_{avg} = 0.24 m/s in the y^+ = 0–10 zone..... 135
4.28 TKE contour map for LD; flow is from right to left. U_{avg} = 0.24 m/s 136
4.29 TKE contour map for water-only flow; flow is from right to left. U_{avg} = 0.24 m/s 137

4.30 TKEs for flow at three different near-wall conditions with U_{avg} = 0.17 m/s in the y^+ = 0–10 zone 138
4.31 TKEs for flow for three different conditions near the wall with U_{avg} = 0.24 m/s in the y^+ = 0–10 zone 139
4.32 Percentage difference in TKEs for continuous bed versus LDs with U_{avg} = 0.17 m/s in the y^+ = 0–10 zone; continuous bed has higher TKE 140
4.33 Differences in TKEs for continuous bed versus LDs with U_{avg} = 0.24 m/s in the y^+ = 0–10 zone; the continuous bed has higher TKE 141

5.1 Idealization of burst-sweep activity from sand bed emerging from near-wall to core turbulent flow [9] 152
5.2 Simultaneous record of local velocity components *U* and *V* versus time 155
5.3 Burst and sweep assessment performed by comparing the signs of fluctuating velocity components u' and v' - the four-quadrant method [5] 155
5.4 Two distinct critical particle entrainment regimes as function of the wall shear stress and size range found in the bed [15] (silica sand-water) 157
5.5 Main forces considered for removal and grading of particles from a sand bed during slurry transportation 158
5.6 Attraction and buoyant forces contributing to particle removal (silica sand-water) 159
5.7 Entraining forces acting on particles exposed to turbulent core flow (calculation is done for silica sand slurry at U_{avg} = 0.36 m/s, *Re* = 27,660) 162
5.8 Main components of experimental rig 163
5.9 Near-wall burst initiation and dissipation snapshot obtained by processing the PIV data (average flow velocity 0.19 m/s) 166
5.10 PIV measured burst frequency (number of burst/100s) assessed at four levels in the boundary layer and the frequency calculated (at Z1) using "Cleaver and Yates (C&Y)" method [9] 167
5.11 Schematic illustration of burst evolving from pipe wall to turbulent core flow [19] 168
5.12 Concentration shift between transported sand bed and slurry (initial sand mixture of d_p > 50 μm - superficial slurry velocity of 0.33 m/s – *Re*=27,899; LD bed sample was taken 135 minutes after the start of the experiment) 170
5.13 Change of particle size distribution in the moving lenticular bed deposits with time (d_p < 60 μm, slurry flow velocity is 0.33 m/s; LD bed sample was taken 135 minutes after the start of the experiment) 171
5.14 Change of particle size distribution in the moving lenticular bed deposits with time (d_p < 60 μm, slurry flow velocity is 0.36 m/s) 172

6.1 Dimensionless Shield's diagram for entrainment of bed particles, first introduced in 1936 [2] 180
6.2 Particle removal mechanisms by burst activity in turbulent flow at the surface [9, 17] 182
6.3 Balance of forces on a particle in a deposit during pipe flow 184
6.4 Downward forces acting on particles as a function of particle diameter and particle and fluid densities for all flow velocities 190
6.5 Force balance for particles at 0.25 m/s velocity (*Re* = 25,395) 192
6.6 Force balance for particles at 0.34 m/s velocity (*Re* = 34,537) 193
6.7 Force balance for particles at 0.39 m/s velocity (*Re* = 39,616) 194
6.8 Flow system for experiments, with relevant components identified 195
6.9 Closeup view of isolation valve number 2 196
6.10 (a) Bottom extractor used for extracting samples from the bed load; (b) bed extraction apparatus 197
6.11 Micron-rated filter bag in the return line, to capture particles during circulation 198
6.12 Pump and electric motor assembly for the flow loop – particles accumulated in both the suction and discharge sections of the pump assembly 199
6.13 LabView software used for analysis, logging, and display of experimental data 200
6.14 Automated PSD analyzer – Leica DM6000M with a movable stage with scanning capability in the x y, and z directions using variable scan patterns 202
6.15 Summary of experimental procedure 206
6.16 Schematic illustration of the experiment and sampling schedule 207
6.17a PSD of Phillips domain after 10 min flow at 0.25 m/s 209
6.17b PSD of Phillips domain after 20 min flow at 0.25 m/s 210
6.17c PSD of Phillips domain after 30 min flow at 0.25 m/s 210
6.17d PSD of Phillips domain after 45 min flow at 0.25 m/s 211
6.18a PSD of Phillips domain after 10 min flow at 0.34 m/s 213
6.18b PSD of Phillips domain after 20 min flow at 0.34 m/s 213
6.18c PSD of Phillips domain after 30 min flow at 0.34 m/s 214
6.18d PSD of Phillips domain after 45 min flow at 0.34 m/s 215
6.19a PSD of Phillips domain after 10 min flow at 0.39 m/s 216
6.19b PSD of Phillips domain after 20 min flow at 0.39 m/s 216
6.19c PSD of Phillips domain after 30 min flow at 0.39 m/s 217
6.19d PSD of Phillips domain after 45 min flow at 0.39 m/s 218
6.20a PSD of intermediate domain after 10 min flow at 0.25 m/s 220
6.20b PSD of intermediate domain after 20 min flow at 0.25 m/s 221

6.20c PSD of intermediate domain after 30 min flow at 0.25 m/s..... 222
6.20d PSD of intermediate domain after 45 min flow at 0.25 m/s 222
6.21a PSD of intermediate domain after 10 min flow at 0.34 m/s 224
6.21b PSD of intermediate domain after 20 min flow at 0.34 m/s 225
6.21c PSD of intermediate domain after 30 min flow at 0.34 m/s..... 225
6.21d PSD of intermediate domain after 45 min flow at 0.34 m/s 226
6.22a PSD of intermediate domain after 10 min flow at 0.39 m/s 228
6.22b PSD of intermediate domain after 20 min flow at 0.39 m/s 228
6.22c PSD of intermediate domain after 30 min flow at 0.39 m/s..... 229
6.22d PSD of intermediate domain after 45 min flow at 0.39 m/s 230
6.23a PSD of Shields domain after 10 min flow at 0.25 m/s..... 232
6.23b PSD of Shields domain after 20 min flow at 0.25 m/s 233
6.23c PSD of Shields domain after 30 min flow at 0.25 m/s..... 233
6.23d PSD of Shields domain after 45 min flow at 0.25 m/s 234
6.24a PSD of Shields domain after 10 min flow at 0.34 m/s..... 234
6.24b PSD of Shields domain after 20 min flow at 0.34 m/s 235
6.24c PSD of Shields domain after 30 min flow at 0.34 m/s..... 235
6.24d PSD of Shields domain after 45 min flow at 0.34 m/s 236
6.25a PSD of Shields domain after 10 min flow at 0.39 m/s..... 236
6.25b PSD of Shields domain after 20 min flow at 0.39 m/s 237
6.25c PSD of Shields domain after 30 min flow at 0.39 m/s..... 237
6.25d PSD of Shields domain after 45 min flow at 0.39 m/s 238
6.26a PSD of mixed domain after 10 min flow at 0.25 m/s 240
6.26b PSD of mixed domain after 20 min flow at 0.25 m/s 240
6.26c PSD of mixed domain after 30 min flow at 0.25 m/s..... 241
6.26d PSD of mixed domain after 45 min flow at 0.25 m/s 242
6.27a PSD of Mixed domain after 10 min flow at 0.34 m/s..... 243
6.27b PSD of Mixed domain after 20 min flow at 0.34 m/s..... 244
6.27c PSD of Mixed domain after 30 min flow at 0.34 m/s 245
6.27d PSD of Mixed domain after 45 min flow at 0.34 m/s..... 246
6.28a PSD of mixed domain after 10 min flow at 0.39 m/s 247
6.28b PSD of mixed domain after 20 min flow at 0.39 m/s 247
6.28c PSD of mixed domain after 30 min flow at 0.39 m/s..... 248
6.28d PSD of mixed domain after 45 min flow at 0.39 m/s 249
6.29 Division of the PSD curve into Phillips, intermediate, and Shields domains as used in Table 6.3 251

List of Abbreviations and Symbols

Abbreviations

2D	=	Two-dimensional
C	=	Concentration
CS	=	Coherent structures
FOV	=	Field of view
GPM	=	U.S. gallons per minute (gpm)
GBs	=	Glass beads
hp	=	Horsepower, 1 hp = 746 watts
HWA	=	Hot wire anemometry
ID	=	Inner diameter
in.	=	Inch, inches = 25.4 mm
IWs	=	Interrogation windows
kPa	=	kilopascal, a unit of pressure, 1 kPa = 0.145 psi
L	=	Liter, unit of volume, 1 L = 1/1000 m^3
LDs	=	Lenticular deposits (sand bed)
LDV	=	Laser doppler velocimetry
LSL	=	Laminar sublayer
MFT	=	Mature fine tailings
MPD	=	Managed pressure drilling
min	=	Minute, minutes
OD	=	Outside diameter
PIV	=	Particle image velocimetry
PSD	=	Particle size distribution
Re	=	Reynolds number (dimensionless)
RPM, rpm	=	Revolutions per minute
SG	=	Specific gravity (or relative density)
TKE	=	Turbulent kinetic energy
UBD	=	Under-balanced drilling
VDC	=	Volts of direct current
VFD	=	Variable frequency device
VITA	=	Variable interval time averaging
VISA	=	Variable interval space averaging
vol%	=	Volume percent
wt%	=	Weight percent

Arabic symbols

A_p	=	Projected areas of particles normal to the flow, (m^2)
D	=	Pipe diameter (m)
D	=	Grain size (m)
F_a	=	Attraction force (N)
F_b	=	Net weight force (N)
F_c	=	Updraft under a burst (lift force), (N)
F_d	=	Hydrodynamic drag force (N)
F_f	=	Friction force (N)
F_N	=	Normal force perpendicular to the direction of flow (N)
U	=	Instantaneous velocity in streamwise (axial) direction (m/s)
$\overline{U}$	=	Average velocity in streamwise (axial) direction (m/s)
V	=	Instantaneous velocity in wall-normal (radial) direction (m/s)
$\overline{V}$	=	Average velocity in wall-normal (radial) direction (m/s)
V_p	=	Volume-equivalent diameter of particles, (m^3)
X_{cr}	=	Critical grain size Reynolds number, $X_{cr} = u_{cr}^{*} D / \nu$
Y_{cr}	=	Critical mobility number in Shields graph, $Y_{cr} = \rho u_{cr}^{*2} / \gamma_S D$
c_1	=	Attraction force constant, $c_1 = O(10^{-5})$
c_2	=	Burst updraft constant, $c_2 = O(10)$
c_d	=	Drag coefficient in hydrodynamic drag force, $c_d < O(1)$
d	=	Particle diameter (μm)
d_{50}	=	Grain diameter at which 50% of the sediment sample is finer than. Sediment sizes d_{10} and d_{85}, for example, are associated with 10% and 85% finer than.
d_e	=	Particle equivalent diameter (μm)
f	=	Friction factor (coefficient)
f	=	Function
g	=	Acceleration due to gravity (9.81 m/s^2)
l_y	=	Normal distance from the pipe wall (m)
l_y^+	=	Dimensionless normal spacing from the pipe wall
psid	=	pounds per square inch differential, unit of pressure
r^+	=	Particle Reynolds number, $r^+ = u^* d_p / \nu$
u^* (u_τ)	=	Friction (shear) velocity (m/s), $u^* = \sqrt{\tau_w / \rho}$
u_{cr}^*	=	Critical shear velocity (m/s), $u_{cr}^* = \sqrt{\tau_0 / \rho}$
u'	=	Fluctuation velocity in streamwise (axial) direction (m/s)
u^+	=	Dimensionless velocity

v'	=	Fluctuation velocity in wall-normal (radial) direction (m/s)
y	=	Distance from pipe wall (m)
y^+	=	Dimensionless distance from the pipe wall, $y^+ = yu^* / \nu$

Greek symbols

Δ	=	Difference operator
$\Delta P/\Delta x$	=	Frictional pressure drop over the length x
α	=	Burst development angle
γ_S	=	Specific weight of a grain in fluid
ε	=	Pipe roughness coefficient
μ		Dynamic viscosity (also absolute viscosity), unit Pa·s
μ_k	=	Coefficient of kinematic friction (or dynamic friction)
μm	=	micrometer, 10^{-6} m
μ_s	=	Coefficient of static friction
ν	=	Kinematic viscosity (m^2/s), $\nu = \mu / \rho$
ρ	=	Density (kg/m^3)
τ_0	=	Shear stress interacting between the flow and bed surface (Pa)
τ_w	=	Wall shear stress (Pa)

Subscripts

f	=	fluid
p	=	particle
w	=	wall

1 Introduction and Background

1.1 Introduction

Effective removal of drilling solids is essential for the successful drilling of horizontal and extended-reach wells. Insufficient solids removal results in costly problems such as pipe sticking, excessive torque and drag, and difficulties in well completion (casing/cementing and logging). Studies on the transport of solid-liquid mixtures (i.e., slurries) in pipes and annuli are also pertinent to the design and operation of other oil field technologies such as proppant transport in hydraulic fracturing, cleaning of sand from production wells, and hydrotransport of oil sands. Newly adopted drilling technologies, including managed pressure drilling (MPD) and under-balanced drilling (UBD), require good control of solids transportation. Cold production of "fluidized" zones in reservoirs is another application of slurry transportation.

Slurries are solid-liquid mixtures in which the solids are in suspension; they are formed when insoluble particulates are added to and mixed with the suspending liquid. Slurries vary in solids concentration and are more viscous and generally of higher density than the liquid in which they are formed.

Slurry transport is used widely in the oil sands extraction industry. On-line conditioning and froth separation during pipeline transportation of mined oil sands has been replacing conventional batch reactors, with great economic advantage. According to Inter Pipeline Fund statistics for 2011, approximately

786,000 barrels per day of oil sand bitumen blend is shipped by pipeline in Canada (approximately 35% of Canada's oil sands production). This includes the Cold Lake, Corridor, and Polaris pipeline systems, some 2500 km of pipeline in all.

Maintaining optimal conditions for hydrotransport of oil sands represents a major challenge, mainly due to the extreme variability of feedstock grade and sand-clay content.

In addition to pipeline transportation of highly concentrated slurries for cold production of mined oil sand, in situ thermal production (mainly from unconsolidated oil sand formations) is usually accompanied by entrainment and deposition of fines during pipe flow. The accumulation of fines on the bottom of horizontal wells presents special problems as the concentration of fines is usually under 5wt% and the transport velocity is below the critical entrainment value.

The size distribution of "fines" typically produced from Athabasca, Cold Lake, and Lloydminster oil sand formations ranges from 1 to 300 μm. The work described here specifically addresses slurry transport related to in situ thermal extraction using horizontal wells.

Figure 1.1 shows a typical cumulative size distribution curve for oil sands obtained from the Firebag Formation. Also shown are typical particle size distributions for pond tailings and mature fine tailings (MFT) from oil sands.

Particles with a broad range of sizes varying from submicron to 2000 µm are typical in surface-mined oil sands.

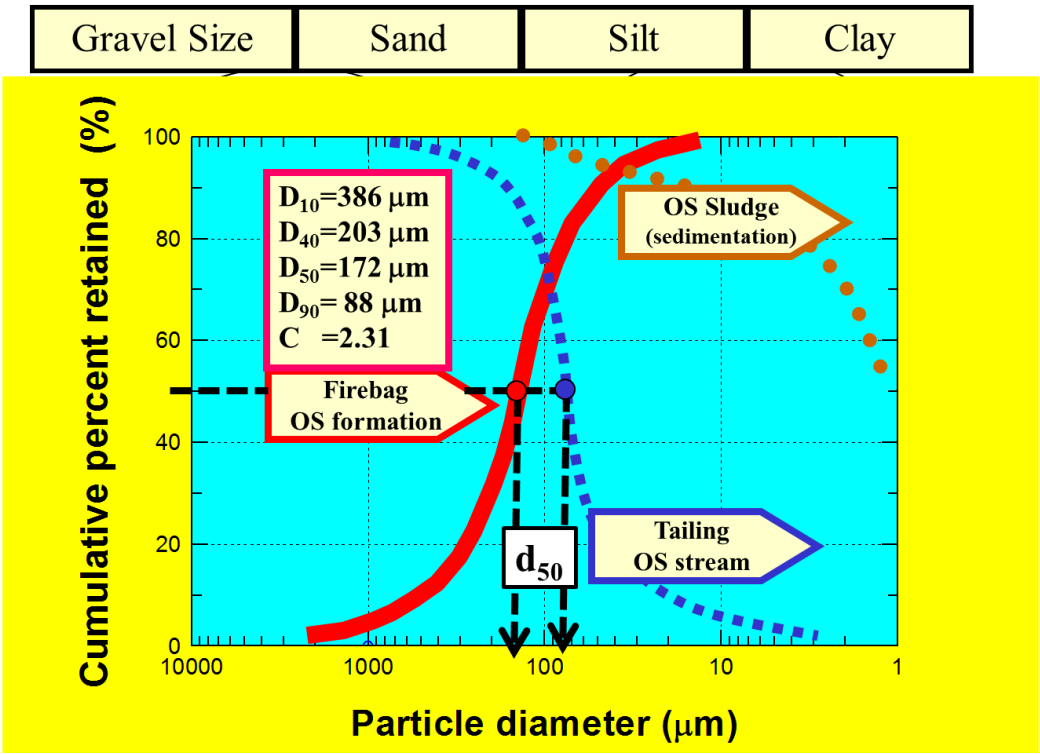

Figure 1.1 Particle size distribution for typical oil sand and tailings ponds resulting from processing the mined outcrop[1]

Slurry transportation variables that need to be considered are: particle size, shape and density; fluid viscosity, density, and velocity; solids size and concentration; and pipe diameter. Depending on the solids size and concentration, as well as the relative fluid-solid densities, a number of flow patterns have been identified.

---

[1] P. Toma and G. Korpany (ARC) – personal communication

Newitt et al. [1] performed slurry experiments using 120 µm (diameter) particles in a 3/4-inch diameter pipeline. Figure 1.2 shows the results of slurry experiments by Newitt et al. [1]. Based on their observations, six distinct slurry flow patterns have been suggested: lenticular deposit, stationary deposit with ripples, suspended flow with saltation, suspended flow with moving bed, fully suspended flow, and blocked pipe.

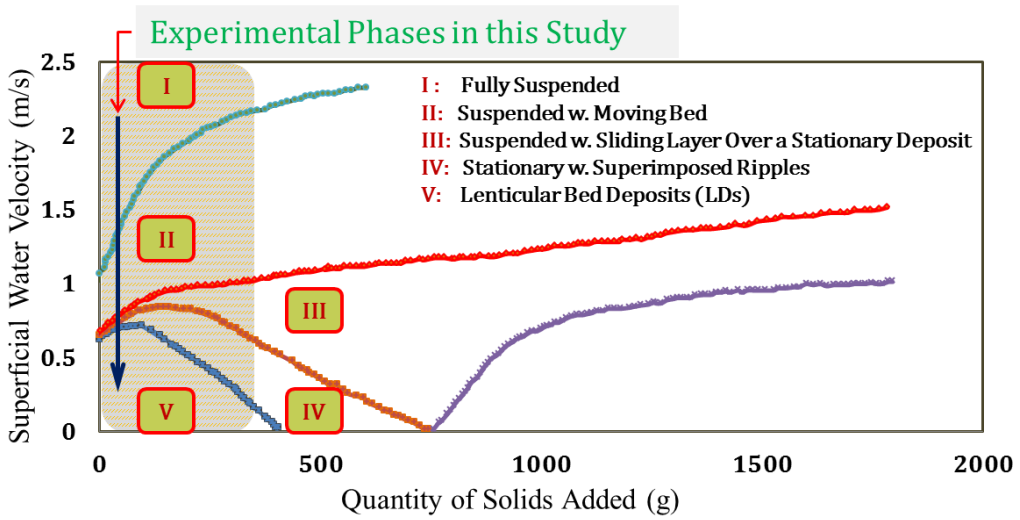

Figure 1.2 Slurry flow categories based on patterns of Newitt et al. [1]

Working with "one size" slurries, Newitt et al. [1] and Shamlou [2] agreed that particles smaller than 30 µm would lead to homogenous-flow suspensions, and deposition of those particles would occur in the laminar flow regime. Slurry flow under this condition has been treated as single-phase flow. Similar flow patterns occurred in experiments of Newitt et al. [1] for different particle types having different densities.

Brown and Heywood [3] mentioned that the individual particles in deflocculated slurries, such as silica sand slurry, act as the flow units, which often results in Newtonian flow behavior. However, Shook et al. [4] indicated that slurries with median particle size smaller than 30 µm are usually non-Newtonian, unless the particle concentration in the slurry is low. They believe that the viscosity of the slurry should be determined experimentally because of the lack of satisfactory models for predicting the rheology of the vast majority of industrial slurries.

A simplified picture may consider just two main modes of transporting a given slurry: (i) as a liquid-solid mixture, and (ii) as a moving bed plus a slurry mixture. This study focuses on the second mode, and, in particular, the formation and transport of moving beds.

Most of the laboratory slurry research available so far has utilized narrow particle size distributions, often characterized by the d_{50} of a certain field condition (see Figure 1.1). An alternative approach is to avoid any scaling and replicate field conditions in the laboratory.

The essential features of sand bed transportation (a preferred strategy for transport of “cold production” and drill cuttings) are the continuous interchange of particles between the moving bed and the interfacing slurry flowing at much higher velocity. Further, this aspect cannot be properly understood unless two essential conditions are observed in the laboratory: (i) a broad spectrum of fine sizes, and (ii) turbulent flow in the moving slurry above the bed. The bed-slurry (radial) transport of fines is a dynamic process involving particle entrainment and

deposition. The laboratory rig used in the present work is furnished with a special "bed extraction probe" designed to capture this aspect.

The design of the dedicated test rig used for our experiments considered the following capabilities, essential for capturing and understanding bed slurry transport: (i) turbulent transport of slurry; (ii) controllable slurry concentration (preferably under 1 vol%), a broad spectrum of size distributions, and the possibility to "design" a specified mixture; (iii) controllable slurry flow rates and accurate maintenance of a desired (superficial) velocity achieved with the aid of a computer-controlled slurry pump and magnetic flowmeter; (iv) measurements of velocity and turbulence in a zone of a few millimeters or less at the interface of the moving bed and (diluted) slurry; (v) monitoring and control of size distribution shifts with the aid of a custom-designed "bed extraction probe"; (vi) automated assessment of size distribution for sizes from 1 to 500 μm; (vii) reducing/preventing (unwanted) slurry deposition in the moving and return portions of the loop.

All of the above features were designed, installed, tested, and commissioned in a slurry flow observation loop 15 m long consisting of nine segments of optical (laser transmission) glass pipe (95 mm ID). This loop was then utilized to obtain the experimental results presented in this dissertation.

The particle image velocimetry (PIV) setup commissioned and used during this investigation was essential to produce salient information on the role of "near-wall" turbulent activity in (i) shaping the sand bed/slurry interface from the

(initially) uniform bed deposit, (ii) modification of the velocity and turbulence spectrum related to the naturally shaped interface, (iii) in-depth explanation of the effect of the naturally shaped interface in minimizing turbulent energy dissipation (also indicated through a relative reduction of pressure drop), (iv) the role of near-wall (interface) turbulence (coherent structures) in selective entrainment-extraction of particles (out of an initial "designed" size distribution).

The effects of these complex slurry characteristics on selective deposition-removal activity during transportation at velocities near the critical deposition value cannot be observed in the laboratory when a "single equivalent size" (or narrow size distribution around d_{50}) is used.

In this study, an approach utilizing a broad range of particle sizes was adopted for assessing the synergistic behaviors determined by the coexistence of complex populations of sizes and shapes. During progressive series of experiments, specific size-concentration ranges in the slurry were examined systematically (e.g., constant overall solids concentration with varying size-specific particle concentration).

The work investigates the effect of particle size on the mechanism of selective (size-dependent) removal of solid particles from an accumulation of solids at the bottom of the pipe, and deposition of particles from the bulk flow.

The effect of broadening the size-concentration distribution on the occurrence of specific flow patterns and on the transition from one pattern to another (initially observed for single-size slurry) is also investigated.

1.2 Statement of the Problem

Microscopic studies on the structure of the turbulent boundary layer revealed that, within the viscous sublayer region adjacent to the surface, the fluid flow is not entirely laminar as suggested by the conventional boundary layer theory. Instead, a cyclic phenomenon was observed, which involved fluid ejections (bursts) from the sublayer and sweeps towards the solid/fluid interface from the outer flow region [5-7]. The numerical data bases [8] as well as measurements via particle image velocimetry [9] reveal the existence of inclined, thin shear layers of concentrated spanwise vorticity. All these more-or-less organized features have been called coherent structures (CS) [10]. Despite the consensus that coherent structures provide important clues to understanding wall turbulence, considerable controversy remains as to what the coherent structures are, and what specific roles they play. In general terms, coherent structures might be considered as organized motions that are persistent in time and space and contribute significantly to the transport of heat, mass, and momentum [11]. One of the major motivations for investigating and characterizing turbulent coherent structures arises from the fact that they play an important role in turbulent transport processes near boundaries [12]. Theoretical studies [13, 14] and experimental observations [15, 16] suggest

that near-wall turbulent organized motions could be responsible for the re-suspension of the particles from the surface of the bed deposits. This entrainment process is related to the fact that such coherent motions strongly contribute to the vertical turbulent transfer of momentum [12]. The concept of critical bed shear stress for the initiation of motion of a sediment particle lying in a bed of similar particles has long occupied a central position in the theory of solids transport [17, 18]. Currently, models used by industry for prediction of solids transport in pipes and annuli are largely based on the assumption of steady, uniform flows in which the fluid turbulence, and hence the sediment transport, can be characterized by the bed shear stress [19]. Both experimental measurements and theoretical considerations, however, suggest that, these assumptions are not valid for treating solids transport over deposit beds because the flow is not uniform and the local turbulence is not necessarily characterized by the local bed shear stress [15, 16, 20].

In non-uniform (unsteady) flows, the turbulent fluctuations even close to the bed do not necessarily scale with the local shear stress. Spatially separated near-bed points at the same height above the bed and having the same local bed shear stress can have significantly different turbulent intensities in non-uniform flows [21, 22]. Moreover, turbulent fluctuations in instantaneous bed shear stress and random exposure of the bed grains to the flow can make it possible for particles to move even at very low values of the mean bed shear stress [23]. The critical shear stress concept may not be sufficient to fully explain the removal of solids from bed deposits under turbulent flow conditions. A good understanding of near-bed

particle deposition and removal, therefore, requires a detailed investigation of the associated flow field, which truly accounts for the physics involved.

In this work it was of particular interest to observe and quantify the effects of different particle size groups on bed formation and, then, to develop strategies for in-line selective removal of fines.

The selective exchange of mass between the moving bed and the bulk of suspended slurry flowing above is controlled by dynamic (turbulent flow–related), gravitational, and inter-particle contact forces. Different particle size groups have offsetting effects on inducing and suppressing the “local” (bulk or near-interface) turbulent activity of liquid slurry during hydrotransport.

A large number of published experimental investigations offer empirical models for quick estimation of critical (deposition) velocity and frictional pressure drop. The experimental results and practical formulas obtained usually rely on a single “selected” size (e.g., median size) to represent a broad range of particle sizes. There is a great need to improve the present understanding of various size-concentration effects on solids transport (deposition-removal) between the bulk turbulent slurry flow and the deposit bed at near-critical velocities. Such understanding will provide the necessary background for developing practical in-line separation strategies.

1.3 Objectives of the Research

The goals of the present research study can be summarized as follows:

- Design and develop a large-scale experimental facility that can be used for studying multiphase flow of solid-liquid mixtures (i.e., slurry flow) in horizontal pipelines.

- Use measurements of velocity and associated turbulent fluctuations obtained using PIV to evaluate the occurrence, intensity, and frequency of near-wall (bed/flow interface) turbulent coherent structures (i.e., turbulent burst and sweep activity).

- Conduct experiments to examine how the near-wall turbulent coherent structures are influenced by the geometry of bed deposits. Three flow modes are studied: water only, continuous bed, and lenticular deposits (LDs). The role of near-wall turbulent activity in shaping the interface of the deposit is given special attention.

- Study the effect of near-wall turbulence on selective (size-dependent) removal of particles from beds deposited in pipelines. Sand beds formed using four different particle size ranges are investigated: $d_p <$ 60 µm, Phillips domain; $d_p >$ 170 µm, Shields domain; intermediate sizes (170 µm > d_p > 60 µm); and mixed sizes (poly-sized).

- Based on visual observations (supported by video recordings) of slurry flow in a horizontal pipeline, provide qualitative information on the

sequential transition between various flow patterns during slurry transport.

1.4 Methodology

Although solids entrainment and deposition mechanisms in turbulent flow have been studied extensively over the years, our understanding of particle interactions with turbulent coherent structures is still limited. Progress toward such understanding has been relatively slow because of the difficulties inherent in simultaneously measuring local solids transport and adjacent near-bed fluid flow at turbulence-resolving frequencies without disturbing the flow. With the introduction of non-intrusive measurement techniques such as particle image velocimetry (PIV), it is now possible to determine the velocity field and observe particle deposition/re-suspension simultaneously under non-uniform flow conditions. Recent studies have shown that near-bed turbulent fluctuations and the random exposure of bed grains to the flow make it possible for particles to move – even at very low values of the mean bed shear stress. Characterization of the near-bed turbulence and thereby the solids transport in such flows, therefore, requires more information than just the local bed shear stress.

The next steps required for developing a more comprehensive model for accurately predicting the evolution of solids transport and/or bed erosion are: (i) to define the near-bed turbulent structure for flow in pipes and ; (ii) to improve

our understanding of the coupling between near-bed turbulent structure and solids transport.

An extensive experimental study was therefore conducted to investigate the coherent structures in the viscous sublayer of turbulent flow and their influence on deposition/re-suspension of solid particles during non-uniform solid/liquid flow in a pipeline system.

Figure 1.2 shows the slurry flow patterns observed by Newitt et al. [1], obtained using glass beads 120 µm in diameter in a 3/4-inch tube at Imperial College laboratory. These results are used as a baseline in the present study. The critical removal-deposition velocity (in a 95-mm ID tube) is assessed and compared with values in existing literature models such as the Oroskar and Turian model [24]. The grey patterned area in Figure 1.2 delineates the research area addressed in this study. Starting with fully suspended (homogeneous) slurry flow, there is a transition to a continuous bed as flow velocity is reduced, followed by a transition to LDs as the velocity is reduced further. The LD pattern is the most commonly seen pattern in nature and in the upper surface of the most other slurry flow patterns. This experimental study utilizes a broad range of particle sizes resembling the particle size distribution in oil sands in order to assess the specific size effects in selective removal-deposition of particles during hydrotransport.

In selective removal of particles, certain forces are more dominant than others, depending on the particle flow regime and particle size. The force balance model acting on different particle sizes in the slurry flow is analyzed and the selective

removal-deposition of particles is described in terms of the dominant forces. By observing and quantifying the selective removal-deposition action, this study analyzes the size-specific controlling forces and offers a better understanding of this size-related bed-slurry transfer action.

Particle size regimes based on the dominant forces acting on particles were originally developed by Phillips [25] and are categorized as: (i) small particle regime (Phillips domain), in which attraction forces present between particles and the pipe wall and among particles and act as the dominant downward force and the dominant upward force is the “updraft under a burst”; (ii) intermediate particle regime (intermediate domain), in which attraction forces have limited effect and gravitation is a major downward force, and the dominant lift force is the burst; and (iii) larger particle regime (Shields domain), in which the attraction forces can be completely disregarded and the effective downward force is gravitation and the dominant lift force is the drag force.

Figure 1.3 is a flow chart illustrating the experimental methodology. Table 1.1 describes the PIV and particle size distribution (PSD) shift experiments, which were initially completed as a baseline. When the experimental setup was ready, initial series of experiments were carried out to evaluate the effects of different forces on various particle size regimes. Both instantaneous and fluctuation velocities streamwise and normal to the flow were measured to assess the near-wall conditions. Bulk velocity was recorded by a magnetic flowmeter installed vertically in the flow loop system.

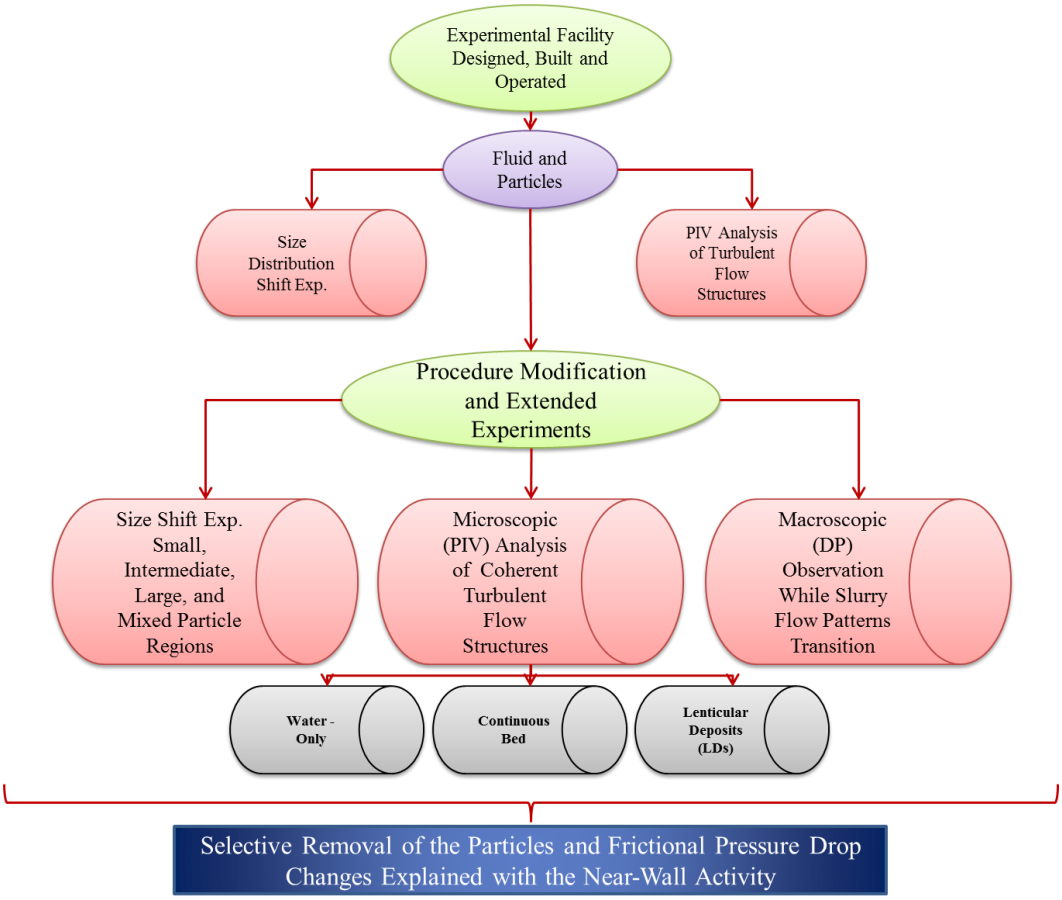

Figure 1.3 Illustration of the experimental methodology

Figure 1.3 and Table 1.2 set out the extended experiments covering the three particle size domains including the Phillips (small sizes), intermediate, and Shields (large sizes) domains. Size-concentration experiments were performed to observe and measure the effects of particle concentration on slurry pattern transitions and on selective deposition-removal for various particle sizes.

Experiments were also conducted combining the three domain sizes to study the effects of various forces on particle removal and deposition for broad PSDs. The experiments were also extended to study the effect of slurry flow pattern

transitions (continuous bed to LDs) on frictional pressure drop at constant velocity.

Table 1.1
Baseline experimental case studies

Baseline experiments				
PIV experiments (water only)				
Velocity (m/s)	**Cases**			**IWs (Pixels)**
	Water only	Continuous bed	LDs	32 x 32
0.110	•	–	–	•
0.155	•	–	–	•
0.190	•	–	–	•
0.203	•	–	–	•

Size shifting experiments				
Velocity (m/s)	**Particle size regions**			
	Phillips domain	Intermediate domain	Shields domain	Mixed domain
0.33	•	–	–	•
0.36	•	–	–	–

Table 1.2
Extended experimental bed-slurry study

Bed slurry experiments				
Slurry flow pattern transition (DP)				
Velocity (m/s)	**Patterns (C = 0.5 vol%)**		**DP changes** (Constant velocity)	**Repeated**
	Continuous bed	LDs		
0.45	•	–	–	•
0.41	•	•	•	•
0.37	–	•	–	•
PIV experiments				
Velocity (m/s)	**Cases**			**IWs (Pixels)**
	Water only	Continuous bed	LDs	16 x 16
0.17	•	•	•	•
0.24	•	•	•	•
Size shifting experiments				
Velocity (m/s)	**Particle size regions (C = 0.3 vol%)**			
	Phillips domain	Intermediate domain	Shields domain	Mixed domain
0.25	•	•	•	•
0.34	•	•	•	•
0.39	•	•	•	•

The generation or suppression of near-interface turbulent activity is an important focus of this study. An advanced and non-intrusive tool – PIV – was used to quantify the frequency and intensity of the near-wall turbulent activity. It was assumed that the sublayer region dominated by local turbulent burst-sweep action is responsible for selective particle removal. Coherent structures (burst-sweep) are analyzed and compared with available model predictions.

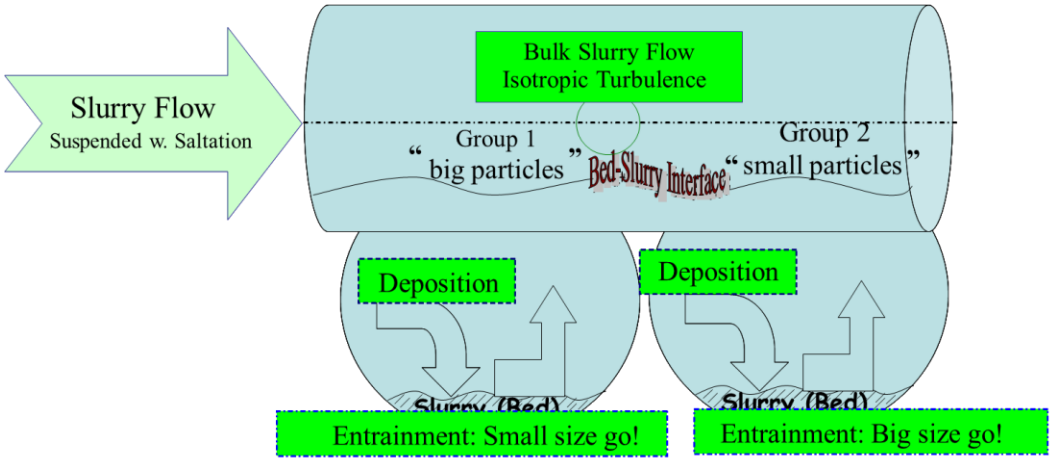

Figure 1.4 Schematic of selective deposition-removal between the slurry bed and the bulk flow

To study PSD shifting, four groups of experiments were conducted. Particle sizes for each experiment were selected in a way that corresponds largely to one of these four specified groups:

Group 1 – mostly particles smaller than 100 µm, Phillips domain

Group 2 – d_{50} around 100 µm, intermediate domain

Group 3 – mostly particles larger than 100 µm, Shields domain

Group 4 – full range of sizes, similar to oil sands particle size range, 1–500 µm, mixed domain

One of the essential types of information obtained during the experimental program (Tables 1.1 and 1.2) is the selective deposition-removal at transport (bulk) velocities below the critical deposition velocities (Figures 1.2 and 1.4). This information has not been consistently assessed in the literature so far and is considered essential in the present investigation. It is assumed that for a certain "initial concentration" and at a certain bulk velocity (maintained constant at a value below the critical deposition velocity) a steady size-concentration is achieved in the bed and in the slurry above. This pseudo-equilibrium size-concentration characteristic is assessed for each of the experiments in Tables 1.1 and 1.2 at each level of velocity. Sampling of the deposited bed is conducted accordingly

At equilibrium, the lift forces acting on a solid particle are equal to the holding forces. The net result of attractive, gravitational, and turbulence-related forces acting on individual particles depends on the particle distance from the sand bed or wall and the particle size. For example, a small particle (e.g., between 1 and 60 µm) lying at the bottom of the flow channel or on the pipe bed is expected to be immersed in the viscous sublayer.

Entrainment of (stagnant) fluid from the viscous sublayer into the main (turbulent) stream has been observed in both atmospheric turbulent phenomena and duct (internal) flow. The development of coherent structures responsible for the observed entrainment and jets emerging from the viscous layer has been schematically illustrated by Praturi and Brodkey [6] as a process evolving from the viscous layer intrinsically associated with turbulent flow conditions. The intermittent bursting nature of the “laminar” layer, also called “intermittency”, reported by Townsend [26] and Corrsin and Kistler [27], is not yet sufficiently understood and exploited.

It is assumed at this stage of the study that entrainment and re-deposition mechanisms controlled by buoyant and turbulent local conditions are taking place simultaneously at two different locations:

- Turbulent core
- Viscous sublayer (previously called laminar sublayer)

Figure 1.5, using the Praturi and Brodkey [6] conceptual description of span-wise vortices responsible for inflow-outflow viscous sublayer activity, suggests a mass transport of particles from the bed into the main (turbulent) flow supported by intermittent out-bursting from the viscous sublayer.

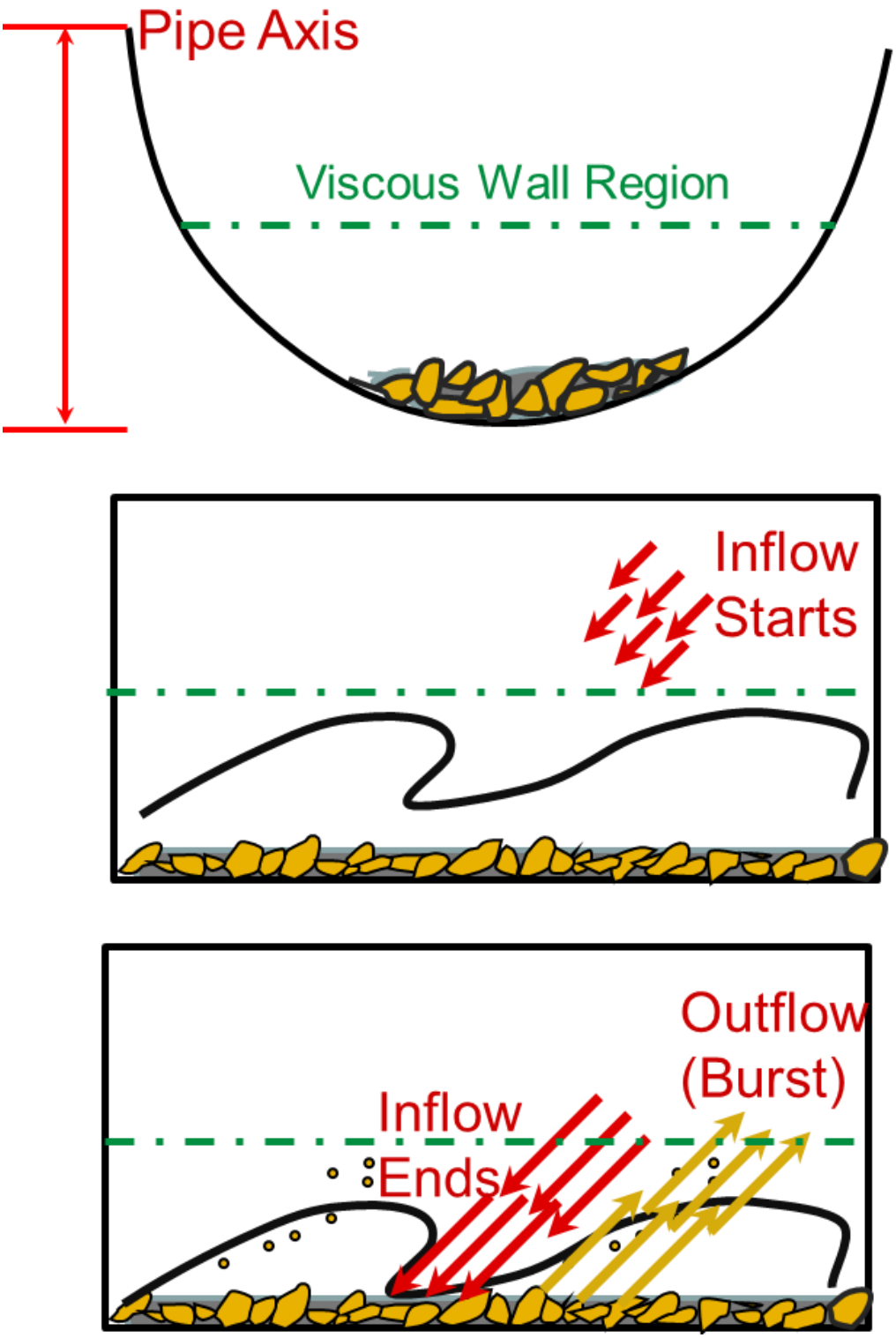

Figure 1.5 Idealized description of laminar sublayer (LSL) and two-stages of intermittent inflow-outflow condition responsible for selective entrainment of bed particles into main turbulent flow (after Praturi and Brodkey [6])

A statistical description of this activity was suggested first by Cleaver and Yates [13, 28] and was recently used to explain selective (size-specific) removal of fines (or crystals) from the viscous sublayer (or fines bed) region (Absil and Ooms [29], Toma et al. [30]). Phillips [25] suggested that the removal-deposition activity controlled by intermittency of the viscous sublayer preferentially removes relatively large particles from a bed populated by small particle sizes, say, up to approximately 60 μm.

At the outset of this experimental study it is assumed that a co-current, secondary size-sorting process takes place that could be described by the buoyant-turbulent forces active in the turbulent core. This process was observed and described first by Shields [17], and is well documented and considered essential for assessing sedimentation (Yalin [31]) for a particle size range usually in excess of 100 μm.

The “Shields” (assumed) core-turbulent sorting activity results in the preferential entrainment of relatively small particles. The “Phillips” sorting activity results in the preferential entrainment of larger particles.

The existence of two entrainment zones limited by two separate and divergent wall shear stress versus (equivalent) particle diameter was experimentally confirmed by Absil and Ooms [29] using a gas tunnel and calcium carbonate particles and Toma et al. [32]. The effectiveness of the removal mechanism in the Phillips zone was also indirectly confirmed by Toma et al. [30] using a waxy crude fluid. However, the synergistic action of two (apparently) independent

deposition-removal mechanisms when a broad range of particle sizes are exposed to the turbulent shear action is not well understood.

The experiments performed use only water and water-wet silica, avoiding the occurrence of any gas/liquid interface.

1.5 Contributions of the Present Research

The demand for hydrotransport of solid-liquid mixtures through pipelines over short and long distances remains strong. In particular, the oil sands mining industry depends heavily on slurry hydrotransport by pipeline, as it has proved operationally successful and economically effective.

As with any other industry, the improvement and maturation of the pipeline hydrotransport industry is affected by many factors. Improved understanding of the various components of the system will enable improved and more accurate designs and ensure better performance outcomes, lower capital and maintenance costs, and more reliable and safe systems to meet the industry requirement for economical, high-quality, continuous production.

Considerable experimental work has been conducted to study the effects of different particle entrainment regimes in air, but not enough experiments have been performed in aqueous media. Bagnold [33], while working on particle entrainment from air flow, pointed out that, for particles smaller than 50–80 μm, the attraction force cannot be ignored and the threshold velocity for this range of

sizes is higher due to cohesion effects. The present study investigates a broad range of coexisting particle sizes.

The aim of this study is to increase the knowledge and understanding of the slurry flow pipeline transportation in optimizing handling techniques and developing engineered solutions for pipeline system design in an effort to reduce energy consumption and achieve better and more economical outcomes.

The research presented in this thesis aims to increase our knowledge and understanding of slurry pipeline transportation, especially for velocities below the critical removal and deposition velocity, which typically occurs in the industry due to the transportation limitations.

However, the specific contributions of this study are as follows:

- Design and construct a large-scale experimental facility that could be used for studying multi-phase flow of solid-liquid mixtures (i.e., slurry flow) in horizontal pipelines

- Studied the effect of coherent structures of near-wall turbulence on radial transport of fines to/from interface to the bulk flow by using the advanced PIV technique

- Investigated the effect of the naturally shaped interface in minimizing turbulent energy dissipation using both microscopic and macroscopic measurements:

- Microscopic PIV measurements of coherent structures

- Macroscopic pressure drop measurements

- Conducted series of experiments with a broad spectrum of particle sizes to study the effect of different forces on selective removal of particles exposed to the turbulent flow from the bed and changes in the initial PSD with time. Measurements of PSD shifting are made possible with the aid of a specially designed bed extractor. The experimental results are used to validate the hypotheses for selective removal of particles from the bed

The results obtained using the proposed approach are expected to open new avenues for controlling in-line classification-separation methods applicable to surface-mined oil sand slurry processing and transport.

1.6 Structure of the Thesis

The overall structure of this thesis is as follows:

Chapter 1 introduces the subject and briefly discusses the significance of slurry transportation, especially in oil sands production. It also provides brief background information on the topics addressed in this study.

Chapter 2 describes the experimental setup. This includes components of the experimental loop and its control system as well as the operating conditions and intended project accomplishments. Detailed descriptions of the components and their operation are given in the relevant chapters.

In Chapter 3, the methodology of PIV data acquisition is explained and the analysis methodology is presented. Validation of the data obtained is explained and sample images and vector maps are provided.

Chapter 4 focuses on the reduction of frictional pressure drop associated with formation of natural lenticular deposits during pipeline transport of low-concentration slurries. Findings from the experimental measurements are further assessed by PIV measurements to assess the turbulent kinetic energy in the experimental cases.

Chapter 5 presents preliminary results from the experiments and the use of PIV to assess the effects of near-wall turbulence on selective removal of particles from the slurry bed. This part has been already published as a journal paper and is, therefore, presented as a separate chapter.

Further and more comprehensive experimental results on selective removal and deposition of particles from the slurry bed are presented in Chapter 6. The results are summarized and compared against the hypotheses.

Chapter 7 presents conclusions from the study and makes recommendations for future work.

Keywords: bed, interface, turbulent flow, selective removal, lenticular deposit, PIV, particle size distribution

1.7 References

[1] Newitt, D. M., Richardson, J. F., Abbott, M., and Turtle, R. B., 1955, "Hydralic Conveying of Solids in Horizontal Pipes," Chemical Engineering Research and Design, 33a(-), pp. 93 - 113.

[2] Shamlou, P. A., 1987, "Hydraulic Transport of Particulate Solids," Chemical Engineering Communications, 62(1-6), pp. 233-249.

[3] Brown, N. P., and Heywood, N. I., 1991, *Slurry Handling : Design of Solid-Liquid Systems, Elsevier Handling and Processing of Solids Series.*, Elsevier Applied Science, London; New York.

[4] Shook, C. A., Gillies, R. G., and Sanders, R. S. S., 2002, *Pipeline Hydrotransport : With Applications in the Oil Sand Industry, Src Publication ; No. 11508-1e02.*, SRC Pipe Flow Technology Centre, Saskatoon, SK.

[5] Corino, E. R., and Brodkey, R. S., 1969, "A Visual Investigation of the Wall Region in Turbulent Flow," Journal of Fluid Mechanics, 37(01), pp. 1-30.

[6] Praturi, A. K., and Brodkey, R. S., 1978, "A Stereoscopic Visual Study of Coherent Structures in Turbulent Shear Flow," Journal of Fluid Mechanics, 89(02), pp. 251-272.

[7] Yung, B. P. K., Merry, H., and Bott, T. R., 1989, "The Role of Turbulent Bursts in Particle Re-Entrainment in Aqueous Systems," Chemical Engineering Science, 44(4), pp. 873-882.

[8] Jimenez, J., Moin, P., Moser, R., and Keefe, L., 1988, "Ejection Mechanisms in the Sublayer of a Turbulent Channel," Physics of Fluids, 31(6), pp. 1311-1313.

[9] Liu, Z. C., Landreth, C. C., Adrian, R. J., and Hanratty, T. J., 1991, "High Resolution Measurement of Turbulent Structure in a Channel with Particle Image Velocimetry," Experiments in Fluids, 10(6), pp. 301-312.

[10] Robinson, S. K., 1991, "Coherent Motions in the Turbulent Boundary Layer," Annual Review of Fluid Mechanics, 23(1), pp. 601-639.

[11] Marusic, I., Mckeon, B. J., Monkewitz, P. A., Nagib, H. M., Smits, A. J., and Sreenivasan, K. R., 2010, "Wall-Bounded Turbulent Flows at High Reynolds Numbers: Recent Advances and Key Issues," Physics of Fluids, 22(6), pp. 065103-24.

[12] García, M., López, F., and Niño, Y., 1995, "Characterization of near-Bed Coherent Structures in Turbulent Open Channel Flow Using Synchronized High-Speed Video and Hot-Film Measurements," Experiments in Fluids, 19(1), pp. 16-28.

[13] Cleaver, J. W., and Yates, B., 1973, "Mechanism of Detachment of Colloidal Particles from a Flat Substrate in a Turbulent Flow," Journal of Colloid and Interface Science, 44(3), pp. 464-474.

[14] Absil, F. G. J., 1986, "The Entrainment of Particles by a Turbulent Boundary Layer," Ph.D. thesis, Delft University of Technology, Netherland,

[15] Nelson, J. M., Shreve, R. L., Mclean, S. R., and Drake, T. G., 1995, "Role of near-Bed Turbulence Structure in Bed Load Transport and Bed Form Mechanics," Water Resour. Res., 31(8), pp. 2071-2086.

[16] Sumer, B., Chua, L., Cheng, N., and Fredsøe, J., 2003, "Influence of Turbulence on Bed Load Sediment Transport," Journal of Hydraulic Engineering, 129(8), pp. 585-596.

[17] Shields, A., 1936, "Anwendung Der Ahnilchkeitsmechanik Und Der Turbulenzforschung Auf Die Geschiebebewegung Mitteilungen Der Preuss," Versuchsanst. F. Wasserbrau und Schiffbau, Berlin, Heft, 26(see Yalin, M. S., 1977), pp.

[18] Bagnold, R. A., 1973, "The Nature of Saltation and of 'Bed-Load' Transport in Water," Proceedings of the Royal Society of London. A. Mathematical and Physical Sciences, 332(1591), pp. 473-504.

[19] Gavignet, A. A., and Sobey, I. J., 1989, "Model Aids Cuttings Transport Prediction," SPE Journal of Petroleum Technology, 41(9), pp. 916-921.

[20] Lavelle, J., and Mofjeld, H., 1987, "Do Critical Stresses for Incipient Motion and Erosion Really Exist?," Journal of Hydraulic Engineering, 113(3), pp. 370-385.

[21] Nelson, J. M., Mclean, S. R., and Wolfe, S. R., 1993, "Mean Flow and Turbulence Fields over Two-Dimensional Bed Forms," Water Resour. Res., 29(12), pp. 3935-3953.

[22] Mclean, S. R., Nelson, J. M., and Wolfe, S. R., 1994, "Turbulence Structure over Two-Dimensional Bed Forms: Implications for Sediment Transport," J. Geophys. Res., 99(C6), pp. 12729-12747.

[23] Niño, Y., Lopez, F., and Garcia, M., 2003, "Threshold for Particle Entrainment into Suspension," Sedimentology, 50(2), pp. 247-263.

[24] Oroskar, A. R., and Turian, R. M., 1980, "The Critical Velocity in Pipeline Flow of Slurries," AIChE Journal, 26(4), pp. 550-558.

[25] Phillips, M., 1980, "A Force Balance Model for Particle Entrainment into a Fluid Stream," Journal of Physics D: Applied Physics, 13(2), pp. 221.

[26] Townsend, A., 1949, "The Fully Developed Wake of a Circular Cylinder," Australian Journal of Chemistry, 2(4), pp. 451-468.

[27] Corrsin, S., and Kistler, A. L., 1954, "Free-Stream Boundaries of Turbulent Flows," Technical Report No. National Advisory Committee for Aeronautics; Report 1244,

[28] Cleaver, J. W., and Yates, B., 1976, "The Effect of Re-Entrainment on Particle Deposition," Chemical Engineering Science, 31(2), pp. 147-151.

[29] Absil, F. G. J., and Ooms, G., July 1-4, 1986, "The Entrainment of Particles by a Turbulent Spot in a Laminar Boundary Layer," eds., Ecully, France, pp.

[30] Toma, P., Ivory, J., Korpany, G., Derocco, M., Holloway, L., Goss, C., Ibrahim, J., and Omar, I., 2006, "A Two-Layer Paraffin Deposition Structure Observed and Used to Explain the Removal and Aging of Paraffin Deposits in Wells and Pipelines," Journal of Energy Resources Technology, 128(1), pp. 49-61.

[31] Yalin, M. S., 1977, *Mechanics of Sediment Transport*, Pergamon Press, Oxford; New York.

[32] Toma, P., Zeinali, H., and Kuru, E., 2010, "Selective Extraction of Fines During Bed-Slurry Transportation - an Effect of Turbulent Burst-Sweep Activity: Experimental and Theoretical Investigations," 7th North American Conference on MultiphaseTechnology. Banff, Canada, 2-4 June 2010, pp. 325-342.

[33] Bagnold, R. A., 1960, "The Re-Entrainment of Settled Dust," International Journal of Air Pollution, 2(3), pp. 357-363.

2 Description of Multiphase Flow Experimental Facility

2.1 Introduction

The slurry flow loop described here and illustrated in Figure 2.1 was designed, and developed to study the dynamics of solid-liquid (multiphase) flow phenomena applicable in variety of industrial applications. The flow loop was designed to facilitate slurry transport in a horizontal pipeline and to allow visualization of bed deposits and their propagation at the bottom of the pipe.

The flow-loop enables extraction of samples from bed deposits which can be further analyzed for determination of solids concentration and particle size distribution (PSD). Flow loop is also equipped with state-of-the-art instrumentation, particle image velocimetry (PIV), allows measurement of instantaneous and fluctuation 2D velocities in the investigation area.

The slurry loop was constructed using transparent optic quality glass, first to visualize slurry flow patterns, and, second, to enable the use of PIV to obtain the instantaneous velocity vector field. The glass tubes are interconnected by custom-designed and -built stainless steel unions that facilitate installation and use of various instruments, including pressure taps, pitot tube, special bottom extractors, and, if needed the capability to install isokinetic probe and extract slurry samples to obtain the cross-sectional concentration distribution. The loop operates continuously at turbulent flow conditions. The pipe ID is 95 mm and the loop is

approximately 15 m long. The upper horizontal section is approximately 1.8 m above the laboratory floor (see Figure 2.1 and 2.2).

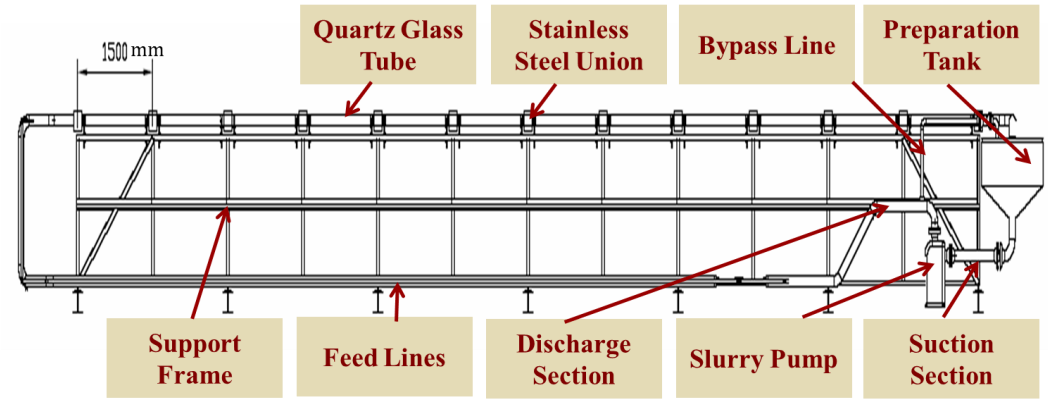

Figure 2.1 The side view of the frame module of the horizontal multiphase experimental facility

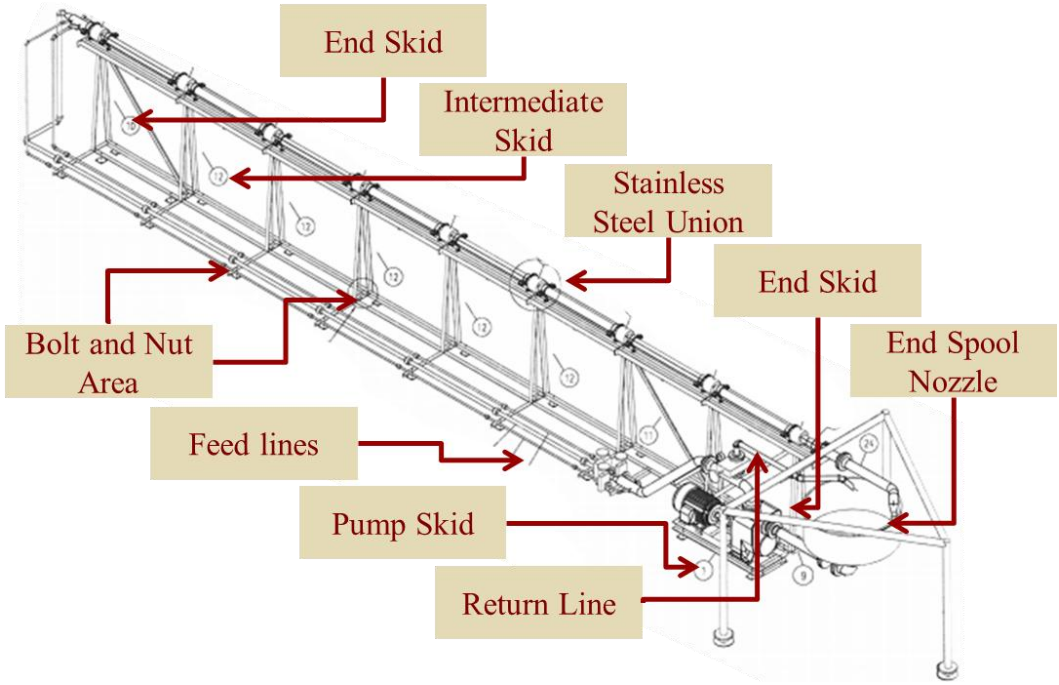

Figure 2.2 The top view of the frame module of the horizontal multiphase experimental facility. The module assembly consists of the frame and all the modules supporting the glass tubes

The loop accommodates experiments at different flow rates. The bulk flow velocity in the visualization section can be controlled in a range from 0.15 to 1.5 m/s without pipe modifications. In this work, the system was run at velocities below the critical deposition velocity to perform experiments involving slurry transport with a bed deposit.

In addition to facilitating the experimental research described in this dissertation, this flow loop continues to serve as a base for ongoing research into slurry and multiphase flow.

2.2 Safety Features

Safety was a paramount consideration in designing and installing the flow loop setup. Special provisions are required whenever a system has the potential for high pressure/supercritical conditions and utilizes laser beams, both in the initial design phase and during system operation. The slurry loop location, piping, operational procedures, and bypass line were key safety considerations during the design and construction.

2.2.1 System Location

The slurry flow loop was located in a lab with a rectangular shape, approximately 30 m long, 5 m wide, and with two exit doors, each 1.9 m wide. The loop in total, including the pipeline and preparation and recirculation tank, is approximately 17 m long and is positioned roughly in the middle of the lab, which provides enough

space on both sides to walk around the loop safely and, in the case of danger, evacuate the area safely.

2.2.2 Piping and Bypass Line

The slurry flow loop utilizes two feed lines with IDs of 38.1 mm (1-1/2 in.) and 63.5 mm (2-1/2 in.); both are smaller than the visual test section (95 mm ID). The feed lines were made smaller than the visual section to ensure that particle deposition during experimental runs is confined to the visual section and does not occur in the feed lines. Bulk flow velocity in a pipe is inversely proportional to the square of pipe diameter; so, for example, if the flow velocity for a given flow rate is 1 m/s in the visual section, it would be 6.2 m/s in the 38.1-mm feed line or 2.2 m/s in the 63.5-mm feed line. This slurry loop operates below the critical deposition velocity (the velocity at which particles start depositing at the pipe bottom) in the visual section, but the choice of much smaller feed lines prevents deposition in these lines during experiments. The flow loop was designed to operate at pressure up to 100 psig, however, the normal operating pressure for the system is atmospheric. An emergency pump shutdown handle is positioned close to the variable-frequency device (VFD) and, in case of any danger, can shut the whole system down.

A rupture disk is located after the discharge part of the pump and opens into the bypass line emptying into the tank. The rupture disk is set at 70 psig. If the pressure spikes above this value for any reason, most likely due to closed valves

in the system, the rupture disk yields and the discharged flow is directed to the tank.

2.2.3 Operating Procedures

The system is a closed design, but modifications made to the loop allow the system to operate as an open loop. Two valves are provided, at the both ends of the test section. Deposited particles can be held in an isolated section while the rest of the loop is cleaned of any particles. In this way, because no new particles are introduced to the loop, operation would be similar to the open loop case.

The operating procedure for the flow loop is critical from the standpoints of safety and experimental repeatability. For preparation of the slurry, particles are added to the aqueous system and whereas the particle size distribution (PSD) is very important for selective removal particles from the bed, the system is cleaned between each experiment. It is also drained immediately following each experiment and cleaned again before being filled with tap water to clear away rust and debris. All system components are made from non-rusting materials, including the feed lines (made of PVC), union joints (made from stainless steel), and galvanized inner parts. However, the use of some corrosion-susceptible parts was unavoidable, such as the slurry pump. It was therefore necessary to drain the system after each experiment and clean it again before refilling the system.

For safety, before turning on the pump, a walk-around inspection of the whole system should be completed. All valves must be checked to make sure that flow lines are not closed and the system is safe to operate.

2.3 Experimentation

2.3.1 Slurry Flow Loop Set-up

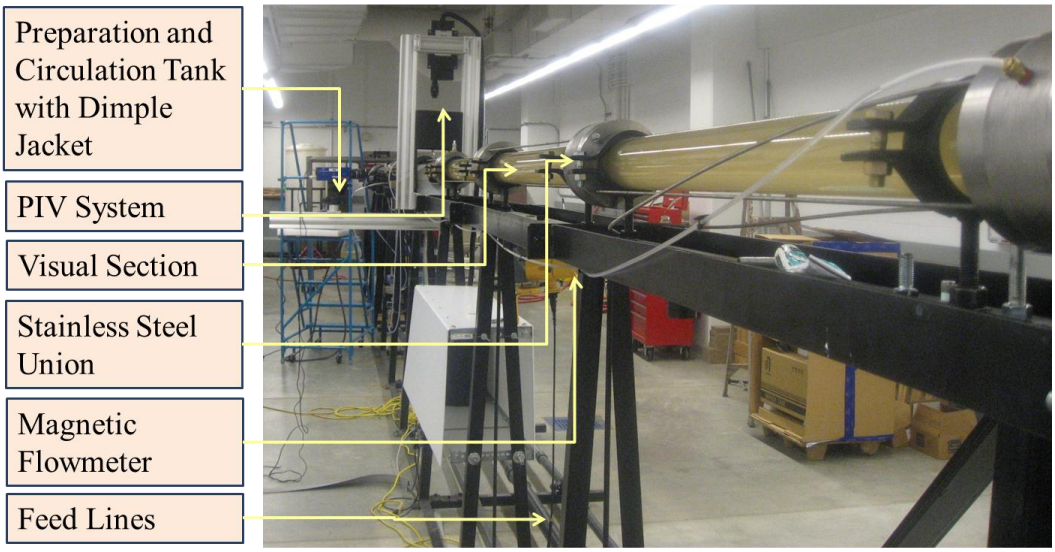

Figure 2.3 The photo of the experimental setup. The PIV measurement location is also shown

Figure 2.1 and 2.2 includes a schematic of the slurry flow loop frame. Figure 2.3 shows the employed experimental setup. The upper part of the loop is made up of transparent quartz glass tubes each 1.5 m long and connected by custom-designed stainless steel unions. Both ends of the two feed lines are connected by "quick connector" hose couplings.

The slurry flow loop consists of instrumentation, control, and communication subsystems and a number of major components.

2.3.1.1 Preparation and circulation tank

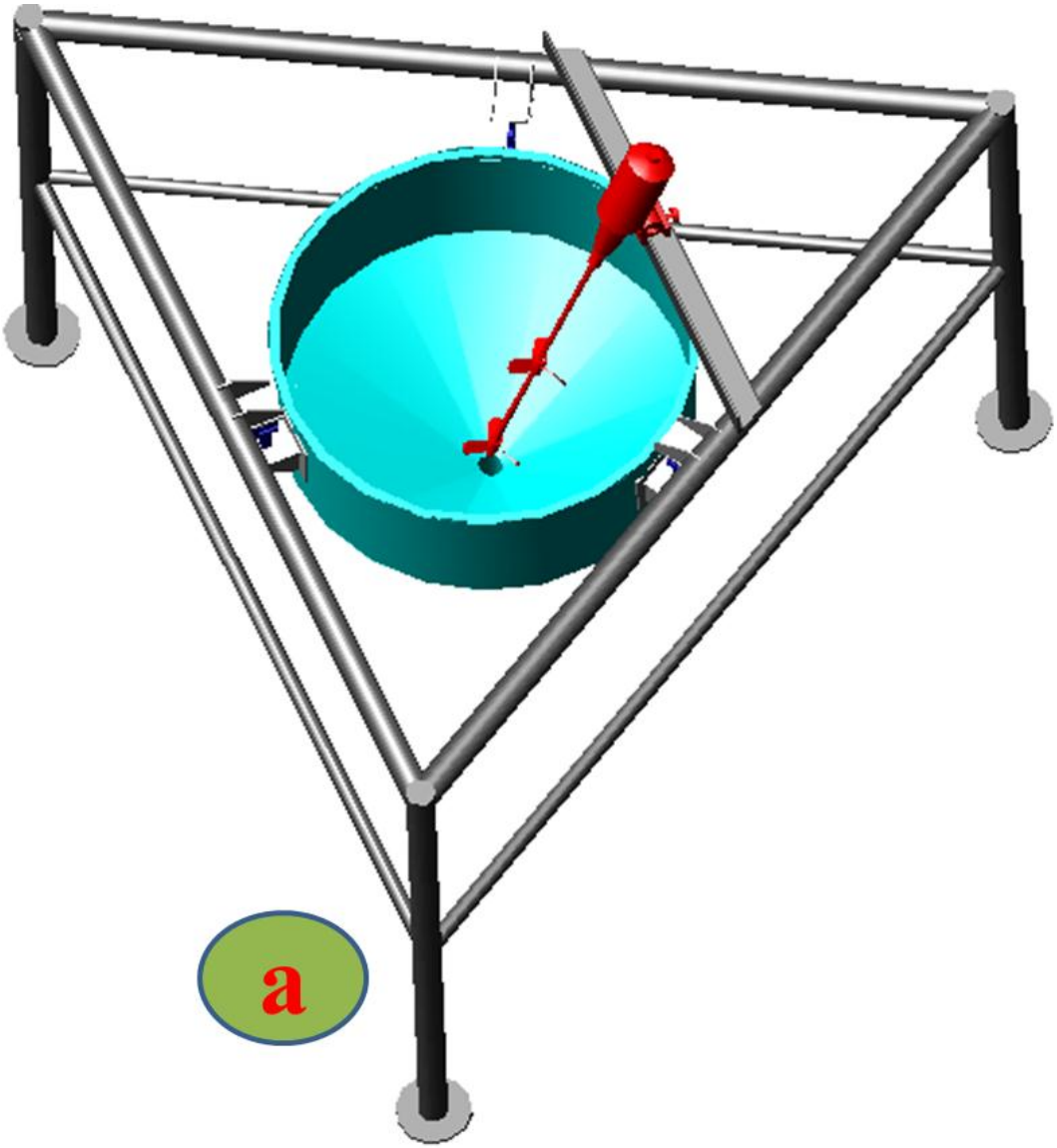

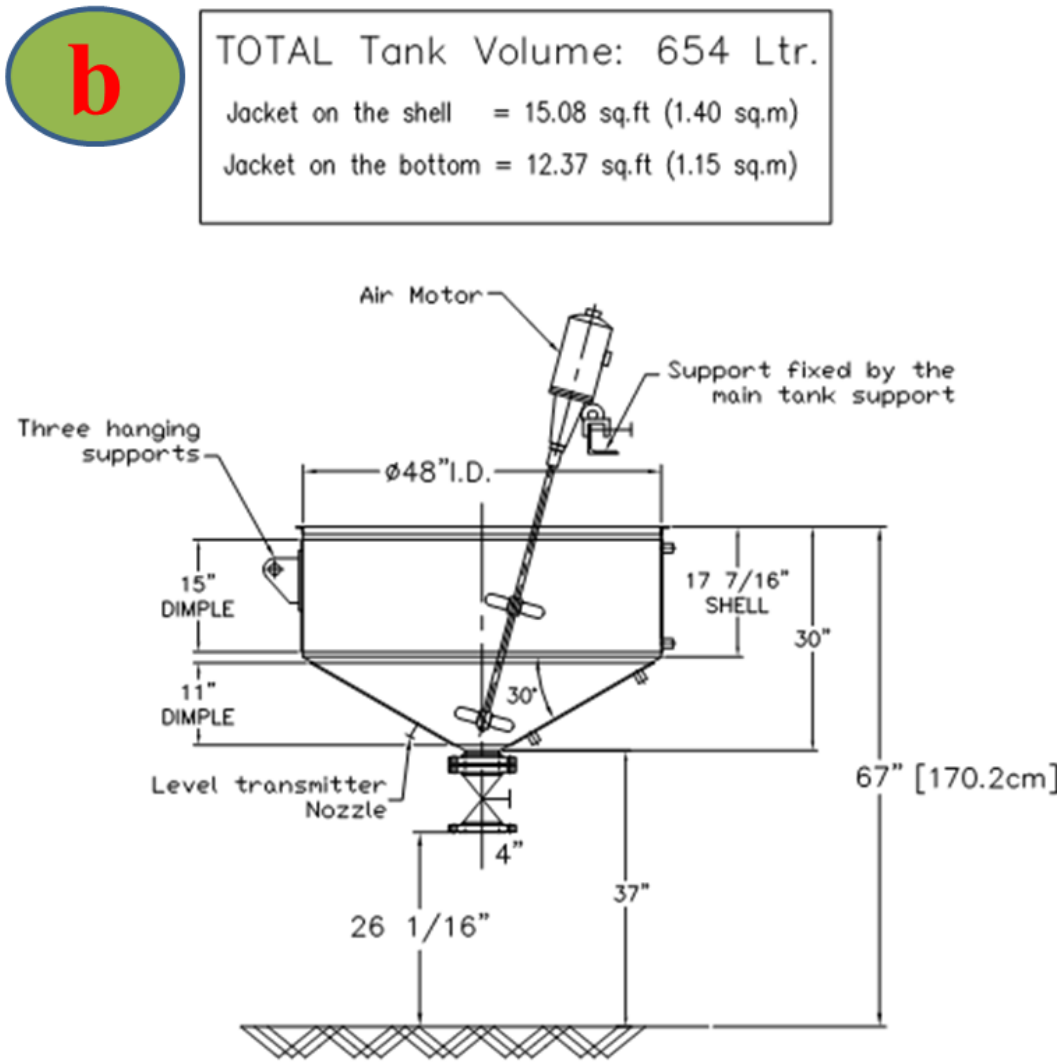

Figure 2.4 Slurry preparation and circulation tank with pneumatic agitator installed; (a) top view, (b) side view (dimensions are given)

Preparation and circulation tank equipped with:

- Dimple jacket for heating and cooling
- Pneumatic agitator for mixing the slurry

- Baffles to prevent vortices at the tank, propellant sloshing, and air suction into the system

- Micron-rated filter bag positioned inside the stainless steel collar to catch the particles as needed

2.3.1.2 Flow lines in the loop

The flow lines in the slurry flow loop for running the experiments are listed below:

- 102 mm (4 in.) flow line from tank to the suction part of the pump

- 102 mm (4 in.) flow line from discharge part of the pump to the feed lines

- 50.8 mm (2 in.) bypass line after pump discharge directed to the preparation tank

- high-pressure hose between the bypass line and the feed lines to install the rupture disk for safety

- 38.1 mm (1½ in.) and 63.5 mm (2½ in.) feed lines with quick connectors at both ends

- 63.5 mm (2½ in.) vertical section which connects the feeding lines to the visual test section

- 95 mm ID (3.74 in.) with 5-mm thick transparent quartz glass pipe each 1.5 m long were connected custom-designed stainless steel unions

- 95 mm ID return line with diameter reduced to 2 in. before it ends at the tank

2.3.1.3 Control valves at the flow lines

Mechanically operated pinch valves along the flow line for controlling the flow of slurry and isolating the experimental section from the rest of the loop. The pinch valves are lined with rubber and are therefore corrosion resistant in the presence of slurry and sand particles. Their locations in the flow loop are as follows:

- 4-in. pinch valve at the bottom of the preparation tank to disconnect the tank from the rest of the loop as needed.

- 2-in. pinch valve after the pump discharge section in bypass line. The bypass line is for partial return of flow to the tank if needed, and the rupture disk line is connected to the bypass line.

- 4-in. pinch valve after bypass divider section, before the feed lines. Closing this valve helps in cleaning the loop, especially the inner parts of the pump.

- 2.5-in. pinch valve right before the vertical section after the feed lines. This valve is used when particles need to be deposited in the test section – after all particles are deposited selective-removal experiments can be started. While this valve s closed in combination of the next 4-in. pinch valve, the rest of system can be cleaned of particles and filled with tap water.

- 4-in. pinch valve after test section and before the return line. This valve, in combination of the 2.5-in. valve described above, is used to isolate the test section.

- 4-in. three-way valve to divert the flow perpendicular to the flow direction for cleaning purposes, as needed.

2.3.1.4 Slurry flow loop instrumentation

Starting from the preparation tank, the following instruments are incorporated:

- Three load cells, model Artech 20210-2.5kT S-Beam load cells, alloy steel, class III in combination with SSWM-Vll-B tension weighing module – used for tank weighing, scale conversions, and in-line force measurement applications. The tank hangs from these three load cells weighing module to measure the slurry concentration by weighing the added particles and the water.

- Pressure transducer installed at the bottom of the tank to measure the hydrostatic pressure, from which the depth of the added water can be obtained.

- Pressure transducer was installed right after the pump discharge to measure pump output pressure. There is pressure gauge on the pump as well, so the readings from both can be compared for accuracy and the pressure gauge provides instantaneous feedback.

- Temperature transmitter (sensor) was installed after the pump discharge to measure the temperature of the circulating liquid/slurry in the system.

- Magnetic flowmeter was installed in the 2.5-in. vertical flow line section. By measuring the flow rate the bulk velocity after that section of the flow loop can be calculated. The magnetic flowmeter was chosen because it is the best option in the presence of erosive materials.

- Two differential pressure transducers were installed in the test section. The first hole was tapped on the first union (entrance) and the other hole was tapped at the last union, approximately 14 m apart. The second differential pressure transducer was installed between fifth and seventh stainless steel unions in the middle of the loop, with taps being 3 m apart.

- A pitot tube and an isokinetic extraction probe measure the velocity and slurry concentration, respectively, at different levels of the cross-section. Alternatively, PIV is a much more advanced and error-free technology, and was therefore used instead.

- Two custom-designed bottom extractors (see Figure 2.5) are installed at the fifth and seventh unions from the entrance. Using these bottom extractors and with the help of the vacuum pump, samples can be taken from the bed deposits.

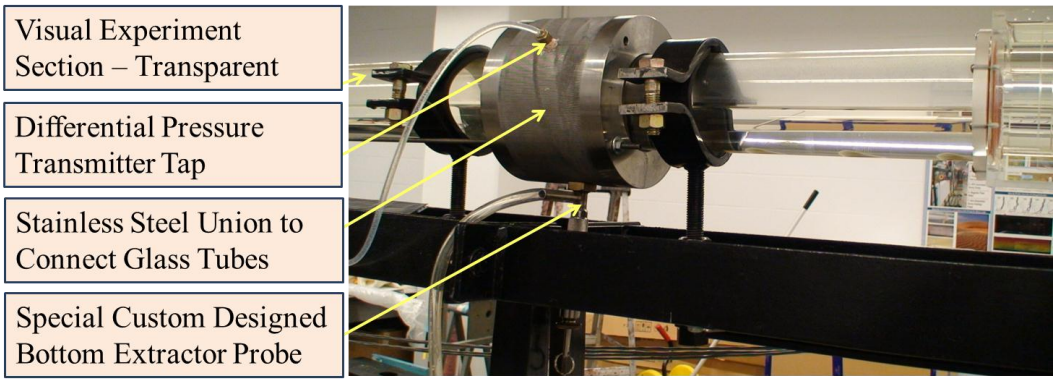

Figure 2.5 Bottom extractor probe to sample deposits at the pipeline bottom

2.3.2 Particle Image Velocimetry (PIV) System

Particle image velocimetry (PIV) is a nonintrusive, whole-flow-field technique that was used to measure the instantaneous velocity vector maps in the investigation area. PIV was used approximately 5.5 m downstream from the entrance, where the flow is completely developed (see Figure 2.6). The PIV

consists of a CCD camera, a double-pulsed laser, an optical arrangement to convert the laser output to a light sheet, a synchronizer, and, if needed, tracer particles can be added to the flow.

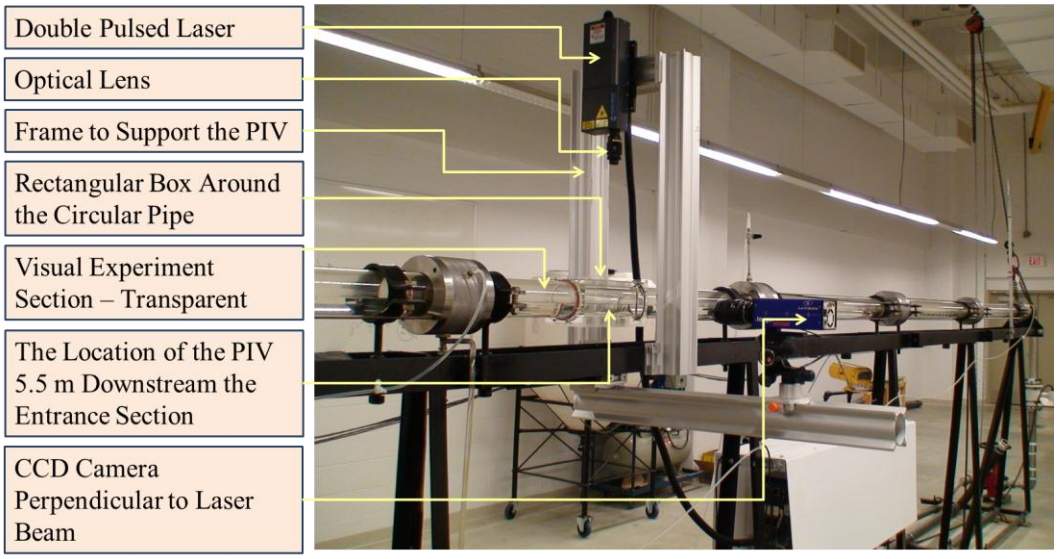

Figure 2.6 PIV system location approximately 5.5 m downstream the entrance

2.3.3 Slurry Flow Loop Pump and Control System

A Gorman-Rupp self-priming centrifugal pump (model U4B60S-B/F), size 4 in. x 4 in. , maximum operating pressure 883 kPa (128 psi) ADI-fitted, cast iron casing, ADI hardened impeller, wear-plate and seal plate and oil-lubricated pump – used for the slurry flow loop. Pump is directly driven by a 30-hp, 3-phase, 1750-rpm, 460-V, TEFC electric motor. Pump and motor are mounted on a common base plate with coupling and guard. The pump can handle approximately15% quartz /water in suspension. The pump also was equipped with variable frequency device (VFD) to control pump speed to obtain different bulk flow rates. The VFD varies

the frequency of input power to the motor, thereby controlling motor speed. The VFD is a Teco Westinghouse model MA 7200-4030-N1.

Figure 2.7 shows the pump performance curve. The performance curve for centrifugal pumps is a tool that one can see how a pump will perform in terms of head and flow. The head is giving in the vertical axis and the feed flow variables were plotted in the horizontal axis.

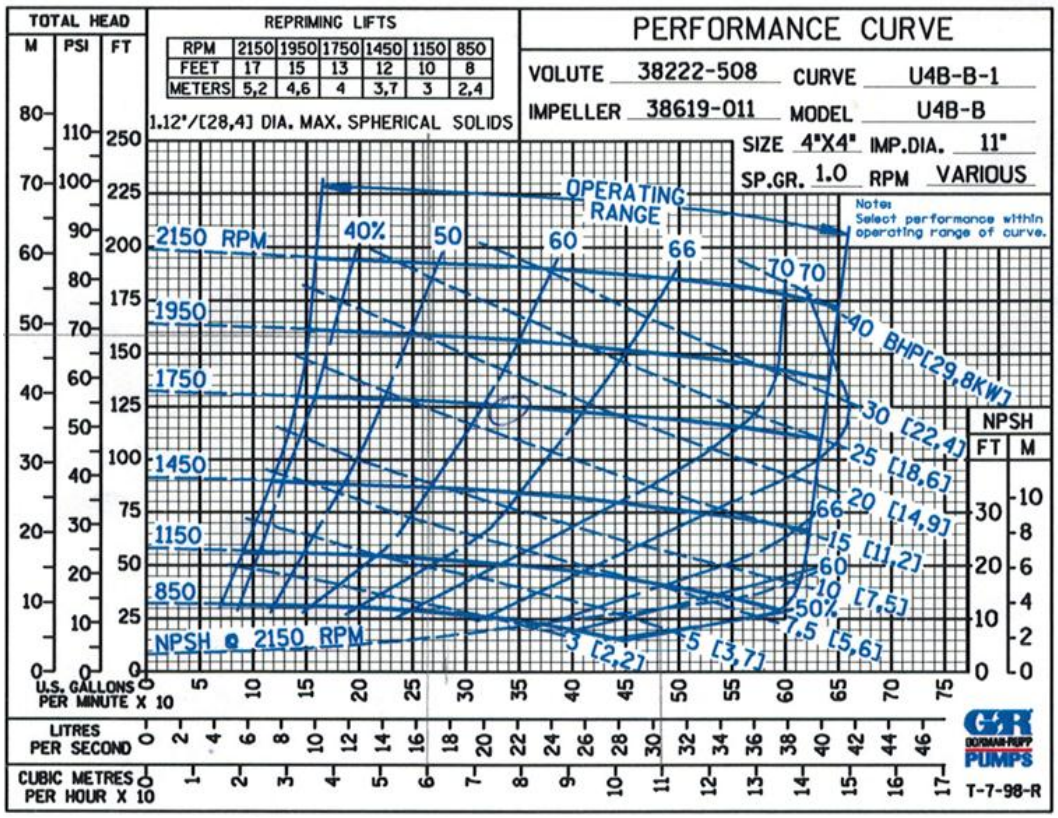

Figure 2.7 The pump performance curve which also provides information on pump efficiency. The pump operates at the intersection of the pump's performance curve and the system head curve

2.3.4 LabView for Data Acquisition and Instrument Control

All instrumentation components in the slurry flow loop were connected to the LabView monitoring and control system, and were controlled by a dedicated computer. Some instruments are only monitored via LabView software and some are controlled as well as monitored. The VFD accepts 0-5 V, 0–10V, and 4–20 mA analog inputs to control the pump motor speed. The VFD provides 0–10 V analog output; accordingly, the inputs from the VFD to LabView were 0–10 V signals.

A 12-VDC excitation voltage for the load cells (cells accept from 10 VDC to a maximum of 15 VDC) is provided by an external power supply through LabView. The load cells output is 3.0020 mV/V at 2500 lb. The rest of the slurry flow loop instruments, which are listed above, have 4–20 mA analog outputs wired to the LabView input. Data from all instruments connected for monitor and control in LabView, can be viewed in real time and stored on the computer for further analysis.

2.3.5 Automated Image Analyzer for PSD Analysis

The automated image analyser, Leica DM6000M with objective lenses 2.5, 5, 10, 20, and 50x in combination with Leica Application Suite (LAS) and QParticles software were used for PSD analysis (see. Figure 2.8). The appropriate objective lens should be chosen depending on the particle sizes. The objective lens number denotes the lens magnification; for example, 10x.

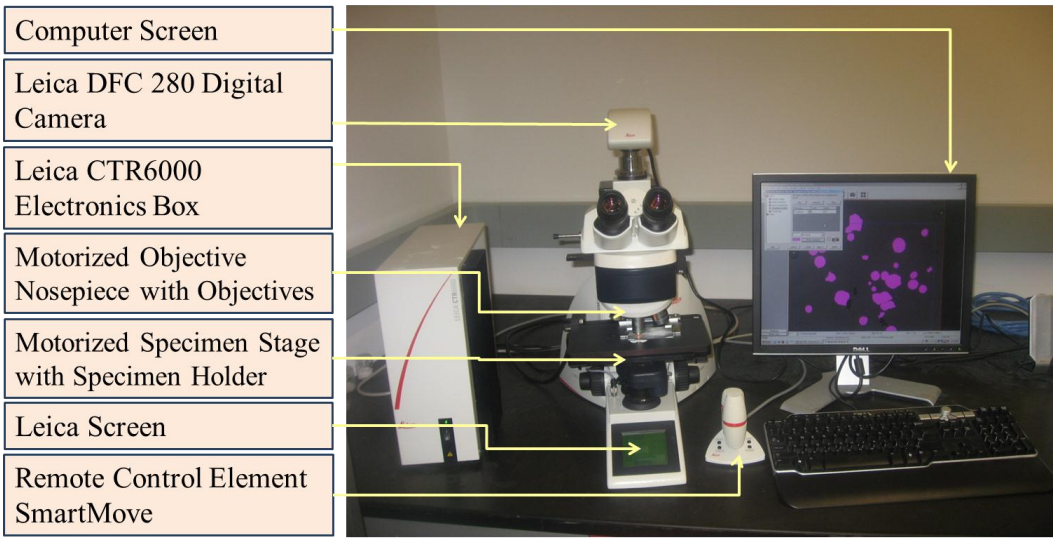

Figure 2.8 Leica automated image analyser for PSD analysis

The microscope used is equipped with a digital DFC 280 camera that transfers the real-time images to the software, and further analyses of the images captured by the automated microscope are performed. The microscope is equipped with a motorized XY stage and can also can be focused in the Z-direction. To analyze the PSD using the automated image analyzer, a good monolayer sample should first be prepared on the microscope slide and the right objective lens and focus should be selected. The specimen should be flat and perpendicular to the objective, and a scan pattern should then be defined. The microscope scans the specimen by moving it relative to the fixed objective lens in a regular meandering pattern.

An object of known size, a stage micrometer, was used to calibrate and frequently check the microscope calibration. In addition, to check for the measurement accuracy, the PSD of known particles performed by commercial sieving was

compared to results obtained by the microscope. The measurements were in good agreement. It should be mentioned that the smallest screen mesh in commercial sieving is 38 µm; commercial sieving is therefore not a suitable analysis method when dealing with particles smaller than 40 µm.

2.4 Slurry Flow Loop Operation and Project Accomplishments

Observations and measurements of the horizontal transport characteristics of slurries and identification of the most effective parameters in controlling slurry flow are essential for improving our knowledge of the transport dynamics. The specific objectives of each subsection are given below.

I. Design and build an industrial-scale slurry flow loop to operate in turbulent flow condition and mimic the actual operating conditions in industry. As sometimes, scale up the process from laboratory to field condition might be a challenge and even sometimes may not follow the same pattern and application.

II. Visualization of the process improves understanding of the true features of the phenomena under study. For this reason, the experimental section was built out of transparent quartz glass. In addition, PIV is needed to capture images from the illuminated tracer particles in the fluid flow, and it is essential to have a clear and transparent environment for the experiments.

III. Most of the research on particle deposition and removal has been conducted in flumes or in open channels and rivers. Fewer studies are devoted to the particle deposition and removal in actual pipelines. Understanding particle deposition-removal mechanisms in pipelines can facilitate the design and optimization of pipeline transportation systems.

IV. Most of the turbulent flow activities happen near the wall of the pipe. The state-of-art technology, PIV, helps to measure the effects of different parameters, including bed geometry, effectiveness of additives, and so on in enhancing or suppressing the turbulent activities adjacent to the wall.

V. All experiments with deposit beds in this study were based on dunes that formed naturally under defined conditions of pipe flow. The resulting measurements and observations of flow conditions and dune behaviour documented here therefore reflect actual pipe flow conditions and particle-flow dynamics, similar to those encountered in the field.

VI. A special bottom sample extraction probe is designed and built into the slurry flow loop to extract the samples from pipeline deposits for analysis of PSD.

VII. The automated image analyser is used for PSD analysis to study the effect of near-wall turbulent coherent structures on size-selective removal and deposition, and consequently the effect on PSD shifting. The smaller particle size analysis of extracted samples is not trackable by commercial sieving, therefore, the Leica image analyser system is applied to observe the turbulent flow effects for the broad range of particle sizes.

VIII. The small-scale wet/wet differential pressure transducer is applied to measure the differential pressure in the pipeline in the existence of the bed and water –only flow and study the effect of geometry on the frictional pressure drop.

IX. Slurry flow patterns are commonly categorized into several identifiable states. All slurry flow patterns are obtainable using the constructed slurry flow loop with suitable slurry concentrations and flow rates. All experiments in this research are conducted at the velocities below the critical deposition velocity and with low solids concentrations, mostly below 2 vol%.

The detailed operating information for each instrument and specifics on applications in individual experiments are provided in the corresponding chapters.

3 Methodology of Particle Image Velocimetry (PIV) Data Acquisition and Analysis

3.1 Introduction

Direct velocity measurements in the near-wall region of pipe flow described in the literature are mainly based on intrusive techniques such as single-point measurement by hot-wire anemometry. Most of the other available data are from simulations. Very few data are available for non-intrusive techniques such as particle image velocimetry (PIV).

During pipe flow, coherent structures develop in the viscous region. The presence of well-structured motions near the wall in the viscous sublayer results in the formation of low-speed streaks [1]. Once established, these motions usually evolve into turbulent core flow. Non-intrusive PIV laser optical measurements of the near-wall pipe flow is utilized to quantify the turbulent structures.

PIV has been used successfully in fluid dynamic applications related to fluid flow in a variety of fields including engineering sciences, biomedicine, atmospheric sciences, and aerodynamics, as well as many other fluid and flow-related disciplines.

Some typical examples of PIV applications in research are, indoor air flow distribution [2], spray characteristics measurement [3], whole-field measurement of ice velocities [4], wall heat transfer characteristics [5], free jets [6], and two-phase bubbly flows [7]. The ability of PIV to measure the whole field

instantaneously, consequently makes it possible to identify and measure the velocity fluctuations in a fluid flow, including large- and small-scale spatial structures in turbulent flow, even at high Reynolds numbers (unsteady flows).

This chapter summarizes past research using PIV instrumentation and describes the experimental setup and measurement technique, as well as validation of the experimental data for different experimental scenarios.

3.2 History and Milestones of PIV Measurement

Milestones in the research and development of PIV measurement in turbulent flow structures are summarized in Table 3.1.

Table 3.1
Summary of R&D on measurements by PIV

Ref.	Author / Year / Nature of the article	Major Findings	Remarks
[8]	Wallace et al. / 1972 / Experimental	Burst and sweep motions have larger time scales than wallward and outward interactions. Sweep has a contribution to Reynolds stress equal to that of ejection. The contributions of wallward and outward interactions account for the surplus stress, over and above ejection and sweep events.	Hot-film measurements in fully developed channel flow to assess Reynolds stress production are done at $y^+ \simeq 15$. The classified Reynolds stress including ejection, sweep, wallward, and outward interactions were identified using quadrant analysis based solely on fluctuation velocity signs, without consideration of any further conditions.

[9]	Adrian, R. J. / 1991 / Review	Compared different experimental techniques for the measurement of whole, instantaneous fields of scalars and vectors. Different techniques and modes of operation were assessed and compared. The 2D PIV technique is capable of providing accurate, high-quality measurements of instantaneous fields in a variety of laboratory-scale flows of gases and liquids.	Adrian is among the pioneers who helped to develop the PIV technique.
[10]	Westerweel et al. / 1997 / Analytical and Experimental	By the use of window offset (integer part of the displacement in pixel units) method, they showed improvement of the signal-to-noise ratio of weak turbulence data in the PIV processes.	By applying the window offset in the interrogation analysis, they implemented the procedure in processing software. There was no interruption at the time of the image acquisition.
[11]	Schmeeckle et al. / 1999 / Numerical and Experimental	The high-order Godunov scheme referred to as the CIP (cubic interpolated pseudo-particle) method was used in numerical simulations to solve Navier-Stokes and incompressible continuity equations. The fundamental PIV algorithm is to do the cross-correlation of the pixels of the same small "interrogation" area of two consecutive frames. They conclude that coherent structures at the re-attachment are highly three-dimensional. Therefore, they recommended that, in dune transport, one should consider the role of near-bed vortices in enhancing motion and transport.	Open-channel experiment with eight dunes. The measurements were done on the sixth dune. The experimental dune was 80 cm long, 40 cm wide, and 4 cm high.
[12]	Nakagawa & Hanratty / 2001 / Experimental	After analysis of fluctuating velocity field measurements they found that turbulent structures over a wavy wall are similar to those over a smooth surface, in spite of the fact that the mechanisms by which the wall maintains the turbulence are different.	Velocity was measured simultaneously with two components, LDV and PIV, at about 6000 locations. The size of the interrogation spot was 1.4 mm x 1.3 mm, which is too large to capture the fine-scale turbulence structures.
[13]	Lumley & Yaglom / 2001 / Review	They reviewed the progress of turbulence research in the last 100 years. They believe that our understanding of turbulence after 100 years is exploratory or still in its infancy. Only 13 papers on turbulence were published before 1900. They identified two threads in turbulence research: practical effects and physics of turbulence. Turbulence measurement techniques have been around for more than a century. First it was visualization, then hot-wire anemometry (over 100 years old), LDV technique (early 1960s), and 10 years later, a PIV technique.	Understanding from turbulence studies is applied; no comprehensive theory and no prediction of accuracy are demanded by designers. In order to be able to contribute to turbulence theory, one should be familiar with the nature of the experiments from the beginning, not only the resulting engineering approach.

[14]	Hyun et al. / 2003 / Experimental	They used well-established LDV to validate the PIV measurements, as LDV data were previously validated by the hot-wire anemometry technique. They compared the instantaneous and fluctuation velocity profiles obtained by PIV with those obtained by LDV and found good agreement. In their experiment they also studied the physics of the flow over dunes and got some information about coherent structures that could not be readily measured with LDV.	The experiment was conducted on fixed dunes with 400 mm wavelength, 20 mm high in an open channel flume with a 610 mm x 610 mm cross section and 10 m long.
[15]	Mao, Ye / 2003 / Experimental	In the introduction of his paper it was pointed out that some researchers had showed that the bursting phenomenon frequency for a rough surface is the same as for a smooth surface. However, in his observation, as roughness increases, multi-ejection motions are encouraged.	He studied the effects of five different roughnesses, from 0.01 mm to 10 mm, on bursting phenomena in a recirculating flume by using PIV and visual observation.
[16]	Rabenjafiman-antsoa et al. / 2007 / Experimental	PIV and ultrasonic velocity profiling (UVP) techniques were used to measure the coherent vertical structures in dune topology in a 4-cm ID glass pipe 1 m long. They found that, for the region very close to the bed, the data from UVP are better than those from PIV because of the light reflection from the artificial acrylic dune. They observed that coherent vertical structures were generated at the separation zone along the shear layer and developed further to the reattachment point.	Two fixed dunes 11 cm long, 1.5 cm high, and with lee slip angles of 45° were used in the experiment for reproducibility purposes.
[17]	Detert et al. / 2007 / Experimental	Their experiment utilized a gravel bed in a flume. Pressure sensors were mounted in the gravel layers. There was a considerable pressure drop where high-speed fluid interacted with lower-speed fluid. They concluded that this pressure drop could be the initialization point of the entrainment of single grains.	The flume was 16.5 m long and 0.9 m wide. A gravel bed 0.10 m high with particles size of d_{10} = 7.7 mm and d_{85} = 13.2 mm was placed at the bottom.
[18]	Balachandar & Bhuiyan /2007 / Experimental	Using a flume, they studied the effects of rough surfaces with aspect ratios of 0.1 to 0.15 of roughness height (ribs and dunes) to the depth of flow. Three different rib arrangements with two types of dunes were examined and the results were compared with the smooth open channel. In the near-wall zone y/d < 0.1 the effect of sweep is comparable to ejection. Based on quadrant analysis of coherent structures, the ratio of sweep to burst contribution was found to be approximately 0.8.	The open-channel recirculation flume had a rectangular cross section of 610 mm x 610 mm and was 10 m long. All measurements were done along the centerline in order to minimize the effects of secondary flow.

[19]	Wagner et al. /2007/ Experimental	By using combined stereo-PIV and PLIF, they measured the velocity and concentration fields simultaneously in a plume over a flat surface and over a wavy wall. Two main differences between them are: the lateral meandering of the scalar plume over a wavy surface, and the influence of the geometry in the separation zone. They found that a wavy wall enhances the turbulent momentum and scalar fluxes.	Flow channel with a train of 72 sinusoidal waves with a wavelength of 30 mm and wave amplitude of 1.5 mm.
[20]	Stoesser et al. /2008/ Simulation	Large-eddy simulation (LES) was applied over a train of 22 two-dimensional fixed dunes attached to the bottom of the flume. Time-averaged stream-wise velocities; streamwise, spanwise, and wall-normal turbulence intensities; and Reynolds shear stresses from simulations were compared with experimental data from another researcher. There was good agreement between the results.	The dune height in simulation was 20 mm, the dune wavelength was 400 mm, and the ratio of dune length to water depth was set at 5.
[21]	Husted et al./2009/ Experimental	Non-intrusive techniques, PIV, and phase Doppler anemometry (PDA), were used to measure the mist spray size and velocity for two high-pressure nozzles: a hollow-cone nozzle and a full-cone nozzle. They observed that, over a large range of particle velocities and particle sizes, PDA is a better technique than PIV. PIV is a better option when the droplet velocities of all the different sizes are similar.	PIV can measure the transient area and dynamics of the spray. However, PDA is good for steady-state conditions.
[22]	Deshpande et al. / 2009 / Experimental and Analytical	An experiment was conducted in jet loop reactors to explore the mean and turbulence parameters by using PIV, LDV, and HFA. The turbulence dissipation rate from computational fluid dynamics (CFD) was compared with the experimental values. At the end, they evaluated the mean flow pattern by LDV, turbulence parameters by HFA, and turbulence structures by PIV.	The drawback of HFA is that it cannot measure negative velocities, so the results of mean velocities cannot be reported. In the PIV measurements the vector spacing was 0.75 mm, which is 20 times more than the Kolmogorov length scale (η); as a result the dissipation scale is not resolved sufficiently.

In this study the PIV technique was used to investigate the occurrence and intensity of the near-wall coherent structures (burst-sweep) in turbulent flow for

different experimental conditions; water-only flow, continuous bed, and naturally shaped lenticular deposits in pipe flow.

3.3 Experimental Setup

The experimental setup is shown in Figure 3.1. Measurements were conducted in a 95-mm ID transparent glass pipe. The PIV instrument was placed approximately 5.5 m downstream from the entrance. A double-pulsed laser (532 nm green light Nd:YAG) was used, with a beam diameter of 0.35 cm, beam divergence of 4 milliradians, wavelength of 532 nm, and a lens with a variable focal length of 30–200 cm. Output power was 0.75 W, pulse energy 50 mJ, single-pulse duration 6 ns, and pulse repetition frequency15 Hz. A fast-frame-transfer CCD camera was used.

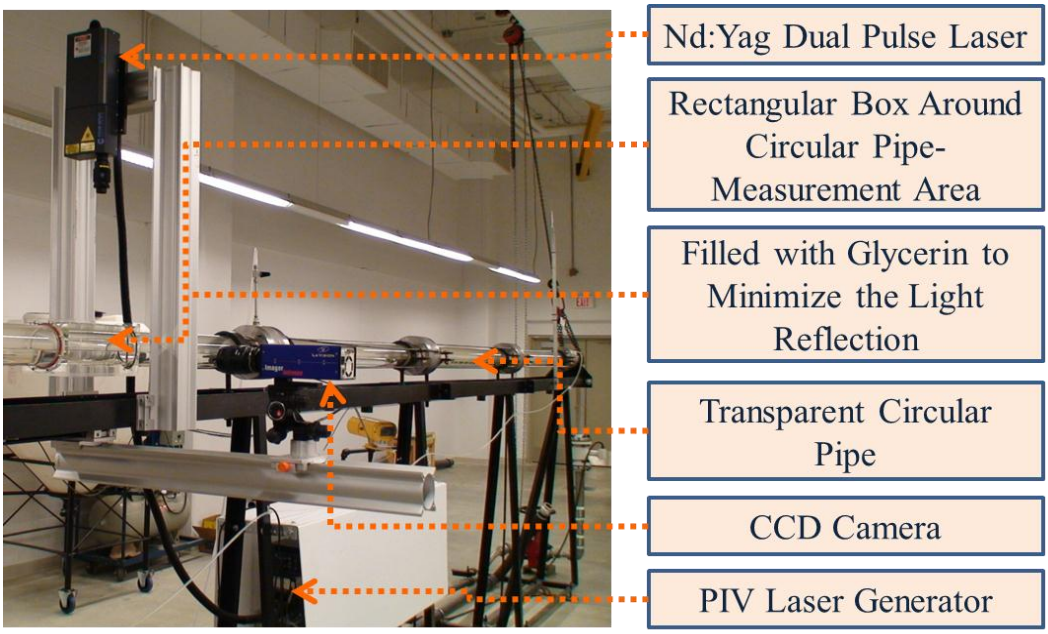

Figure 3.1 PIV system setup used for the experiments

3.3.1 Transparent Glass Pipeline

The pipeline in this setup is made of clear and colorless Simax glass with 105 ± 1.7 mm OD, 95 ± 0.5 mm ID, and a refractive index of 1.47 at 532 nm wavelength. This material belongs to the group of clear hard borosilicate glasses "3.3". The refractive index of Simax glass is close to that of pure quartz.

3.3.2 Light Sources (Particle Illumination)

The double-pulsed Nd:Yag laser system was installed perpendicular to the CCD camera. The integrated double-pulsed Nd:Yag laser in the PIV system generates infrared and visible radiation at high energies. The glass pipe reflects part of the laser light, which distorts the measurements and therefore the processed data on velocity vector fields. A large part of this reflection is due to the cylindrical shape of the pipe and some is due to the different refractive indices of different media through which the light travels, such as from air to glass and from glass to the fluid. Steps were taken to minimize the laser light reflection and refraction; complete elimination of distortion is impossible.

3.3.3 Rectangular Box Around Convex Pipe Surface

A rectangular box was made for the measurement area around the circular pipeline in order to minimize the convex effect of the pipe surface and to improve the optical measurement condition (see Figure 3.2). This box was filled with clear glycerol, which has a refractive index of 1.473, very similar to that of the Simax

glass. The box itself was made of Pyrex glass and the front part parallel to the camera was made of transparent quartz glass. Therefore, the pipeline, the fluid in rectangular box around the pipe's convex surface (glycerol), and the front side of the rectangular box have more-or-less the same refractive indices. This helps to reduce or eliminate the distorted area in PIV measurements in the pipe flow. The presence of the glycerol confined to the rectangular box around the circular pipe helped to reduce reflection and consequent distortion in the computed velocity vectors by 80%. The remaining distorted areas were well above the pipe wall or feature surfaces in the LD case, and could therefore be discarded without any influence on the statistical data analysis (see Figure 3.4a and Figure 3.8).

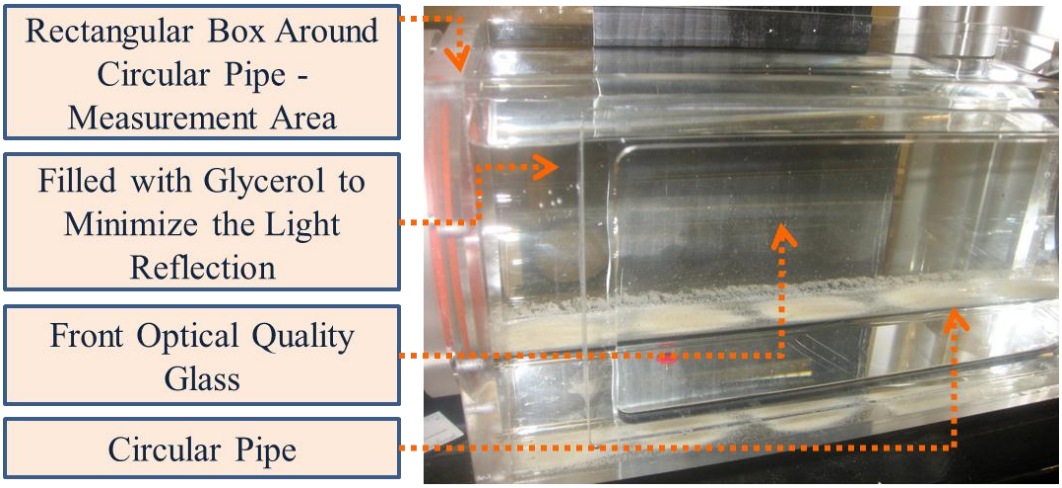

Figure 3.2 Rectangular box around the circular pipe filled with glycerol to minimize reflection and distortion

3.3.4 High-Resolution PIV Camera

The camera used for the experiments was a LaVision Imager intense model; it has a CCD chip with a resolution of 1376 x 1040 pixels (see Figure 3.3). Two lenses

were available for the experiments: normal, Nikon AF Nikkor 50 mm 1:1.4D; and micro, Nikon AF Micro-Nikkor 60 mm f/2.8D. The former gives a field of view (FOV) of 64.88 x 48.4 mm at the closet possible focus and the latter gives an FOV of 27.5 x 20.8 mm. The micro lens gives better special resolution and deep focus to the investigation area, resulting more particles per interrogation window in cross-correlation.

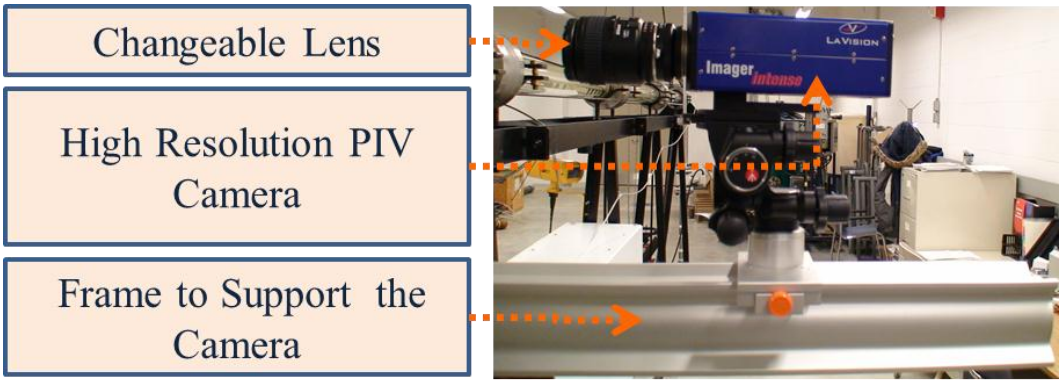

Figure 3.3 Digital PIV CCD camera – high resolution

3.3.5 PIV System Specifications and Model

The 2D PIV (planar PIV) system used in this experiment was provided by LaVision Inc., with DaVis 7.2 software for image and vector processing. Double-pulsed Nd:YAG through DaVis software was synchronized with the CCD camera to capture double-frame images for later cross-correlation processing.

The time interval between laser pulses and double-frame exposures can be specified in the DaVis software based on the flow velocity. In order to compute the velocity vectors for a PIV recording, the distance travelled by the particles and

time *dt* separating the two laser pulses are required. The unit for *dt* is µs. It has minimum and maximum values given by

$$Frame\ transfer\ time\ \left(0.1-1\ \mu s\right) \le dt \le \min\left(L,C\right)$$

where L = 1/laser rep-rate, C = 1/camera rep-rate. As a rule of thumb, the velocity resolution is between 5 and 10 pixels when the *dt* is right for that velocity. The laser intensity should be adjusted so that no parts in the captured images are saturated, or in other words, the intensity should be set below maximum grey level, which is 255 counts for an 8-bit camera and 4095 counts for a 12-bit camera.

For the experiments conducted, the time intervals between the double-frame exposures were set to 620 µs and 850 µs for bulk velocities of 0.24 m/s and 0.17 m/s, respectively.

3.3.6 Tracer (Seeding) Particles

Usually, the flow medium must be seeded with particles, droplets, or bubbles for the PIV measurement. Seeding is especially necessary when the flow medium is air. In the present case, the flow medium was water and the impurities in the water itself made it possible to track the particles without the need to seed the flow medium. The number of particles was sufficiently high for the image area to be divided into very small interrogation windows (IWs) when the micro lens was used.

3.4 Measurement Technique

3.4.1 Principle of Measurements

PIV is a nonintrusive technique that has been used primarily for measurements of velocity vector fields. Its operating principle is based on the velocity definition:

$$\text{Velocity}\left(\frac{m}{s}\right)=\frac{\text{Displacement, }\Delta d\ (m)}{\text{Elapsed Time, }\Delta t\,(s)} \tag{3.1}$$

Double-pulsed laser beams illuminate the flow in sequence based on a set elapsed time (*dt*) between pulses, while the CCD camera captures the corresponding double-frame images. This elapsed time is used in a cross-correlation technique employed for computation and evaluation. In order to use the auto-correlation technique, a single-frame image with double exposures must be captured. Since cross-correlation gives better and more reliable results than auto-correlation, cross-correlation was applied to all measurements in this study. The PIV instrument measurement frequency was fixed at five, meaning that five velocity vector fields were computed every second from the double-frame images.

3.4.2 PIV Recordings

The experimental slurry flow loop was designed to operate continuously in turbulent flow conditions. Because turbulent flow is chaotic in nature, turbulent flow measurements should be averaged over time or space in order to obtain the quasi-steady-state condition to predict turbulent flow behavior. PIV can record an

unlimited number of single- or double-frame images consecutively as long as the dedicated computer's memory and RAM capacity allow. From further analysis it was found that, for the coherent structures in the turbulent flow, the best results were obtained when a cumulative effect was used with a minimum of 50 velocity vector fields. However, over 100 velocity vector fields is even better. The coherent structures analysis did not improve noticeably when more than 100 velocity vector fields were used for the analysis [23]. Therefore, to maximize measurement efficiency, 100 velocity vector fields were considered for all analysis. However, 300 double-frame images were captured for each experiment and the image average was computed based on 300 frames and then the first 100 instantaneous velocity vector maps were considered for further analysis. The time span required to obtain 300 double-frame images was 60 s. In this work, the instantaneous velocity vector maps were computed and the average velocity vector map was computed. By subtracting the computed average velocity vector map from each individual instantaneous velocity vector field the fluctuation velocity vector fields were obtained for each individual instantaneous velocity vector field. The time-averaging technique or variable-interval time-averaging (VITA), which was first used by Blackwelder and Kaplan [24] to obtain local averages of some phenomena, was applied for the analysis and is described as

$$Q(x_i, t, T) = \frac{1}{T}\int_0^T Q\left(x_i, s\right) ds \qquad (3.2)$$

where *T* is the averaging time; in some cases it is more convenient to use variable-interval space-averaging (VISA), which is essentially the same as VITA, except that the averaging is done in space.

3.4.3 Raw Images and Frequency Filter

Besides placing a rectangular box around the circular pipe and filling it with glycerol, a number of other techniques were applied to reduce distortion in the measurement area as well. After recording the double-frame images, the images were averaged. The averages of the images are the parts that can be seen in all images, in other words, non-moving parts, which are usually sources of distortion and background noise. By subtracting the averaged image from each image, some of the distortion can be removed from the images. Sometimes the distorted areas were not in the analyzed areas; in these cases the areas could be masked before beginning the computation process. By applying these techniques, the distortion areas were filtered out of the images before further processing.

3.4.4 Image Processing

The steps involved in the image acquisition and processing include improving the image quality by eliminating the distorted areas, detecting the particles in the images, and measuring their displacement in IWs. The particles in the double-frame images are cross-correlated to measure the separation of pairs of particle images between successive frames. Each image is divided into much smaller IWs. The sizes of the IWs, measured in pixels, are: 512 x 512, 256 x 256, 128 x 128, 64

x 64, 32 x 32, 16 x 16, 12 x 12, 8 x 8, 6 x 6, and 4 x 4. In computations for the velocity vectors, window overlaps of 87%, 75%, 50%, 25%, 0%, and −100% can be used to reduce or increase the grid size of the vector field. For example, −100% overlap doubles the vector grid spacing — supposing that the IW size is 32 x 32 pixels, the vector grid spacing would be 64 pixels. In other words, for every 64 pixels one vector is computed. Each time the IWs are reduced in size, the resolution is increased accordingly. For further analyses see Table 3.2.

Table 3.2

Interrogation window sizes for 27.5 mm x 20.8 mm measurement region

IW, pixels x pixels	IW, mm x mm	Overlap	No. of row-wise & column-wise data $\left(DP_x \times DP_y\right)$	No. of data points	Grid size of the vector field, mm $\left(L_x \times L_y\right)$	IW in wall unit $\left(L_y^+\right)$
4 x 4	0.08 x 0.08	−100%	130 x 172	22360	0.16 x 0.16	1.81
		0%	260 x 344	89440	0.08 x 0.08	0.90
		25%	347 x 459	159273	0.06 x 0.06	0.68
		50%	520 x 688	357760	0.04 x 0.04	0.45
		75%	1040 x 1376	Exceeded 1431040	0.02 x 0.02	0.23
		87%	N/A	N/A; grid spacing is ≤ 1 pixel	N/A	N/A
6 x 6	0.12 x 0.12	−100%	87 x 115	10005	0.24 x 0.24	2.71
		0%	173 x 229	39618	0.12 x 0.12	1.36
		25%	260 x 344	89440	0.08 x 0.08	0.90
		50%	347 x 456	159273	0.06 x 0.06	0.68
		75%	1040 x 1376	Exceeded 1431040	0.02 x 0.02	0.23
		87%	N/A	N/A; grid spacing is ≤ 1 pixel	N/A	N/A
8 x 8	0.16 x 0.16	−100%	65 x 86	5590	0.32 x 0.32	3.61
		0%	130 x 172	22360	0.16 x 0.16	1.81
		25%	173 x 229	39617	0.12 x 0.12	1.36
		50%	260 x 344	89440	0.08 x 0.08	0.90
		75%	520 x 688	357760	0.04 x 0.04	0.45
		87%	1040 x 1376	Exceeded 1431040	0.02 x 0.02	0.23
12 x 12	0.24 x 0.24	−100%	43 x 57	2451	0.48 x 0.48	5.42
		0%	87 x 115	10005	0.24 x 0.24	2.71
		25%	116 x 153	17748	0.18 x 0.18	2.03
		50%	173 x 229	39617	0.12 x 0.12	1.36
		75%	347 x 459	159273	0.06 x 0.06	0.68
		87%	1040 x 1376	Exceeded 1431040	0.02 x 0.02	0.23

16 x 16	0.32 x 0.32	−100%	32 x 43	1376	0.64 x 0.64	7.23
		0%	65 x 86	5590	0.32 x 0.32	3.61
		25%	87 x 115	10005	0.24 x 0.24	2.71
		50%	130 x 172	22360	0.16 x 0.16	1.81
		75%	260 x 344	89440	0.08 x 0.08	0.90
		87%	520 x 688	357760	0.04 x 0.04	0.45
32 x 32	0.64 x 0.64	−100%	16 x 21	336	1.28 x 1.28	14.46
		0%	32 x 43	1376	0.64 x 0.64	7.23
		25%	43 x 57	2451	0.48 x 0.48	5.42
		50%	65 x 86	5590	0.32 x 0.32	3.61
		75%	130 x 172	22360	0.16 x 0.16	1.81
		87%	260 x 344	89440	0.08 x 0.08	0.90
64 x 64	1.28 x 1.28	−100%	8 x 11	88	2.56 x 2.56	28.90
		0%	16 x 21	336	1.28 x 1.28	14.46
		25%	22 x 29	638	0.96 x 0.96	10.84
		50%	32 x 43	1376	0.64 x 0.64	7.23
		75%	65 x 86	5590	0.32 x 0.32	3.61
		87%	130 x 172	22360	0.16 x 0.16	1.81
128 x 128	2.56 x 2.56	−100%	4 x 5	20	5.12 x 5.12	57.82
		0%	8 x 11	88	2.56 x 2.56	28.90
		25%	11 x 14	154	1.92 x 1.92	21.69
		50%	16 x 21	336	1.28 x 1.28	14.46
		75%	32 x 43	1376	0.64 x 0.64	7.23
		87%	65 x 86	5590	0.32 x 0.32	3.61
256 x 256	5.12 x 5.12	−100%	2 x 3	6	10.24 x 15.68	177.07
		0%	4 x 5	20	5.12 x 5.12	57.82
		25%	5 x 7	35	3.84 x 3.84	43.36
		50%	8 x 11	88	2.56 x 2.56	28.90
		75%	16 x 21	336	1.28 x 1.28	14.46
		87%	32 x 42	1344	0.66 x 0.66	7.45
512 x 512	10.24 x 10.24	−100%	N/A	N/A	N/A	N/A
		0%	2 x 3	6	10.24 x 15.68	177.07
		25%	3 x 4	12	7.68 x 7.68	86.73
		50%	4 x 5	20	5.12 x 5.12	57.82
		75%	8 x 11	88	2.56 x 2.56	28.90
		87%	16 x 21	336	1.32 x 1.32	14.91

The dimensionless normal spacing, l_y^+, is calculated as $l_y^+ = {l_y u^*}/{\nu}$ in wall units, where l_y is the normal distance from the pipe wall in m, u^* is the friction velocity in m/s, and ν is the kinematic viscosity in m^2/s.

In a simulation, one method of capturing the minute features is to reduce the grid size. The smaller the grid size, the better the spatial resolution and accuracy. In the past, the only options for research measurement apparatus, whether intrusive, such as hot-wire anemometry, or nonintrusive, such as LDV, were single-point

measurements. These could not measure motion in turbulent flow. Current state-of-the-art imaging technology, PIV, offers significant advantages over earlier techniques. Unlike single-point measurement techniques such as HWA and LDV, the PIV system provides information on the spatial structure of the flow. Rather than being restricted to single-point measurements, PIV enables the measurement of motions such as those of coherent structures (CS) from their creation regions to their dissipation regions, and also offers high-resolution grid sizes.

3.4.5 Cross-Correlation Technique

Cross-correlation is a technique based on a double frame with double exposure. The technique utilizes a single correlation with a higher and unambiguous peak in each IW to identify the particle displacement, *dx*. Usually at least 3 to 4 particles should be available in each IW to enable cross-correlation and obtain the velocity vector. Otherwise, the number of spurious velocity vectors increases and one cannot get reliable velocity vector fields. Using PIV it is possible to obtain information about the turbulent flow in the boundary layer and regions close to the pipe wall (viscous wall region). A few approaches can be considered to increase the measurement resolution to obtain better and more reliable data. Options for better data resolution include reduction of the investigation area, use of higher camera resolution, use of micro lenses focusing deeply into the investigation area, and, possibly, some other techniques. Since the camera CCD chip resolution in this study was kept constant, the alternative was to zoom in on the investigation area and shrink the FOV window. For this reason the camera's

normal lens was replaced with the micro lens (Nikon AF Micro-Nikkor 60 mm f/2.8D), which provided a 27.5 x 20.8 mm FOV. Not only did this modification reduce the size of the FOV window to obtain more detailed velocity information about the investigation area, but also, by focusing deeper into the FOV, there was a sufficient number of particles in the smaller IW for cross-correlation (e.g., 16 x 16 pixels). The cross-correlation results here were obtained using a square IW. For the analysis in this research, the data from a 32 x 32 pixel IW and 16 x 16 pixel IW with 50% overlap were used. The former IWs for each velocity vector field gives 5,590 data points and the latter IW gives 22,360 data points (see Table 3.2). The choice of IW size strikes a balance between the accuracy of the captured data and the spatial resolution of the IW; choosing a smaller IW and not having enough particles for cross-correlation tends to reduce the signal-to-noise ratio and consequently increases the number of spurious velocity vectors. Therefore, a smaller IW can be selected to obtain accurate data and avoid spurious vectors as long as there are sufficient particles for cross-correlation. The data accuracy must be validated. On the other hand, having IWs with better spatial resolution makes it possible to measure the smaller-scale turbulent motion.

3.5 PIV Data Validation

PIV data captured from experiments should be validated. At the beginning of the experiments, when the normal Nikon AF Nikkor 50 mm 1:1.4D lens was used with the CCD camera, the 32 x 32 IWs with 50% overlap were used for cross-correlation. As increasing the spatial resolution would provide more information,

especially in the near-wall region, shrinking the IWs for this purpose would represent considerable progress. However, before the IW size is reduced, one needs to make sure that there will be enough particles for each IW to permit cross-correlation. If there are insufficient particles in the IWs and one tries to further reduce the IW grid size, there will be spurious vectors pointed in different directions rather than vectors more-or-less parallel to the direction of flow and of the same magnitude as the average velocity measured by the magnetic flowmeter. That would be the first indication that there are insufficient particles for cross-correlation and that further reduction of the IWs would give spurious vectors. If the particle numbers in the IWs are sufficient, further analysis is required to ensure that the signal-to-noise ratio is acceptable.

Our approach was to replace the normal lens with a micro lens to allow deeper focus into the investigation area, capturing more particles and thus improving spatial resolution. This results in a reduction of the FOV from 64.88 x 48.4 mm (at the closet possible focus distance) to 27.5 x 20.8 mm, and consequently includes more particles for cross-correlation in order to further reduce the IWs from 32 x 32 pixels to 16 x 16 pixels. For all analysis, the 50% overlap option was used as it was shown that 50% overlap eliminates correlation errors effectively [25].

3.5.1 Particle Image Density for PIV Measurements

Figures 3.4a–3 4c illustrate typical PIV images that have been used for cross-correlation. For all measurements, no external seeding was applied. All particle

images in the figures are due to impurities in the tap water used for the experiments. Figure 3.4a shows particle images for water-only flow at the bulk velocity of 0.24 m/s. Figure 3.4b is for the continuous bed and 3.4c shows the downstream and stoss sections of the LD case. Figures 3.4b and 3.4c show the grid size for the 16 x 16 pixel IW. The whole boxes shown in those figures are 64 x 64 pixels and the quarter section illustrated is 16 x 16 pixels. The number of particle images inside the box is identifiable and the histogram of the particle image distribution will be discussed.

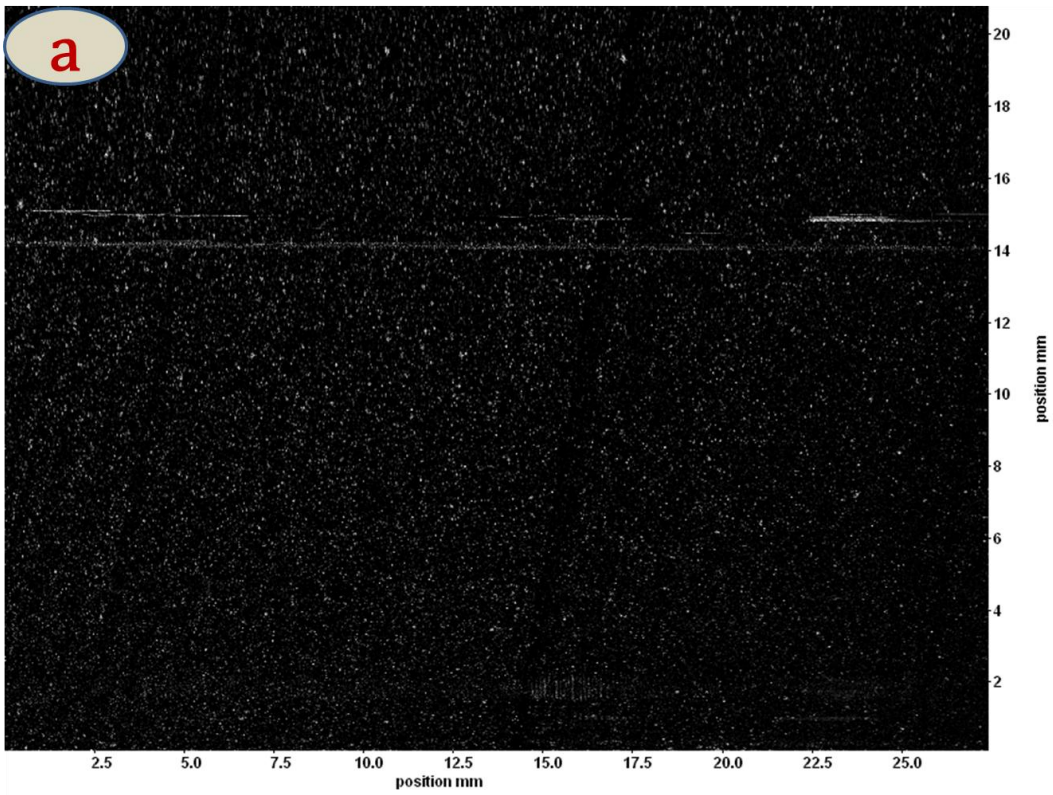

Figure 3.4a Typical PIV image for water-only flow. Particles in the image are just impurities from the tap water and are not due to external seeding

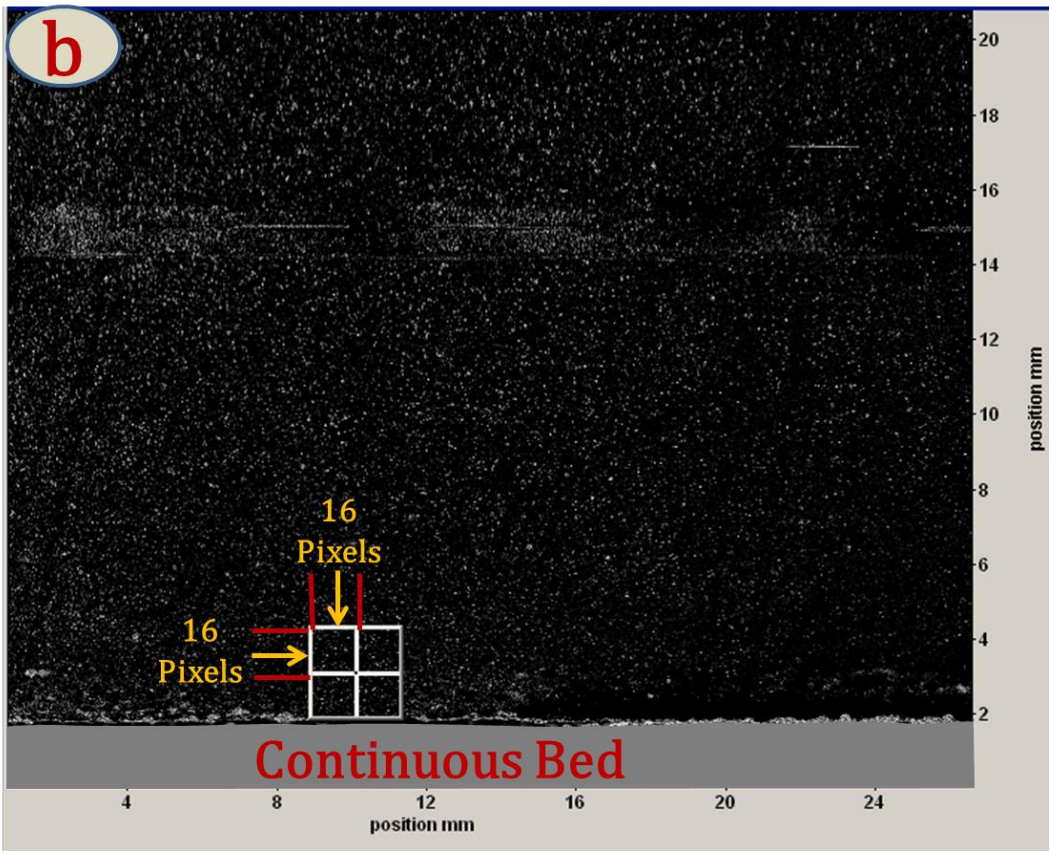

Figure 3.4b Typical PIV image for continuous bed, no external seeding, 16 x 16 pixel grid size with available particles for cross-correlation

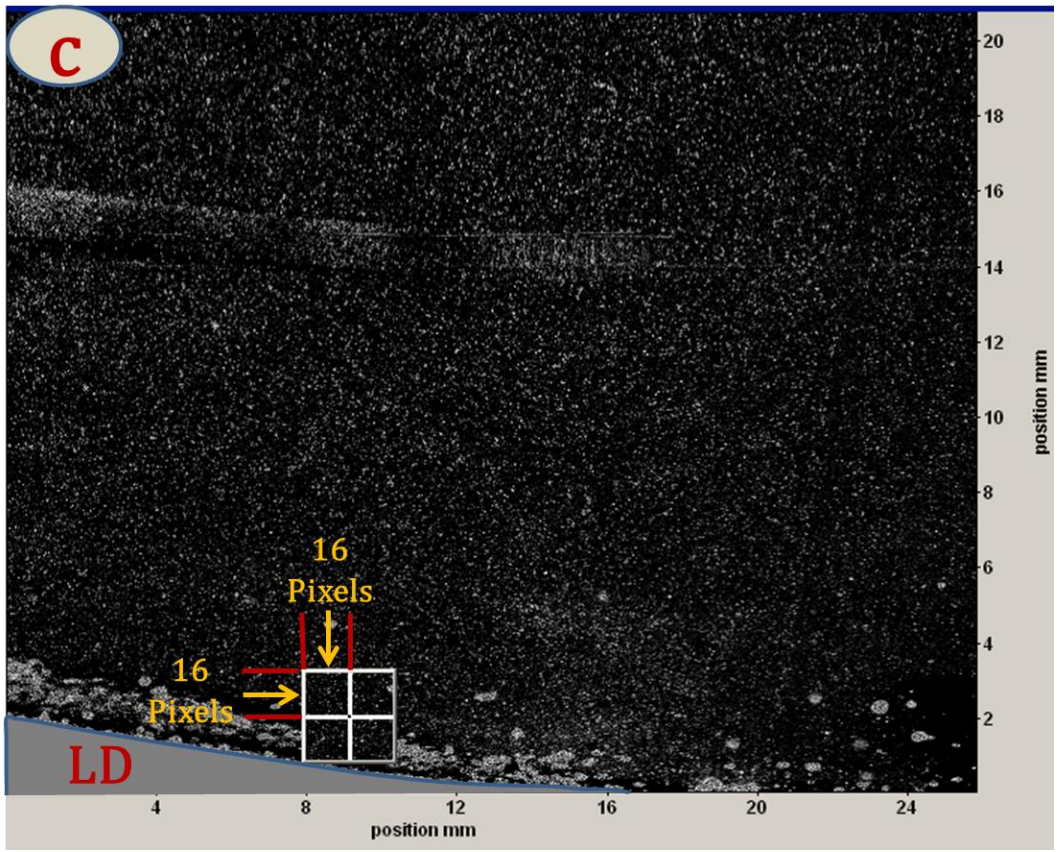

Figure 3.4c Typical PIV image for LD, no external seeding, 16 x 16 pixel grid size with available particles for cross-correlation

3.5.2 Correlation Map for the Specified IW

Figure 3.5 shows a typical correlation map for a 16 x 16 pixel IW. The cross-correlation between two particle images in the IWs of the consecutive frames will yield the average displacement vector. The correction in IWs is affected by the number of available particles for cross-correlation and also the signal-to-noise ratio. The peak correlation height relative to other correlation heights in IWs is a good indicator of signal-to-noise ratio. The higher the correlation peak compared

to the neighboring noise peaks in the IWs, the better the correlation and reliability of the data.

The distance from the center of the cross-correlation to the highest correlation peak is considered the mean displacement and the direction from the center to the displacement correlation peak is the velocity vector direction for that IW. The reliability and performance of PIV depends upon the reliable detection of the displacement of correlation peaks among noise peaks in the IW. In other words, the signal-to-noise strength in correlation peak detection is crucial.

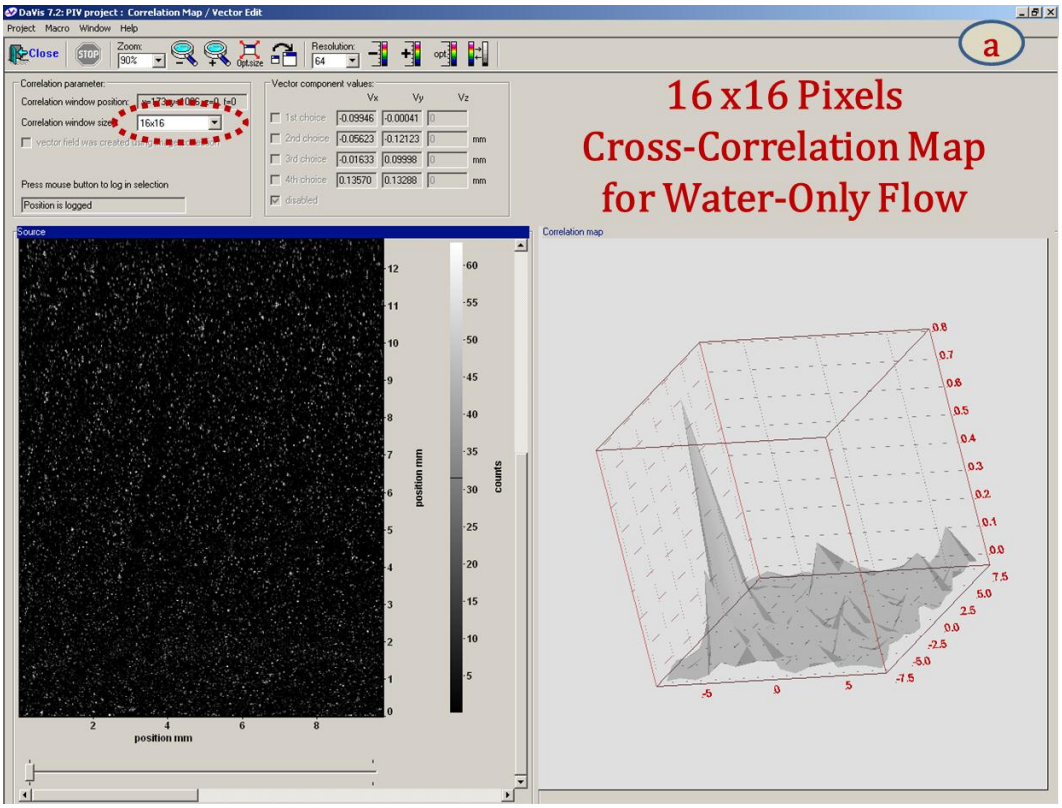

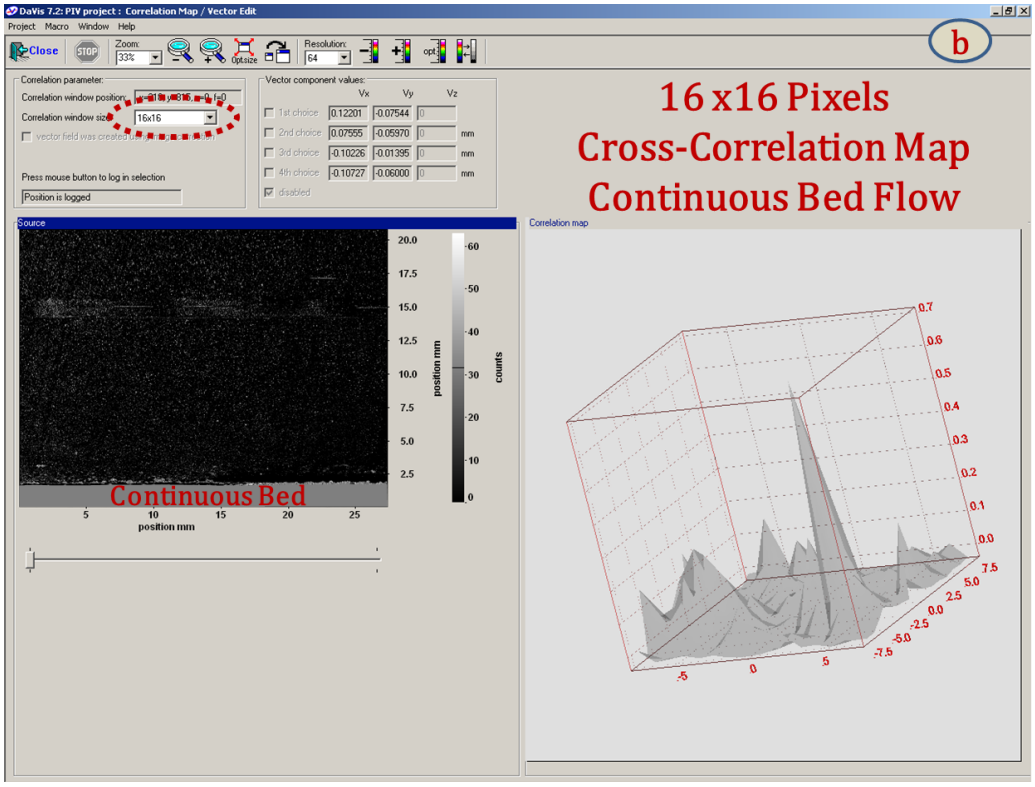

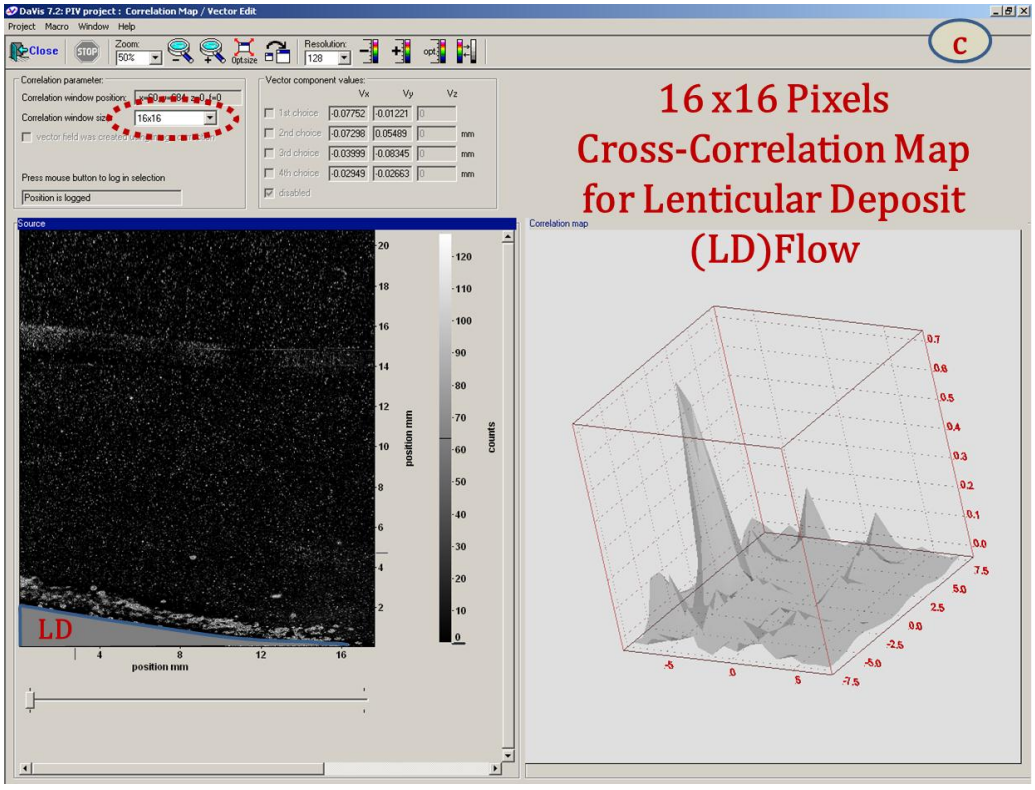

Figure 3.5 Typical 3D correlation maps of 16 x 16 cross-correlation IWs. (a) water-only flow, (b) continuous bed, and (c) LD

Keane and Adrian [26] among many other researchers have studied the detectability issue of the displacement correlation peak. As a rule of thumb, if the displacement correlation peak is approximately two times or more higher than the neighboring peaks in the IWs, the data obtained from the cross-correlation should be reliable. Typical displacement correlation peaks for the water-only flow, continuous bed, and LDs are shown in Figures 3.5a–3.5c, respectively.

3.5.3 Histogram of the Particle Images

Figures 3.6a–3.6c show the histograms of the particle images in frames for water-only flow, continuous bed, and LD flow, respectively. The presence of 3 to 4 image pairs in each interrogation window for cross-correlation optimization is recommended [27]. In the histogram shown below each frame (Figures 3.6a – 3.6c), the horizontal axis shows the number of particle images and the vertical axis illustrates the number of pixels containing that specific number of particle images. The camera resolution of the PIV for the experiments is 1376 x 1040 pixels, and for each velocity vector map, each pair of images is cross-correlated and the displacement of the particles is obtained. Therefore, in total there would be 2,862,080 pixels in the pair of images. The typical statistics for the numbers of particle images/frames for the water-only, continuous-bed, and LD flows are 10,606,100, 34,593,400, and 56,781,900 counts per pair of frames, respectively. That gives, on average, 3.7, 12.1, and 19.8 counts per pixel for the water-only, continuous bed, and LD flow cases, respectively. The higher particle image counts for the continuous-bed and LD cases are due to recirculation of the slurry

during which micron-size particles are not captured by the micron-rated filter bag inside the recirculation tank (depends on filter type used). Considering a 16 x16 pixel IW for cross-correlation, each grid size on average would have 29.6, 96.8, and 158.4 image pairs in each IW for water-only, continuous bed, and LD flows, respectively. Therefore, for all cases there are enough particle images for 16 x 16 pixel IW cross-correlation.

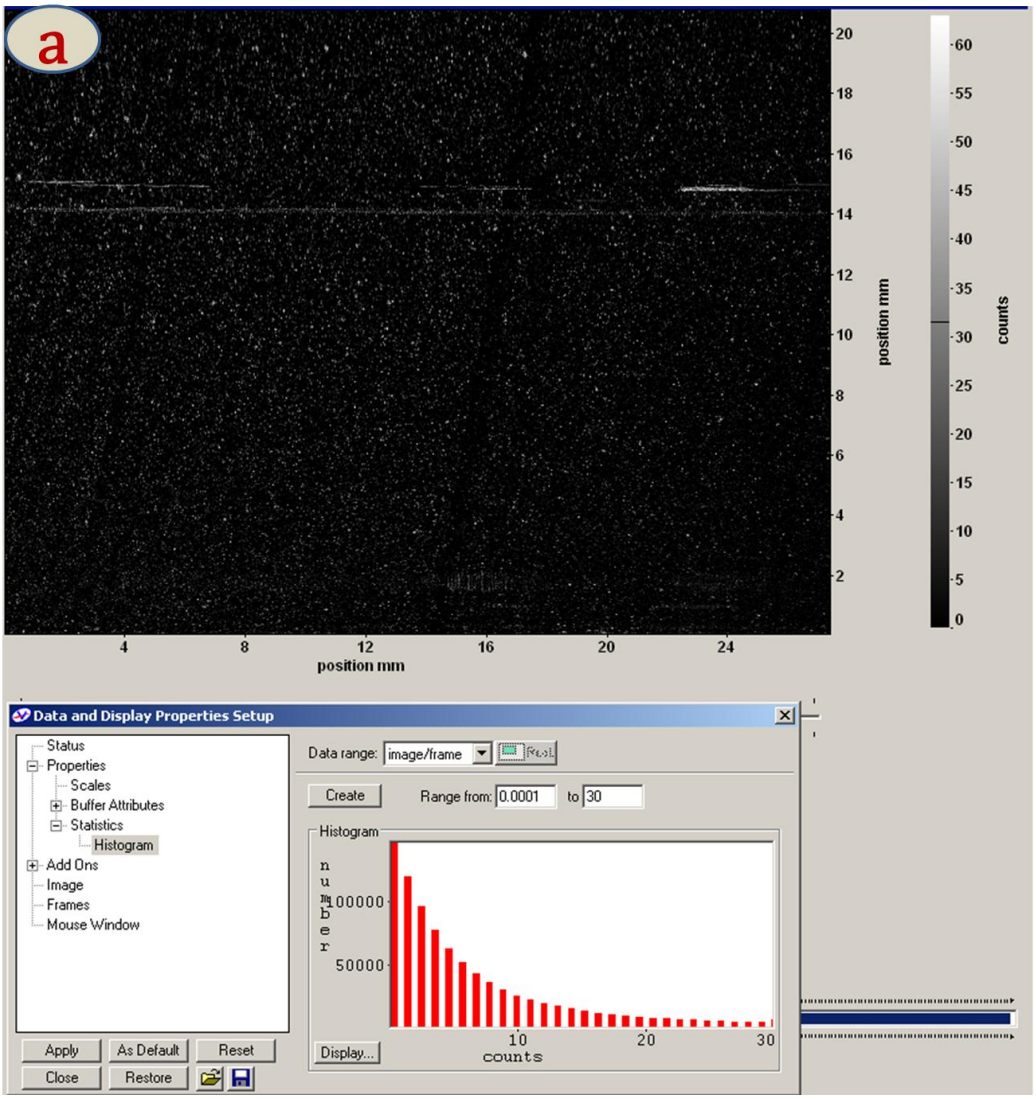

Figure 3.6a Histogram of particle distribution in water-only flow. Horizontal axis shows the number of particles and the vertical axis shows the number of pixels containing a specific number of particles

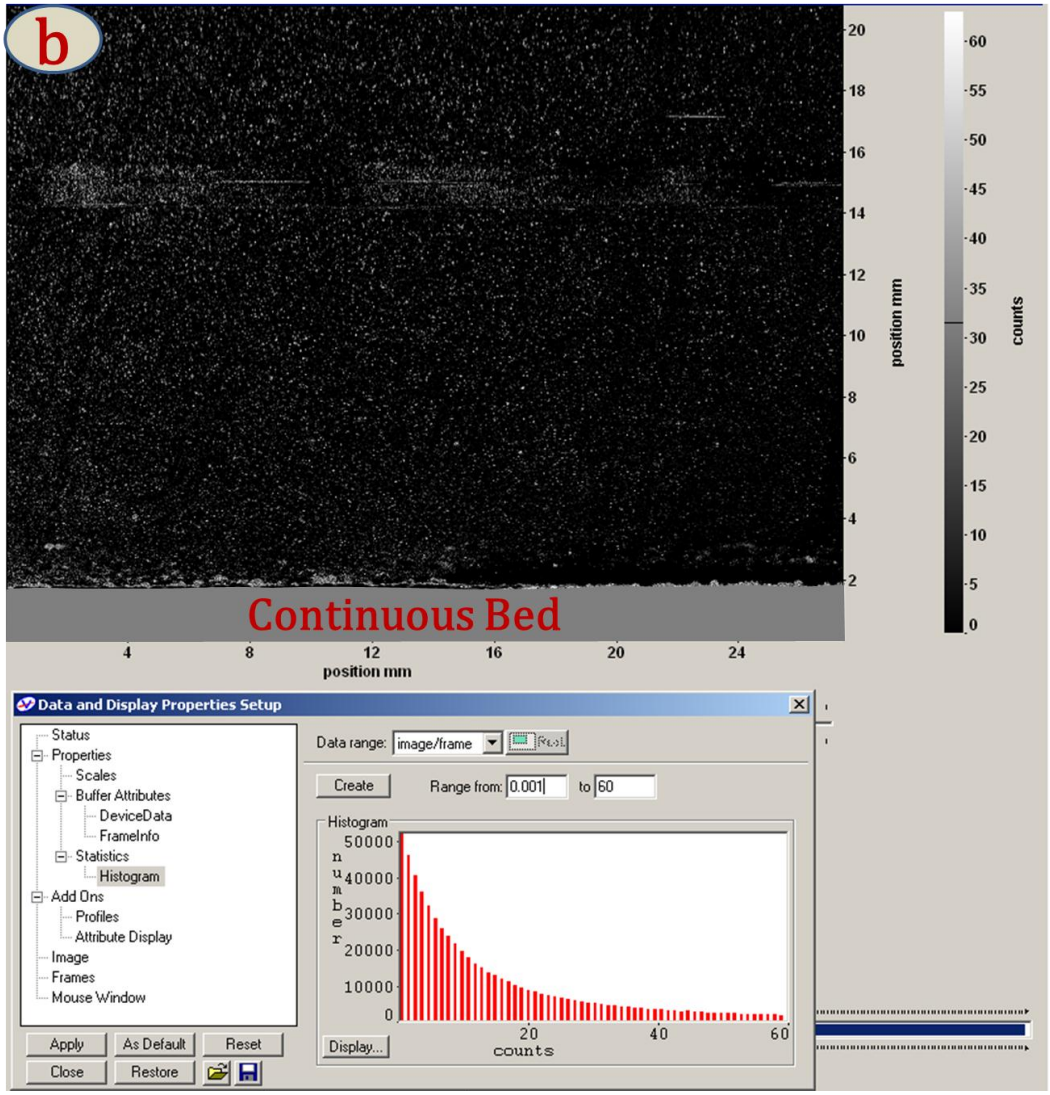

Figure 3.6b Histogram of particle distribution in continuous-bed flow. Horizontal axis shows the number of particles and the vertical axis shows the number of pixels containing a specific number of particles

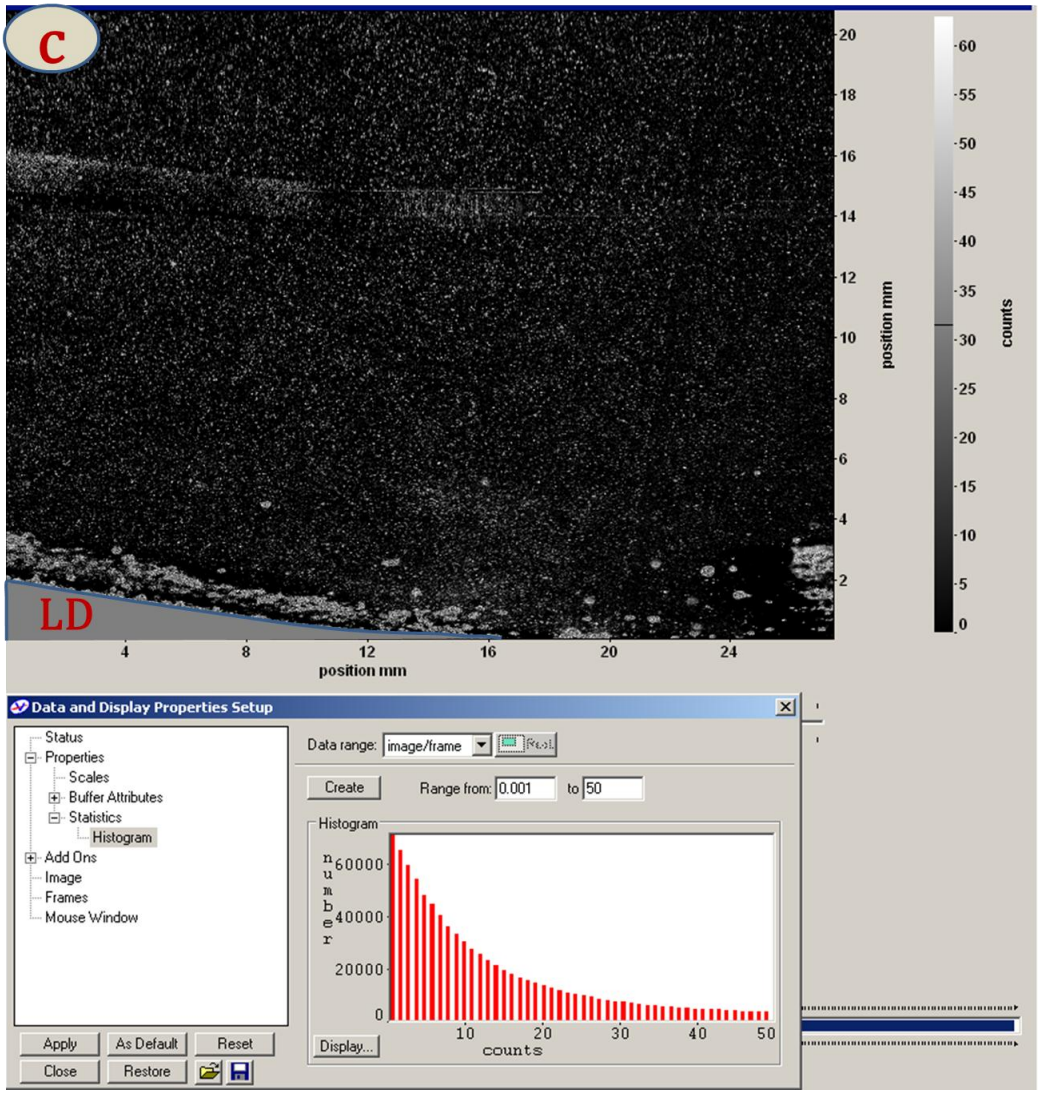

Figure 3.6c Histogram of particle distribution in LD flow. Horizontal axis shows the number of particles and the vertical axis shows the number of pixels containing a specific number of particles

3.5.4 Velocity Vector Map from PIV Measurements

PIV is a nonintrusive technique that measures the velocity of micrometer-sized particles in the flow with the assumption that the velocities of these particles are the same as the flow velocity. PIV from cross-correlation of two consecutive

particle frames gives the whole flow field of the instantaneous velocity vector. The 2D PIV measures the two components of the real-time velocity. Depending on the dedicated computer capacity, a series of instantaneous velocity vector fields can be measured over the desired time. The time average of the instantaneous velocity vector maps can be computed and, by subtracting the computed average velocity field from each instantaneous velocity vector field, the fluctuation velocity vector is obtained.

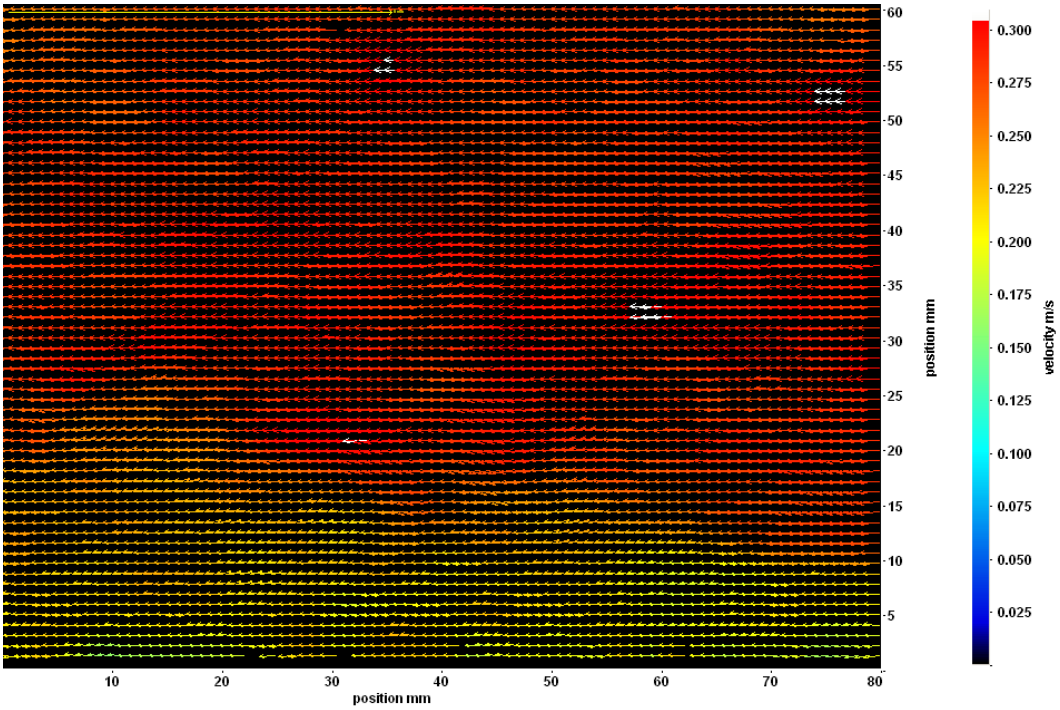

Figure 3.7 Typical velocity vector map for water-only flow using normal lens, U_{avg}= 0.24 m/s, 32 x 32 pixel IW with 50% overlap, flow direction from right to left

Figure 3.7 shows the instantaneous velocity vector map obtained at the bulk velocity of 0.24 m/s. This velocity vector map was obtained by using the normal lens with 32 x 32 pixel IW with 50% overlap. The velocity vector map in this case is a matrix with 65 rows and 86 columns, which contains 5,590 data points.

Figures 3.8a and 3.8b show the velocity vector maps obtained using the micro lens for the bulk velocity of 0.24 m/s. The velocity vector map on the top (Figure 3.8a) is computed by applying the 32 x 32 pixel IW with 50% overlap and the velocity vector map on the bottom (Figure 3.8b) is computed by applying the 16 x 16 pixel interrogation window with 50% overlap for the same condition. Figure 3.8a contains 65 rows and 86 columns (5,590 data points); however, Figure 3.8b contains 130 rows and 172 columns (22,360 data points) for the same image frame. The number of data points in Figure 3.8b is four times that in Figure 3.8a. Figure 3.7 and Figure 3.8a both contain the same number of data points; the difference is that Figure 3.7 was taken using the normal lens whereas Figure 3.8a was taken using the micro lens. The investigation area in Figure 3.8a is approximately one-eighth the size of the investigation area in Figure 3.7 for the same number of data points. This deep focusing provides detailed information about the area of interest in our study.

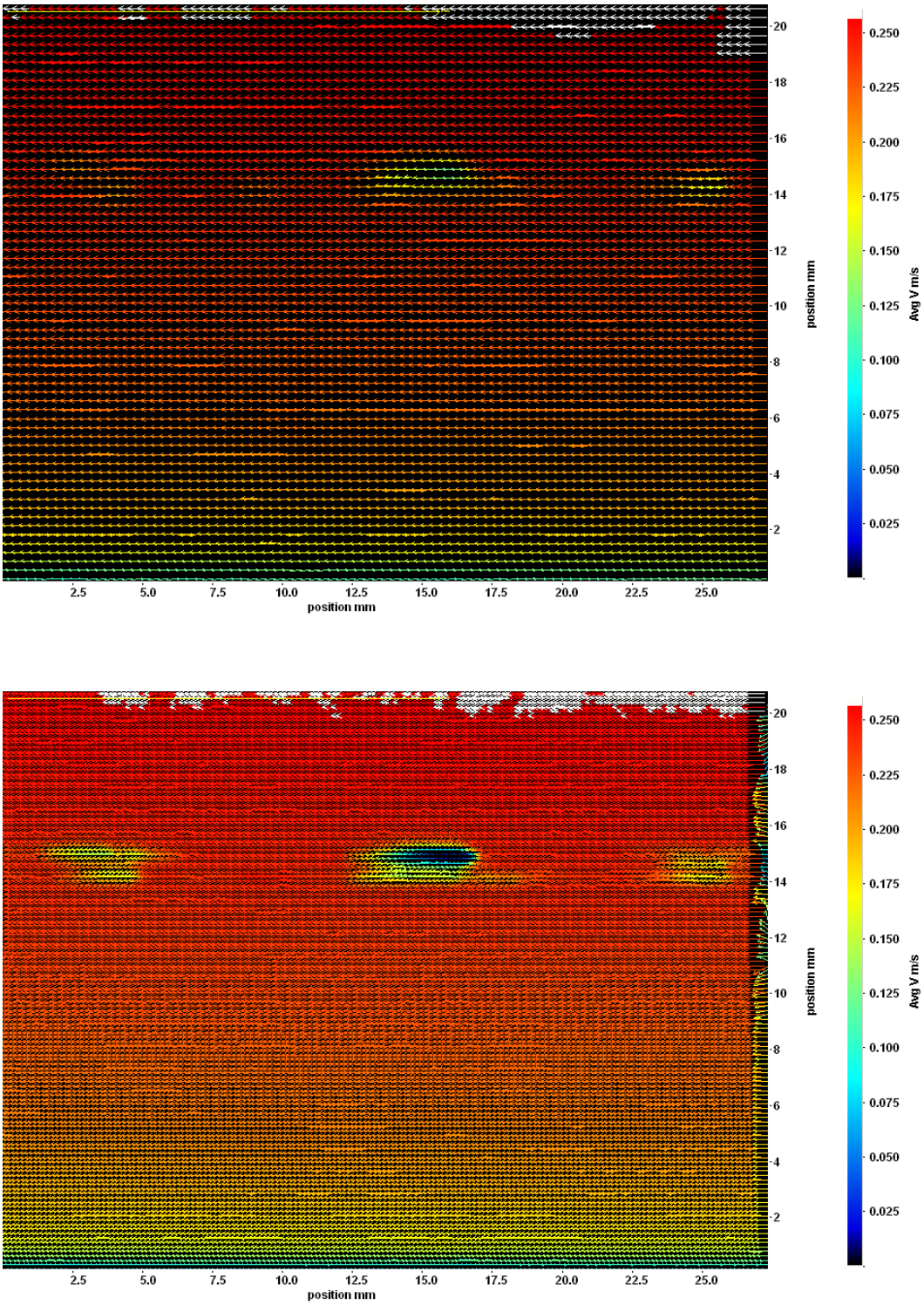

Figure 3.8 Velocity vector map for water-only flow, U_{avg} = 0.24 m/s using micro lens. (a) Upper map is 32 x 32 pixel IW with 50% overlap, (b) Lower map is 16 x 16 pixel IW with 50% overlap

3.5.5 Comparison of Velocity Profile Data from PIV with the Universal Velocity Profile

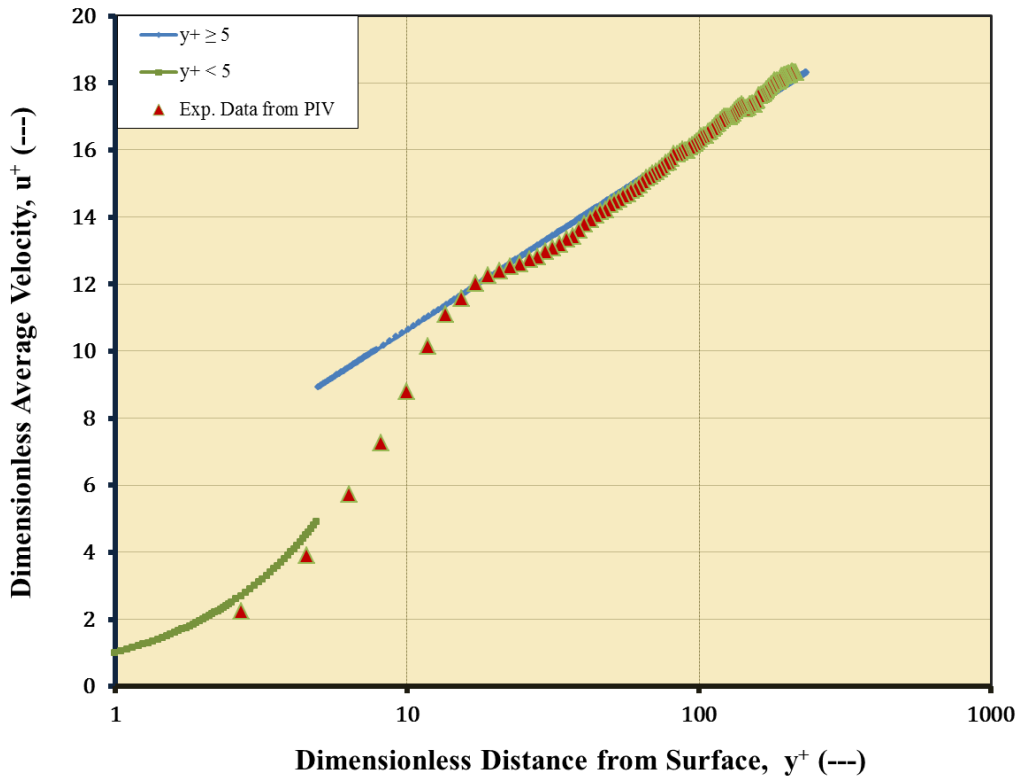

Figure 3.9 Data obtained from PIV for 16 x 16 pixel IW with 50% overlap in pipeline at U_{avg} = 0.24 m/s (*Re* = 24,379); green line for the near-wall profile of $y^+ < 5$; blue line for $y^+ \geq 5$; red line for the data from PIV

Figure 3.9 illustrates the experimental mean velocity profile obtained from PIV data and compared with the universal velocity profile. Experimental data were obtained from pipeline measurements at 25°*C* and an average velocity of 0.24 m/s. The PIV data were computed using a 16 x 16 pixel IW cross-correlation with 50% overlap. The smooth continuous blue line shows the logarithmic law of the wall:

$$\begin{cases} u^+ = y^+ & for\ \ y^+ < 5 \\ u^+ = \dfrac{1}{0.41}\ln y^+ + 5.2 & for\ \ y^+ \geq 30 \end{cases} \tag{3.3}$$

where 0.41 and 5.2 are constants. The logarithmic law of the wall, first introduced by von Karman [9, 28], has been used frequently since then; u^+ and y^+ are dimensionless velocity and the wall-unit distance from a pipe surface, respectively, which are normalized by friction velocity, u^*.

The graph in Figure 3.9 and other validation discussed earlier, verifies that the data obtained from the PIV measurements are reliable and consistent with the universally accepted velocity profile. Therefore, PIV data can be used with confidence for further analysis of complex turbulent flow. Additionally, the accuracy and reliability of the PIV data are validated by previous LDV data in the same way that early LDV data were validated by HWA data [14]. The good agreement seen between the universal log-law and the experimental data, illustrated in Figure 3.9, in combination with the PIV data validation discussed earlier, confirms that the experimentally measured data from PIV are correct and reliable.

In PIV measurements, using IWs of 32 x 32 pixels is very common for obtaining the instantaneous velocity vectors [14, 29]; and some researchers have used IWs of 32 x 16 pixels [10, 30-33] and some [34] were able to obtain IWs of 16 x 16 pixels. Herpin et al. [35], using a very-high-resolution CCD camera, managed to obtain IWs of 14 x 14 pixels.

3.6 Discussion and Conclusions

The PIV principle for obtaining a reliable velocity vector map was discussed. Techniques were introduced to minimize the distortion of PIV measurements over the investigation area. A rectangular box filled with glycerol, with the same reflective index as the transparent glass pipe, was implemented to reduce the distortion by 80%.

Spatial resolution was improved using a few simple modifications to the PIV system. First, the investigation FOV was reduced in size by replacing the normal lens with the micro lens in the PIV system, which not only reduced the size of the FOV for better resolution, but also made it possible to focus deeply into the investigation area and capture more particles per IW. Second, in processing the images to obtain the displacement, the IW size was reduced stepwise in the cross-correlation technique and an IW size of 16 x 16 pixels (0.32 x 0.32 mm) was achieved. Of course, each time the size of the IWs was reduced, it was necessary to ensure that there were sufficient numbers of particles in the IW after computation to obtain clear and reliable velocity vector data. An increase in the number of spurious vectors means that there are not enough particles in the IWs for cross-correlation. The above steps improved the spatial resolution of the PIV measurements.

Captured image frames were checked for the availability of sufficient tracer particle images per IW and the computed data from the cross-correlation of the instantaneous velocity vector fields were validated. The validation included

histograms of the particles, signal-to-noise ratio, detection of the displacement peak, and, finally, comparison of the velocity profile obtained from the PIV data to the universal velocity profile. The velocity profile from 16 x 16 pixel IW data shows good qualitative agreement with the universal velocity profile.

Additional improvements in PIV methodology are still possible. By exploring the possibilities for developing this technique to enhance its capabilities, transport phenomena in nature can be better understood and transport mechanisms and turbulence effects in nature can be better described.

3.7 References

[1] Kline, S. J., Reynolds, W. C., Schraub, F. A., and Runstadler, P. W., 1967, "The Structure of Turbulent Boundary Layers," Journal of Fluid Mechanics, 30(04), pp. 741-773.

[2] Cao, G., Sivukari, M., Kurnitski, J., Ruponen, M., and Seppänen, O., 2010, "Particle Image Velocimetry (PIV) Application in the Measurement of Indoor Air Distribution by an Active Chilled Beam," Building and Environment, 45(9), pp. 1932-1940.

[3] Ikeda, Y., Yamada, N., and Nakajima, T., 2000, "Multi-Intensity-Layer Particle-Image Velocimetry for Spray Measurement," Measurement Science and Technology, 11(6), pp. 617.

[4] Ettema, R., Fujita, I., Muste, M., and Kruger, A., 1997, "Particle-Image Velocimetry for Whole-Field Measurement of Ice Velocities," Cold Regions Science and Technology, 26(2), pp. 97-112.

[5] Son, S. Y., Kihm, K. D., and Han, J. C., 2002, "PIV Flow Measurements for Heat Transfer Characterization in Two-Pass Square Channels with Smooth and 90° Ribbed Walls," International Journal of Heat and Mass Transfer, 45(24), pp. 4809-4822.

[6] Cenedese, A., Doglia, G., Romano, G. P., De Michele, G., and Tanzini, G., 1994, "LDA and PIV Velocity Measurements in Free Jets," Experimental Thermal and Fluid Science, 9(2), pp. 125-134.

[7] Lindken, R. L., and Merzkirch, W. M., 2002, "A Novel PIV Technique for Measurements in Multiphase Flows and Its Application to Two-Phase Bubbly Flows," Experiments in Fluids, 33(6), pp. 814-825.

[8] Wallace, J. M., Eckelmann, H., and Brodkey, R. S., 1972, "The Wall Region in Turbulent Shear Flow," Journal of Fluid Mechanics, 54(01), pp. 39-48.

[9] Von Kármán, T., 1930, "Mechanische Ähnlichkeit Und Turbulenz," Proceedings in Third International Congress for Applied Mathematics, Stockholm, pp. 85-105.

[10] Westerweel, J., Dabiri, D., and Gharib, M., 1997, "The Effect of a Discrete Window Offset on the Accuracy of Cross-Correlation Analysis of Digital Piv Recordings," Experiments in Fluids, 23(1), pp. 20-28.

[11] Schmeeckle, M. W., Shimizu, Y., Baba, H., and Ikezaki, S., 1999, "Numerical and Experimental Investigation of Turbulence over Dunes in Open-Channel Flow," Monthly Report of the Civil Engineering Research Institute, 551(-), pp. 2-15.

[12] Nakagawa, S., and Hanratty, T. J., 2001, "Particle Image Velocimetry Measurements of Flow over a Wavy Wall," Physics of Fluids, 13(11), pp. 3504-3507.

[13] Shah, M. K., 2008, "Effects of Pressure Gradient on Two-Dimensional Separated and Reattached Turbulent Flows," Ph.D. thesis, University of Manitoba, Winnipeg, Manitoba.

[14] Piirto, M., Saarenrinne, P., Eloranta, H., and Karvinen, R., 2003, "Measuring Turbulence Energy with PIV in a Backward-Facing Step Flow," Experiments in Fluids, 35(3), pp. 219-236.

[15] Mao, Y., 2003, "The Effects of Turbulent Bursting on the Sediment Movement in Suspension," International Journal of Sediment Research, 18(2), pp. 148-157.

[16] Rabenjafimanantsoa, A. H., Time, R. W., and Saasen, A., 2007, "Characteristic of the Velocity Profiles over Fixed Dunes in Pipe," Annual Transactions - Nordic Rheology Society, 15(-), pp. 141-148.

[17] Detert, M., Weitbrecht, V., and Jirka, G. H., 2007, "Simultaneous Velocity and Pressure Measurements Using PIV and Multi Layer Pressure Sensor Arrays in Gravel Bed Flows," HMEM 2007, ASCE-Conference in Lake Placid, pp. 1-6.

[18] Balachandar, R., and Bhuiyan, F., 2007, "Higher-Order Moments of Velocity Fluctuations in an Open-Channel Flow with Large Bottom Roughness," Journal of Hydraulic Engineering, 133(1), pp. 77-87.

[19] Wagner, C., Kuhn, S., and Rudolf Von Rohr, P., 2007, "Scalar Transport from a Point Source in Flows over Wavy Walls," Experiments in Fluids, 43(2), pp. 261-271.

[20] Stoesser, T., Braun, C., Garcia-Villalba, M., and Rodi, W., 2008, "Turbulence Structures in Flow over Two-Dimensional Dunes," Journal of Hydraulic Engineering, 134(1), pp. 42-55.

[21] Husted, B. P., Petersson, P., Lund, I., and Holmstedt, G., 2009, "Comparison of PIV and PDA Droplet Velocity Measurement Techniques on Two High-Pressure Water Mist Nozzles," Fire Safety Journal, 44(8), pp. 1030-1045.

[22] Barnea, D., Shoham, O., and Taitel, Y., 1982, "Flow Pattern Transition for Vertical Downward Two Phase Flow," Chemical Engineering Science, 37(5), pp. 741-744.

[23] Zeinali, H., Toma, P., and Kuru, E., 2009, "Near-Wall Turbulent Transport Knowledge for Suitable Flow Assurance Strategies," ASME Conference Proceedings, 2009(43475), pp. 575-582.

[24] Blackwelder, R. F., and Kaplan, R. E., 1976, "On the Wall Structure of the Turbulent Boundary Layer," Journal of Fluid Mechanics, 76(01), pp. 89-112.

[25] Hart, D. P., 1998, "The Elimination of Correlation Errors in PIV Processing," 9th International Symposium on Applications of Laser Techniques to Fluid Mechanics, 13-16 July, Lisbon, Portugal, pp. 8.

[26] Keane, R. D., and Adrian, R. J., 1990, "Optimization of Particle Image Velocimeters. I. Double Pulsed Systems," Measurement Science and Technology, 1(11), pp. 1202.

[27] Raffel, M., Willert, C. E., Wereley, S. T., and Kompenhans, J., 2007, *Particle Image Velocimetry: A Practical Guide*, Springer,

[28] Pope, S. B., 2000, *Turbulent Flows*, Cambridge University Press, Cambridge; New York.

[29] Recktenwald, I., Alkishriwi, N., and Schröder, W., 2009, "PIV-LES Analysis of Channel Flow Rotating About the Streamwise Axis," European Journal of Mechanics - B/Fluids, 28(5), pp. 677-688.

[30] Shah, M. K., Agelinchaab, M., and Tachie, M. F., 2008, "Influence of PIV Interrogation Area on Turbulent Statistics up to 4th Order Moments in Smooth and Rough Wall Turbulent Flows," Experimental Thermal and Fluid Science, 32(3), pp. 725-747.

[31] Shah, M. K., and Tachie, M. F., 2009, "PIV Investigation of Flow over a Transverse Square Rib in Pressure Gradients," Journal of Turbulence, pp. N39.

[32] Tachie, M. F., and Shah, M. K., 2008, "Favorable Pressure Gradient Turbulent Flow over Straight and Inclined Ribs on Both Channel Walls," Physics of fluids 20(9), pp. 095103.

[33] Lavoie, P., Avallone, G., De Gregorio, F., Romano, G., and Antonia, R., 2007, "Spatial Resolution of PIV for the Measurement of Turbulence," Experiments in Fluids, 43(1), pp. 39-51.

[34] Saikrishnan, N., Marusic, I., and Longmire, E., 2006, "Assessment of Dual Plane PIV Measurements in Wall Turbulence Using DNS Data," Experiments in Fluids, 41(2), pp. 265-278.

[35] Herpin, S., Wong, C. Y., Laval, J.-P., Stanislas, M., and Soria, J., 2007, "Comparison of High Spatial Resolution Stereo-Piv Measurements in a Turbulent Boundary Layer with Available Dns Dataset," 16th Australasian Fluid Mechanics Conference, Crown Plaza, Gold Coast, Australia, pp.

4 Reduction of Frictional Pressure Drop Associated with Formation of Natural Lenticular Deposits[1]

4.1 Introduction

Liquid flow in pipes or channels at velocities below the critical removal value is accompanied by the transport of particles deposited at the bottom of the pipe or channel (particle bed). This phenomenon commonly occurs during production of heavy oil (containing sand) using horizontal wells, as well as during the hydrotransport of oil sand slurry from the mine site to the extraction plant.

A sufficiently large fraction of fine particles is required to stabilize the slurry system to prevent settling and ease the restart process during the pipeline slurry transport [1] . For example, a 439-km pipeline between Arizona and Nevada transports a slurry containing 20 wt% solids with particle sizes varying from 8 mesh to minus 325-mesh (2380 μm to ≤ 44 μm) [1]. Considerable effort is required to remove the fine particles at the end of the process.

Two phenomena related to sand bed transportation have been identified: (a) natural (spontaneous) formation of a well-organized train of individually clustered sand deposits (lenticular deposits - LDs) from an initially continuous bed, and (b) the advance of the LDs including the slow transport of the LDs accompanied by jumping of individual sand grains from one dune to the next at a higher speed.

[1] A version of this chapter has been presented. Zeinali, H., Toma, P., and Kuru, E., 2010. ASME International Mechanical Engineering Congress and Exposition (IMECE2010), November 12–18, 2010, Vancouver, British Columbia, Canada

The experimental work summarized in this study and a review of the pertinent literature focus on the following:

(a) the formation of lenticular deposits (LDs) and concentration-size-velocity relations, (b) the effect of LDs on frictional pressure drop, and (c) the complex role of turbulence (near the sand/liquid interface) in the natural shaping of LDs.

To assess the near-wall turbulence and pressure drop during the formation and transportation of LDs, photographic (static and video) observations as well as measurements of velocity distribution and turbulence characteristics with the aid of a non-intrusive (laser) particle image velocimetry (PIV) instrument were performed simultaneously. The goal of this research was to address the following questions:

- What are the flow conditions and slurry concentrations leading to the occurrence of LDs in pipeline flow?
- What are the effects of naturally formed LDs on:
  - frictional pressure drop?
  - turbulence (measured in the vicinity of LD/water interface)?

4.2 Background

Lenticular bed deposits have captured the attention of scientists since the early 20th century. Brigadier Ralph Alger Bagnold (1896–1990) was among the

pioneering scientists who paid close attention to formation of sand dunes (and LDs as a particular case). Bagnold reproduced some field observations (made in the Libyan desert) in the laboratory [2].

Laboratory experiments on slurry deposition-entrainment performed with the aid of a 19-mm (3/4-inch) flow loop and bulk velocities in the range of 0–1.8 m/s (0–5.8 ft/s) were used by Newitt et al. [3] to identify flow patterns. The slurry patterns assessed for different quantities of solids added to their system and at different transport velocities (but for a uniform size of glass beads with a diameter of 120 μm) were characterized as (see Figure 4.1): (a) "fully suspended flow", (b) "suspended flow with moving bed", (c) "suspended flow with a layer of particles sliding over a stationary deposit", (d) "stationary deposit with superimposed ripples", and (e) "isolated deposits" (lenticular deposits – LDs).

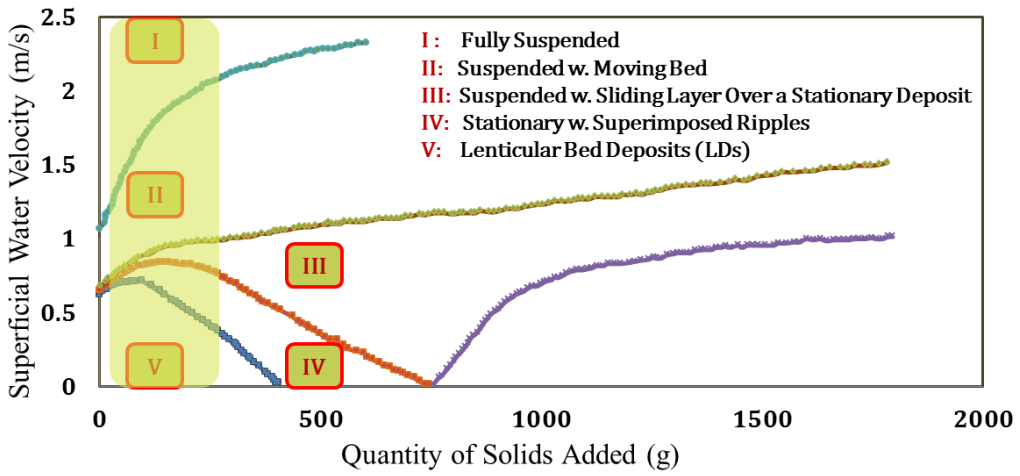

Figure 4.1 Slurry flow pattern for a broad range of solids concentrations and flow velocities (Newitt et al. [3])

Figure 4.1 illustrates different flow patterns for a range of superficial water velocities (calculated as if the carrier fluid occupies the entire pipeline cross section) versus the quantity of solids added to the flow loop. The slurry loop volume is not given in their paper, so the quantity of added solids cannot be converted to a concentration. The shaded rectangular area in Figure 4.1 corresponds to the investigation area of our study, in which we observed similar flow patterns when the flow rate in the slurry loop was reduced from the highest to the lowest setting. The major difference introduced in the present study is the use of a broad range of particle sizes – a new dimension in the study of slurry deposition-removal.

An experimental study by Thomas [4] on dynamics and flow patterns during sand bed transportation suggested a generalized phase diagram of particles using the Reynolds number (expressed with the aid of shear velocity, u^*) versus the normalized particle terminal settling velocity for a dilute slurry. For uniform-sized particles, knowing the density and diameter of the particles, the diagram can be used to obtain the onset velocities for different flow regimes including: (a) transverse dunes (assimilated with LDs), (b) longitudinal ripples, (c) heterogeneous, and (d) homogeneous slurry flow. Limited to a mono-sized slurry, Thomas' study and further publications have the merit of focusing on the occurrence and stability of LDs in the complex map of slurry flow patterns.

Kennedy [5] developed an analytical model to predict ripples, dunes, antidunes, and transitions from one configuration to another by applying the Froude number versus the lag distance between the local sediment transport rate and the local

velocity at the mean level of the bed. The model predicts the formation of ripples, dunes, and antidunes, and the occurrence of transitions from one configuration to another. The results from their model compared well with the experimental observations, particularly for deposits resulting from concentrations in excess of 1 vol%, above the concentration limit for the occurrence of LDs.

Buckles et al. [6] performed an experiment in a rectangular loop over a series of large-amplitude (artificially modeled) dunes with 50.8 mm wavelengths by using laser doppler velocimetry (LDV) to measure the instantaneous and fluctuation velocities over a sinusoidal dune surface. They were able to obtain the velocity profile, streamline map, pressure distribution, flow intermittency, turbulent intensity, wall shear stress distribution, shear layer map, and separation and reattachment regions over large-amplitude wavy dune surfaces.

Kapdasli and Dyer [7] carried out a flume experiment to calculate the total shear stress for five well-sorted sands from 137 μm to 500 μm in size to determine the threshold of grain movement on a rippled bed.

Doron et al. [8] developed a two-layer model to predict the pressure drop of different slurry flow patterns. They compared model results with data they obtained from a 2-inch pipeline loop and found satisfactory correlations.

Toma et al. [9] conducted an experiment with a 76-mm Plexiglas flow loop using two types of particles: silica (SG 2.63, size 82–427 μm) and plastic particles (SG 1.53, size 153–605 μm). They observed and quantified the dynamics of sand bed deposition (transverse and longitudinal dunes) at various carrier fluid velocities.

They suggested practical methods to enhance the sand removal for horizontal wells.

Doron and Barnea [10] proposed a three-layer model using two-phase continuity equations and force balance for the different phases to predict slurry flow patterns and transitions from one configuration to another. They also conducted experiments to confirm their model results. Because of the limitations of their experimental rig, the LD pattern was not prevalent. The experimental setup included a transparent pipe with a 3-mm diameter; acetal spheres with a density of 1240 kg/m^3 were used for the experiments. Their model can predict the solid-liquid flow pattern map based on the flow conditions of the system and the slurry concentration.

Belcher and Hunt [11] investigated the structure of the flow over hills and waves, particularly the interaction between the inner and outer turbulent flow regions, special features including the separation and reattachment points, and a closed separated flow region for shallow and steep slopes.

Nino et al. [12] ran an experiment in a rectangular open channel to observe and quantify the entrainment of particles from smooth and roughened (rippled) surfaces. The experiments were done using particles of five different sizes ranging from 38 μm to 530 μm. Considering the ratios of particle diameter to bed roughness diameter, force balances, the upward turbulent lifting force, and the weight of submerged particles acting downwards, they found that the hiding effect for the particles is smaller than the effect of bed roughness. They concluded that

higher shear stress is required to entrain small particles into the suspension from the bed load.

A number of experimental studies have recently aimed at measuring and understanding the role of a wavy-shaped interface to promote and suppress turbulent activity. Walker and Nickling [13] pointed out that, even though there has been good progress in understanding the dynamics of a dune's lee side (aspects such as flow separation, re-attachment, reversal cells, shear and boundary layers), our understanding of the lee side of dunes is limited to comparisons with the stoss side. This is due to a lack of appropriate instrumentation with the necessary precision, as well as theoretical limitations of flow analysis over complex topography. In their review paper, a model for evaluating surface pressure and shear stress over the dune crest was presented. Over the dune, the surface pressure is minimal and the shear stress is maximal; beyond the crest, the pressure rises and the surface shear stress falls rapidly.

Mao [14] simulated ripples, dunes, and sand wave structures on a flume test loop with five kinds of materials including smooth organic glass, waterproof sand paper, and organic glass flats. He tried to quantify his observation of burst (ejection) and sweep coherent structures and their effects for different surface roughnesses. Considering that the ejection happens in the low-velocity regions near the wall, he divided the flow area of sand waves into free-turbulent and through-turbulent areas based on the different flow states and coherent structures.

Best, in his review paper [15], suggested that dunes create heterogeneous and isotropic permeability fields in sandy braided rivers in the subsurface, as dune-like interfaces form the majority of the deposits. Therefore, subsurface flow predictions for aquifers and hydrocarbon reservoirs become difficult. Recent field investigations and numerical modeling studies have advanced the understanding of the dynamics and kinematics of dunes. The differential pressures due to dune morphology create an additional net drag force on the flow indicated as “form drag”. Data from rivers show that low-angle dunes (mean = 8.4°) represent the majority of the dune shapes. It has been argued that the transition from 2D to 3D dune forms might be connected to drag reduction over the dune. Best highlighted five areas for future research focus: (1) the influence of dune lee-side angle, (2) the influence of dune three-dimensionality, (3) superimposition and amalgamation as part of modification of the flow field, (4) turbulent flow around the dunes, and (5) the influence of suspended slurry flow.

Toyama et al. [16] carried out an experimental and numerical simulation study of the dune effect as a roughness that resists sediment transportation. They measured dune transport velocity and found it to be in agreement with the results from the literature models. In their simulation and experiments, the results were better matched for dunes with step length of 50 particle diameters (50d) rather than 20d.

Venditti [17] used acoustic doppler velocimetry (ADV) to obtain the three components of flow velocities over the bed for configurations including a fixed flat bed, 2D dunes, and four different kinds of 3D dune morphologies (full-width saddles, full-width lobes, sinuous crests, and irregularly shaped crests). The

experiments were conducted in a flume channel 17 m long, 0.52 m wide, and 1 m deep. Ten wooden dunes were constructed. For each configuration, 35–37 velocity profiles were obtained along the flume centerline at 0.014–0.018 m apart and with 10–15 vertical measurement locations. Each measurement was completed in 90 s. The lowest point in the velocity measurement in each configuration was at a height of ~ 5 mm above the bed and extended to ~ 0.08–0.11 m above the dune. From those measurements, simple turbulence and velocity relations such as mean streamwise and vertical velocities, turbulence intensity, streamwise and vertical Reynolds stress, and turbulent kinetic energy were obtained empirically and compared. Venditti noted that some irregular 3D dunes have 20% less flow resistance than straight-crested 2D and sinuous-crested dunes.

Stoesser et al. [18] ran a simulation to obtain the velocity relations over a 2D dune with a wavelength of 400 mm and a height of 20 mm in channel flow using large-eddy simulation (LES). Their results for velocity profiles, fluctuation velocities, and Reynolds shear stress over different parts of the dune were in agreement with the experimental results of another researcher.

Mianaei and Keshavarzi [19] carried out an experiment in a glass-wall flume 0.70 m wide, 0.60 m high, and 15.5 m long using three different dune configurations. They measured the velocity field over the dunes using ADV and captured images with a digital camera. They found that the mean instantaneous shear stress ratio of burst and sweep sections are higher on the dune stoss side compared than on the lee side; therefore, they concluded that entrainment is the dominant phenomenon on the stoss side whereas particle deposition is dominant on the lee side.

Wilson and Brebner [20] conducted a series of experiments in a 95-mm (3.74-inch) ID pipeline using a variety of slurry concentrations. Figure 4.2 summarizes some of Wilson and Brebner's most important results. Figure 4.2 illustrates the variation of head loss (pressure drop) with flow rate at different slurry concentrations. Numerical modeling of the data illustrates four different slurry flow patterns areas: (a) continuous bed area, (b) sliding deposit area, (c) no deposition area, and (d) dunes area. The area of particular interest for this dissertation (concentrations under 1 vol%) is not well represented. They recorded the head loss as the flow pattern changed from a continuous bed to a no-deposition case corresponding to an elevated flow rate. The reduction in pressure drop in this case was mainly due to the increase in cross-sectional area open to flow as a result of the flow pattern changing from a continuous bed to no bed (all solids in suspension). Shaded area #1 in Figure 4.2 shows the conditions under which a continuous bed blocked a portion of the pipeline and resulted in a relatively large pressure drop. Following a period of increased flow rate, the slurry flow pattern changed to a sliding pattern (area #2). As the flow rate was increased further, the flow reached the point where there was no deposition (area #3). This sequence of flow pattern changes was observed as long as the slurry concentration was above 2 vol%. For slurry concentration lower than 2 vol% (area #4), however, the progression of the flow pattern changes was different. Area #4 shows observations at a low slurry concentration and lower flow rates.

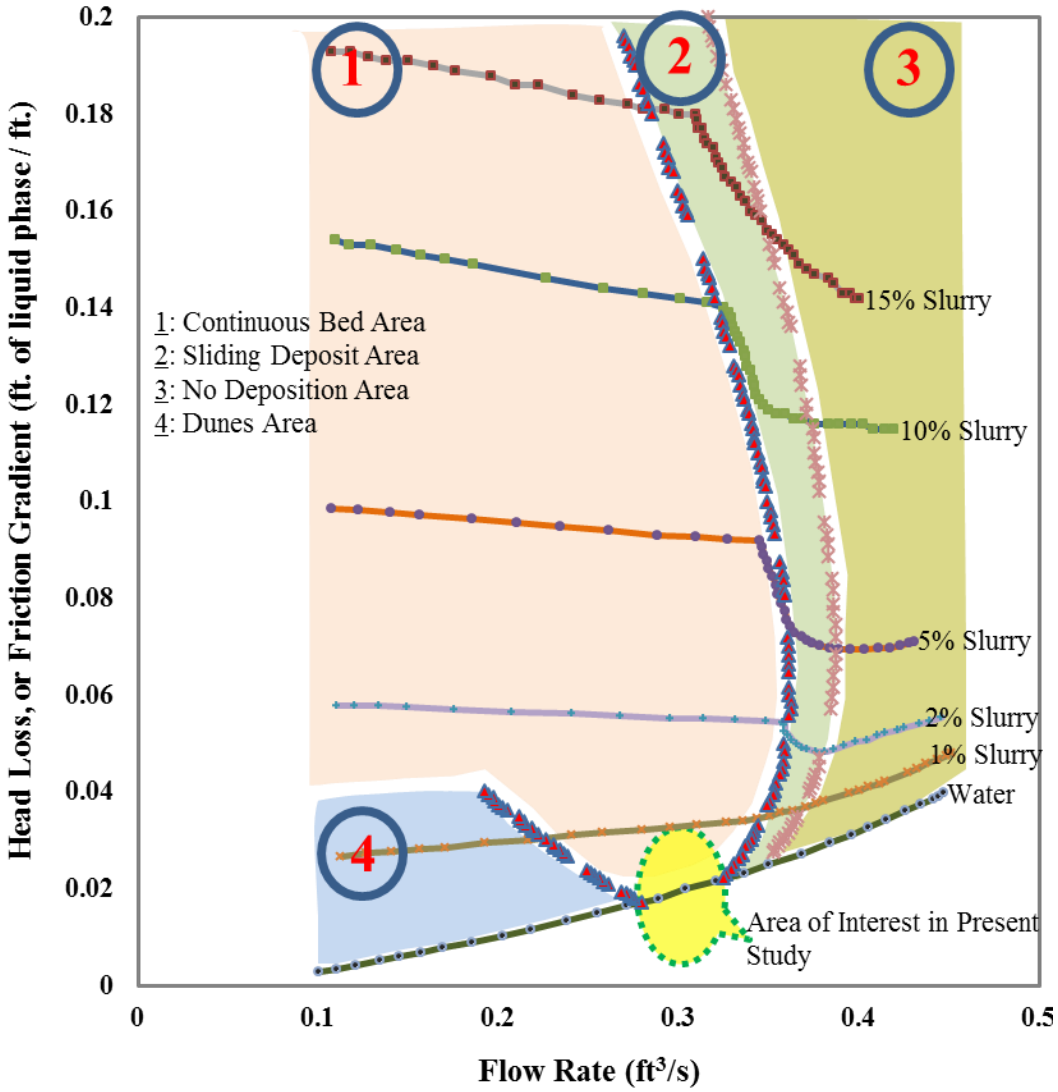

Figure 4.2 Friction gradient versus flow rate for different sand slurry concentrations and dunes in a 95-mm ID pipeline (particle mean diameter 685 µm) [20]

Wilson and Brebner identified the flow pattern in this area as "dunes" (Figure 4.2, area #4). Although they observed the development of LDs, Wilson and Brebner did not provide detailed analysis of this particular flow pattern. For example, the characteristics of the flow pattern and pressure drop in the area where their best fit

of the dune line reaches the water line (i.e., the area highlighted by the circle in Figure 4.2) was not well described in their work.

The aim of the present work is to focus on the flow pattern and changes in pressure drop in this not-so-well-defined region of flow that is nonetheless relevant for the commercial transport of mineral slurries. In particular, the experiments conducted in this study investigate the effects of flow pattern transitions at low slurry concentrations and low flow rates. In this work, the flow rate is kept constant during transitions in the slurry flow regime. The objective is to investigate how changes in the slurry flow pattern affect the pressure drop and the turbulent kinetic energy of the flow, while the cross-sectional area open to flow remains unchanged. It should also be mentioned that the minima in pressure drop versus flow rate curves observed for concentrations in excess of 1 vol% are attributed to reduction of the depth of the deposited bed with velocities above the critical removal velocity (e.g., not related to formation of LDs as in our study using low-concentration slurries and velocities below the critical deposition velocity).

4.3 Experimental Setup and Materials

A flow loop (Figure 4.3) was designed and built for the slurry flow experiments. Components of the flow loop included a slurry preparation and recirculation tank, tap water flowmeter, slurry pump, bypass line, 1.5-inch and 2.5-inch slurry loop feed lines, magnetic flowmeter, a 95-mm ID optical-quality horizontal glass

pipeline approximately 15 m long, differential pressure transducers, PIV instrumentation, and a PIV measurement area. The first differential pressure transducer has a range of 0–1 psid (0–6.89 kPa) with full-scale accuracy of ±0.25%. The second differential pressure transducer has a range of 0 to 6 inches H_2O (0 – 1.49 kPa) with a nominal accuracy of ±0.17%. The slurry flow was driven by a centrifugal pump equipped with a VFD speed control system to set and regulate the flow velocity in the pipeline.

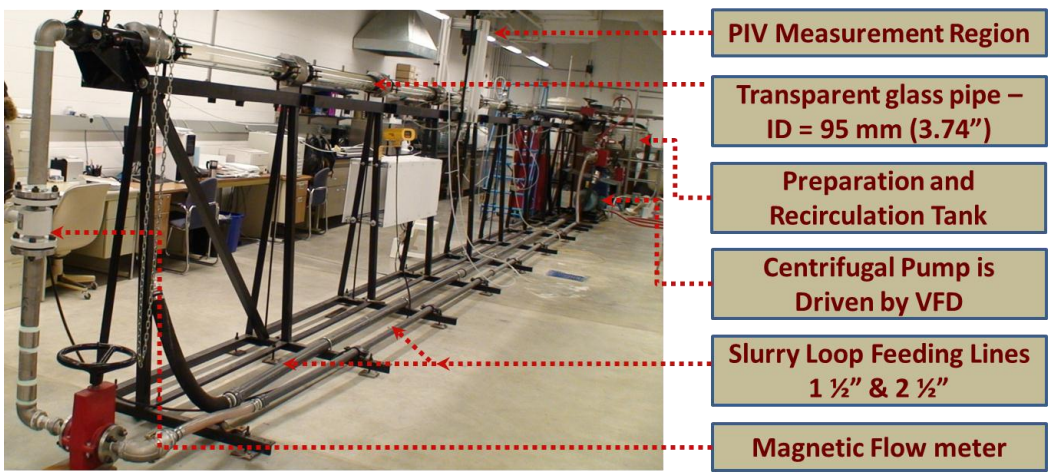

Figure 4.3 Flow loop setup for slurry experiments

The solid particles used for the experiments were silica sand and glass beads with a density of 2630 kg/m^3. The manufacturer's particle size distribution (PSD) data are given in Tables 4.1–4.3.

Table 4.1
PSD of Sil 325

	ASTM sieve no. (opening)	Cumulative retained %
Sieve analysis (Typical mean wt% cumulative retained)	#100 (150 µm)	1.9
	#140 (106 µm)	2.9
	#200 (75 µm)	5.8
	#270 (53 µm)	11.0
	#325 (45 µm)	4.8
	> #325 (< 45 µm)	73.6

Table 4.2
PSD of Sil 1

	ASTM sieve no. (opening)	Cumulative retained %
Sieve analysis (Typical mean wt% cumulative retained)	#45 (355 µm)	0.4
	#50 (300 µm)	8.1
	#60 (250 µm)	35.1
	#80 (180 µm)	42.7
	#100 (150 µm)	8.1
	#120 (125 µm)	4.4
	> #120 (< 125 µm)	1.2

Table 4.3
PSD of glass beads 2429 (A-soda lime glass)

Mean value	10% finer than	50% finer than	90% finer than	100% finer than
83 µm	72 µm	83 µm	99 µm	123 µm

4.3.1 General Observations of Slurry Flow Patterns

The type of flow pattern in a pipeline depends on variables such as flow velocity, pipe diameter, slurry concentration, solid particle size, and the viscosity and density of the carrier fluid.

A homogeneous suspension was observed when 0.5 vol% silica sand #325 slurry was pumped at the highest possible flow rate of 0.009 m^3/s (540 L/min) through the flow loop (bulk velocity 1.27 m/s). When the flow rate was reduced to 0.006 m^3/s (bulk velocity 0.85 m/s), the flow became heterogeneous. When the flow rate was further reduced to 0.005 m^3/s (300 L/min), the critical deposition velocity (0.71 m/s) was reached (i.e., particles started settling at the bottom). Between the flow rates of 0.005 m^3/s and 0.004 m^3/s (300–240 L/min), the flow regime was a moving bed. The transition to a three-layer saltation pattern, with a stationary bed at the bottom and moving bed above, with heterogeneous flow above that, was observed at a flow rate of 0.004 m^3/s (bulk velocity 0.56 m/s). When the flow rate was reduced to 0.0029 m^3/s (bulk velocity 0.41 m/s), a transition from saltation to LDs was observed. As the flow rate was reduced further, the flow pattern was still LDs; however, the distance between LDs increased until nearly stationary LDs were observed.

Using the Oroskar and Turian [21] model and assuming a median particle diameter (d_{50}) of 40 µm at 24°*C*, the critical slurry velocity was calculated as 0.76 m/s, 7% higher than the experimentally observed value of 0.71 m/s. The difference could have been due to the use of the median particle diameter in the calculation, whereas the experimental system utilized a broad PSD.

Depending on their shapes, LDs are described as barchans, crescentic (transverse) ridges, linear (longitudinal), star, reversing, or parabolic [22].

Figure 4.4a The parabolic form of LDs

Figure 4.4b The barchan form of LDs

Two different LD forms were observed during our experiments. After transitioning from a continuous bed, the form of LDs was parabolic (Figure 4.4a).

In this form, sand grains are transported by avalanching. When the velocity is reduced further and as time passes, the parabolic form changes to the barchan form (Figure 4.4b).

The parabolic LDs are not physically separated from each other, i.e., just before the tail of one LD ends, the head of the next one starts. Barchan LDs are discrete and there is usually a gap between dunes which varies from one third to twice the length of the LD itself. The transport velocity of parabolic LDs is higher that of the barchan LDs. When the average flow velocity was 0.34 m/s, the transport velocity of parabolic LDs was 10.8 cm/min, and for the barchan LDs, it was 5.4 cm/min.

The crest-to-crest distance between parabolic dunes was 7 cm on average. The tail-to-head length of the parabolic LD varied from 0 to 2 cm. When the crest-to-crest distance between barchan LDs was 7 cm, the distance from the tail to the head of the next LD varied from 2 to 3.5 cm (Figures 4.4a and 4.4b). The spacing between the LDs at the beginning of the experiment was small and sometimes nonexistent; as time elapsed, the distance between the LDs increased and reached almost 10 cm after 30 min at the average velocity of 0.34 m/s.

The average LD height was 2–4 mm, measured directly from the perimeter of the pipeline containing the LD. PIV pictures (Figure 4.5) were also used for LD height measurements.

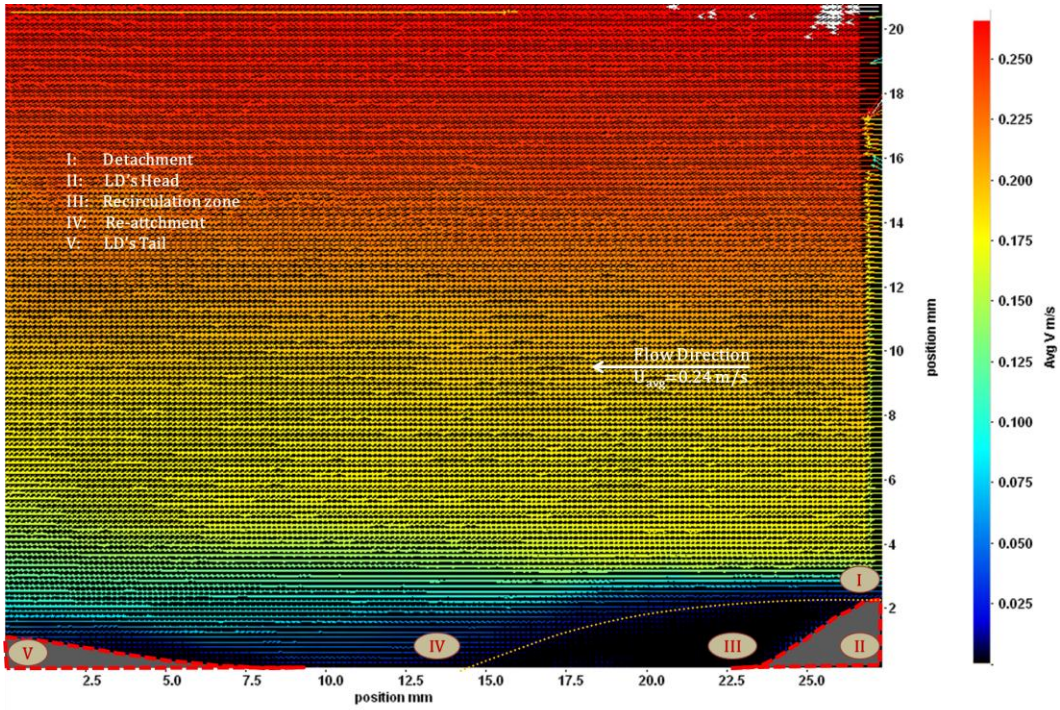

Figure 4.5 Detachment and re-attachment points as well as recirculation zone in an LD; the sidebar gives the magnitude of the velocity field in m/s.

The LDs in the pipeline usually had a stoss length of 5 cm with a lee length of 1 cm. This makes the LD aspect ratio (height/total length) 0.07. The inverse of the LD aspect ratio is the LD index, which was calculated as 14.

The interface between unconsolidated sand and a river, sea, or moving aeolian fluid (liquid or air) is often observed as wave-like shapes identified as dunes. In nature they can reach heights from a few meters (in fluvial systems) to a hundred meters (in an aeolian desert environment), and may reach a few hundred meters in length. A general characteristic of all “dunes” is their periodic aspect and recurring shape; they involve specific dynamics, including a macroscopic effect

of axial transportation and concurrent microscopic actions of sand removal and deposition.

LDs that form during pipeline transport of slurries are a special case of "spontaneously occurring" dunes and are the main subject of this study. The factors controlling the occurrence of LDs as well as the characterization of LDs are discussed below.

4.3.1.1 Effect of slurry concentration on the formation of LDs

Discrete LDs are observed only in dilute slurries. In the current experimental setup, LDs were observed at less than 1 vol% concentration. When slurries with concentrations higher than 1 vol% were used, uniform LDs were not observed at the bottom of the pipe (Figure 4.6a).

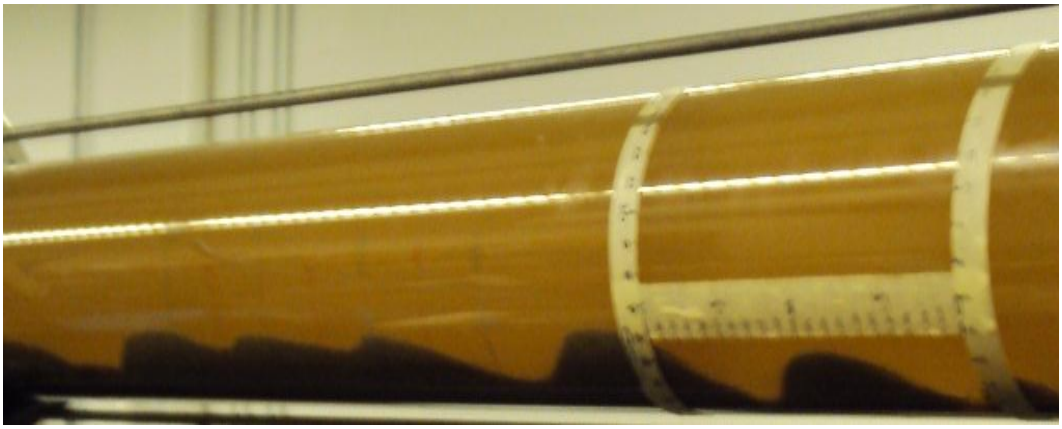

Figure 4.6a Bed form for slurry concentration greater than 1 vol%

Figure 4.6b Bed form for slurry concentration of 0.5 vol%

The dunes formed were irregular in shape, length, and height. Discrete LDs are observed only at low slurry concentrations and low flow rates (Figure 4.6b). Patterns similar to LDs can be seen on the surface of other flow patterns as well. For example, when there is a stationary bed with a moving bed on top, the moving bed could be formed by saltation similar to LDs.

4.3.1.2 Mechanisms and velocity of LD propagation movement

Lenticular dunes can be moved by saltation, near-wall coherent structure activities such as burst and sweep, and sometimes by rolling. Evaluation of burst-sweep occurrence and frequency was discussed in detail in an earlier study [23].

Burst activity takes particles from the bed and, as the burst evolves, it transports the particles to the core [24]. In contrast, sweep activity brings particles back from

turbulent core flow to the bed. Both activities were observed during the experiments.

The propagation velocity of LDs on the bottom of the conveying pipeline is a function of bulk fluid velocity, fluid density, viscosity, and the density, size, and shape of the particles. Experiments were conducted using different median particle sizes and fluid velocities. In order to evaluate the effect of particle size on LD movement, the other operational parameters were kept constant. The results are listed in Table 4.4 and plotted in Figure 4.7. The results of the experiments were compared with experimental data of Toma et al. [9].

Table 4.4

LD propagation velocities for different median diameters and fluid velocities

Median particle diameter	**Average fluid velocity (m/s)**		
***d_{50}* (µm)**	**0.25**	**0.34**	**0.39**
	LD transport velocities (cm/min)		
20	0.94	3.34	6.26
110	1.40	8.53	19.04
125	1.66	8.71	20.16
240	2.02	13.32	24.66

As the data in Table 4.4 and the plots in Figure 4.7 show, as the particle size increases, the propagation velocity of LDs also increases for a given fluid velocity. Increasing the carrier fluid velocity increases the LD propagation velocity. This finding is in agreement with Toma et al. [9] experimental results in 3 inch (76 mm ID) Plexiglas tube. However, the small differences between the

results might be due to differences in the pipe inner diameter and the experimental methodology employed in studies.

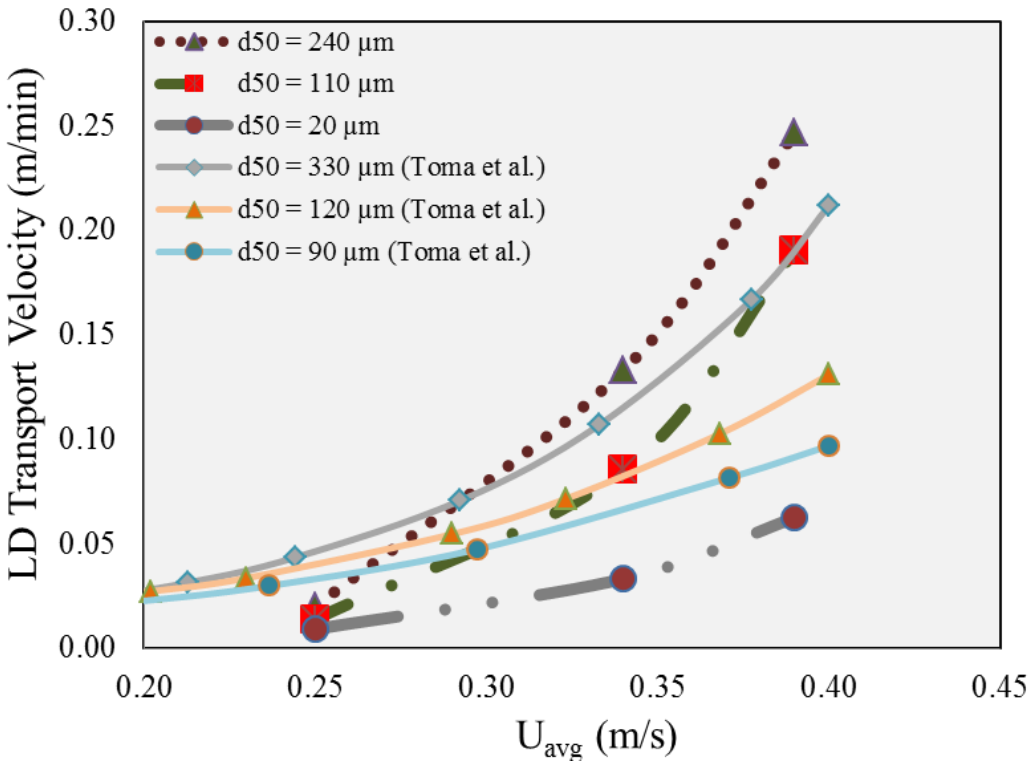

Figure 4.7 LD propagation velocities in pipe at different fluid velocities and particle sizes. The data in this study were compared with the data from Toma et al. [9] experiments

4.4 Effect of LD Formation on Frictional Pressure Drop

Pressure drop measurements were conducted at different flow rates using stepwise flow rate reductions. The flow rate was kept constant for 30 to 40 min in order to stabilize and observe any changes of the bed including dune formation and

shaping, as well as propagation velocity. The flow rate was then dropped rapidly to a lower value.

In order to determine a reference (baseline) pressure drop, the first experiment was conducted with water only. The accuracy of the pressure drop measurements was validated by comparing the measured and calculated frictional pressure drops for water-only flow, as shown in Figure 4.8.

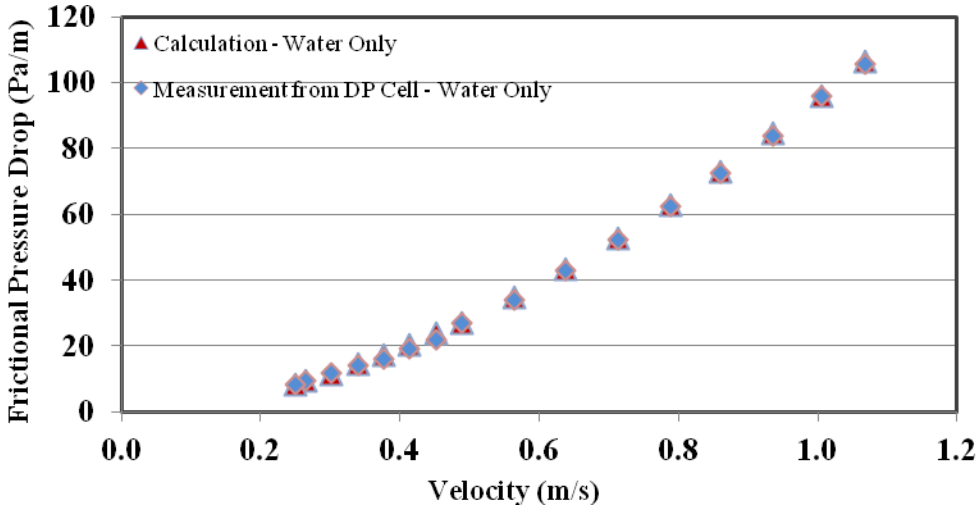

Figure 4.8 Base data for calibration of DP cells – measured versus calculated frictional pressure drop

Experiments were conducted using 0.5 vol% silica sand #325 with a median diameter of 40 µm. Special care was taken to minimize pump speed variations (below 1/1000) and, thus, minimize fluctuations of the measured flow velocity and pressure drop. As the slurry flow rate was reduced from the highest to the

lowest values, the following progression of flow and deposition patterns was observed: homogeneous, heterogeneous, moving bed, stationary bed with moving bed on top, and LDs. Each of these flow pattern changes were clearly seen during a complete experimental run. The LDs were parabolic at the beginning, with essentially no space between them. As time passed, the distance between the tail and head of adjacent LDs increased gradually as the parabolic LDs changed to barchan shapes.

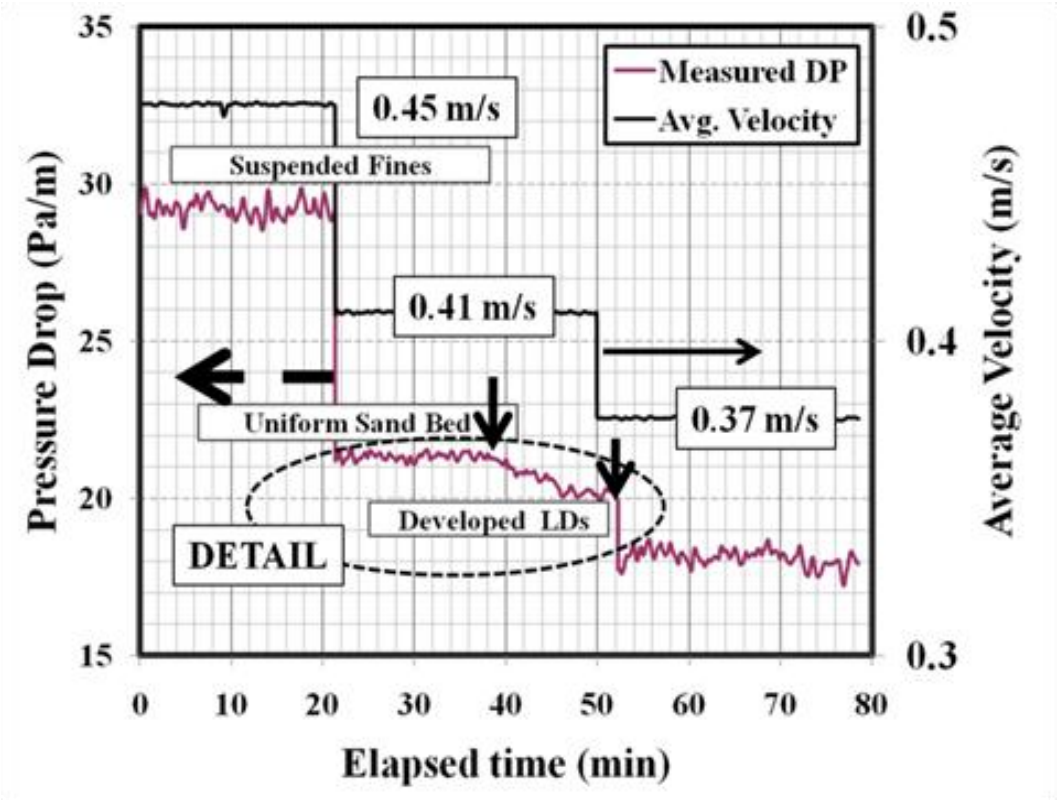

Figure 4.9 Recorded pressure drop versus time during transitions from continuous bed to LDs

One salient observation was that, during the transition from continuous bed to LDs, the frictional pressure drop decreased. Formation of LDs was associated with a reduction of the turbulent dissipated energy loss during the natural formation of LDs out of the (initially) uniformly deposited sand. Figure 4.9 represents a snapshot of the recorded velocities and pressure drops measured, along with the presence of a continuous bed and transitions from continuous bed to LD patterns. The transition from continuous bed to LD flow patterns occurred at an average bulk velocity of 0.41 m/s.

The frictional pressure drop values measured before the flow pattern transition (velocity 0.45 m/s), during the transition (velocity 0.41 m/s), and after the transition (velocity 0.37m/s), are shown in Figure 4.10, Figure 4.11, and Figure 4.13, respectively. In these figures, the calculated frictional pressure drop values for smooth pipe and “sand bed” – equivalent rough surface – conditions are also included for comparison.

The friction factor defined by the Blasius equation (Eq. 4.1) was used to calculate the pressure drop for water flow through smooth pipe:

$$f_{Blasius} = 0.3164 \big/ \mathrm{Re}^{1/4} \tag{4.1}$$

The calculation of the “sand bed” pressure drop is modeled by incorporating the relative roughness friction factor in Churchill's equation [25]. A detailed description of Churchill’s equation is given in Appendix 4.A. An absolute

roughness value (for the sand bed) of 150 µm resulted in the best match between the measured and the calculated pressure drops, which required the ratio between smooth and rough (interface) areas, η , to be 0.82 in Eq. 4.3:

$$\eta = S_{liquid} / S_{interface} \tag{4.2}$$

$$Dp_{calc.} = \eta \times Dp_{fr.-smooth} + (1-\eta) \times Dp_{fr.-interface} \tag{4.3}$$

The selected interface distribution coefficient (η = 0.82) was previously estimated using an actual concentration of C = 0.5 vol% and the assumed bed porosity of 0.52. The frictional pressure drop remained unchanged over time when there was a continuous bed (Figure 4.10).

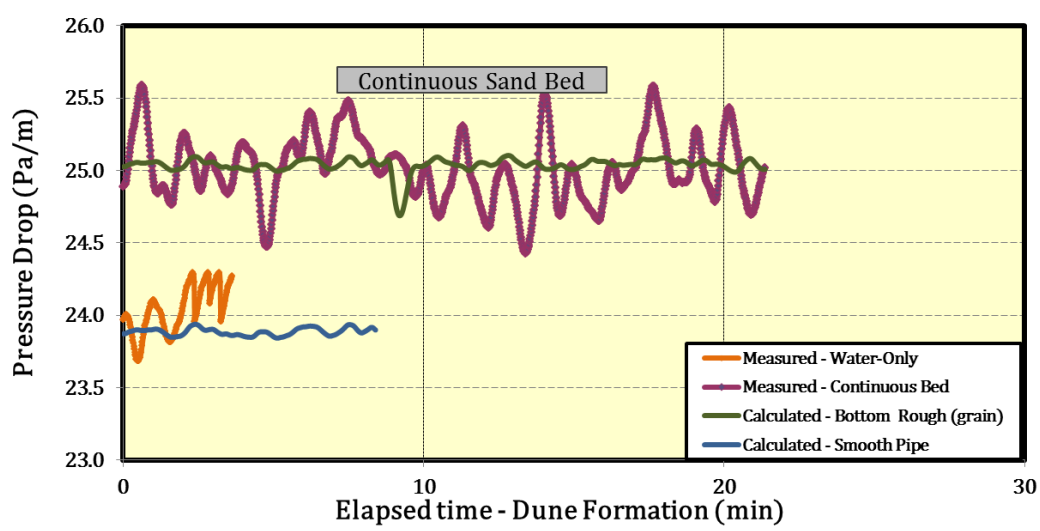

Figure 4.10 Measured and calculated frictional pressure drops due to flow over a continuous bed. Average flow velocity is 0.45 m/s

Figure 4.11 shows the variation of the frictional pressure drop as the flow pattern transforms from a continuous bed to LDs. When the velocity was set to 0.41 m/s, the flow pattern was initially a stationary bed with a moving bed on top for about 17 min. Following this initial period, the flow pattern gradually changed from a continuous bed to LDs. Transformation of the continuous bed to LDs was associated with a reduction in the frictional pressure drop.

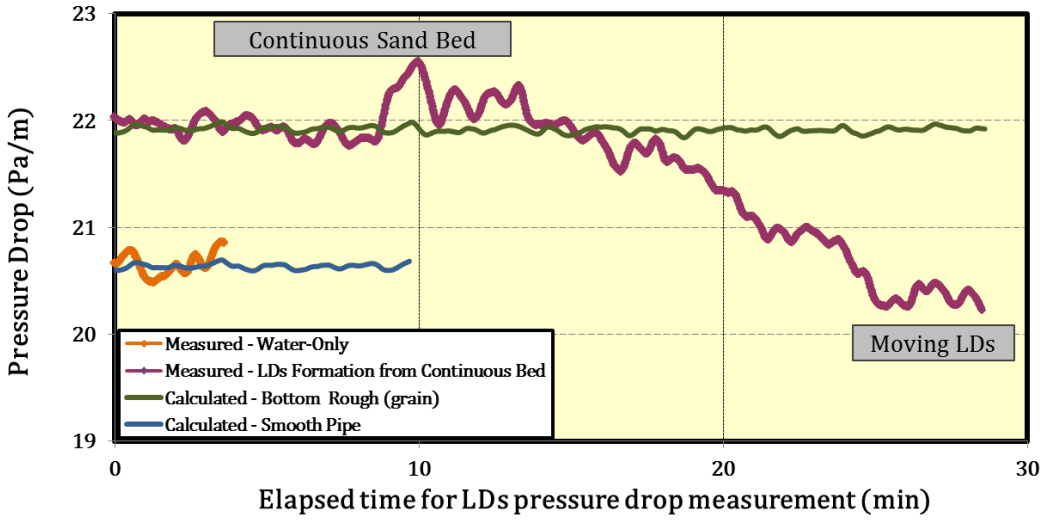

Figure 4.11 Effect of dune formation on frictional pressure drop. Average flow velocity is 0.41 m/s

Despite minor fluctuations in the flow velocity, the measured pressure drop, shown in Figure 4.12, indicates a decreasing trend (estimated to be more than ten times that of the recorded fluctuations). The relative change in the frictional pressure drop recorded during flow pattern transition with respect to that for the flow of water in the smooth pipe was calculated. As the figure shows, an 8%

reduction in frictional pressure drop was observed during the change in flow pattern from a continuous sand bed to LDs.

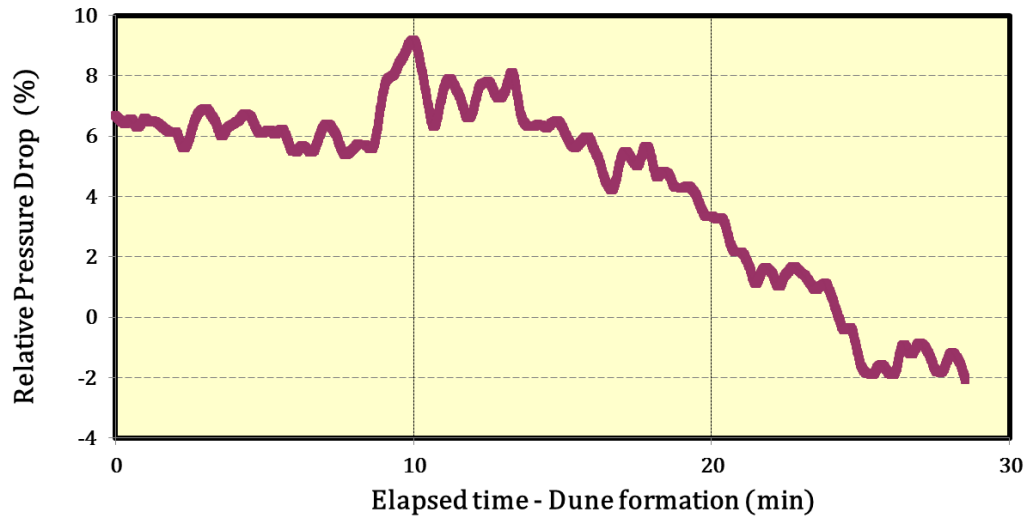

Figure 4.12 Effect of dune formation on frictional pressure drop (normalized with respect to frictional pressure drop in water flow)

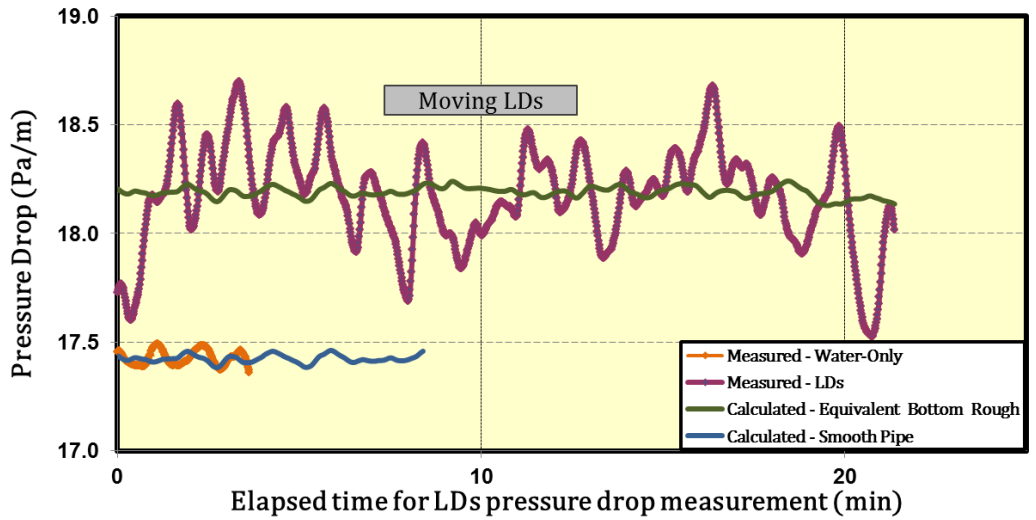

Figure 4.13 Frictional pressure drop due to flow over LDs. Average flow velocity is 0.37m/s

Figure 4.13 shows the measured and calculated (assuming equivalent roughness) frictional pressure drops associated with the flow over the LDs after the full transition to LDs. The frictional pressure drop remained relatively constant as long as the flow pattern stayed as LDs.

In order to assess the degree of variation in the measurements, experiments were repeated to observe the effect of flow pattern variation on the frictional pressure drop. The results are shown in Figure 4.14 and Figure 4.15. As Figure 4.15 illustrates, the frictional pressure drop difference at the constant velocity during re-formation from continuous bed to LDs in the repeated experiment is 7%. Approximately the same percentage of frictional pressure drop reduction was observed in the both experiments, confirming the repeatability of the measurements.

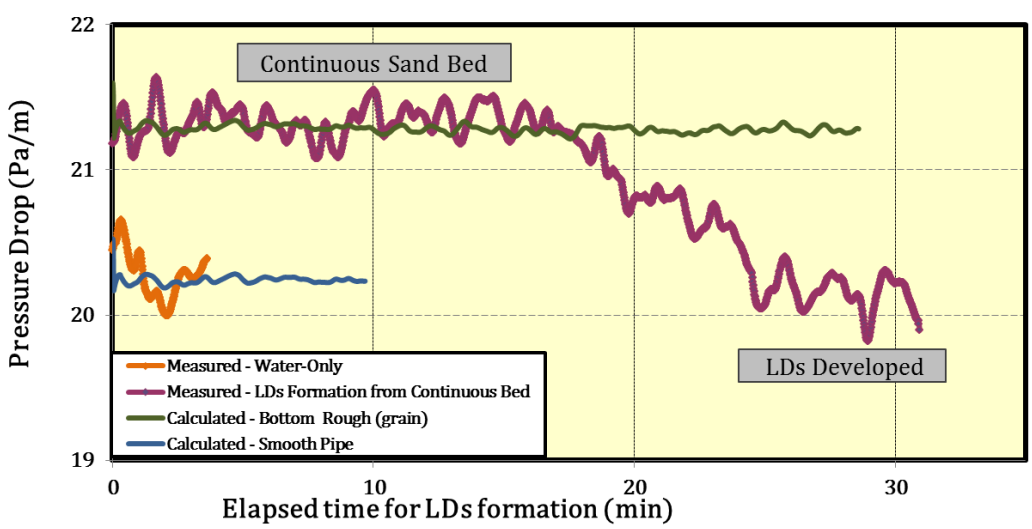

Figure 4.14 Effect of dune formation on frictional pressure drop (repeated experiment, U_{avg} = 0.41m/s)

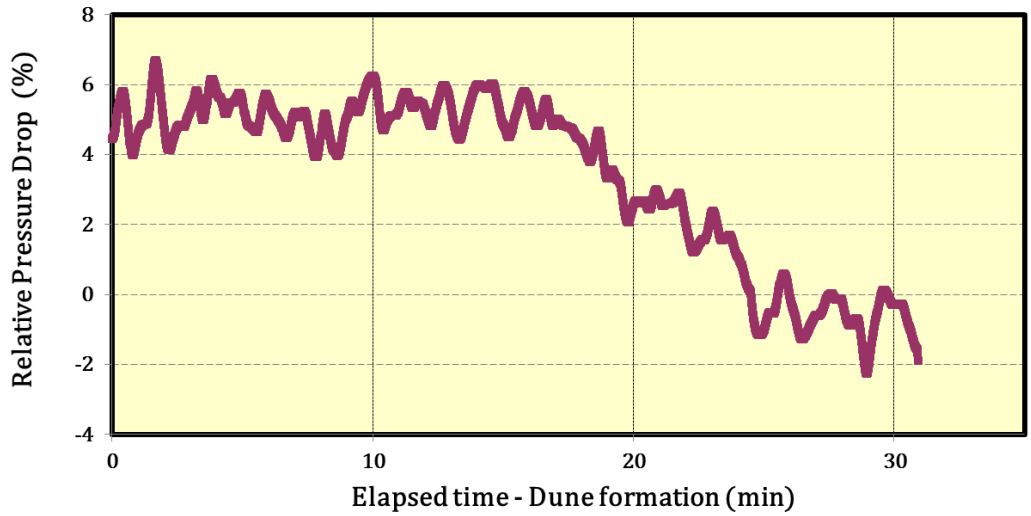

Figure 4.15 Effect of dune formation on frictional pressure drop (normalized with respect to frictional pressure drop due to water flow, repeated experiment, U_{avg} = 0.41m/s)

Researchers have reported that suppressing near-wall coherent structures (burst and sweep events) by various means such as having riblets, bumps, and flaps, helps to reduce the frictional pressure drop or drag [26]. In addition, many studies have been conducted on the effect of burst-sweep and turbulent kinetic energy (TKE) suppression on drag reduction by using additives such as polymers [27-29]. In drilling, walnut shells are added to the mud to help in reducing the frictional pressure drop and drag by suppressing coherent structures near the wall. For this study the burst and sweep frequencies and TKE for the three cases – water-only flow, continuous bed, and LDs – were evaluated and compared to explain the effect of re-formation of the continuous bed to LDs on the frictional pressure drop.

The drag force is defined as

$$Drag\ \ force = \tau_w \times wetted\ \ area \tag{4.4}$$

τ_w is the wall shear stress in units of Pa, which for fully developed turbulent flow in the pipe is

$$\tau_w = \frac{D}{4}\frac{\Delta P}{\Delta x}\ \left(Pa\right) \tag{4.5}$$

where D is the pipe diameter and $\Delta P/\Delta x$ is the frictional pressure drop over the length x (m) in the flow direction.

The wall shear stress in terms of the Darcy-Weisbach friction factor is

$$f = {8\tau_w}\Big/{\rho\overline{U}^2} \tag{4.6}$$

Equations (4.4–4.6) illustrate the relationship between drag force and frictional pressure drop along the pipeline. They are proportional to each other – reduction in drag means reduction in frictional pressure drop and vice versa. Therefore, the

effects of burst-sweep and TKE on frictional pressure drop were evaluated as a common procedure. In other words, how frictional pressure reduction and coherent structures are relevant and how deformation of a continuous bed to LDs affects burst-sweep frequencies and TKE. Improved understanding of these phenomena would help address many operating challenges in industry, including pipeline transport in horizontal and extended-reach drilling and for on-line slurry transport. The results of our investigation are given in the sections that follow.

Burst activity takes particles from the bed and, as the burst evolves, it transports the particles to the core [24]. In contrast, sweep activity brings particles back from turbulent core flow section to the near-wall region. The bursting phenomenon accounts for most of the TKE production in the near-wall region and is also responsible for maintaining the turbulent drag on the wall [26]. Accordingly, reduction of the coherent structures near the wall (burst-sweep) by any means reduces the frictional pressure drop or drag. This prospect provides an incentive to compare the near-wall characteristics of the flow stream for the experimental cases – water-only, continuous bed, and LDs.

4.5 Burst-Sweep and TKE in the Near-Wall Region

The phenomenon of drag force reduction by polymer addition was reported in the 1960s, and later drag reduction was achieved by introducing riblets to the inner wall surface [26]. The common way to approach the drag reduction phenomenon is by study of near-wall coherent structures. A non-intrusive optical technique,

PIV, which can measure the velocity field of the control volume, was used in this work to study the effects of coherent structures on frictional pressure in re-formation of the continuous bed to LDs at a constant flow rate.

Near-wall turbulent activities such as burst, sweep, and upward and downward interactions (i.e., turbulent coherent structures) are considered as the main source of TKE [30, 31]. The near-wall area $y^+ \leq 100$ is normally considered for the coherent structures assessment, and includes the sublayer, the buffer zone, and part of the logarithmic region [32]. The presence of low-speed streaks at the boundary layer very close to the wall has been identified by many researchers [30, 33-36]. After creation, these low-speed streaks grow, oscillate, and break up into coherent structures known as burst and/or sweep. The $0 \leq y^+ \leq 10$ zone is reportedly associated with occurrence of low-speed streaks, the source of the burst activity [35], and above this region, these streaks start to oscillate. The region $10 \leq y^+ \leq 30$ is reported as the area where major turbulent activities take place [35].

Near-wall turbulent activity such as burst, sweep, and upward and downward interactions were analyzed for three different near-wall flow conditions: LDs, continuous bed, and smooth pipe. Assessment of turbulent coherent structures requires measurements of instantaneous velocity near the wall. Due to the chaotic nature of turbulent flow, instantaneous velocity measurements should be averaged over time (VITA) or space (VISA) to obtain quasi-steady-state data indicating a trend (i.e., repeatability).

4.5.1 PIV Experimental Setup and Test Conditions

Figure 4.16 shows the major components of the PIV setup: a source of laser light, Nd:YAG (neodymium-doped yttrium aluminum garnet, Nd:Y3Al5O12) which produces double-pulsed 532-nm high-intensity laser light; a charge-coupled device (CCD) camera positioned perpendicular to the thin laser sheet; and a rectangular investigation area constructed around the circular pipe.

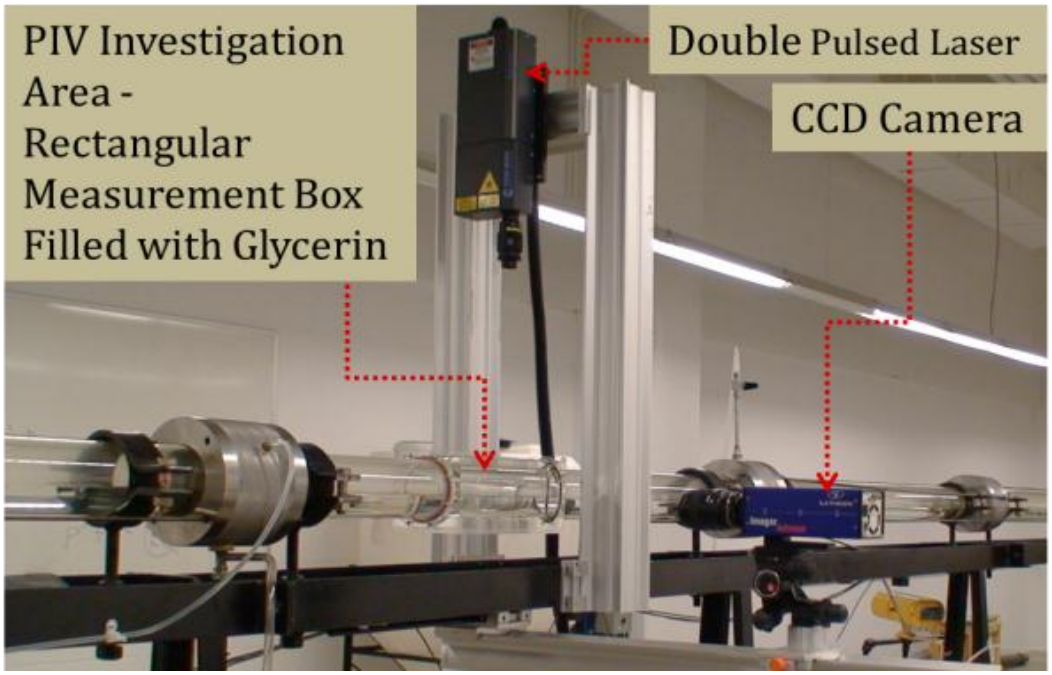

Figure 4.16 PIV setup on the slurry flow loop

Particles or impurities in the water in the pipeline are illuminated by green laser light and the images are captured by a CCD camera. There were enough particles in each interrogation window (IW) for cross correlation of the particles in 16 x 16

pixels (usually 4–5 particles for each IW), which means there was no need to seed the flow. Using a cross-correlation technique, the velocity vector is computed by dividing the dominant cross-correlated displacement by a fixed time interval, which was chosen at the beginning of the experiment for each velocity (the time step between double frames varies from experiment to experiment as the focus conditions and the bulk flow velocity vary). The PIV setup was designed to measure instantaneous fluid velocity over an area of 28 x 20 mm^2. Instantaneous velocity field data were obtained over 20 s at the PIV frequency of 5 fields per second (5 Hz), providing 100 velocity vector fields for each case under investigation. The specifics of the data management by the PIV tool are summarized in Table 4.5.

Table 4.5
Specifics of data management with PIV

Measurement time span	20 s
Sampling (PIV) frequency	5 Hz
Number of instantaneous velocity vector fields for each case	100
Number of data columns in each velocity vector field	172
Number of data rows in each velocity vector field	130
Total number of data in each velocity vector field	22,360

Figure 4.17 shows how the investigation area was divided into horizontal zones with Z-I, Z-II, and Z-III. The area was also divided vertically into four subzones

to represent the LD parts including the stoss (tail), crest (body), slipface or lee-side (head), and space between the head and tail of the next LD (trough or interdune). For comparison, the size of the control volumes for the other two cases, i.e., water-only flow in smooth pipe and slurry flow over a continuous bed, were kept identical to the LD control volume.

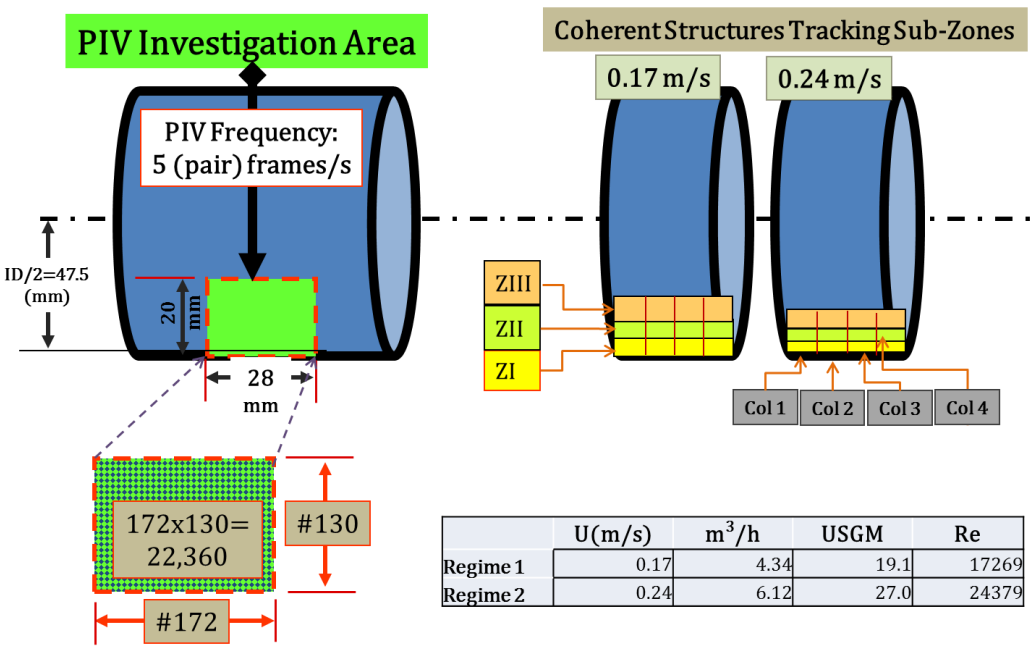

	U(m/s)	m^3/h	USGM	Re
Regime 1	0.17	4.34	19.1	17269
Regime 2	0.24	6.12	27.0	24379

Figure 4.17 Horizontal and vertical divisions of the PIV investigation area and the number of columns and rows for the experimental measurement field

Table 4.6 summarizes the PIV measurements conducted for three different near-wall conditions: water only, continuous bed, and LDs. The experiments were repeated at two different average fluid velocities of 0.17 m/s and 0.24 m/s. Given the low slurry concentration used in this study and the small proportion of the

pipe cross section occupied by the continuous bed and LDs, the cross-sectional flow area was considered to be the same for all three cases to simplify the calculation.

Table 4.6

Summaries of PIV experiments

Roughness condition	
	Water only
	U_{avg1}= 0.17 m/s Re_1= 17,269 $u_{\tau 1}$= 0.01 m/s
	U_{avg2} = 0.24 m/s Re_2 = 24,379 $u_{\tau 2}$ = 0.013 m/s
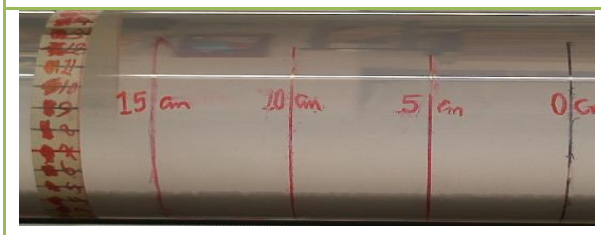	***Continuous bed***
	U_{avg1}≈ 0.17 m/s Re_1≈17,269 $u_{\tau 1}$≈ 0.01 m/s
	U_{avg2} ≈ 0.24 m/s Re_2 ≈ 24,379 $u_{\tau 2}$≈0.013 m/s
	Lenticular deposits
	U_{avg1} ≈ 0.17 m/s Re_1≈ 17,269 $u_{\tau 1}$ ≈ 0.01 m/s
	U_{avg2} ≈ 0.24 m/s Re_2 ≈ 24,379 $u_{\tau 2}$ ≈ 0.013 m/s

4.5.2 Near-Wall Velocity Profiles Obtained from PIV Measurements

The velocity distribution associated with near-wall turbulence was investigated previously by conducting experiments using artificially induced dunes [15, 37-40] and also by direct numerical simulation and other simulation techniques [18, 41]. However, in the present study, naturally occurring LDs and a continuous bed were

used to determine the velocity distribution resulting from near-wall turbulent activities.

Figure 4.18 shows the instantaneous velocity vector maps obtained from PIV measurements for the three different near-wall flow conditions. These maps were computed for each integration area using image pairs cross-correlated with each other pixel by pixel.

In the cross-correlation technique, the image frames are divided into smaller subsections called integration windows (IWs), such as 64 x 64 pixels, 32 x 32 pixels, 16 x 16 pixels, and 8 x 8 pixels, with overlapping or non-overlapping options. The smaller the IW, the higher the resolution of the velocity vector field. This is true, however, only if there is a sufficient number of particles in the integration area to be detected and cross-correlated. If not, the integration area should be enlarged until cross-correlation can be done successfully.

The velocity vector maps in Figure 4.18 were obtained by cross-correlation of 16 x 16 pixels with 50% overlap. The number of data points in the 28 x 20 mm^2 investigation area was 22,360. These figures are just a snapshot of the instantaneous velocity field obtained from PIV measurements. As the turbulent flow is chaotic and abruptly changes with time and space, the burst-sweep events assessment was done for each individual fluctuation velocity field, and the individual results were averaged and computed via MATLAB code. As the whole dune length (trough, stoss, crest, and lee) couldn’t fit in one frame, the analysis of the LD velocity profile was obtained by combining three velocity fields taken at

the same condition, but for different time periods, and placing them beside each other to complete LD cycle, as shown in Figure 4.18a. The control surface of the velocity vector field for the continuous bed and water-only flow assessment was set identical to the LD to have the evaluation section under the same assessment conditions.

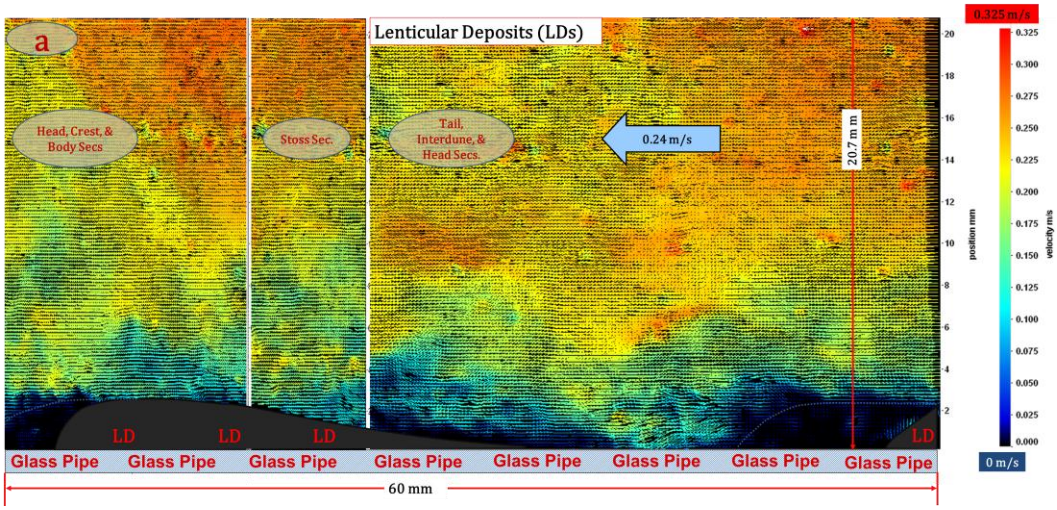

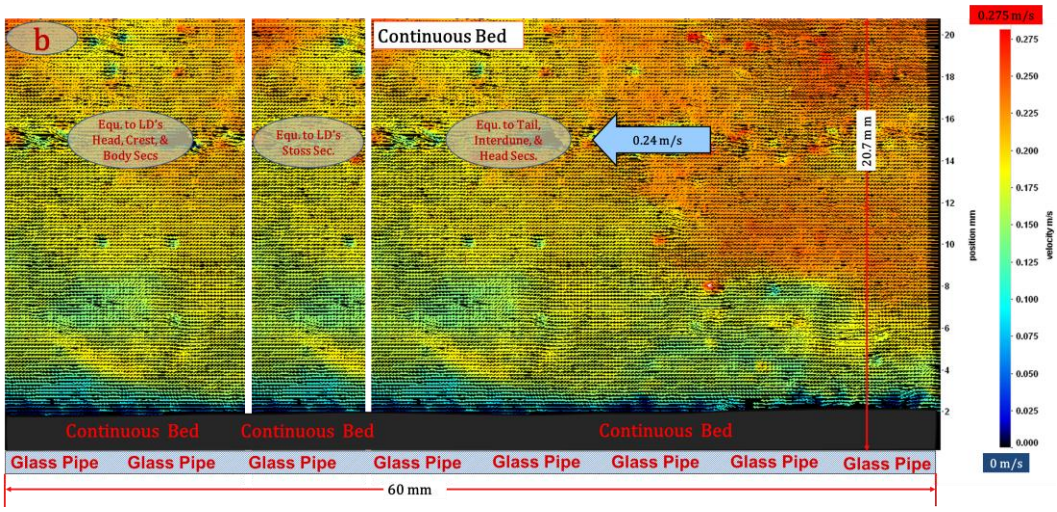

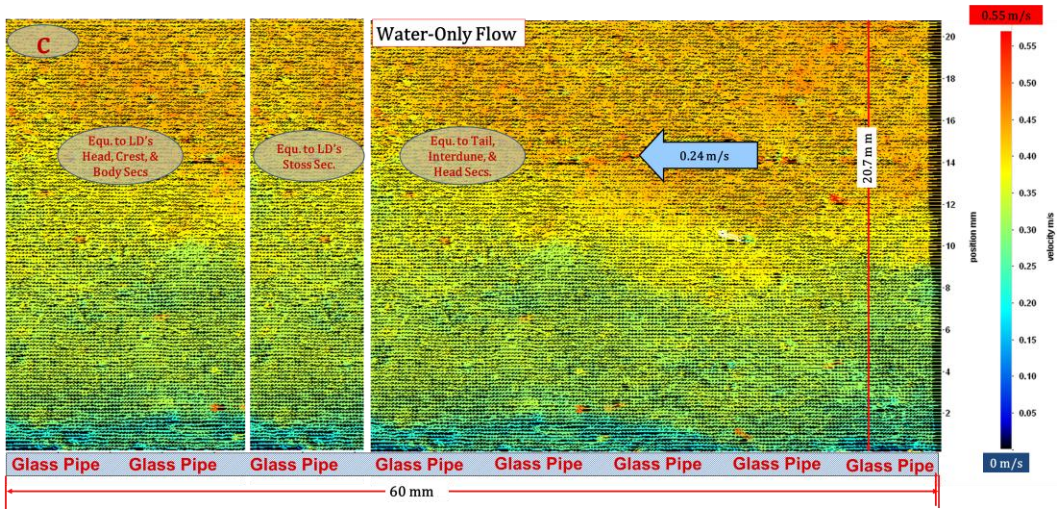

Figure 4.18 Velocity profile from PIV measurements for three cases: (a) water only, (b) continuous sand bed, and (c) LD for the average velocity of 0.24 m/s

The measured streamwise velocity profile obtained from PIV for the 0.17-m/s velocity (*Re* = 17,269) is shown in Figure 4.19 for water-only flow in the pipeline. The PIV data for the velocity profile are compared with the log-law profile for the turbulent flow. The green curve shows the $y^+ < 5$ region and blue line shows the log-law region plotted from a dimensionless distance of 5. As can be seen (Figure 4.19), there is good match between the measured data from PIV and the model velocity profile results from Eq. (4.7).

$$\begin{cases} u^+ = y^+ & y^+ < 5 \\ u^+ = \dfrac{1}{0.41}\ln\left(y^+\right) + 5.2 & y^+ \geq 30 \end{cases} \tag{4.7}$$

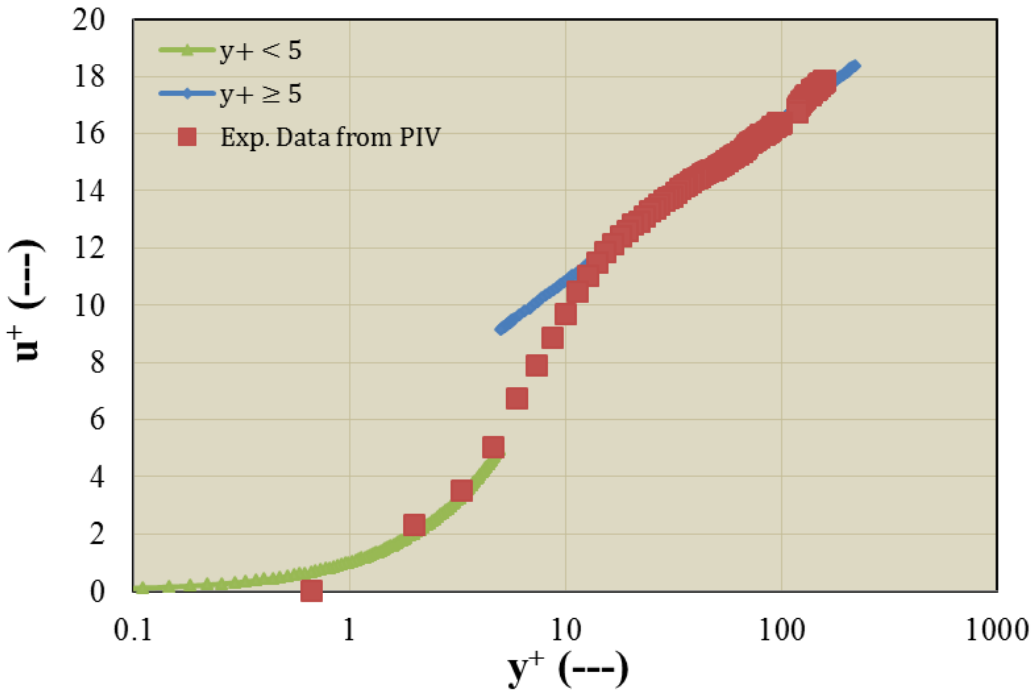

Figure 4.19 Mean velocity profiles for the model and experimental data from PIV for U_{avg} = 0.17 m/s (*Re* = 17,269)

where 0.41 is the von Karman constant, 5.2 is the constant of integration, and both are universal [42, 43].

Figure 4.20 illustrates the velocity profile over the naturally shaped LD. The profile has been divided into five sections: (1) the region upstream from the LD head; (2) the head (lee area); (3) the body and tail (stoss region); (4) the area just before the tail, between the LDs (interdune); and (5) the downstream part of the recirculation zone between the LDs. The smooth red line in Figure 4.20 indicates a velocity profile calculated using the Prandtl-Taylor model [44] for fully developed turbulent flow in a cylindrical pipe. The rough blue lines indicate the

dune velocity profiles for each subsection obtained by averaging the data over 16 columns (~ 2.4 mm in length), such that a relatively smooth profile is obtained in order to make it comparable with the model results. The rough green lines show the velocity profiles for the water-only flow cases, which were obtained in the same manner as those for the dune.

Previously published data from measurements using non-intrusive instruments covered the area starting from a few millimeters above the objective surfaces [17, 18, 39]. However, in the present study, the measurement technique using a non-intrusive PIV instrument allowed the capture of velocity data directly above the dune surface. In Figure 4.20, one column of data contains 130 vertical data points over the full measured height of 20 mm from the pipe and/or bed surface; the velocity profiles in Figure 4.20 show only half of the measured height.

In sections 1 and 5 of Figure 4.20, negative velocity values were measured, indicating the existence of a recirculation zone after the dune crest. The velocity profile over the stoss side is fairly similar to the model and the water-only flow profile (section 3 of Figure 4.20). Over the lee side and the area after the reattachment point, the velocity profiles are lower than those predicted by the model (red lines) and are measured in the water-only flow case (green lines) as can be seen in sections 2 and 4 of Figure 4.20.

Figure 4.20 shows how dune formation and development in turbulent flow affects the velocity profile compared to that of the water-only flow, especially close to the wall. It illustrates the deviations of the velocity profiles at the different

locations of the dune from the universal velocity profile. This is an interesting topic for further study.

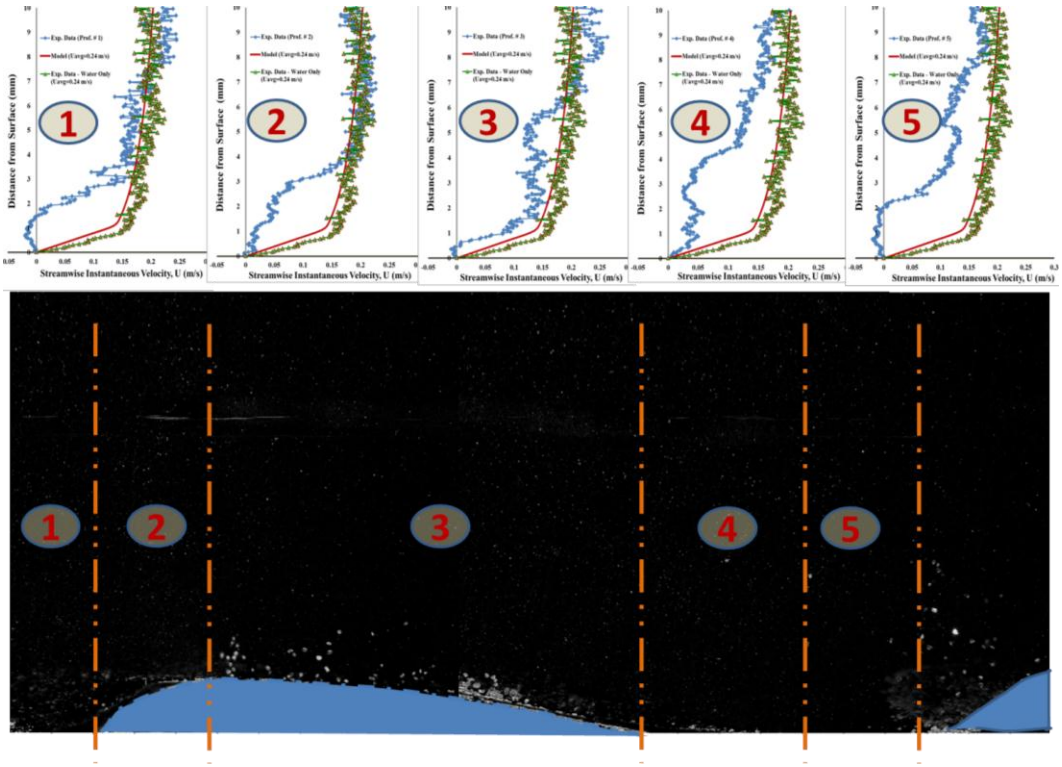

Figure 4.20 Velocity profile over LD obtained from PIV measurement. Flow direction is from right to left. Smooth red lines are the model calculation, green lines are the experimental data for the water-only flow, and blue lines are the experimental data over different sections of the LD

4.5.3 Velocity Maps for LDs, Continuous Bed, and Water-Only Flow

Figure 4.21 illustrates the velocity contour map for the full dune. All aspects of the dune, consisting of a trough (the space between two LDs), stoss, crest/brink, and lee are shown. In the lee, after the dune head, there is a recirculation zone with −0.004 m/s velocity, shown by the maroon shading. The extent of the

circulation zone is usually 3–5 times the dune crest height and is also a function of the Reynolds number. Figures 4.22 and 4.23 show the velocity maps for the continuous bed and water-only flow cases in the pipe, respectively. The flow direction for all cases is from right to left, with an average transport velocity of 0.24 m/s. The color bar on the right-hand side is velocity in m/s and, in the two latter cases, the area was set identical to the full dune area (the same control volume) in order to facilitate comparison.

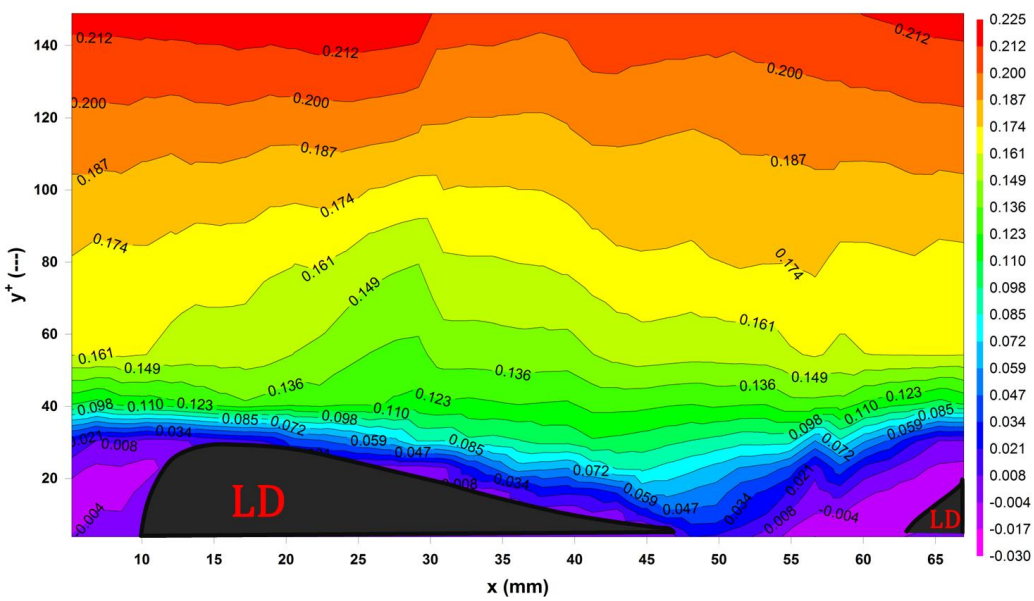

Figure 4.21 Velocity map for full dune. Flow is from right to left with U_{avg} = 0.24 m/s. The dune profile is drawn manually for clarity

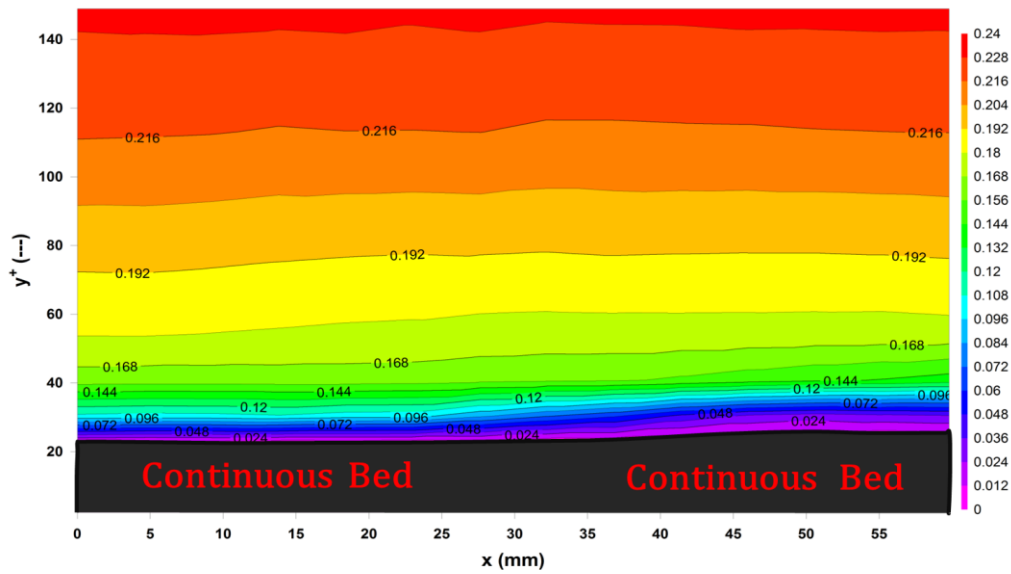

Figure 4.22 Velocity map for uniform bed equivalent to full dune area with U_{avg} = 0.24 m/s. The bed profile is drawn manually for clarity. Flow is from right to left

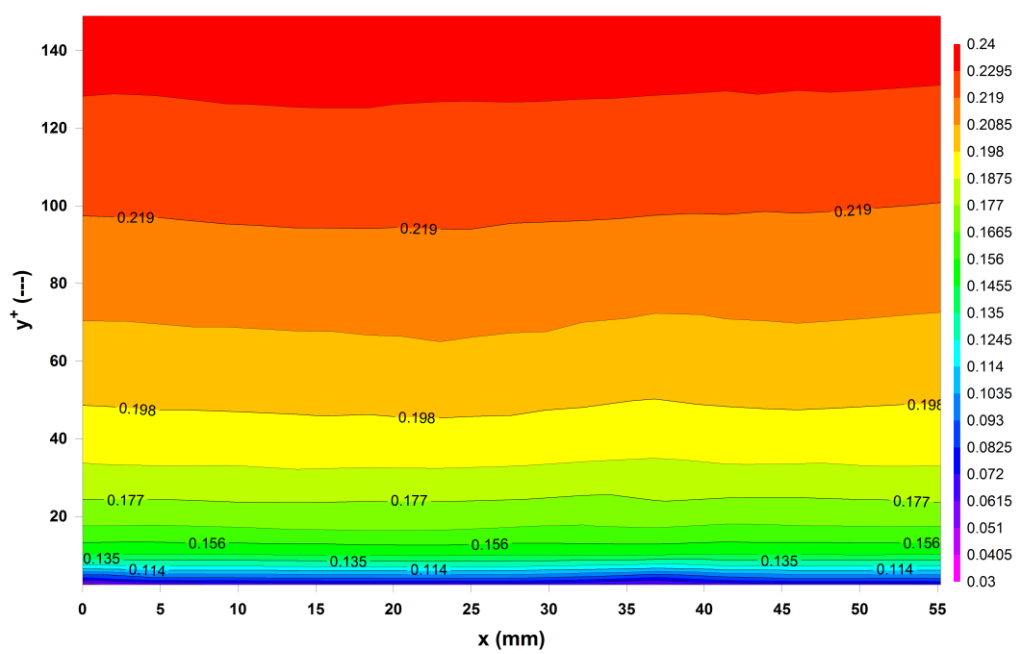

Figure 4.23 Contours of constant velocity for water-only flow equivalent to full dune investigation area (control volume). Flow is from right to left with U_{avg} = 0.24 m/s.

4.5.4 Assessment of Near-Wall Coherent Structures

Turbulent coherent structures were investigated in detail, as they are the main contributors to near-wall TKE. Coherent structures near the wall were identified as inward interaction, burst, sweep, and outward interaction. Figure 4.24 summarizes the quadrant technique used to identify the coherent structures. A detailed explanation of the quadrant technique is given in Appendix 4.B.

The data from PIV were obtained by 16 x 16 pixel cross-correlation with a 50% overlap, which means that 22,360 data points were recorded for each velocity vector field. Based on the criteria shown in Figure 4.24, each data point was assigned to one quadrant.

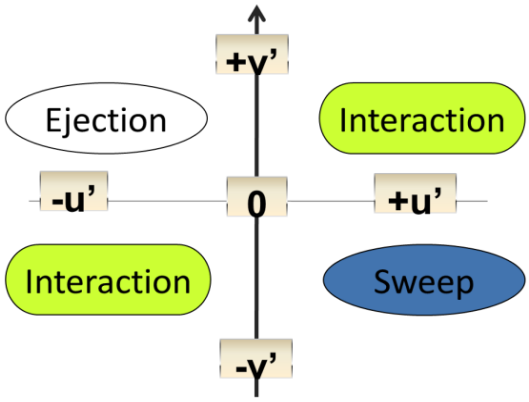

Figure 4.24 Quadrant technique for detection of near-wall coherent structures

Assuming a 2D velocity field, burst and sweep events and TKE were calculated for each section. The frequency of occurrence of any coherent structures was analyzed in each section. Figure 4.25 shows how the LD is broken down into four

sections: space between tail and head (trough or interdune), head (lee), body (crest), and tail (stoss), which together make up the complete dune wavelength for the PIV analysis.

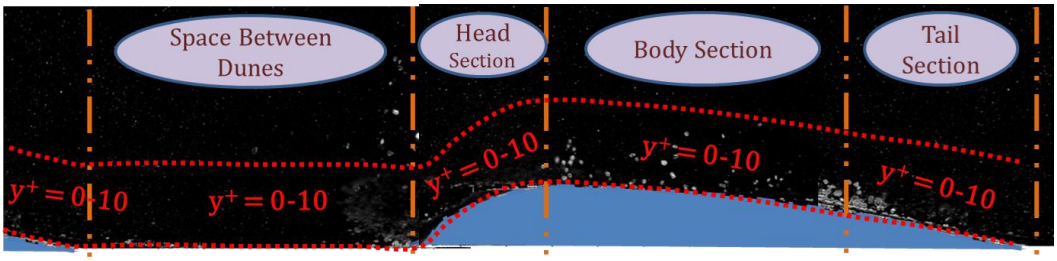

Figure 4.25 LD breakdown into sections; the red broken line shows the wall margins along the LD. The flow is from right to left

In Figure 4.25, the zone between the wall and the upper dashed line (y^+ = 0–10) represents the area where low-speed streaks first appear (i.e., first step for generation of turbulent coherent structures) and it is an important region for their occurrence and analysis.

4.5.5 Comparisons of Frequencies of Turbulent Coherent Structures

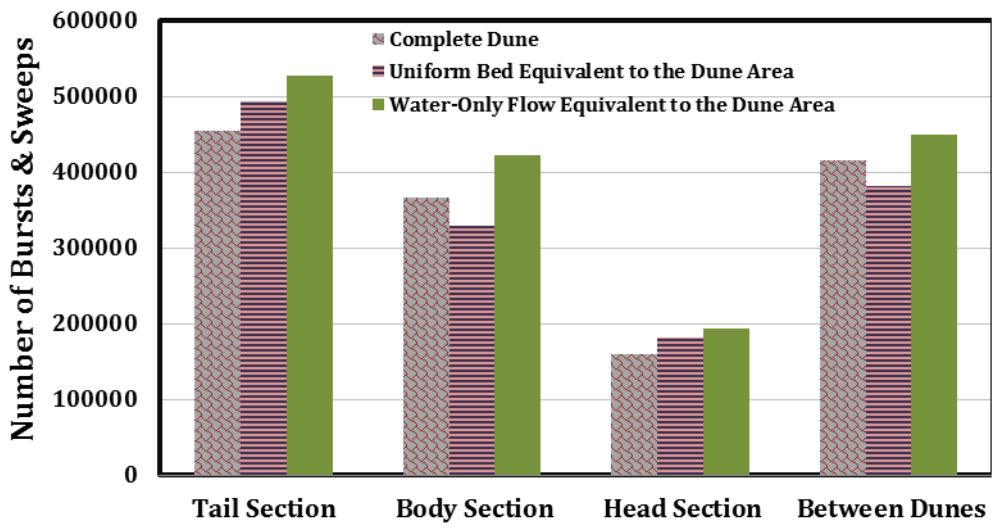

Figure 4.26 Comparison of near-wall coherent structures – burst and sweep frequencies for the three cases at U_{avg} = 0.24 m/s in the y^+ = 0–10 zone

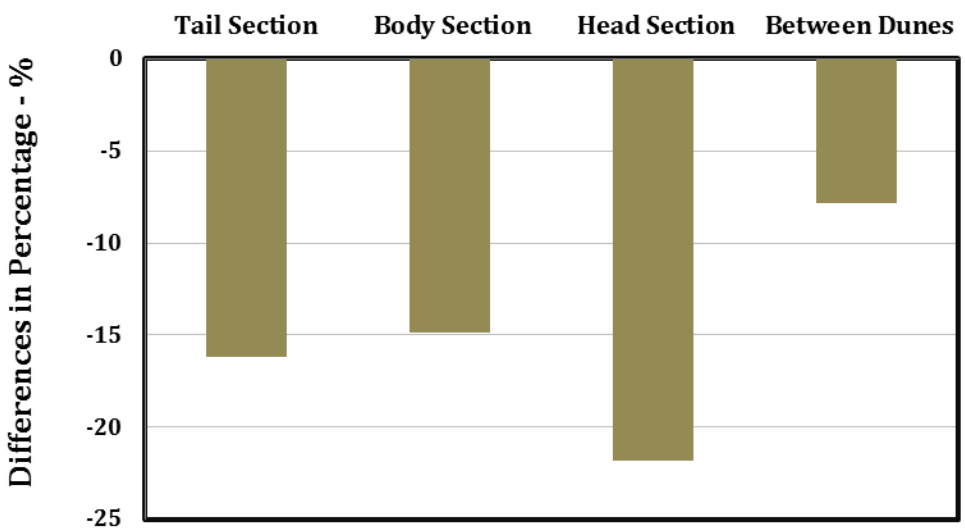

Figure 4.27 Differences in frequencies for LD and water-only flow cases. Water-only flow has a higher burst and sweep frequency than the LD at the given condition; U_{avg} = 0.24 m/s in the y^+ = 0–10 zone

Figure 4.26 shows the frequencies of the burst and sweep for LD, continuous bed, and water-only flow. The average flow velocity is 0.24 m/s and the control volumes of the water-only flow and continuous bed cases are set identical to that of the LD for comparison. The control volume is divided into four sections: head, body, tail, and space between LDs. For all sections, the burst and sweep activity is higher for the water-only flow. In the tail and head sections, the activity is higher for the continuous bed than for the LD and, in the stoss and trough sections, it is higher for the LD than for the continuous bed. Figure 4.27 shows the differences in burst and sweep frequency for the LD and the water-only flow cases. For the given control volume the frequency of burst and sweep events for the water-only case is on average 15% higher than for the LD case.

4.5.6 Assessment of TKE

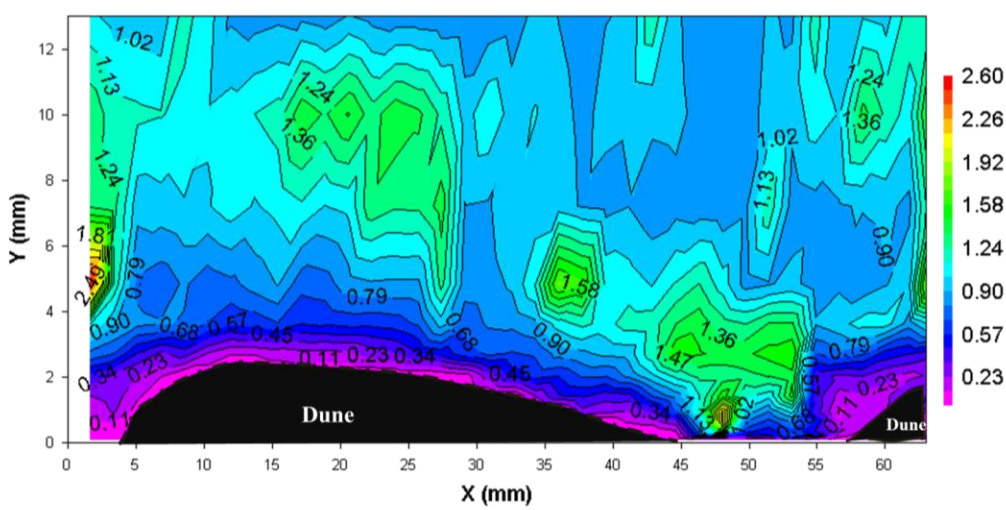

Figure 4.28 TKE contour map for LD; flow is from right to left. U_{avg} = 0.24 m/s

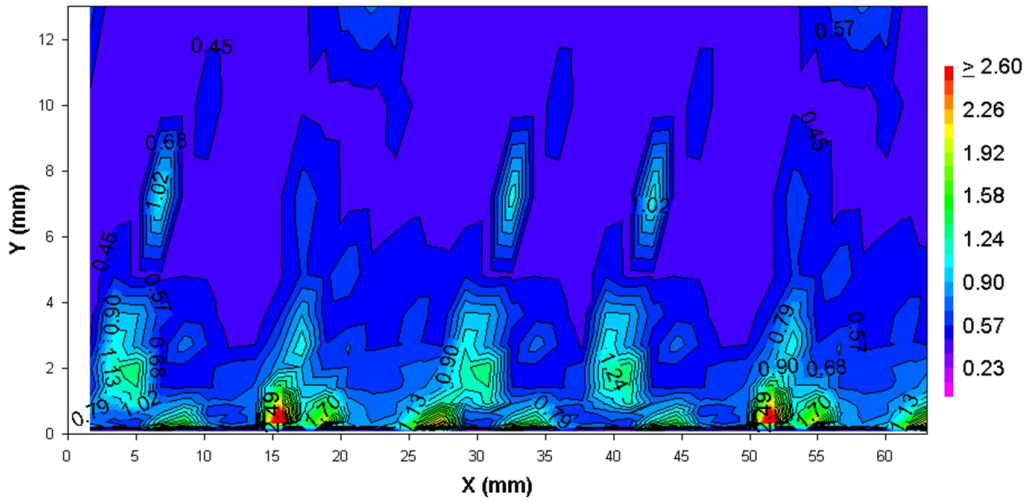

Figure 4.29 TKE contour map for water-only flow; flow is from right to left. U_{avg} = 0.24 m/s

The definition of TKE is

$$TKE = \frac{1}{2}\left(u'^2 + v'^2\right) \tag{4.8}$$

Figures 4.28 and 4.29 show the TKE contour maps for the LD and water-only flow cases. The average flow velocity is 0.24 m/s. The side color bar shows the intensity of the TKE in the investigation area. Near the wall, in the region where the low-speed streaks are generated, the water-only flow case shows a higher intensity than the LD one. In the LD itself, TKE intensity is higher in the trough and stoss regions than in the other regions.

The TKE contributions of burst-sweep events in each section were calculated using Eq. 4.8. The total TKE was calculated as the sum of the TKEs contributed from burst-sweep events.

Figures 4.30 and 4.31 compare the TKEs for three different near-wall flow conditions at velocities of 0.17 m/s and 0.24 m/s, respectively.

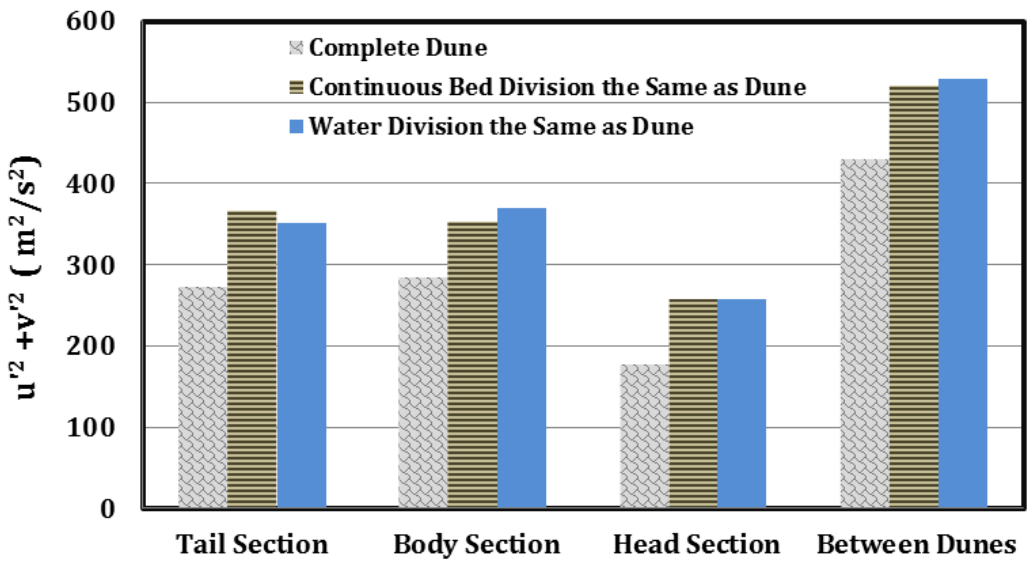

Figure 4.30 TKEs for flow at three different near-wall conditions with U_{avg} = 0.17 m/s in the y^+ = 0–10 zone

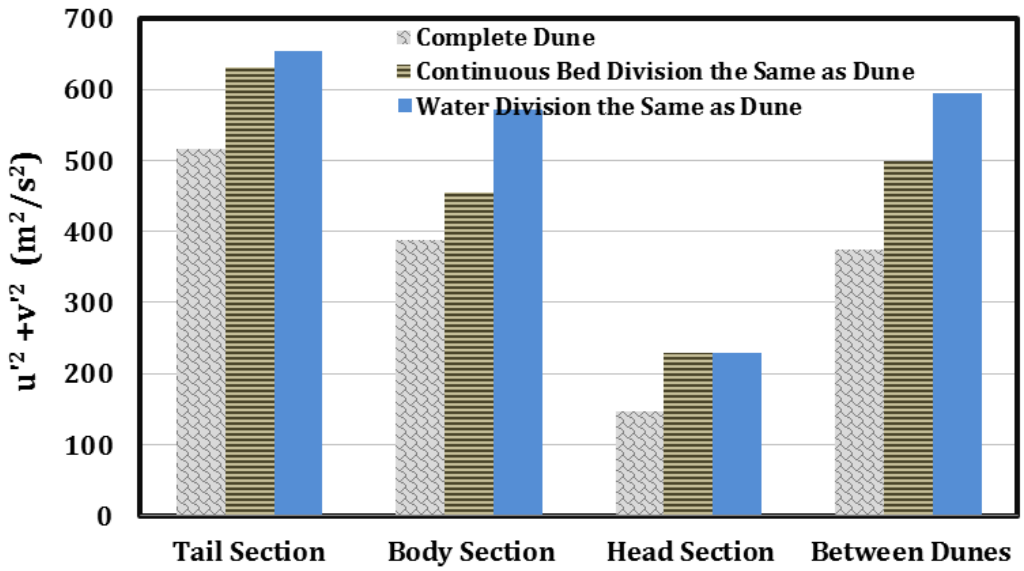

Figure 4.31 TKEs for flow for three different conditions near the wall with U_{avg} = 0.24 m/s in the y^+ = 0–10 zone

TKE in this experiment was found to be lowest for the flow over LDs. Figures 4.32 and 4.33 show the percentage differences in TKE calculated for the continuous bed and for flow over the LDs at velocities of 0.17 m/s and 0.24 m/s, respectively. When the fluid velocity was 0.17 m/s, the difference in TKEs varied from 17% to 31% (Figure 4.32). On average, for this case, the TKE for flow over the continuous bed was 23% higher than for that over the LDs in the zone where low-speed streaks are created (y^+ = 0–10).

When the fluid velocity was 0.24 m/s, the difference in TKEs varied from 14% to 36% (Figure 4.33). On average, the TKE for flow over the continuous bed was 23% higher than that over the LDs in the zone where low-speed streaks are created (y^+ = 0–10).

TKE comparison for flow over the LDs versus the continuous bed indicates that the LD flow pattern is associated with the lower TKE intensity, and confirms that flow over the LDs results in lower frictional pressure losses than flow over a continuous bed. Although there was a continuous bed at the beginning of the experiment, the flow pattern re-formed into the LDs since the latter forms consume less kinetic energy then the former. In conclusion, LDs were shown to be the most stable and efficient form of slurry transport flow at low velocities and solids concentrations since the pressure drop is minimized.

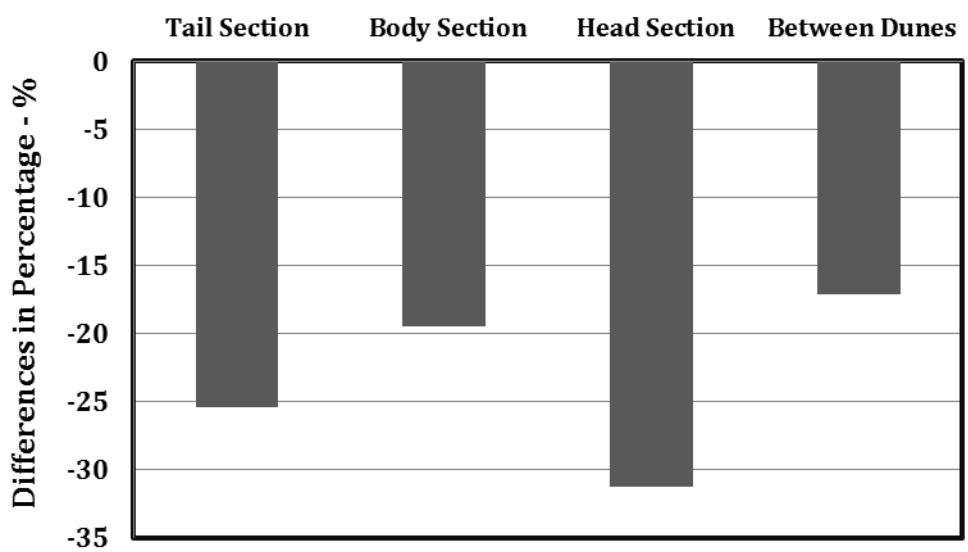

Figure 4.32 Percentage difference in TKEs for continuous bed versus LDs with U_{avg} = 0.17 m/s in the y^+ = 0–10 zone; continuous bed has higher TKE

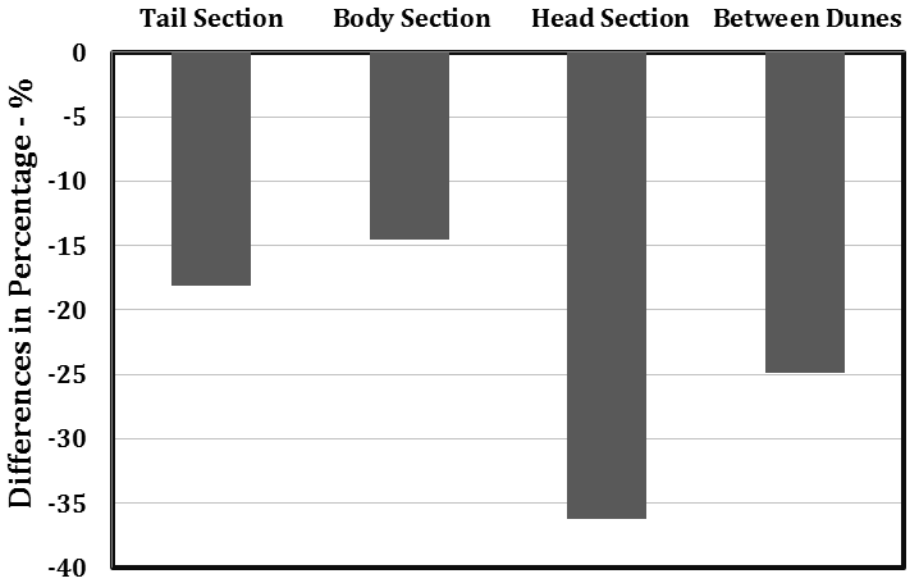

Figure 4.33 Differences in TKEs for continuous bed versus LDs with U_{avg} = 0.24 m/s in the y^+ = 0–10 zone; the continuous bed has higher TKE

This experiment reveals that this natural phenomenon, like others, tends to stabilize at its lowest-energy condition. In the conducted experiments, re-formation from a continuous bed to LDs occurs in such a way as to interfere with the bed and suppress the burst-sweep activity. The low-speed streaks adjacent to the wall are an important part of the burst activity and are a precursor to this phenomenon. In the wall region, the coherent structures (burst-sweep) are responsible for 80% of the TKE [26]. Therefore, measures to overcome these energetic structures adjacent to the wall, for example, by morphological re-formation, bumps, or polymer addition to suppress the burst-sweep activity, could be used to reduce the drag and frictional pressure drop.

In simulation research carried out to assess the effects of obstacle geometry in channel flow, Carlson reported that using the actuator (bump) reduces drag; however, the actuator geometry plays an important role in drag reduction, and in one case he reported 7% drag reduction associated with reductions in TKE production. It was reported that drag reduction can be increased up to 20% [26, 45].

Comparing the TKEs of the continuous bed and LDs for the two different velocities, 0.17 m/s and 0.24 m/s, reveals that the average TKE for the LDs case is 23% lower than for the continuous bed. LD morphology affected the coherent structures near the wall by suppressing the burst-sweep activity, resulting in lower frequency and intensity near the wall for the LDs case. It can be concluded that a 6–8% reduction in frictional pressure drop at the constant slurry transport velocity is due to reformation of the bed morphology and the resulting suppression of burst-sweep activity near the wall and reduction of TKE.

4.6 Conclusions

LDs are characteristic of a special form of slurry bed transport identified by low solids concentration and low flow rate.

As the slurry deposition pattern changes from continuous bed to LDs, a 6–8% reduction in frictional pressure drop is observed.

Direct measurement of near-wall turbulent activity (i.e., burst and sweep events) confirms that the formation of naturally shaped LDs results in a 23% reduction in turbulent kinetic energy (TKE) production, mainly in the burst-generating low-speed streaks region (y^+ = 0–10). The frequency and strength of the burst-sweep events were reduced in the LDs case compared to water-only flow and continuous bed by 15% and 23%, respectively. These reductions, in turn, result in the formation of stable LDs and reduced frictional pressure drop.

Naturally shaped LDs are the most stable and lowest-energy state of slurry transport flow at low solids concentrations and flow velocities below the critical velocity.

4.7 Appendix 4.A

4.7.1 Churchill's Equation:

$$\lambda = 8\left[\left(\frac{8}{\mathrm{Re}}\right)^{12} + \frac{1}{(A+B)^{3/2}}\right]^{1/12} \qquad (4.A-1)$$

$$A = \left\{2.457 \ln\left[\frac{1}{\left(\frac{7}{\mathrm{Re}}\right)^{0.9} + 0.27\frac{\varepsilon}{D}}\right]\right\}^{16} \qquad (4.A-2)$$

$$B = \left(\frac{37530}{\mathrm{Re}}\right)^{16} \qquad (4.A-3)$$

$$Re = \frac{U_{avg} D}{\nu} \qquad (4.A-4)$$

where λ is the pressure drop per unit length, ε is the roughness (the median diameter of the particles has been used as the roughness value), and *D* is the pipe diameter.

4.8 Appendix 4.B

4.8.1 Criteria for Identifying Near-Wall Turbulent Coherent Structures

The most common methodology used for detection of coherent structures is the quadrant technique. Bogard and Tiderman [46] assessed the effectiveness of detection techniques for different turbulent coherent structures and concluded that the quadrant technique is the most trustworthy. In this study, the coherent structures detection technique of Wallace et al. [30] and Brodkey et al. [34] was followed. The technique is summarized in Figure 4.24.

The method uses fluctuation velocity vectors (u' and v') to determine the appropriate quadrant. PIV measurement provides instantaneous velocity vector values (U and V) at each point of interest. PIV analysis software also provides time-average values ($\overline{U}$ and $\overline{V}$) of the instantaneous velocity vector fields. Fluctuation velocity values (u' and v') are then calculated as the difference between the instantaneous velocity vector values and average of the instantaneous velocity vector values.

In the quadrant technique based on the $u' - v'$ signals – streamwise and normal fluctuation velocities – the events are divided into four quadrants: outward interaction (quadrant I), burst or ejection (quadrant II), inward interaction (quadrant III), and sweep (quadrant IV) (see Figure 4.24).

A Matlab code was developed to identify all 22,360 fluctuation velocity data points in each field, where all 100 fluctuation velocity vector fields were measured continuously. Fluctuation velocity data were sorted in five categories:

distorted data which are discarded, Q1, Q2, Q3, and Q4. The measurement area was divided horizontally into $0 \le y^+ \le 10$, $10 < y^+ \le 30$, $30 < y^+ \le 100$. The area was further divided vertically into the tail (stoss), body (crest), head (lee), and spare area between the head and tail of the next LD sections (trough or interdune). Identical categories were kept for the continuous bed and water-only areas, in order to be able to compare the three cases.

4.9 References

[1] Turian, R. M., and Yuan, T.-F., 1977, "Flow of Slurries in Pipelines," AIChE Journal, 23(3), pp. 232-243.

[2] Bagnold, R. A., 2005, *The Physics of Blown Sand and Desert Dunes*, Dover Publications Inc., London.

[3] Newitt, D. M., Richardson, J. F., Abbott, M., and Turtle, R. B., 1955, "Hydralic Conveying of Solids in Horizontal Pipes," Chemical Engineering Research and Design, 33a(-), pp. 93 - 113.

[4] Thomas, D. G., 1964, "Transport Characteristics of Suspensions: Part Ix. Representation of Periodic Phenomena on a Flow Regime Diagram for Dilute Suspension Transport," AIChE Journal, 10(3), pp. 303-308.

[5] Kennedy, J. F., 1969, "The Formation of Sediment Ripples, Dunes, and Antidunes," Annual Review of Fluid Mechanics, 1(1), pp. 147-168.

[6] Buckles, J., Hanratty, T. J., and Adrian, R. J., 1984, "Turbulent Flow over Large-Amplitude Wavy Surfaces," Journal of Fluid Mechanics, 140(-), pp. 27-44.

[7] Kapdasli, M., and Dyer, K., 1986, "Threshold Conditions for Sand Movement on a Rippled Bed," Geo-Marine Letters, 6(3), pp. 161-164.

[8] Doron, P., Granica, D., and Barnea, D., 1987, "Slurry Flow in Horizontal Pipes--Experimental and Modeling," International Journal of Multiphase Flow, 13(4), pp. 535-547.

[9] Toma, P., Harris, P., and Korpany, G., 1994, "Sand Transportation in Long Horizontal Wells - Practical Methods for Reducing the Impact - " Energy-Sources Technology Conference and Exhibition, New Orleans, Louisiana - January 23-27, 94-PET-3(-), pp. 1-11.

[10] Doron, P., and Barnea, D., 1996, "Flow Pattern Maps for Solid-Liquid Flow in Pipes," International Journal of Multiphase Flow, 22(2), pp. 273-283.

[11] Belcher, S. E., and Hunt, J. C. R., 1998, "Turbulent Flow over Hills and Waves," Annual Review of Fluid Mechanics, 30(1), pp. 507-538.

[12] Niño, Y., Lopez, F., and Garcia, M., 2003, "Threshold for Particle Entrainment into Suspension," Sedimentology, 50(2), pp. 247-263.

[13] Walker, I. J., and Nickling, W. G., 2002, "Dynamics of Secondary Airflow and Sediment Transport over and in the Lee of Transverse Dunes," Progress in Physical Geography, 26(1), pp. 47-75.

[14] Mao, Y., 2003, "The Effects of Turbulent Bursting on the Sediment Movement in Suspension," International Journal of Sediment Research, 18(2), pp. 148-157.

[15] Best, J., 2005, "The Fluid Dynamics of River Dunes: A Review and Some Future Research Directions," J. Geophys. Res., 110, F04S02(21), pp. 1-21.

[16] Toyama, A., Shimizu, Y., Yamaguchi, S., and Giri, S., 2007, "Study of Sediment Transport Rate over Dune-Covered Beds," 5th IAHR Symposium on River, Coastal and Estuarine Morphodynamics (RCEM), pp. 1-9.

[17] Venditti, J. G., 2007, "Turbulent Flow and Drag over Fixed Two- and Three-Dimensional Dunes," J. Geophys. Res., 112, F04008(-), pp. 1-21.

[18] Stoesser, T., Braun, C., Garcia-Villalba, M., and Rodi, W., 2008, "Turbulence Structures in Flow over Two-Dimensional Dunes," Journal of Hydraulic Engineering, 134(1), pp. 42-55.

[19] Mianaei, S., and Keshavarzi, A., 2010, "Study of near Bed Stochastic Turbulence and Sediment Entrainment over the Ripples at the Bed of Open Channel Using Image Processing Technique," Stochastic Environmental Research and Risk Assessment, 24(5), pp. 591-598.

[20] Wilson, K. C., and Brebner, A., 1971, "On Two Phase Pressurized and Unpressurized Flow: Behaviour near Deposition Points," In: Advances in solid-liquid flow in pipes and its application (Ed. by I. Zandi), Pergamon Press, Oxford, pp. 175-186.

[21] Oroskar, A. R., and Turian, R. M., 1980, "The Critical Velocity in Pipeline Flow of Slurries," AIChE Journal, 26(4), pp. 550-558.

[22] Mckee, E. D., 1979, "Introduction to a Study of Global Sand Seas," United States Geological Survey, Professional Paper (In Lancaster, chap. 5), pp.

[23] Zeinali, H., Toma, P., and Kuru, E., 2009, "Near-Wall Turbulent Transport Knowledge for Suitable Flow Assurance Strategies," ASME Conference Proceedings, 2009(43475), pp. 575-582.

[24] Phillips, M., 1980, "A Force Balance Model for Particle Entrainment into a Fluid Stream," Journal of Physics D: Applied Physics, 13(2), pp. 221.

[25] Churchill, S. W., 1977, "Frictional Equation Spans All Fluid Flow Regimes," Chemical Engineering 84(24), pp. 91-92.

[26] Lumley, J., and Blossey, P., 1998, "Control of Turbulence," Annual Review of Fluid Mechanics, 30(1), pp. 311-327.

[27] Lumley, J. L., 1973, "Drag Reduction in Turbulent Flow by Polymer Additives," Journal of Polymer Science: Macromolecular Reviews, 7(1), pp. 263-290.

[28] Ptasinski, P. K., Nieuwstadt, F. T. M., Van Den Brule, B. H. a. A., and Hulsen, M. A., 2001, "Experiments in Turbulent Pipe Flow with Polymer Additives at Maximum Drag Reduction," Flow, Turbulence and Combustion, 66(2), pp. 159-182.

[29] Motozawa, M., Ishitsuka, S., Iwamoto, K., Ando, H., Senda, T., and Kawaguchi, Y., 2012, "Experimental Investigation on Turbulent Structure of Drag Reducing Channel Flow with Blowing Polymer Solution from the Wall," Flow, Turbulence and Combustion, 88(1), pp. 121-141.

[30] Wallace, J. M., Eckelmann, H., and Brodkey, R. S., 1972, "The Wall Region in Turbulent Shear Flow," Journal of Fluid Mechanics, 54(01), pp. 39-48.

[31] Willmarth, W. W., and Lu, S. S., 1972, "Structure of the Reynolds Stress near the Wall," Journal of Fluid Mechanics, 55(01), pp. 65-92.

[32] Robinson, S. K., 1991, "Coherent Motions in the Turbulent Boundary Layer," Annual Review of Fluid Mechanics, 23(1), pp. 601-639.

[33] Blackwelder, R. F., and Kaplan, R. E., 1976, "On the Wall Structure of the Turbulent Boundary Layer," Journal of Fluid Mechanics, 76(01), pp. 89-112.

[34] Brodkey, R. S., Wallace, J. M., and Eckelmann, H., 1974, "Some Properties of Truncated Turbulence Signals in Bounded Shear Flows," Journal of Fluid Mechanics, 63(02), pp. 209-224.

[35] Corino, E. R., and Brodkey, R. S., 1969, "A Visual Investigation of the Wall Region in Turbulent Flow," Journal of Fluid Mechanics, 37(01), pp. 1-30.

[36] Kline, S. J., Reynolds, W. C., Schraub, F. A., and Runstadler, P. W., 1967, "The Structure of Turbulent Boundary Layers," Journal of Fluid Mechanics, 30(04), pp. 741-773.

[37] Best, J., 2009, *Kinematics, Topology and Significance of Dune-Related Macroturbulence: Some Observations from the Laboratory and Field*, *Fluvial Sedimentology Vii*, Blackwell Publishing Ltd.,

[38] Ojha, S. P., and Mazumder, B. S., 2008, "Turbulence Characteristics of Flow Region over a Series of 2-D Dune Shaped Structures," Advances in Water Resources, 31(3), pp. 561-576.

[39] Rabenjafimanantsoa, A. H., Time, R. W., and Saasen, A., 2007, "Characteristic of the Velocity Profiles over Fixed Dunes in Pipe," Annual Transactions- Nordic Rheology Society, 15(-), pp. 141-148.

[40] Wagner, C., Kuhn, S., and Rudolf Von Rohr, P., 2007, "Scalar Transport from a Point Source in Flows over Wavy Walls," Experiments in Fluids, 43(2), pp. 261-271.

[41] Schmeeckle, M. W., Shimizu, Y., Baba, H., and Ikezaki, S., 1999, "Numerical and Experimental Investigation of Turbulence over Dunes in Open-Channel Flow," Monthly Report of the Civil Engineering Research Institute, 551(-), pp. 2-15.

[42] Pope, S. B., 2000, *Turbulent Flows*, Cambridge University Press, Cambridge; New York.

[43] Von Kármán, T., 1930, "Mechanische Ähnlichkeit Und Turbulenz," Proceedings in Third International Congress for Applied Mathematics, Stockholm, pp. 85-105.

[44] Nellis, G., and Klein, S., 2009, Cambridge University Press, Heat Transfer, Chap. 4.7.5 (562-565).

[45] Carlson, H. A., 1995, "Direct Numerical Simulation of Laminar and Turbulent Flow in a Channel with Complex, Time-Dependent Wall Geometries," Ph.D. thesis, Cornell University, United States -- New York.

[46] Bogard, D. G., and Tiederman, W. G., 1986, "Burst Detection with Single-Point Velocity Measurements," Journal of Fluid Mechanics, 162(-), pp. 389-413.

5 Effect of Near-Wall Turbulence on Selective Removal of Particles from Sand Beds Deposited in Pipelines[1]

5.1 Introduction

Advances in near-wall turbulence analysis in recent decades – laser Doppler anemometry (LDA), hydrogen bubble visualization, and particle image velocimetry (PIV) – have led to a significant improvement in knowledge and understanding of coherent motions in the turbulent boundary layer [1]. The Prandtl turbulence model suggesting the near wall laminar sublayer fails to explain the erosion-corrosion and selective particle removal activities frequently observed in the near wall region, however it offers a good framework for assessing and scaling of near-wall coherent structures discussed in this paper.

The results of recent investigations conducted by using dedicated instrumentation such as PIV for observing near-wall turbulence revealed that intermittent burst-sweep activities dominate "viscous sublayer" [2-4]. Other studies suggest that an intense radial mass transportation between the wall and core flow can be induced by burst-sweep activities [4, 5].

In this study, the role of burst-sweep activities in the sand grading (involving selective size removal) process has been investigated. Experimental results on selective particle removal from deposited bed to the turbulent core flow are presented.

[1] A version of this chapter has been published. Zeinali, H., Toma, P., and Kuru, E., 2012. Journal of Energy Resources Technology, 134(2), pp. 021003.

5.2 Near – Wall Turbulent Activity (Burst – Sweep)

The discovery of burst-sweep activities [2, 5-7] in the 1960's (see summary in [1]) – nearly seven decades after Prandtl's boundary layer model was presented [8] – provided an enhanced understanding of how the near-wall turbulent flow transport mechanisms function.

Figure 5.1 shows a schematic of burst-sweep activity (also indicated as "coherent motions") observed in the near-wall zone during turbulent pipe flow. Periodic burst activities originating in the vicinity of the wall, jet out into the turbulent core [9]. While on the other hand, alternating sweeps, originating in the core flow, protrude the near-wall zones.

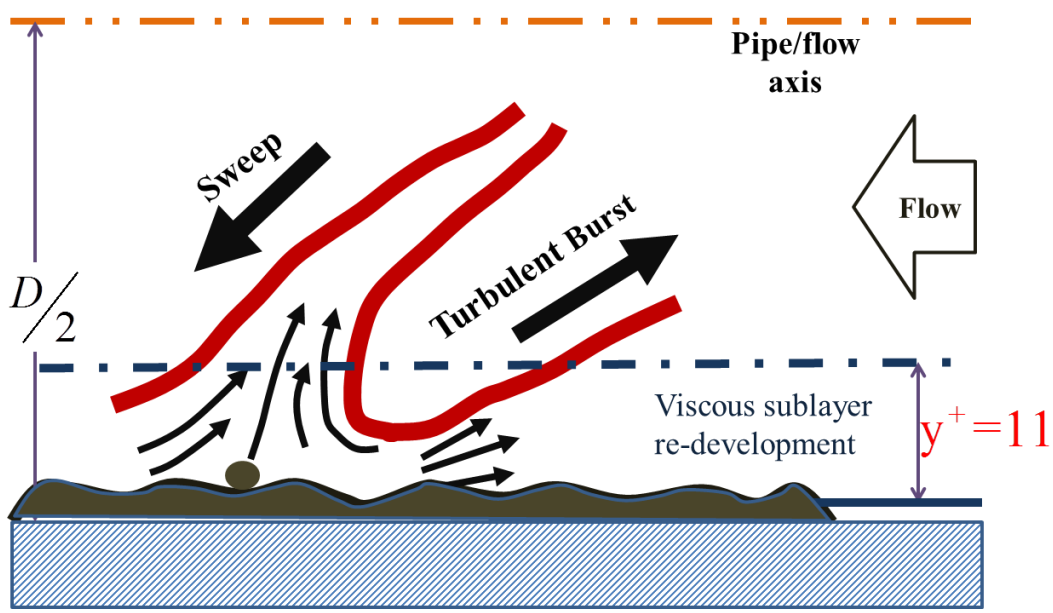

Figure 5.1 Idealization of burst-sweep activity from sand bed emerging from near-wall to core turbulent flow [9]

As a result of inflow-outflow alternating fluid motions, the near-wall or interface region is the source of most of the turbulent kinetic energy production in the boundary layer [1]. This burst-sweep activity sends fluid and particles away from the wall (or interface) zone into the turbulent core flow [6] and at the same time injects a dilute fluid-particles mixture from the core flow into the wall zones.

The powerful radial mass transport activity observed in the near-wall (viscous sublayer) region justifies a broad range of turbulent flow phenomena including: the selective removal of floating waxy crude crystals (aging) [10], the selective removal of particles in the near-wall region (grading) [3, 11] and the wall impact of solids (erosion).

The recent data on burst-sweep action are also central to managing these and various other turbulent flow issues that arise in many other practical applications including: selective removal of sand fines (a problem of particular interest in this experimental study), reduction (or increase) of the frictional pressure drop, and the effectiveness of drag-reduction additives.

5.2.1 Assessment of Burst and Sweep Frequency

A 2D pipe flow velocity field used in this study explains how burst-sweep frequency is measured directly. The assessment of the burst-sweep frequency starts with a high-speed recording of the axial (U) and wall-normal or radial (V) velocity components.

Reynolds' convention for describing the turbulent velocity is used, where $U = \overline{U} + u'$ and $V = \overline{V} + v'$ (u', v' denotes the fluctuating velocity component and $\overline{U}, \overline{V}$ denotes the average velocity component of the axial U and radial V velocity, respectively).

Figure 5.2 illustrates a record of instantaneous velocities (U and V) versus time. Figure 5.3 compares the signs of velocity fluctuations u' and v' to assess the occurrence of a burst event.

According to the Variable Interval Space Average "VISA" [5, 12] method, which was also used for this study, a burst event is considered to have taken place at the observation point and at the recording moment, when $u' < 0$ and $v' > 0$.

An experimental method has been developed for identifying and measuring the frequency and intensity of bursts across the 3 ¾-inch (0.095 m ID) diameter – 15 m long glass pipe during the turbulent flow. Appendix 5.A summarizes the procedure developed for assessing the burst frequency at various transport velocities.

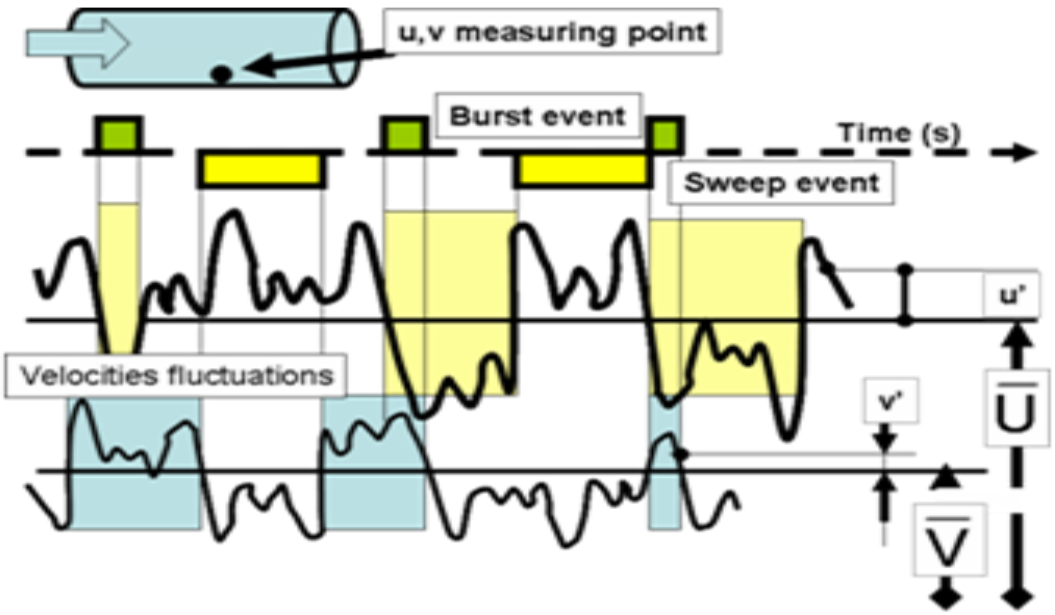

Figure 5.2 Simultaneous record of local velocity components *U* and *V* versus time

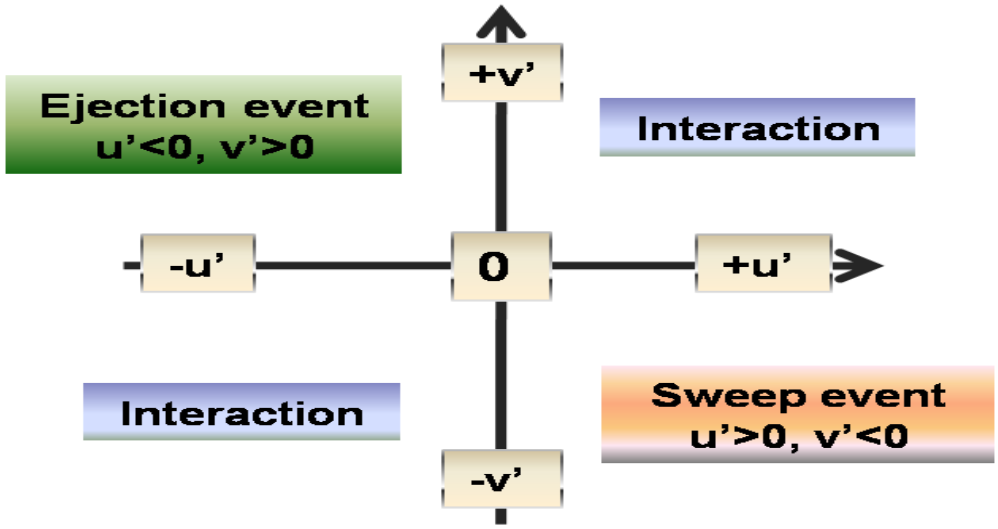

Figure 5.3 Burst and sweep assessment performed by comparing the signs of fluctuating velocity components u' and v' - the four-quadrant method [5]

5.3 Selective Removal of Particles from Bed Deposits

The selective entrainment of solid particles from riverbeds or sand dunes into the main turbulent flow (water or air) was conventionally referred to as sand "grading" [11]. Earlier studies [11, 13, 14] indicated that when the particle size range is between 50 to 1000 μm smaller size particles are preferentially removed from the sand bed by turbulent flow. More recently, observations on selective particle removal were extended to include much smaller particle size ranges (1 to 50μm) [15]. Analyses have shown that, when the particle size range was between 1 to 50 μm, predominantly larger-sized particles (dust, ash, coal, silica) were entrained from deposited beds. This unexpected, but well documented effect [3], increases the concentration of finer particles in the bed, and is therefore, of particular interest in the future development of in-line separation technologies.

Sand particle entrainment into the main turbulent stream, as identified and explained by Shields as a result of shear-flow related lift forces and buoyant forces [13, 14], was considered a major mechanism for controlling marine and river sedimentation and explaining the formation and grading of sand dunes in deserts [11]. For smaller particles (d_p < 50 μm) the van der Waals attraction forces become dominant as it is further explained. Figure 5.4 shows the size of the particles preferentially entrained within the Shield's and the Phillips' particle size ranges (domains) indicated for d_p > 100 μm and 1 < d_p < 50 μm respectively. The threshold wall shear stress versus the equivalent particle diameter data presented in Figure 5.4 suggests that for a certain sand-fluid gravity ratio, there exists two distinct size-dependent domains [15].

The example in Figure 5.4 shows that for a bed populated with particles ranging in size from 1 to 3000 μm, a turbulent flow condition creating a wall shear stress, τ_w, of 2 Pa, will predominantly entrain particles between 5-2000 μm to the main core of the flow. Meanwhile, the concentration of particles $d_p < 5\,\mu m$ and $d_p > 2000\,\mu m$ will progressively increase in the bed [15].

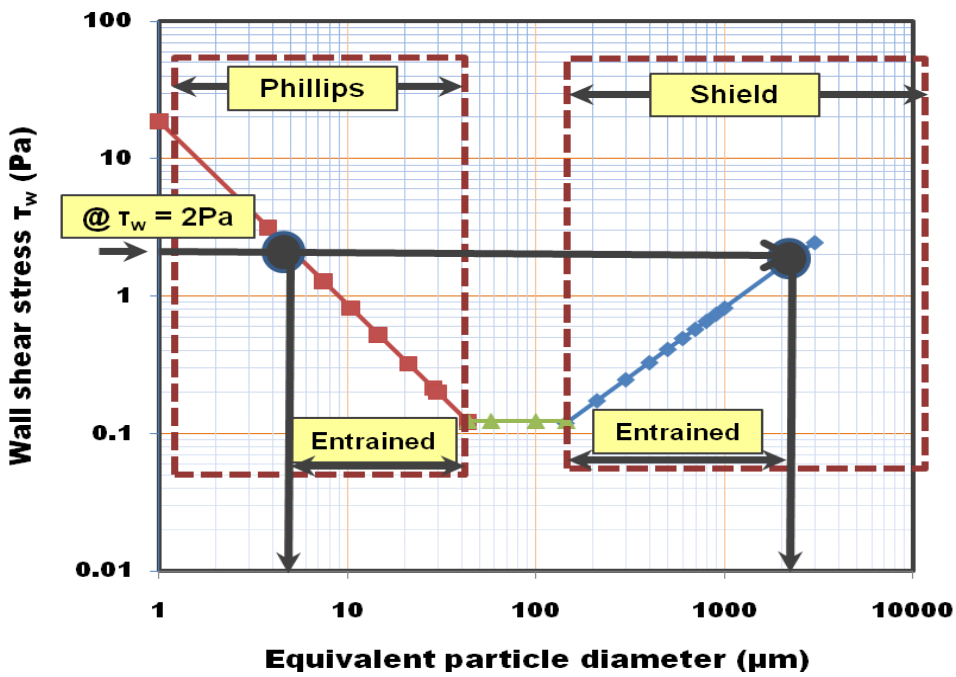

Figure 5.4 Two distinct critical particle entrainment regimes as function of the wall shear stress and size range found in the bed [15] (silica sand-water)

For a bed containing only 1-100 μm size of particles at the same wall shear stress (2 Pa), a different entrainment condition applies. This domain, called "Phillips' domain", entails preferential removal of particles with a particle diameter, d_p,

greater than 4 μm. For this range of particles (small particle regime, 1-100 μm), the concentration of particles whose size is smaller than "critical entrained size" will progressively increase in the bed. A detailed analysis of the forces involved in removal and deposition of the particles is needed to explain the different particle removal mechanisms effective in Phillips and Shields domains. The following section (5.3.1) presents a brief discussion of the forces involved in removal of the deposited particles from a bed.

5.3.1 Forces Involved in Removal of Particles from Bed Deposits

The forces acting on the particles during slurry transportation are shown in Figure 5.5.

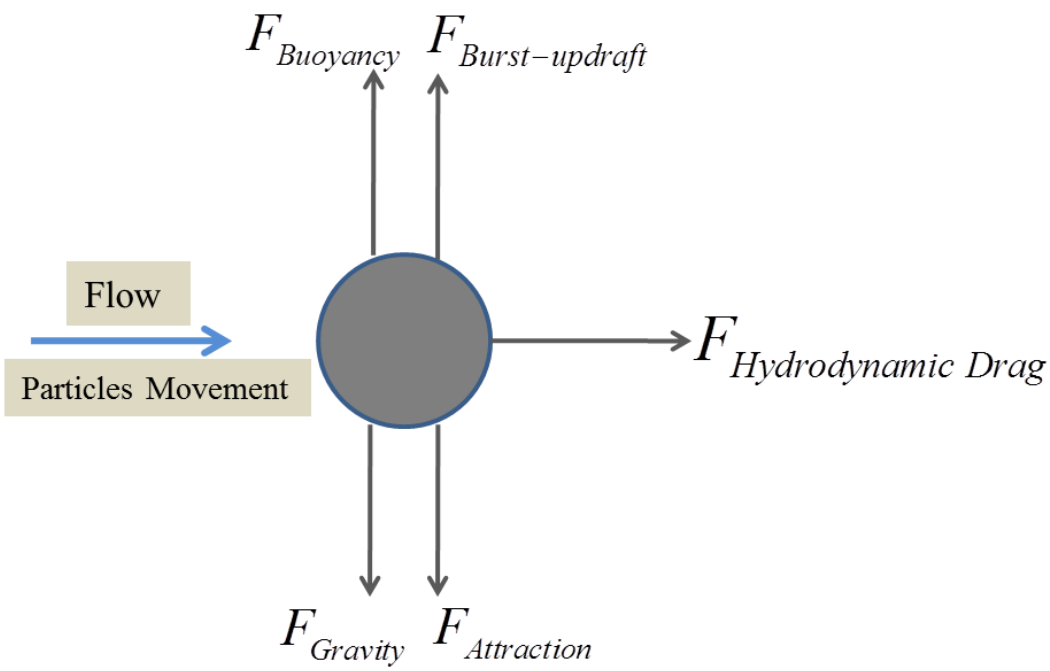

Figure 5.5 Main forces considered for removal and grading of particles from a sand bed during slurry transportation

There are two main forces trying to retain particles in bed deposits. These are attraction force, F_a, and net-weight force which is combination of gravity and buoyancy terms, F_b, defined by Eq. (5.1) and Eq. (5.2) respectively [15].

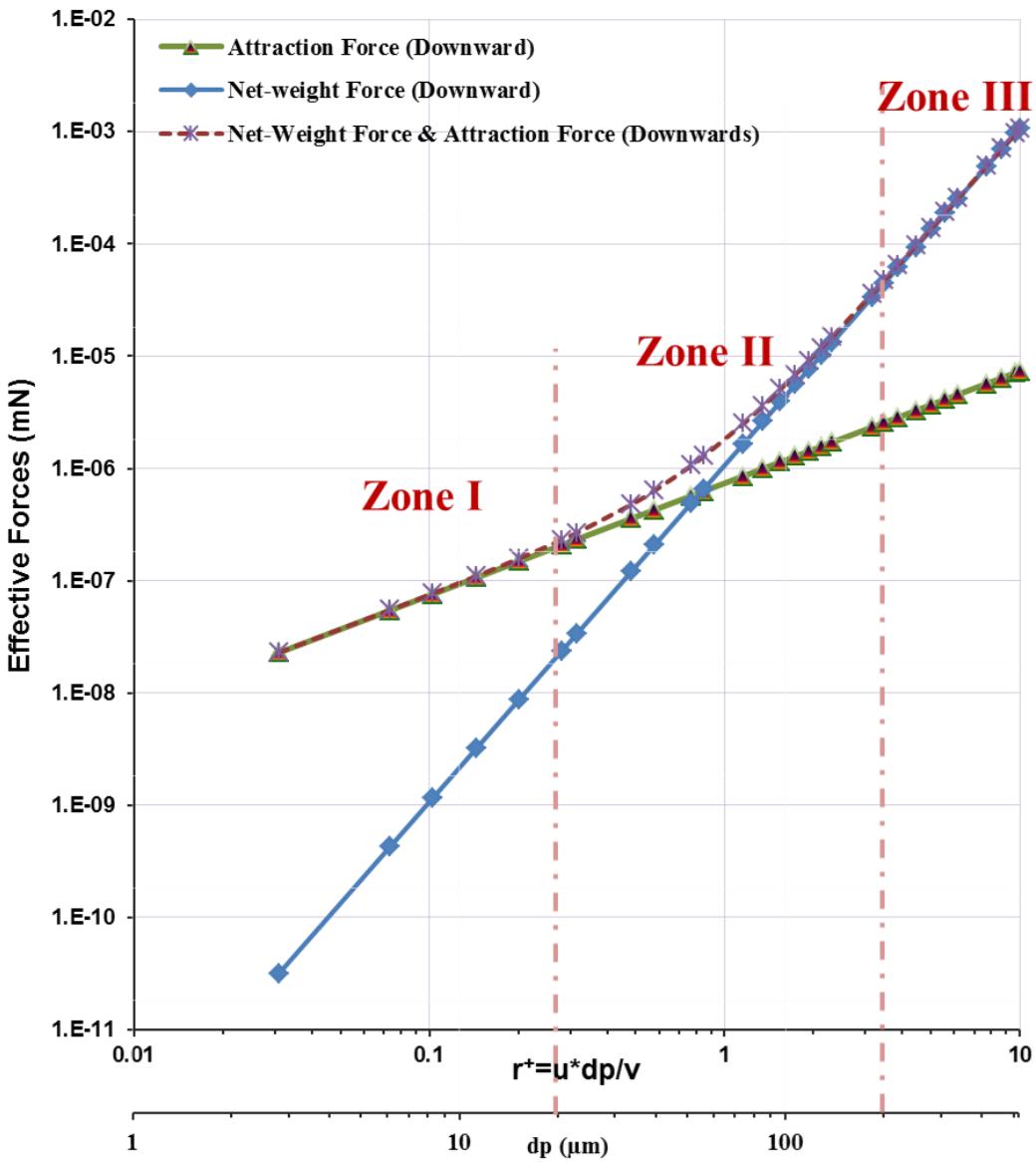

Figure 5.6 Attraction and buoyant forces contributing to particle removal (silica sand-water)

$$F_a = c_1 d_p; \qquad c_1 = O\left(10^{-5}\right) \tag{5.1}$$

$$F_b = \left(\pi/6\right) d_p^3 g\left(\rho_p - \rho_f\right) \tag{5.2}$$

Figure 5.6 presents a comparison of the magnitude of retaining forces as a function of the particle size and particle Reynolds number; $r^+ = u^* d_p / \nu$.

For particle diameter $d_p < 20\,\mu m$, the attraction force is significantly higher than the net-weight force (Figure 5.6 - Zone I). For particle diameter $d_p > 200\,\mu m$, the net-weight force is notably higher than the attraction force (Figure 5.6 - Zone III). For particle diameter between $20 < d_p < 200\,\mu m$, the attraction and net-weight forces are comparable (Figure 5.6 - Zone II).

The two main lifting forces contributing to particle entrainment into the turbulent core flow are “updraft underneath a burst”, F_c, and “hydrodynamic drag”, F_d, defined by Eq. (5.3) and Eq. (5.4) respectively [15].

$$F_c = c_2 \rho_f \nu^2 \left(r^+\right)^3 \qquad r^+ = u^* d_p / \nu \qquad c_2 = O(10) \qquad for\ \ r^+ \le O(1) \tag{5.3}$$

$$F_d = c_d \left(\rho_f \overline{U}^2 / 2\right)\left(\pi d_p^2 / 4\right) \qquad with\ \ c_d \le O(1) \qquad for\ \ r^+ \gg 1 \tag{5.4}$$

The c_d is drag coefficient and defined by Eq. 5.5 [16]:

$$c_d = \frac{V_p\left(\rho_p - \rho_f\right)g}{0.5\rho_f A_p \overline{U}_p^2} \tag{5.5}$$

Figure 5.7 shows the relative magnitude of the lifting forces as a function of particle Reynolds number and particle diameter.

For the selected flow condition (U_{avg} = 0.36 m/s slurry at 20℃) if $r^+ < 0.4$ (Figure 5.7 - Zone I) the magnitude of the attraction force is higher than lifting forces. Therefore, in this case particles with diameter less than 30 µm (corresponding to particle Reynolds number, $r^+ < 0.4$) are not removed.

As illustrated in the example of Figure 5.7 the burst updraft force overcomes the attraction force for $r^+ > 0.4$ (Figure 5.7 - ZoneII). Since the burst is generated within the viscous sublayer, it is reasonable to assume that the updraft force originating from a burst could be effective only on the particles entrained within the viscous sublayer [9].

For example: for an average water velocity of 0.36 m/s at temperature 20˚*C*, the thickness of the viscous sublayer is estimated to be 310 µm. So, in this case we can expect that the burst-updraft force could help to remove any particle which has a size less than 310 µm.

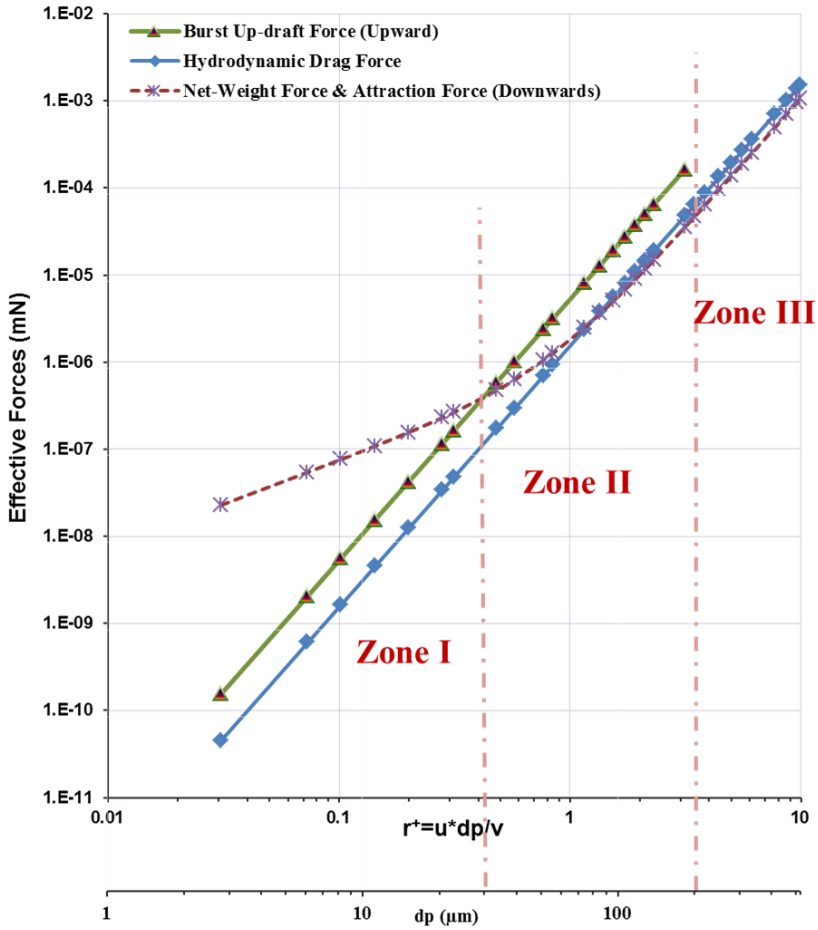

Figure 5.7 Entraining forces acting on particles exposed to turbulent core flow (calculation is done for silica sand slurry at U_{avg} = 0.36 m/s, *Re* = 27,660)

Figure 5.7 illustrates that for the considered case, the upward burst force exceeds by almost an order of magnitude of the hydrodynamic drag force. However, when $r^+ >> 1$ the corresponding particle diameter is greater than the height of the viscous sublayer considerably reducing the effect of the burst-updraft on particle removal. It is possible that the horizontal component of the hydrodynamic drag force exceeds the attraction and buoyant forces making it the main removal mechanism (applicable to Shield's domain – Figure 5.7 – Zone III).

5.4 Experimental Program

To observe and quantify the frequency and strength of burst removal activity and compare it with the selective removal of particles from LD an experimental rig was commissioned and used.

5.4.1 Slurry Flow Loop and Operational Procedure

Figure 5.8 is a view of the slurry flow-loop consisting of nine lengths of 3 ¾-inch (0.095 m ID) – 1.5 m in length of optical glass tubes supported and perfectly aligned by specially designed metallic joints.

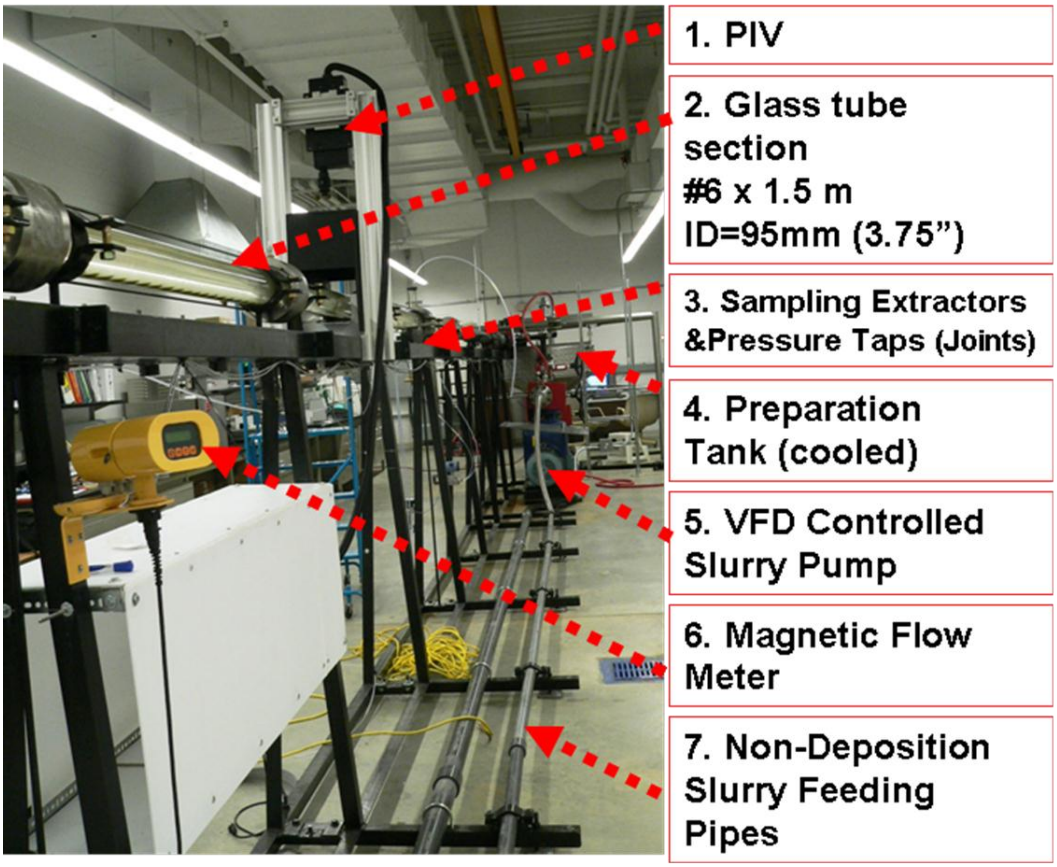

Figure 5.8 Main components of experimental rig

Modification of size-concentration of LD exposed to turbulent aqueous slurry flow is assessed by sampling. Samples are obtained with the aid of a specially designed (bottom) extractor. The size distribution of sampled particles (to diameters $d_p < 1\mu m$) is obtained with the aid of an automated image analyzer microscope (Leica).

The design of metallic joints allows for the installation of differential pressure taps and for convenient mounting of bottom sand extraction probes along the pipeline. High quality of optical glass is compatible with the particle image velocimetry (PIV) instrument [7] used in this study to assess the burst dynamics through non-intrusive recording of instantaneous velocities (*U*, *V*) and respective fluctuation velocities (u', v').

Flow rates from 0.05 m/s (*Re* = 3,400) to 2-3 m/s are rigorously controlled with the aid of a centrifugal pump equipped with a variable frequency drive (VFD). However, the sand grading experiments discussed in this paper are conducted at velocities lower than critical removal values of approximately 0.5 m/s. In this way the presence of a moving bed of sand particles in the Phillips' zone exposed to turbulent flow (of a very diluted aqueous slurry *C* < 1.5 vol%.) is assured.

The standard experimental procedure consists of three stages:

1. <u>Water-sand mixing and deposition</u>: a certain amount of sand or glass beads (size distribution previously determined) is mixed with water at pre-determined concentrations, (*C*), usually less than 1.5 vol%. and re-circulated as homogeneous

slurry above the critical deposition flow rate/velocity estimated for the largest particle size in the mixture. Subsequently flow is interrupted for approximately 36 hours. Prior to resuming the flow, and except the isolated experimental section, fines deposited in the return pipes, mixing tank and pump are carefully washed away.

2. A lenticular bed (LD) deposit formed of well-structured dunes of 2-5 mm in height and 20-50 mm in length is formed within a short initialization time (approximately 10 min) after the flow is resumed and maintained to an average velocity of approximately 0.15 m/s (17 GPM). The LD train is transported at velocities of 0.001-0.003 m/s. Similar conditions have been previously described in the literature [17]. During the axial transport of LD (involving a complex particle saltation and re-deposition movements), a selective removal of sand from LD to core flow takes place mainly under the action of turbulent burst activity. The sweeping activity (alternating the bursts) returns some of the particles, from the (extremely) diluted core flow, back to the LD. As a result of the mainly selective extraction of (larger-size) particles by burst the concentration of fines in the core flow and in the LD is increasing with time.

3. Sand samples are extracted from the LD using two extractors positioned 3 m apart. Approximately 50 minutes are required for the discrete LD to travel between the two extractors locations when the fluid velocity is 0.15 m/s. Sand samples are dried and measured using a Leica DM 6000 high-end automated image analyzing microscope. A specific measuring technique was developed to reduce possible errors mainly due to electrostatic agglomeration effects.

5.5 Results and Discussions

5.5.1 Evaluation of Burst Frequency Using PIV

Figure 5.9 illustrates a burst image obtained by processing the velocity fluctuation ($u' - v'$) data. The near-wall occurrence of "fresh" bursts and the transport of an "older" burst, at an angle of approximately 23° from horizontal axial flow direction are also underlined in Figure 5.9.

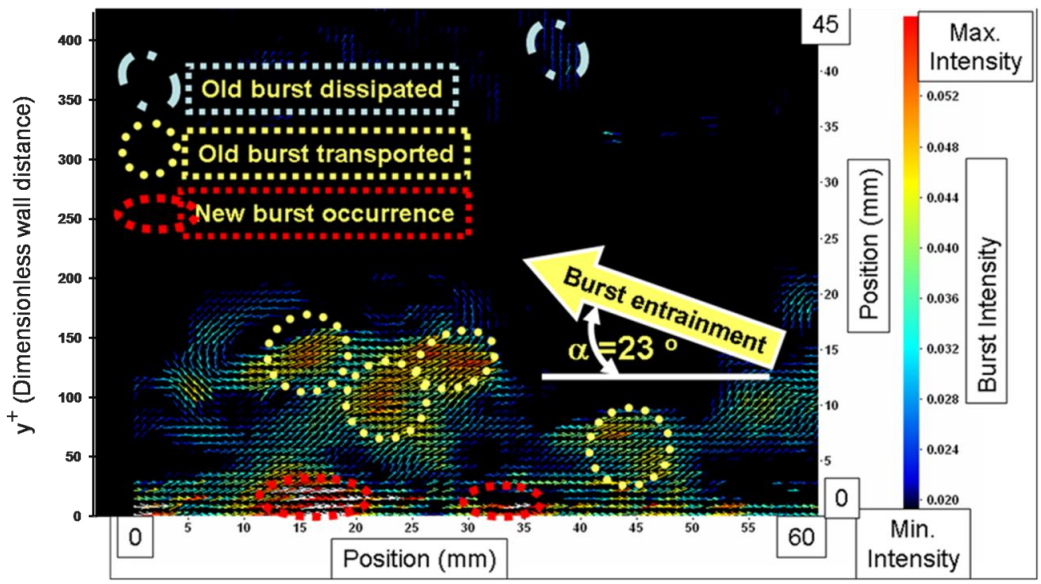

Figure 5.9 Near-wall burst initiation and dissipation snapshot obtained by processing the PIV data (average flow velocity 0.19 m/s)

An algorithm was developed to account for burst displacement with fluid at different levels and local velocities. In this way the points belonging to a certain burst were counted only once. Comparison of the results from this study with the

Cleaver and Yates data [9, 18] modified for pipe flow are given in Figure 5.10 (see also Table 5.A-1 of Appendix 5.A).

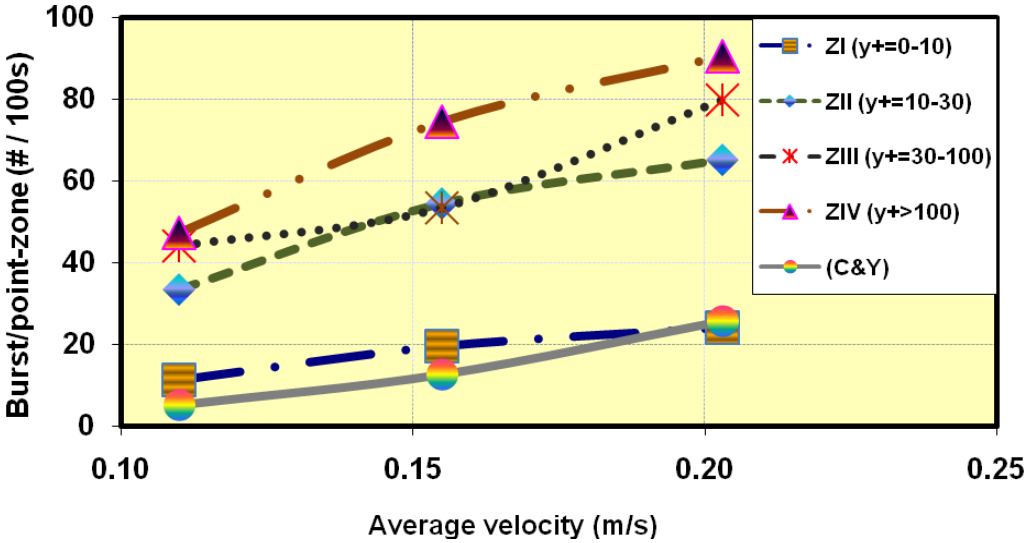

Figure 5.10 PIV measured burst frequency (number of burst/100s) assessed at four levels in the boundary layer and the frequency calculated (at Z1) using "Cleaver and Yates (C&Y)" method [9]

The PIV system evaluates a large number of instantaneous fluid velocities by recording the position modification of small tracers suspended in the turbulent fluid (particle impurities contained in the tap water). The calculation algorithms developed by LaVision provide good spatial resolution for this study. At every 200µs, a high-speed CCD camera captures (65mm x 48 mm) a pair of images of particles from a thin field illuminated by a double pulsed 532 nm laser. Each pair of images is evaluated by cross-correlation and the resulting velocity vector field

contains 5,590 vector arrows. The processing of PIV velocities and fluctuation measurements (See Appendix 5.A for the summary) is further analyzed (Matlab) for assessing the possible burst location (quadrant method – Figure 5.3).

The developed burst assessment algorithm not only satisfactorily compares with the literature model in a near-wall layer (Zone I; y^+ = 0-10), but also clearly indicates the radial expansion of bursts with its displacement from wall to turbulent pipe core. This is in agreement with the description of burst evolution illustrated in Figure 5.11 [19].

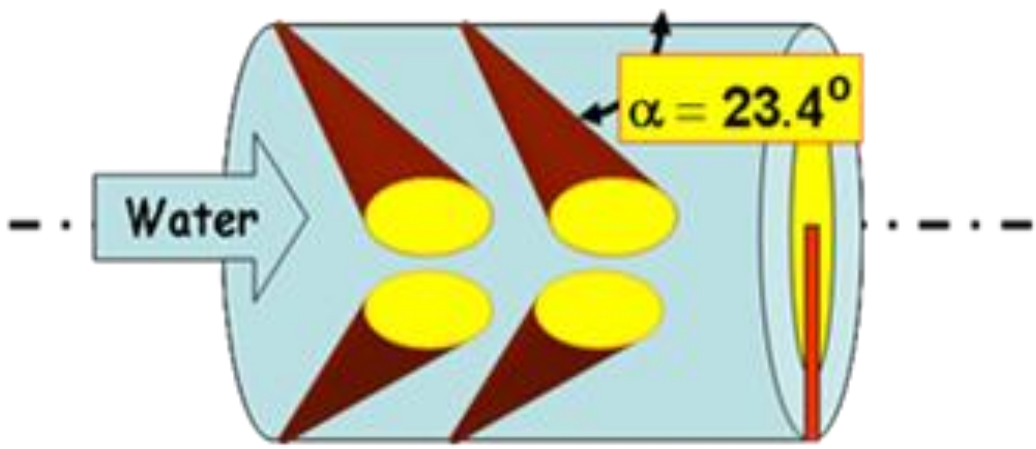

Figure 5.11 Schematic illustration of burst evolving from pipe wall to turbulent core flow [19]

Figure 5.10 and Figure 5.11 indicate the burst radial dissipation and is on line with Townsend [19] simplified description, where bursts are radially expanding during the dissipation process. For velocities between 0.15-0.3 m/s, a burst is

expected every 0.85-0.25 sec respectively in the near-wall zone. The mean time between two bursts is calculated by using Eq. 5.6 [9]:

$$t_{Burst} = 75 \nu / u^{*2} \tag{5.6}$$

The burst frequency increases with velocity; however, for velocities above the critical removal threshold value (assessed for the larger grain size) the entire deposit is removed into the core slurry flow.

5.5.2 Measurements of Selective Particle Removal (Grading)

In order to assess whether the selective removal of fines from a (preliminary) deposited LD sand bed is a consequence of burst entrainment (and sweep re-deposition), the procedure described at section 5.4.1 was repeated at various transport velocities and for various initial sand size mixtures.

Figure 5.12 compares the size distribution of particles in the initial homogeneous slurry (all particles suspended) and from the travelling LD bed exposed to turbulent flow (at 0.33 m/s) for approximately 135 minutes. In this case, the initial slurry contains large particles (d_p > 50 μm – “large particle regime” or “Shield’s domain”). Observation reveals that the particle size distribution of the sampled LD is shifted towards the larger particle sizes when compared to the particle size distribution of the initial slurry. This is mainly due to preferential entrainment of finer particles to the core flow, which occurs in Shield’s domain.

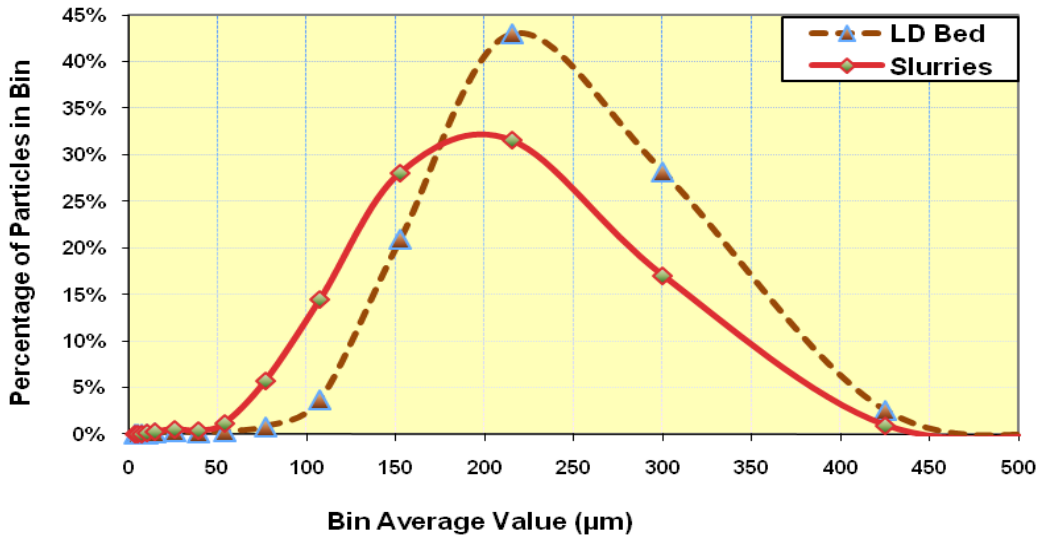

Figure 5.12 Concentration shift between transported sand bed and slurry (initial sand mixture of d_p > 50 µm - superficial slurry velocity of 0.33 m/s – *Re*=27,899; LD bed sample was taken 135 minutes after the start of the experiment)

Data presented in Figure 5.13 and Figure 5.14 were obtained from experiments using particles with diameter d_p < 60 µm. This is assimilated with "fine particle" or "Phillips' domain". The selective removal of finer particles is illustrated in Figure 5.13 which compares the cumulative size distribution of the particles removed from the initial mixture and the size distribution of the particles extracted from the bed after approximately 135 minutes of exposure to the main flow. The preferential removal of coarser particles causes the grading of the LD bed towards finer concentrations when an initial mixture is indicated to be in the "small particle regime" or "Phillips' domain" (d_p < 60 µm).

Additional evidence of removal of coarser fractions from the moving LD into the flowing slurry core is presented in Figure 5.14. Change in the particle size

distribution in the LD bed as a function of time is shown in Figure 5.14. Percentage of extremely small particles (0-10 μm) in the bed appears to increase visibly with exposure time at the expense of decreasing percentage of particles in the 15-25 μm range. This is mainly due to preferential entrainment of coarser particles to the core flow, which occurs in Phillips' domain.

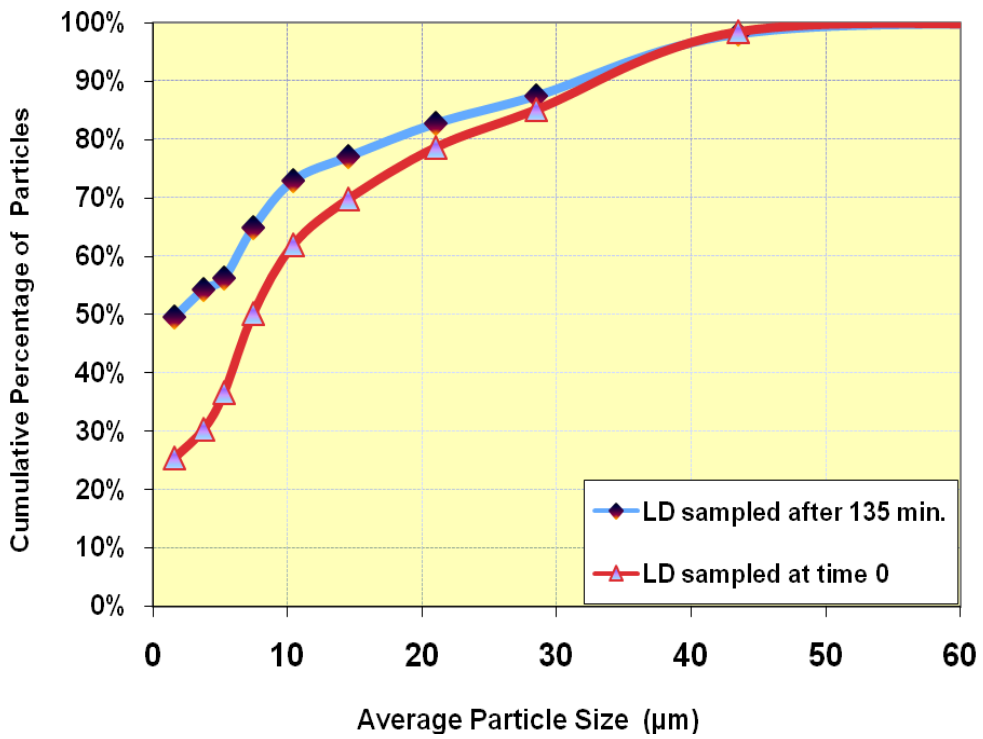

Figure 5.13 Change of particle size distribution in the moving lenticular bed deposits with time (d_p < 60 μm, slurry flow velocity is 0.33 m/s; LD bed sample was taken 135 minutes after the start of the experiment)

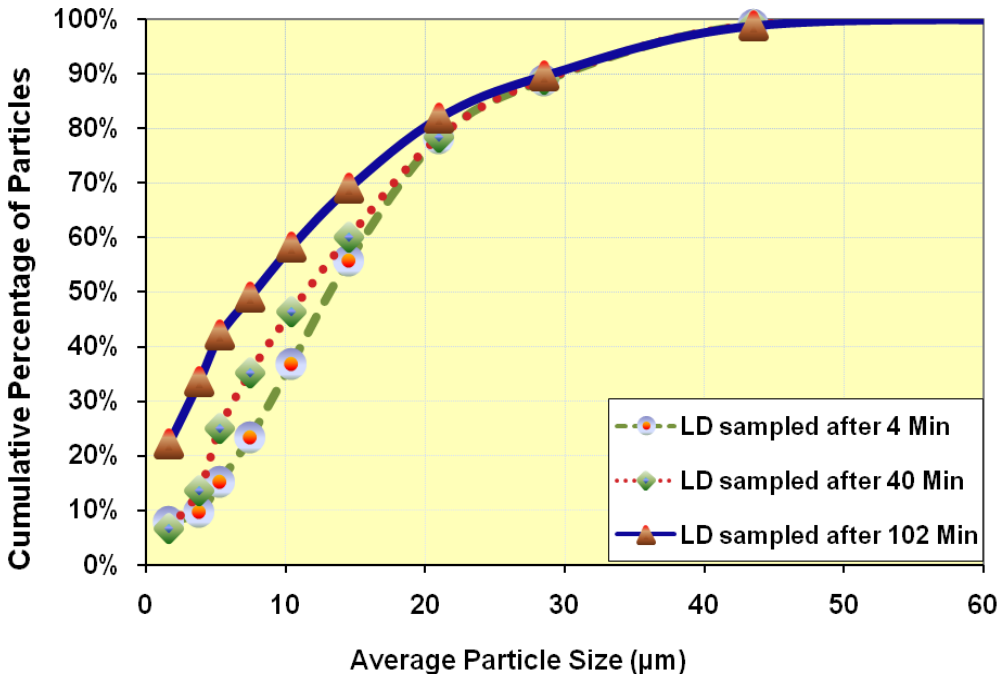

Figure 5.14 Change of particle size distribution in the moving lenticular bed deposits with time (d_p < 60 µm, slurry flow velocity is 0.36 m/s)

5.6 Conclusions

The burst activity initiated in the near-wall zone and the alternating downward sweeps initiated in the core flow during turbulent flow controls the radial transportation of momentum, mass and concentration in a major way.

Direct measurement of burst frequency was achieved using a PIV system in a 3 ¾-inch (0.095 mm ID) glass flow loop. An algorithm for assessing the near-wall burst frequency and its radial dissipation have been developed and validated.

A lenticular moving bed transported during turbulent slurry flow (containing a pre-determined range of particle sizes) have been observed and quantified. Special bed extraction probes have been designed and used to observe the dynamics of particle removal-deposition from a bed.

For a sand bed containing particles with size predominantly less than 60 micron (i.e., Phillips' domain, $d_p < 60$ µm) larger particles are preferentially removed. This is mainly because of the fact that inter-particle attraction forces (e.g., London- van der Waals forces) become dominant in this range and retain the fine particles in bed. However, for a sand bed of particles with size mostly greater than 100 micron (i.e., Shield's domain, $d_p > 100$ µm), the finer particles are removed.

The presence of fine particles in the oil sands slurry adversely affects bitumen extraction from oil sands. Mechanical separation of fines could be a cost and energy efficient way of conditioning oil sands slurry while hydrotransporting via pipeline.

5.7 Appendix 5.A Assessing Burst Frequency Activity with the Aid of PIV

Use of a laser-illuminating Particle Image Velocimetry (PIV) method for observing and quantifying the near-wall turbulent burst-sweep activity included: (a) adapting the existing PIV for pipe flow measurements (including the elimination of un-wanted glare) and (b) comparing the new data to existing data on burst frequency obtained mainly with flat channel geometry.

The following specific problems have been addressed and resolved in this study:

1. Design and validation of a suitable PIV algorithm for processing a package of 500 velocity vector fields obtained from 500 image pairs (each image investigation zone of approximately 66 x 44 mm^2 contains a matrix of 65 rows x 86 columns or 5,590 points where *U* and *V* instantaneous velocity vectors and respective fluctuations are measured and recorded). Images were recorded at a speed of 200 ms/pair (total time: 100 sec). The developed algorithm using Matlab software, included provisions for the elimination of "glare spots" and for assessing the "burst condition" (see VISA [5, 12] technique illustrated in Figure 5.2 and Figure 5.3).

The PIV based method was first validated by comparing the measured flow rate with the calculated flow rate. The integration of PIV measured axial velocity distribution was used to find out "calculated flow rate". The measured axial velocity distribution was also compared to the calculated velocity distribution

using the boundary layer model ("law of the wall"). Relative errors between calculated and measured flow rates were found to be less than 5%.

2. The evaluation of burst frequency included the counting of the number of "local points under burst". Counting was divided into four radial sub-zones such as ZI: $0 \leq y^+ < 10$, ZII: $10 \leq y^+ < 30$, ZIII: $30 \leq y^+ < 100$ and ZIV: $100 \leq y^+$. This allowed for the assessment of burst dynamics from the near-wall occurrence to turbulent core flow mixing. Two major problems have been resolved: (a) finding a convenient method for statistical averaging and (b) avoiding the multiple counting as a result of multiple images describing the same burst evolving from the wall to flow axis. The most reliable averaging method used a cumulative technique for the 500 velocity vector fields. Using 500 image pairs (observation time approximately 100 sec) indicated a high reproducibility rate (observed after minimum of 50 images). For elimination of multiple counting, the axial traveling time of a burst (coherent formation) was considered separately using the actual (measured-calculated) axial transport velocity for each zone and a correction for the measured wall-departure angle.

Table 5.A-1 Number of burst counts during 100 seconds of flow (after correction for evolvement angle and multiple-frames factor)

U (m/s)	$0 \leq y^+ < 10$ ZI	$10 \leq y^+ < 30$ ZII	$30 \leq y^+ < 100$ ZIII	$100 \leq y^+$ ZIV
0.110	11	33	44	47
0.155	20	55	54	74
0.203	24	65	80	91

Table 5.A-1 presents the total number of burst counts captured by 500 frames during 100 seconds of flow in four different zones at three different average velocities.

The burst frequency counts in Table 5.A-1 were obtained by taking into account the following characteristics: burst evolvement angle, elimination of multiple counting of burst frequencies in consequent frames, and parabolic shape of the velocity profile as the velocity changes from zero at the pipe wall to its maximum value at the center of the pipe. Considering differences in the velocity profile, the measurement area was divided into four sections, $0 \le y^+ < 10$, $10 \le y^+ < 30$, $30 \le y^+ < 100$, and $100 \le y^+$ and those characteristics were applied to each section.

5.8 References

[1] Robinson, S. K., 1991, "Coherent Motions in the Turbulent Boundary Layer," Annual Review of Fluid Mechanics, 23(1), pp. 601-639.

[2] Kline, S. J., Reynolds, W. C., Schraub, F. A., and Runstadler, P. W., 1967, "The Structure of Turbulent Boundary Layers," Journal of Fluid Mechanics, 30(04), pp. 741-773.

[3] Sippola, M. R., 2002, "Particle Deposition from Turbulent Flow: Review of Published Research and Its Applicability to Ventilation Ducts in Commercial Buildings," Technical Report No. Lawrence Berkeley National Laboratory, Berkeley, CA. LBNL- 51432.

[4] Corino, E. R., and Brodkey, R. S., 1969, "A Visual Investigation of the Wall Region in Turbulent Flow," Journal of Fluid Mechanics, 37(01), pp. 1-30.

[5] Wallace, J. M., Eckelmann, H., and Brodkey, R. S., 1972, "The Wall Region in Turbulent Shear Flow," Journal of Fluid Mechanics, 54(01), pp. 39-48.

[6] Schoppa, W., and Hussain, F., 2000, "Generation of near-Wall Coherent Structures in a Turbulent Boundary Layer," Current Science, 79(6), pp. 849 - 858.

[7] Adrian, R. J., 2007, "Hairpin Vortex Organization in Wall Turbulence," Physics of Fluids, 19(4), pp. 041301-16.

[8] Gad-El-Hak, M., 1998, "Fluid Mechanics from the Beginning to the Third Millennium," International Journal of Engineering Education, 14(3), pp. 177 - 185.

[9] Cleaver, J. W., and Yates, B., 1973, "Mechanism of Detachment of Colloidal Particles from a Flat Substrate in a Turbulent Flow," Journal of Colloid and Interface Science, 44(3), pp. 464-474.

[10] Toma, P., Ivory, J., Korpany, G., Derocco, M., Holloway, L., Goss, C., Ibrahim, J., and Omar, I., 2006, "A Two-Layer Paraffin Deposition Structure Observed and Used to Explain the Removal and Aging of Paraffin Deposits in Wells and Pipelines," Journal of Energy Resources Technology, 128(1), pp. 49-61.

[11] Bagnold, R. A., 2005, *The Physics of Blown Sand and Desert Dunes*, Dover Publications Inc., London.

[12] Lu, S. S., and Willmarth, W. W., 1973, "Measurements of the Structure of the Reynolds Stress in a Turbulent Boundary Layer," Journal of Fluid Mechanics, 60(03), pp. 481-511.

[13] Shields, A., 1936, "Anwendung Der Ahnilchkeitsmechanik Und Der Turbulenzforschung Auf Die Geschiebebewegung Mitteilungen Der Preuss," Versuchsanst. F. Wasserbrau und Schiffbau, Berlin, Heft, 26 (see Yalin, M. S., 1977), pp.

[14] Yalin, M. S., 1977, *Mechanics of Sediment Transport*, Pergamon Press, Oxford; New York.

[15] Phillips, M., 1980, "A Force Balance Model for Particle Entrainment into a Fluid Stream," Journal of Physics D: Applied Physics, 13(2), pp. 221.

[16] Albion, K., Briens, L., Briens, C., and Berruti, F., 2009, "Modelling of Oversized Material Flow through a Horizontal Hydrotransport Slurry Pipe to Optimize Its Acoustic Detection," Powder Technology, 194(1-2), pp. 18-32.

[17] Thomas, D. G., 1964, "Transport Characteristics of Suspensions: Part Ix. Representation of Periodic Phenomena on a Flow Regime Diagram for Dilute Suspension Transport," AIChE Journal, 10(3), pp. 303-308.

[18] Cleaver, J. W., and Yates, B., 1976, "The Effect of Re-Entrainment on Particle Deposition," Chemical Engineering Science, 31(2), pp. 147-151.

[19] Townsend, A. a. R., 1980, *The Structure of Turbulent Shear Flow*, Cambridge University Press,

6 Experimental Study of Shifting Particle Size Distribution and Selective Removal of Fines from a Pipeline Deposit

6.1 Introduction and Background

Many researchers have investigated particle entrainment from deposit beds. Entrainment occurs when the lifting forces overcome the holding forces. The balance of forces acting on deposit particles determines the entrainment criteria. Shields [1-4] proposed a diagram referred as a "critical stage" to determine critical removal velocity for particle entrainment from sediments (deposit beds). The Shields function $Y_{cr} = f\left(X_{cr}\right)$ relates the critical grain size Reynolds number ($X_{cr} = u_{cr}^{*} D/\nu$) to acquire the critical mobility number ($Y_{cr} = \rho u_{cr}^{*2}/\gamma_S D$) from the Shields curve (see Figure 6.1), where $u_{cr}^{*} = \sqrt{\tau_0/\rho}$ is the critical shear velocity, τ_0 is the shear stress interacting between the flow and the bed surface, D is the gain size, ν is the kinematic viscosity, γ_S is the specific weight of a grain in fluid, and ρ is the density of the fluid.

The experimental results are shown in Figure 6.1 as data points obtained using particle diameters of granular material over 1 mm in size, assuming uniform, cohesionless particles. The data points form an approximately straight line parallel to the axis of the critical grain size Reynolds number (X_{cr}) and exhibit good agreement with the Shields curve in this diagram (corresponding to $d_{50} > \sim$ 200 μm). Hence, the curve in Figure 6.1 can be used with confidence to predict

the initiation of sediment transport for particles over 200 µm in size. Bagnold [5, 6] conducted numerous experiments on particle entrainment in air. His results were subsequently verified, mostly by observations in the Libyan desert.

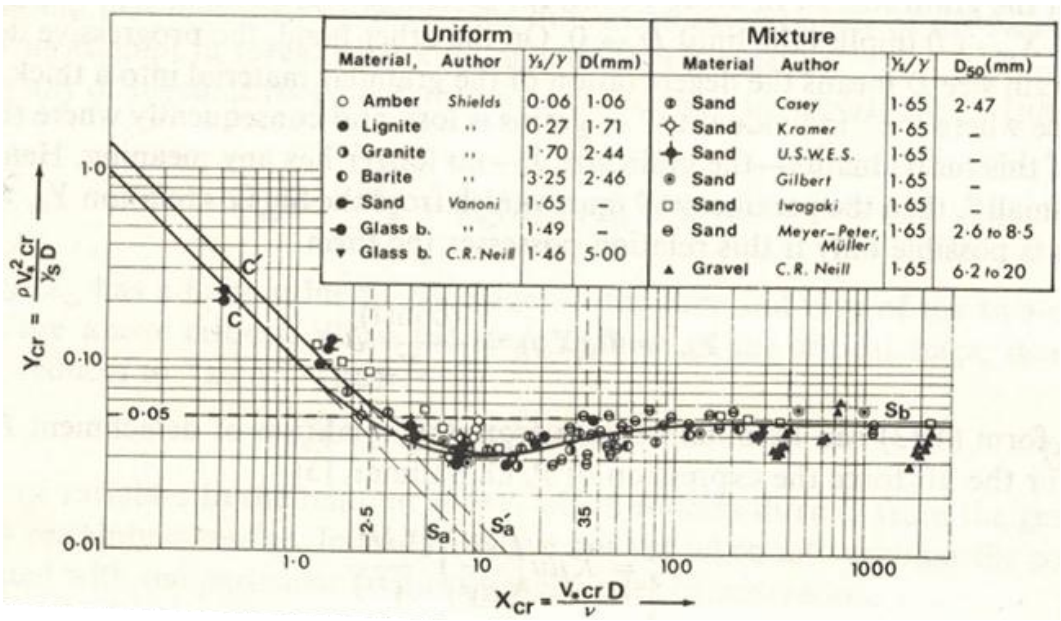

Figure 6.1 Dimensionless Shield's diagram for entrainment of bed particles, first introduced in 1936 [2]

Other studies have been performed to investigate the entrainment of various particles in air, but not enough experiments have been carried out in aqueous media. Bagnold [7] determined the threshold velocity required for particle entrainment in air for particle size greater than 80 µm. Working on particle entrainment in air flow, he pointed out that for particles smaller than 50–80 µm (d_p < 50–80 µm), the attraction force cannot be ignored and the threshold velocity is higher due to cohesion effects.

During hydrotransport, detachment of particles from the bed can occur due to hydrodynamic drag force or “updraft under a burst” depending on the particle size d_p and flow condition, expressed as wall shear stress [8]. Cleaver and Yates [9] pointed out that, to remove particles from the surface, the flow adjacent to the surface should be turbulent. Particle removal due to burst activity is illustrated schematically in Figure 6.2. The viscous region in turbulent flow adjacent to the wall, which is highly sheared, is the region where lift force is generated as “updraft under a burst” [10]. Cleaver and Yates [9] quantified the mean values for the spatial and temporal distribution of the bursts based on research performed by Kline et al. [11], Corino and Brodkey [12], Kim et al. [13], Morrison et al. [14], Rao et al. [15], and Wallace et al. [16]. Cleaver and Yates [9] utilized the available evidence and found that the spatial and temporal burst quantities are similar for flows on flat plates, channels, and pipes. In all cases, the burst length and width were projected to be about $20\,\nu/u^* \sim 40\,\nu/u^*$ in the mean flow direction and $15\,\nu/u^* \sim 20\,\nu/u^*$ in the transverse direction, respectively [9].

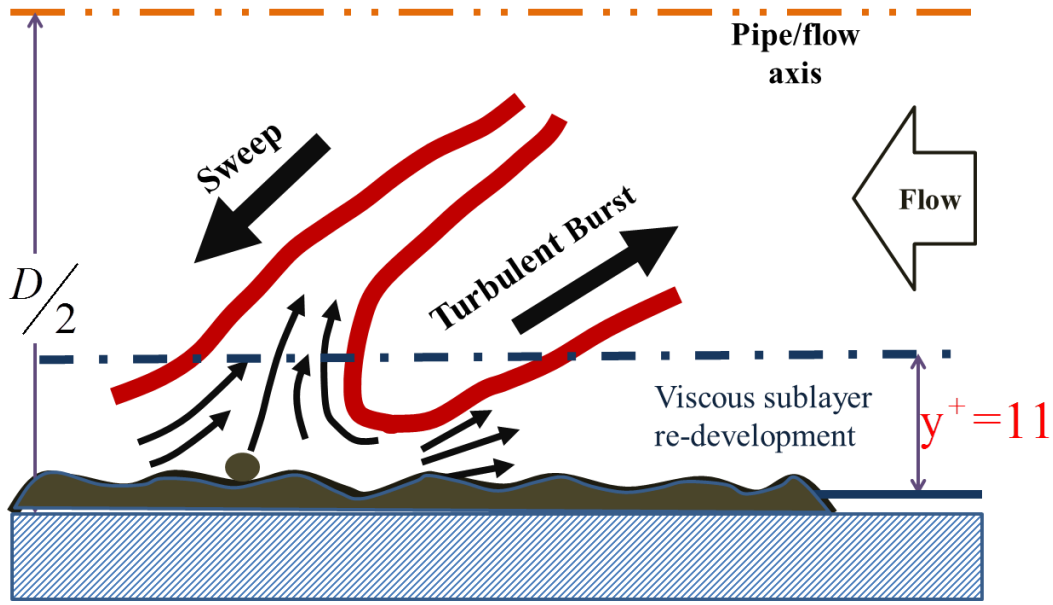

Figure 6.2 Particle removal mechanisms by burst activity in turbulent flow at the surface [9, 17]

Phillips [8] considered the force balance for different particle diameters. The dominant forces vary depending on the particle size and, therefore, the entrainment criteria also vary with size. For smaller particles (d_p <~ 60 μm, Phillips domain), the balance of attraction and buoyancy forces with the "updraft under a burst" force was first introduced by Cleaver and Yates [9]. However, for larger particles (d_p >~ 170 μm, Shields domain) the net weight balances the hydrodynamic drag force. For particle sizes between the Phillips and Shields domains, the net weight balances the "updraft under a burst" force.

The critical removal velocity in a pipeline is defined as the minimum velocity required to remove particles from the bed at the bottom of the pipe [18-20], and the critical deposition velocity is the velocity at which particles start to form a bed

at the bottom of the pipe from fully suspended flows [21]. Researchers have approached this topic from different perspectives. Oroskar and Turian [21] treated this issue in terms of the energy dissipated by turbulent eddies to maintain particles in suspension, and correlated their hypothesis with the experimental data. Considering the velocity that results in removal of 50% of the bed as the critical removal velocity, our observations in the lab were close to the critical removal velocity obtained using the approach of Oroskar and Turian, in which the median diameter of the particles was used for the calculation.

Later, many other researchers used a similar approach for characterizing the incipient motion of particles from the bed. Stevenson et al. [22] applied the force balance to suggest the critical removal velocity by considering rolling and sliding options, and Ramadan et al. [23] introduced a mechanistic model for critical particle velocity. Rabinovich and Kalman [18-20, 24] used force balance and non-dimensional particle Reynolds and Archimedes numbers to describe the incipient motion. Miedema [25] modified the Shield's diagram and Papista et al. [26] modeled the incipient motion of particles by direct numerical simulation.

Particle removal from the bed load can occur with a variety of different slurry flow patterns. Newitt et al. [27] categorized slurry flow into five different patterns: (1) fully suspended flow, (2) suspended flow with a moving bed, (3) suspended flow with a sliding layer or stationary bed, (4) stationary bed with ripples on surface, and (5) lenticular deposits (LDs). Our research is focused on the slurry flow pattern for lenticular deposits, as the surfaces of different slurry flow patterns are similar to the form of LDs.

The experimental research in this work was carried out to better understand hydrodynamic particle removal in the deposit bed in terms of PSD shifts resulting from exposure to turbulent flow.

6.2 Balance of Forces Acting on Particles in Pipeline Flow

In slurry transportation, particles from the bed are transported by being lifted and evolved to the core flow and by sliding or rolling, depending on particle size, shape, and density; fluid velocity; flow conditions; and slurry concentration.

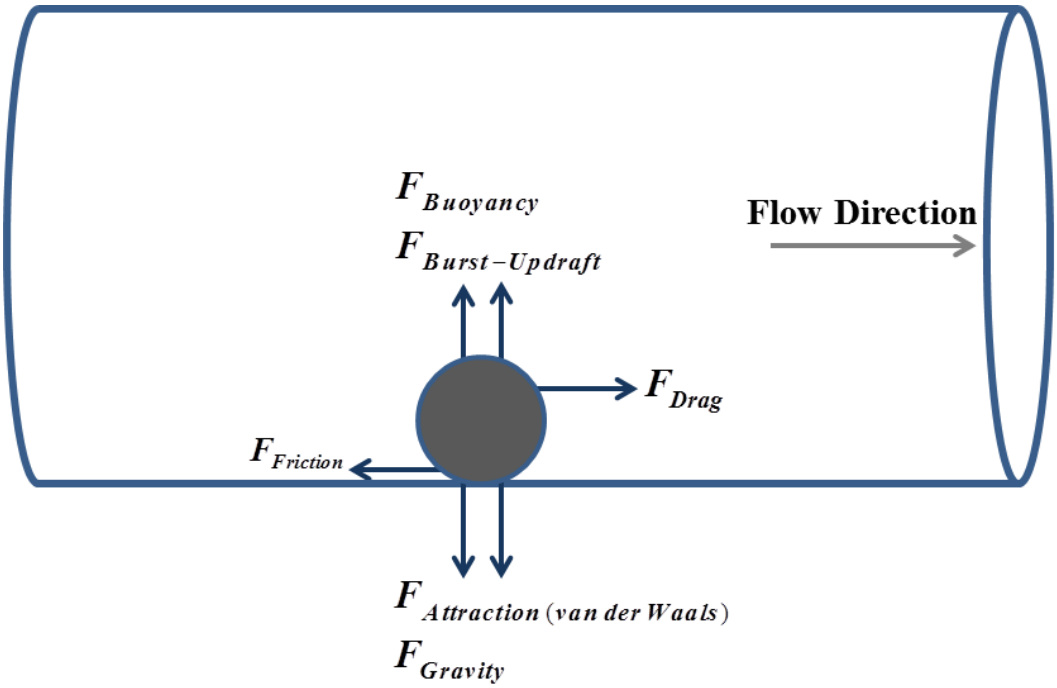

Figure 6.3 Balance of forces on a particle in a deposit during pipe flow

As illustrated in Figure 6.3, several forces may act on particles during hydrotransport. The friction force that tends to prevent sliding motion before particle movement gets started is defined as:

$$F_f = \mu_s F_N \tag{6.1}$$

where μ_s is the coefficient of static friction and F_N is the normal force perpendicular to the direction of flow. Once the particles have started moving, the coefficient of kinematic friction μ_k (or coefficient of dynamic friction) applies, which is usually less than μ_s.

Experiments conducted to measure μ_k [28] found a value of about 0.3 for slurry flow with 500-µm particles. The normal force F_N acting on the particles is the difference between upward and downward forces:

$$F_N = F_{Net\ gravity} + F_{Attraction} - F_{Burst,updraft} \tag{6.2}$$

Depending on the particle size, some forces may be dominant while others are comparatively negligible. Generally, four forces – attraction, net weight, drag, and lift – are sufficient to describe and model particle entrainment [3, 18, 19, 23, 29]. In dilute slurry, the friction force is negligible and can be ignored without causing significant error.

Brownian motion is caused by unbalanced impulses of water molecules on the surfaces of solid particles. These impulses are the result of thermal motion and are dependent on the temperature [30]. Brownian motion might be significant for particles smaller than 1 µm (colloidal size range). However, for the present study the samples were washed initially to eliminate the colloidal-size particles. Therefore, Brownian motion is not considered in this study.

The experiments were conducted using different particle sizes at three different velocities: 0.25 m/s, 0.34 m/s, and 0.39 m/s, which are well below the critical removal velocity.

6.2.1 Forces Involved in Particle Entrainment

The forces acting on particles in an aqueous environment are lift force F_c (updraft under a burst), attraction force F_a, net weight force F_b, and hydrodynamic drag force, F_d (see Figure 6.3).

6.2.1.1 Attraction (van der Waals) force

Attraction forces act between the particles and the pipe wall (adhesion) or between particles (cohesion). Both originate from van der Waals forces as given in [8]:

$$F_a = c_1 d_p \qquad \textit{where} \qquad c_1 = O\left(10^{-5}\right) \qquad (6.3)$$

6.2.1.2 Net weight force

The net weight force (effective gravity) is the difference between gravitational force and buoyancy force, given by

$$F_b = (\pi/6)\Delta\rho g d_p^3 \qquad where \qquad \Delta\rho = \rho_p - \rho_f \qquad (6.4)$$

6.2.1.3 Lift force (updraft due to turbulent burst)

Particles submerged in the turbulent viscous layer adjacent to the wall are subject to updrafts due to turbulent bursts. Robinson [31] defines bursting as a violent, temporally intermittent eruption of fluid away from the wall, that exists in a form of local instability. If the updraft force overcomes the downward forces, F_c can lift the particles from the bed into the flow, as given by [8, 9]:

$$F_c = c_2 \rho_f \nu r^{+^3} \qquad for\ r^+ < 1 \qquad \& \qquad c_2 = O(10) \qquad (6.5)$$

where r^+, the particle Reynolds number, is defined based on friction velocity, $r^+ = u^* d_p / \nu$, and ν is the kinematic viscosity of the fluid, d_p is particle diameter, ρ_f is the fluid density, u^* is the friction velocity given as $u^* = \sqrt{\tau_w / \rho}$, and τ_w is the wall shear stress.

6.2.1.4 Hydrodynamic drag

The lifting of the larger particles in turbulent flow during hydrotransport is due to hydrodynamic force, defined by [8]:

$$F_d = c_d \frac{\pi}{4} d_p^2 \frac{1}{2} \rho_f \overline{U}^2 \qquad for\ r^+ \gg 1 \quad \& \quad c_d \ll O(1) \qquad (6.6)$$

6.2.2 Force Balance for Effective Entrainment

Based on particle size, the effective upward and downward forces can be limited to three different categories. According to Phillips [8], for a small-particle regime (d_p < 60 μm) the condition for entrainment is reached when updrafts due to turbulent bursts overcome the attraction force. For larger particles (d_p > 170 µm), the drag force balances the net weight force and, for the intermediate region, the updraft under a burst balances the net weight force. The force balance is summarized in Table 6.1.

Table 6.1

Summary of force balance models and coefficient values for different domains

Region	Entrainment condition	Parameter Value
Phillips domain (Smaller particles)	$F_a = F_c$ $c_1 d_p = c_2 \rho_f \nu r^{+3}$	c_1 = 1.43E-5 c_2 = 5.25
Intermediate domain	$F_b = F_c$ $(\pi/6)\Delta\rho g d_p^3 = c_2 \rho_f \nu r^{+3}$	c_2 = 5.25
Shields domain (Larger particles)	$F_b = F_d$ $(\pi/6)\Delta\rho g d_p^3 = c_d \frac{\pi}{4} d_p^2 \frac{1}{2} \rho_f \overline{U}^2$	$c_d = \frac{V_p(\rho_p - \rho_f)g}{0.5\rho_{slurry} A_p \lvert \overline{U}_f - \overline{U}_p \rvert^2}$ [29]
Mixed domain	$F_a + F_b = F_c + F_d$	

6.2.2.1 Force balance for the experimental velocities

Force balance analysis was performed for three different velocities. Particle entrainment is function of particle size and wall shear stress. The wall shear stress is given by

$$\tau_w = f_{Moody}\left(\frac{\rho_f \overline{U}_f^2}{8}\right) \tag{6.7}$$

where f_{Moody} is the friction factor from the Moody chart and is given by the Colebrook equation [32]:

$$\frac{1}{\sqrt{f_{Moody}}} = -2.0\,log_{10}\left(\frac{\frac{\varepsilon}{D_{pipe}}}{3.7} + \frac{2.51}{Re\sqrt{f_{Moody}}}\right), \qquad Turbulent\ \ flow \tag{6.8}$$

where ε is the pipe roughness coefficient, D_{pipe} is the pipe inner diameter, and Re is the Reynolds number.

Figure 6.4 shows the downward forces acting on particles, namely attraction and net weight. As shown in Figure 6.4, the attraction force is dominant for particles smaller than 40 μm. For larger particles, the net weight force dominates. However, as summation of downward forces shows, for particles smaller than 20 μm, only the attraction force needs to be considered and the net weight force is

comparatively negligible. Also, for particles larger than 100 μm, only the net weight force is applicable and the attraction force can be completely disregarded. For intermediate particle sizes, the two forces may be comparable, with the attraction force becoming stronger as the size distribution shifts to smaller particles and vise versa.

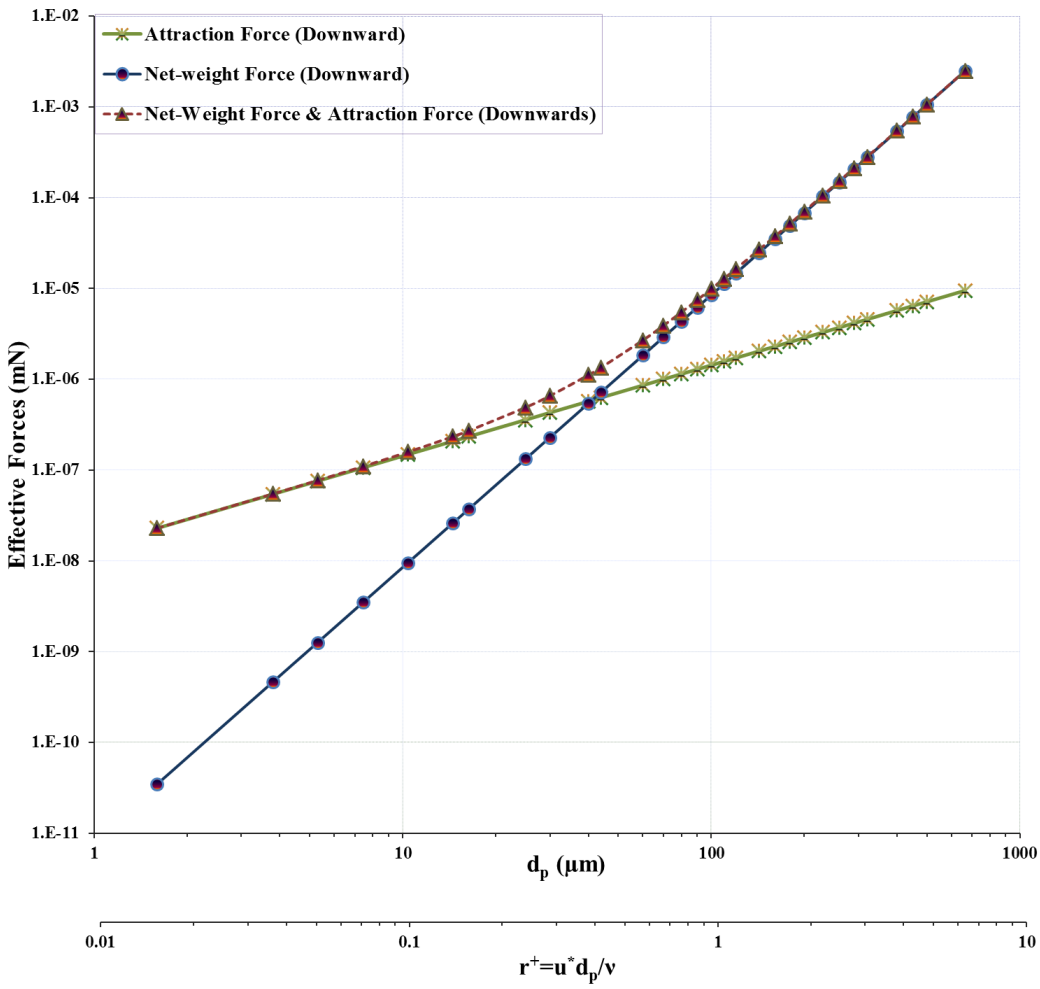

Figure 6.4 Downward forces acting on particles as a function of particle diameter and particle and fluid densities for all flow velocities

The balances of forces acting on particles for the three different velocities are given in Figures 6.5, 6.6, and 6.7. The lifting forces exerted on particles are updraft under a burst and hydrodynamic drag. According to Phillips [8], the updraft under a burst force is effective when the particle Reynolds number is less than order one. On the other hand, the hydrodynamic drag force dominates when the particle Reynolds number is much greater than order one. Therefore, for the lifting forces, the magnitude of the velocity is important and determines which forces are dominant for different particle size ranges.

Figure 6.5 shows the forces acting for the velocity 0.25 m/s (*Re* = 25,395). The figure shows that the lifting forces for particles smaller than 40 μm at 0.25 m/s velocity cannot overcome the holding forces. For particles larger than 40 μm and particle Reynolds number on the order of one, the updraft under a burst force and the hydrodynamic force are comparable. For particle size ranges having particle Reynolds numbers greater than order one the hydrodynamic force is effective. Where two lift forces are comparable, particles may move by rolling, sliding, or saltation under the influence of the hydrodynamic drag force first, and then may be taken out of the bed and into the flow by an updraft under a burst. Another hypothesis is that the particles can burst up directly into the flow from the bed under the influence of an updraft under a burst. As the smaller particles are not removed from the bed at this velocity, the concentration of fine particles in the bed increases as the larger particles are carried out of the bed.

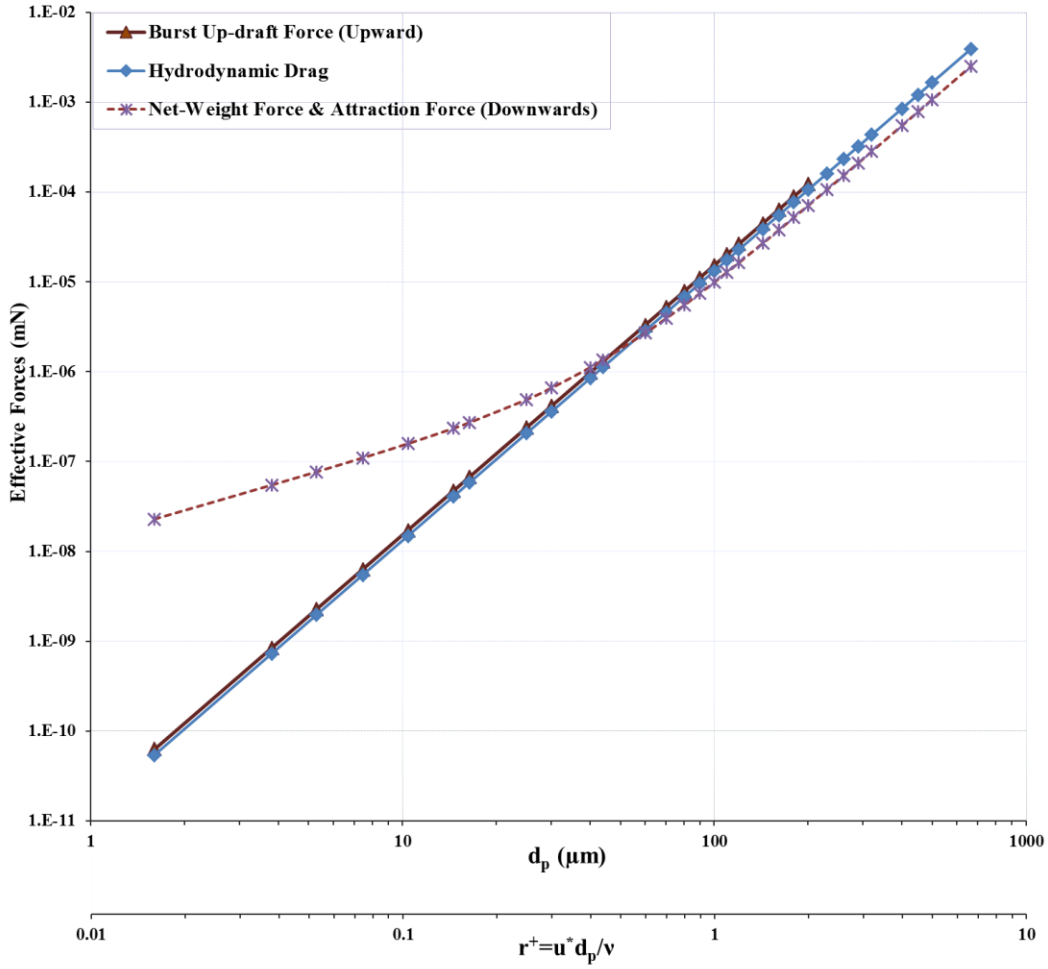

Figure 6.5 Force balance for particles at 0.25 m/s velocity (*Re* = 25,395)

Figure 6.6 illustrates the effective lift forces for 0.34 m/s average flow velocity (*Re* = 34,537). When the average flow velocity is 0.34 m/s, the lifting forces are effective for particles larger than 25 µm. Where the particles Reynolds number is less than order one, the updraft under a burst force is stronger than the hydrodynamic drag force; thus, it can remove particles directly from the viscous sublayer. However, when the updraft under a burst and drag forces are comparable, particles may first roll or slide along the bed and then be ejected

from the bed into the main flow. In the region where the hydrodynamic drag force is effective, particles may roll or slide first and then be lifted by saltation or moved predominately by saltation.

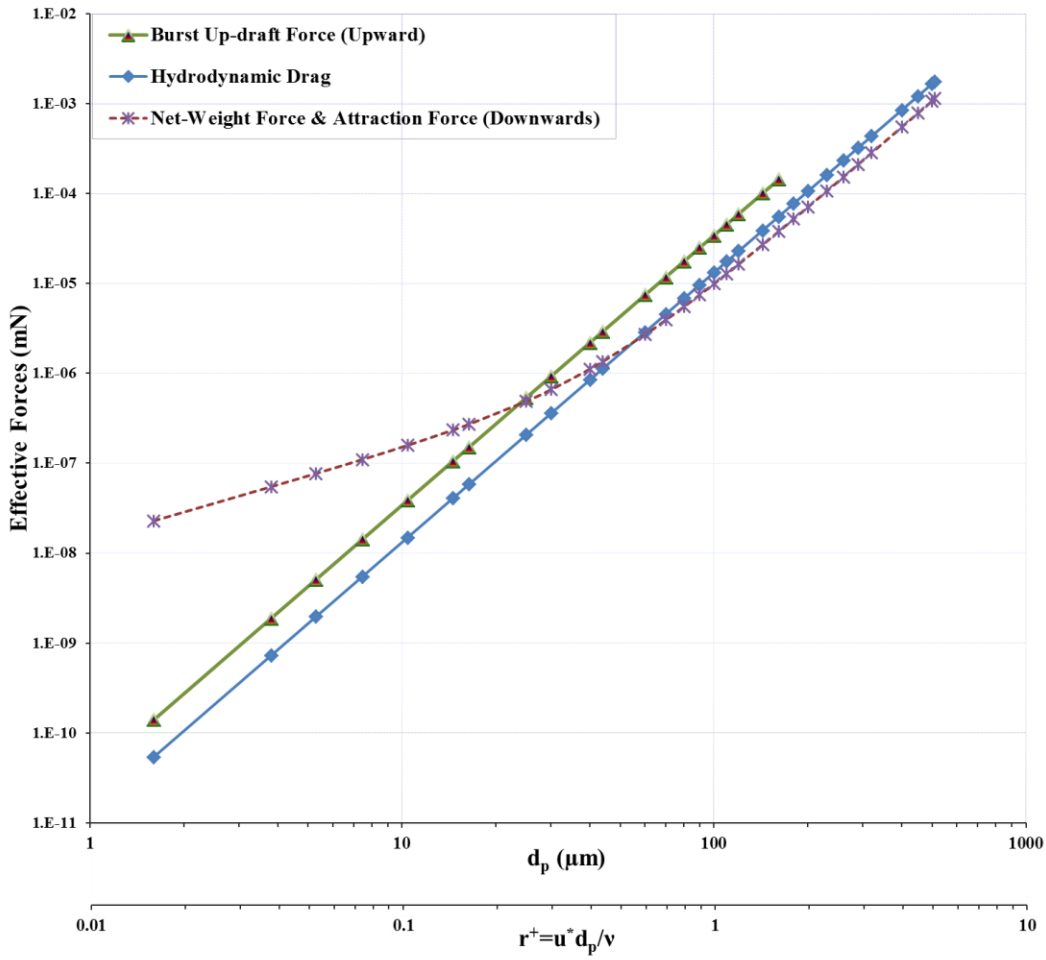

Figure 6.6 Force balance for particles at 0.34 m/s velocity (*Re* = 34,537)

In Figure 6.7, which is for the velocity 0.39 m/s (*Re* = 39,616), the upward force, updraft under a burst, overcomes the downward forces for particles larger than 20

μm. Comparisons of the force balances on particles for three different velocities reveal that, as the average flow velocity increases, the removal of particles from the bed load shifts to smaller particles. Another observation from the comparisons is that, as the velocity increases, the magnitude of the updraft under a burst in the affected area increases compared to the hydrodynamic drag force.

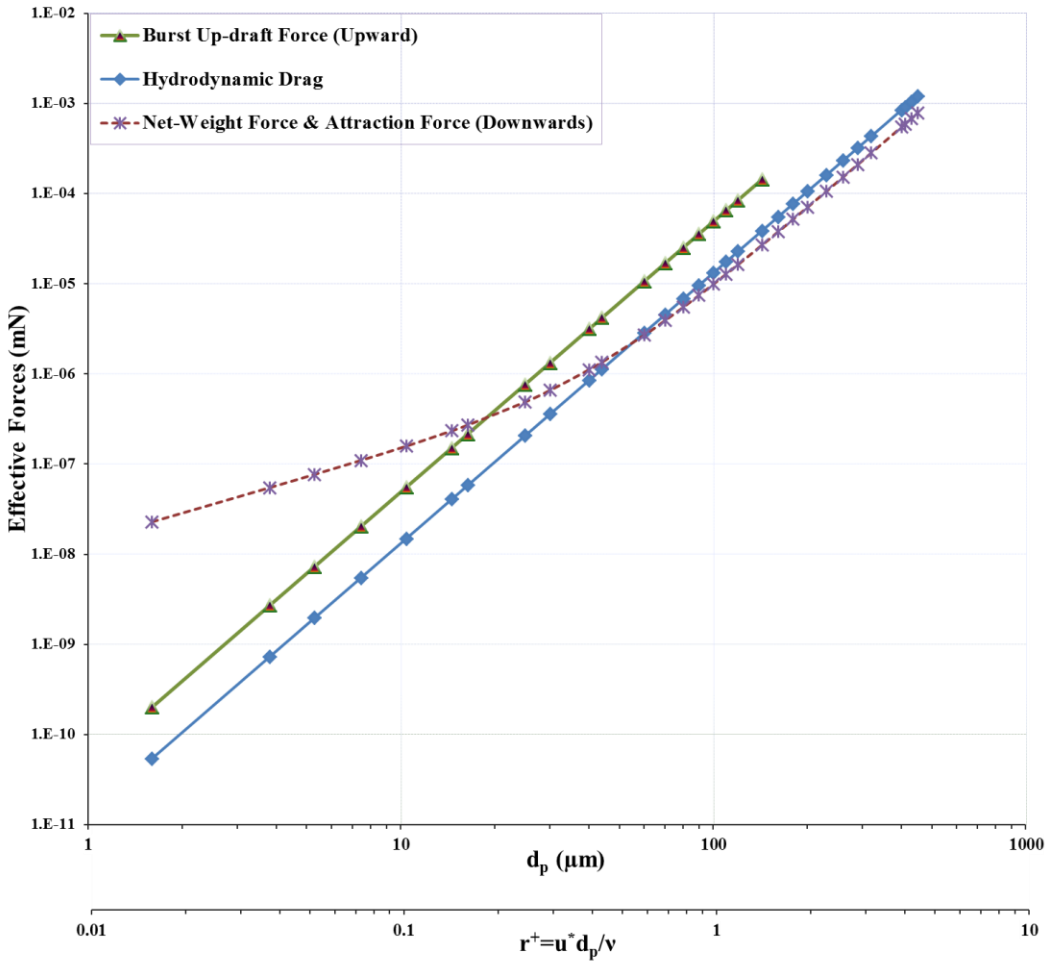

Figure 6.7 Force balance for particles at 0.39 m/s velocity (*Re* = 39,616)

6.3 Experimental Program

An experimental study is conducted to investigate the shift in particle size distribution of a broad range of particle sizes in slurry pipeline transportation. The test facilities and the methodology are described in the sections that follow.

6.3.1 Test Facilities

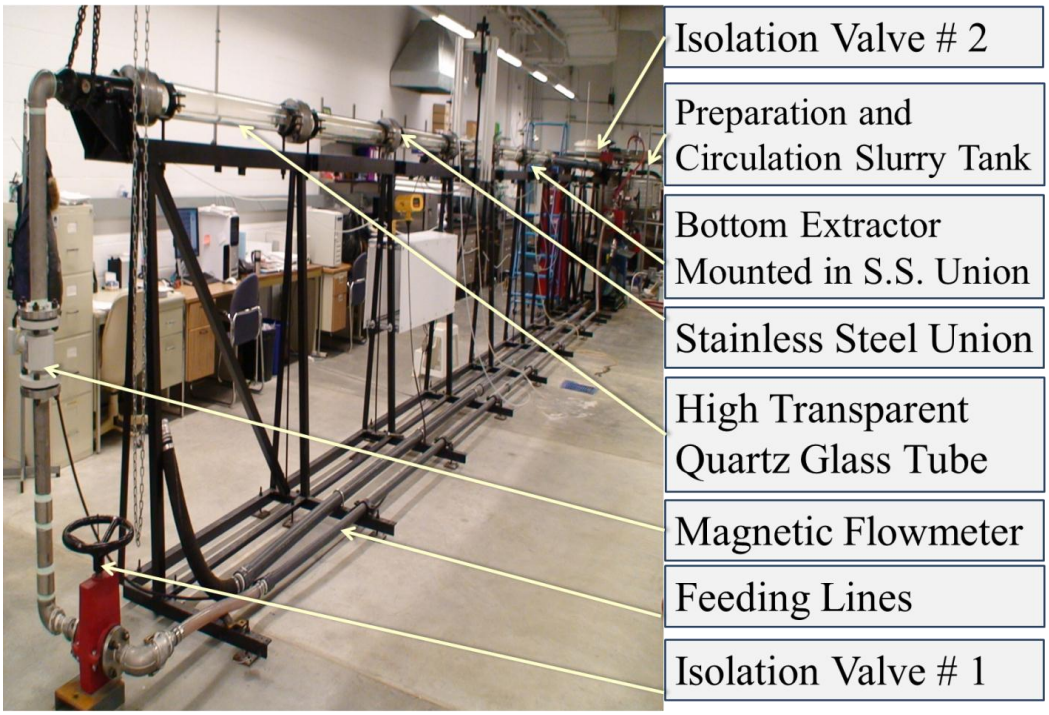

Figure 6.8 Flow system for experiments, with relevant components identified

The slurry flow loop shown in Figure 6.8 was used to conduct all experiments. The experimental rig was equipped with a slurry preparation and circulation tank, agitator, baffle plates inside the tank, centrifugal pump with a VFD drive motor,

bypass line, pressure relief line, various feed lines, isolation valves, bottom extractors, differential pressure transducers, magnetic flowmeter, temperature transmitter, barometer, PIV setup, and LabView software to record the experimental data. The loop was built using transparent glass with 95-mm ID. It is approximately 15 m long and levels off about 1.8 m above the floor.

Figure 6.9 displays a closeup view of the pinch valve located near the end of the loop, before the tube empties into the circulation tank. This valve is closed when the experimental section needs to be isolated from the rest of the loop in order to give sufficient time for particles to be deposited at the bottom.

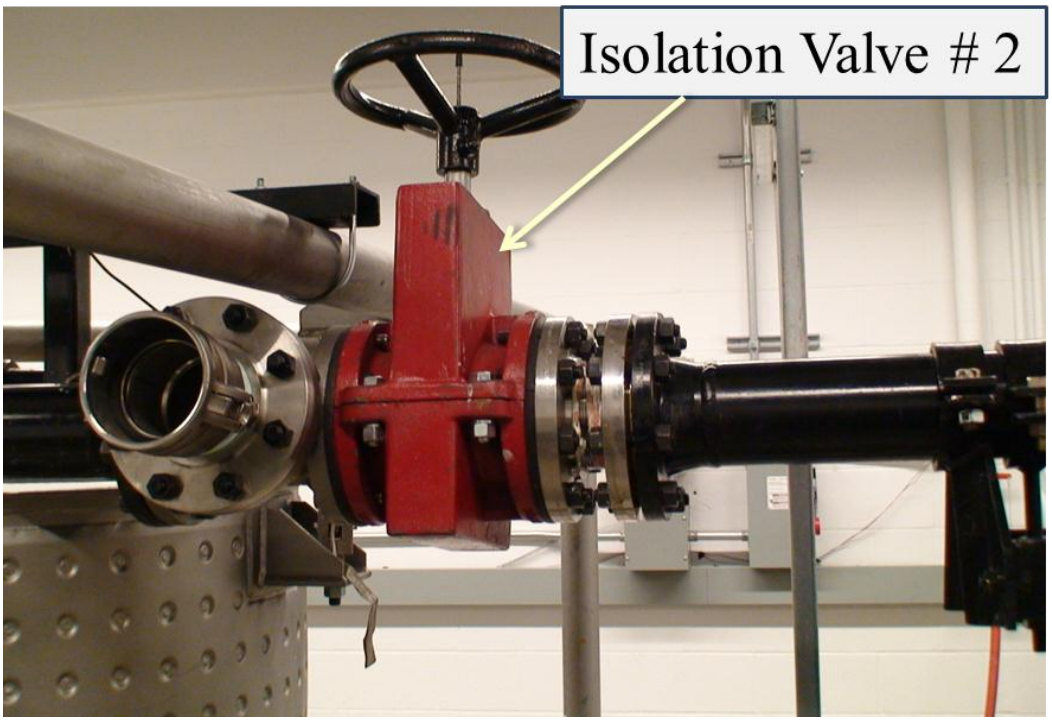

Figure 6.9 Closeup view of isolation valve number 2

Figure 6.10a shows the bottom extractor used to extract samples from the bed load. The bottom extractor is housed in a stainless steel union with smooth inner side. These unions are custom made and have the same ID as the glass pipe. Figure 6.10b shows the apparatus for taking samples for PSD analysis. The hose from the bottom extractor is connected to a vacuum flask and the flask is connected to a vacuum pump. To obtain a sample from the bed, the bottom extractor valve is opened and the vacuum pump is started simultaneously. The bottom bed sample is drawn into the vacuum flask. After extraction, the sample is dried and prepared for analysis.

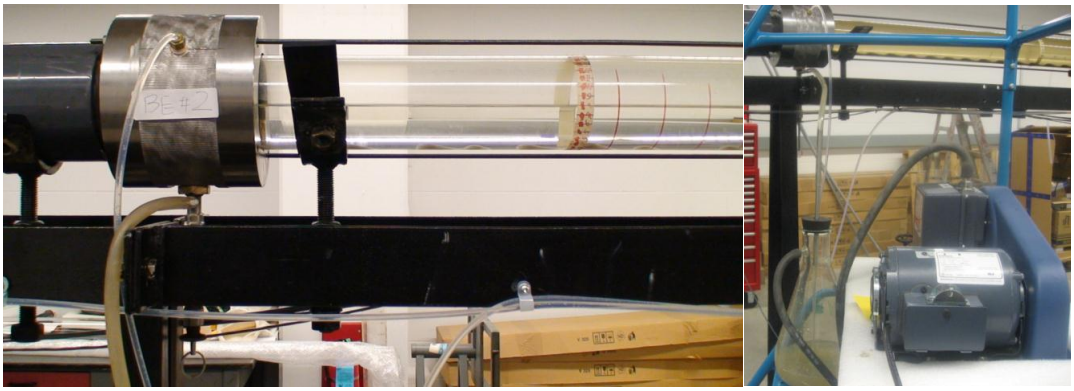

Figure 6.10 (a) Bottom extractor used for extracting samples from the bed load; (b) bed extraction apparatus

Figure 6.11 shows the inside of the preparation and recirculation tank. Baffles are placed inside the tank to break up vortices during preparation and circulation to avoid drawing air into the system. A micron filter bag of the type used for purification in environmental engineering is placed inside the stainless steel collar

to capture particles returning from the experimental section. Thus, the particles are shunted to re-enter the experimental section with the recirculating fluid flow. In this way, even though the flow loop is a closed system, it operates similarly to the open loop.

Figure 6.11 Micron-rated filter bag in the return line, to capture particles during circulation

Figure 6.12 shows the pumping section of the experimental rig. The pump has suction and discharge lines as illustrated in the image. Both lines have large cross-sectional areas that allow particle deposition even at elevated flow rates. The discharge line has a larger cross section than the suction line. After each experiment, both lines were cleaned and all deposited particles were removed to

prevent already-deposited particles from affecting new experiments. The entire experimental rig was then washed a few times.

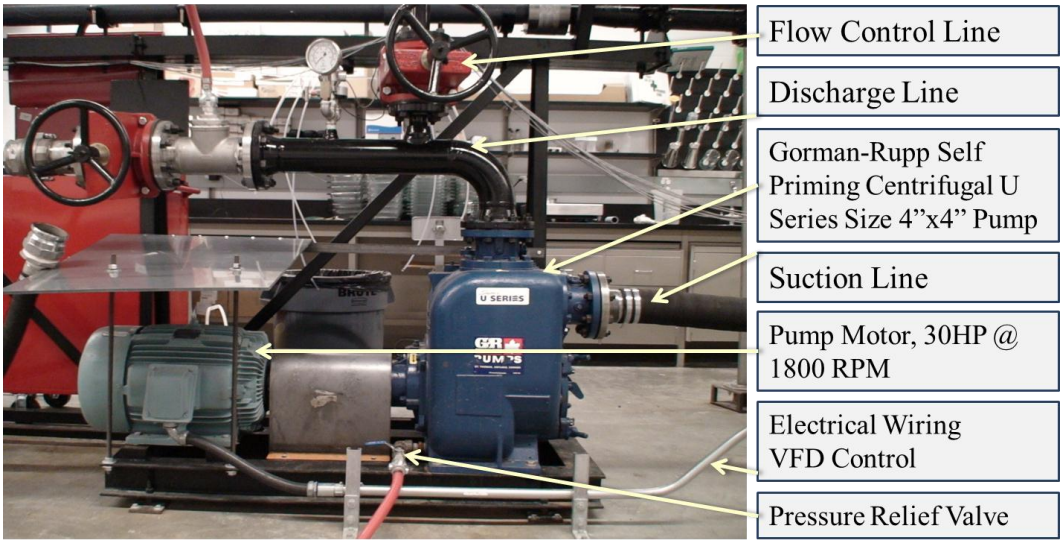

Figure 6.12 Pump and electric motor assembly for the flow loop – particles accumulated in both the suction and discharge sections of the pump assembly

The experimental setup consisted of several instruments, including temperature transmitter, pressure transmitters, differential pressure transducers, load cells, and a variable frequency device (VFD), all hooked up to LabView as shown in Figure 6.13. LabView displays and records all measured parameters; it can also control the pump via the VFD. Some instruments in this setup were part of a two-way communication system and others were used only for transmitting command signals and operating data to LabView.

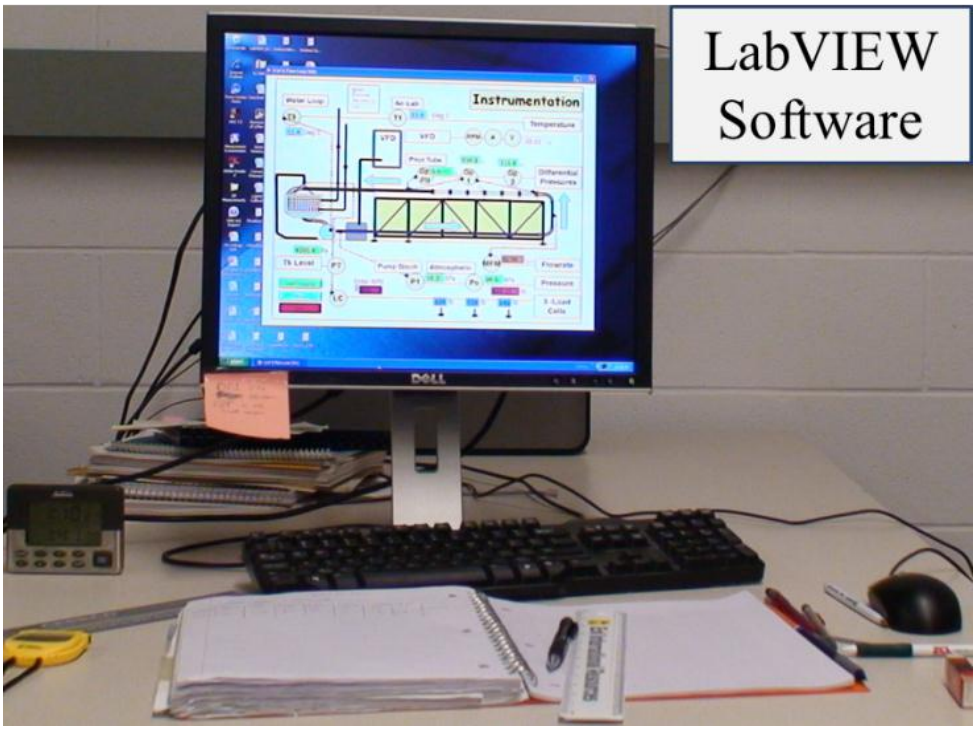

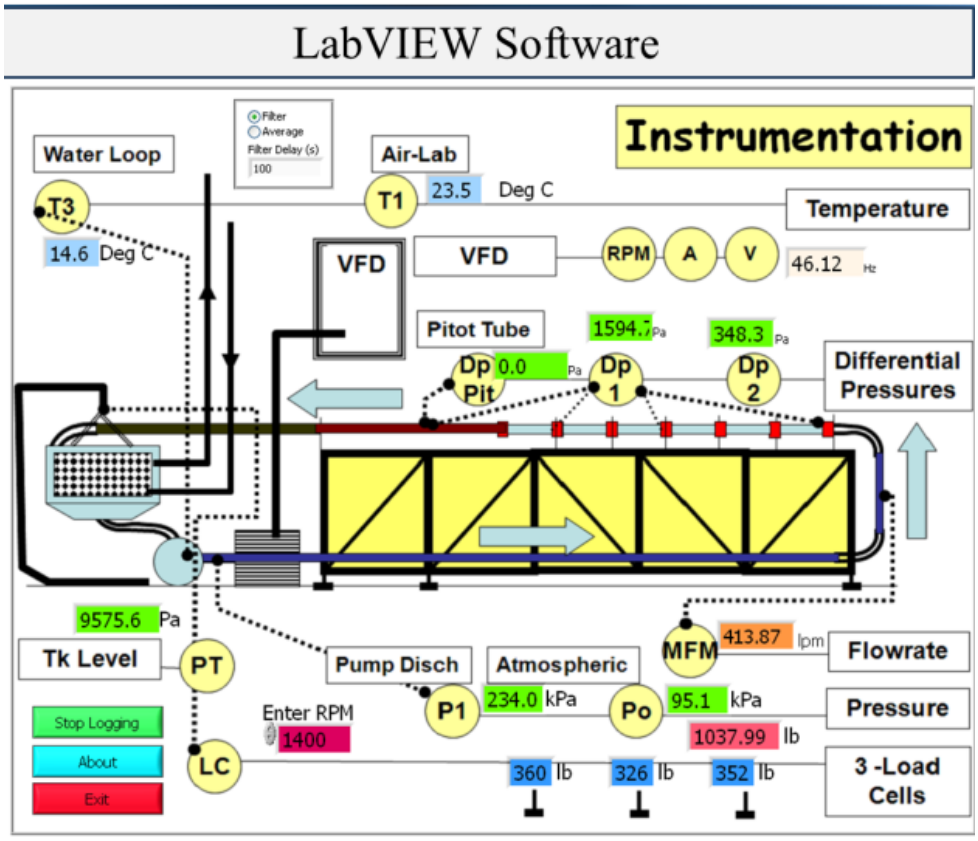

Figure 6.13 LabView software used for analysis, logging, and display of experimental data

After the samples were oven-dried, detailed image analysis of the dry samples was performed to quantify the shift in the PSD. PSD analysis was carried out using an automated image analyzer, Leica DM6000M, shown in Figure 6.14. The automated image analyzer comes with a motorized focus-drive microscope, a Leica DFC camera mounted on top of the microscope, a Leica Materials Workstation, and QParticles analysis software. Using the motorized stages, the sample slide can be easily moved in the x, y, and z directions and, if needed, the location of the specimen can be reproduced in terms of those coordinates. Providing reliable specimens for PSD analysis is tricky, and care is needed to make sure that the specimen represents the whole sample. After each analysis, parameters are extracted and archived that consist of a variety of information items for each scanned image including length, breadth, roundness, aspect ratio, equivalent diameter, and many others.

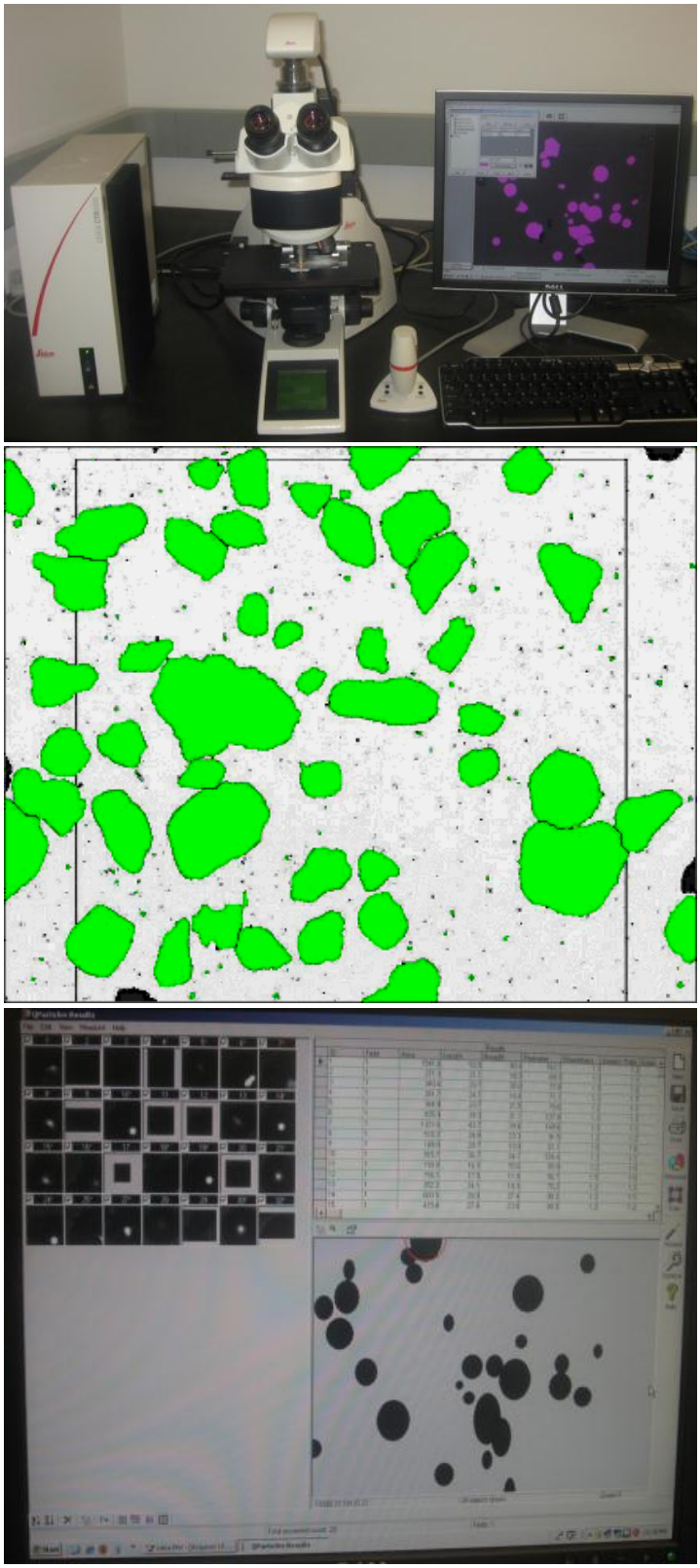

Figure 6.14 Automated PSD analyzer – Leica DM6000M with a movable stage with scanning capability in the x y, and z directions using variable scan patterns

6.3.2 Experimental Methodology

Materials used for the experiments were glass beads from Potters Industries Inc. and mineral blasting sands from Sil Industrial Minerals, both with specific gravity of 2.63. The manufacturers' specifications of the glass beads and blasting sands are given in Table 6.2.

Table 6.2
PSD of glass beads and silica sands for the experiments

Name	Mean value (µm)	10% finer than (µm)	50% finer than (µm)	90% finer than(µm)
GBs 6000A	7	3	8	15
GBs 4000	20	5	18	45
GBs 3000	35	18	35	60
GBs 2429	83	72	83	99
GBs 2024	156	125	151	192
Silica 50-80	237	177	235	297
Silica 40-70	315	210	311	425

In order to analyze shifts in particle size distribution (PSD), twelve experiments were completed at three different velocities, 0.24 m/s, 0.34 m/s, and 0.39 m/s (all well below the critical removal velocity). Four different experiments were conducted at each velocity based on particle size ranges and force balance categorized as Phillips domain (d_p < ~ 60 µm), intermediate domain, Shields domain (d_p > ~ 170 µm), and mixed domain (poly-sized particles). Since most deposits in slurry pipelines are ripples or dune-like patterns, we attempted to produce a dune-like slurry flow pattern. Previous experience revealed that, with

dilute slurry, it is possible to have a dune-like slurry flow pattern with discrete and continuous dunes at slurry concentrations below 1 vol%. All slurries used for the experiments were prepared with the glass beads and sand particles at room temperature and 0.3 vol% concentration. The experimental procedure is presented graphically in Figure 6.15 and described as follows:

- Wash and thoroughly clean the whole system to remove any deposits and rust before slurry preparation.

- Add 500 L of water to the system and, while the tank agitator is running, gradually increase the flow rate. The maximum flow rate should be reached via a few steps and sufficient time should be allowed between each increment. These steps are necessary to de-bubble and de-gas the system before adding solid particles.

- While the system is operating at its maximum flow rate and with the agitator running, gradually add 4 kg of the desired particles to the tank and wait 10–20 min until a homogeneous slurry has formed in all sections of the loop.

- While shutting down the system, quickly close isolation pinch valve #2 to prevent the returning compression wave or backpressure force from creating bubbles in the upper part of the loop. Then close isolation pinch valve #1.

- Wait approximately two days so that particles of all sizes settle at the bottom of the pipeline.

- While waiting for different particle sizes to be deposited in the isolated loop, wash the non-isolated parts including the tank, pump, and feed line and, after removing all particles from these sections, fill them with water.

- Place the micron-rated filter bag on the return line to capture all particles from the deposit section returning to the tank during the experiment.

- Take a base sample before operating at the desired flow rate and then, after opening the isolation section, increase the flow rate to the desired level and perform the experiment.

- Collect samples from deposit beds using bottom extractor at specified intervals of 10, 20, 30, and 45 min of exposure to the flow. Dry the samples and prepare them for image analysis.

The methodology and procedures described above were used for all experiments. The defined experimental steps including preparation, deposition, runs, data processing, and analyses were carried out similarly for all experiments to make sure that the data were consistent from one experiment to another. The execution of each complete experiment, starting with cleaning of the loop, took 10 days on average.

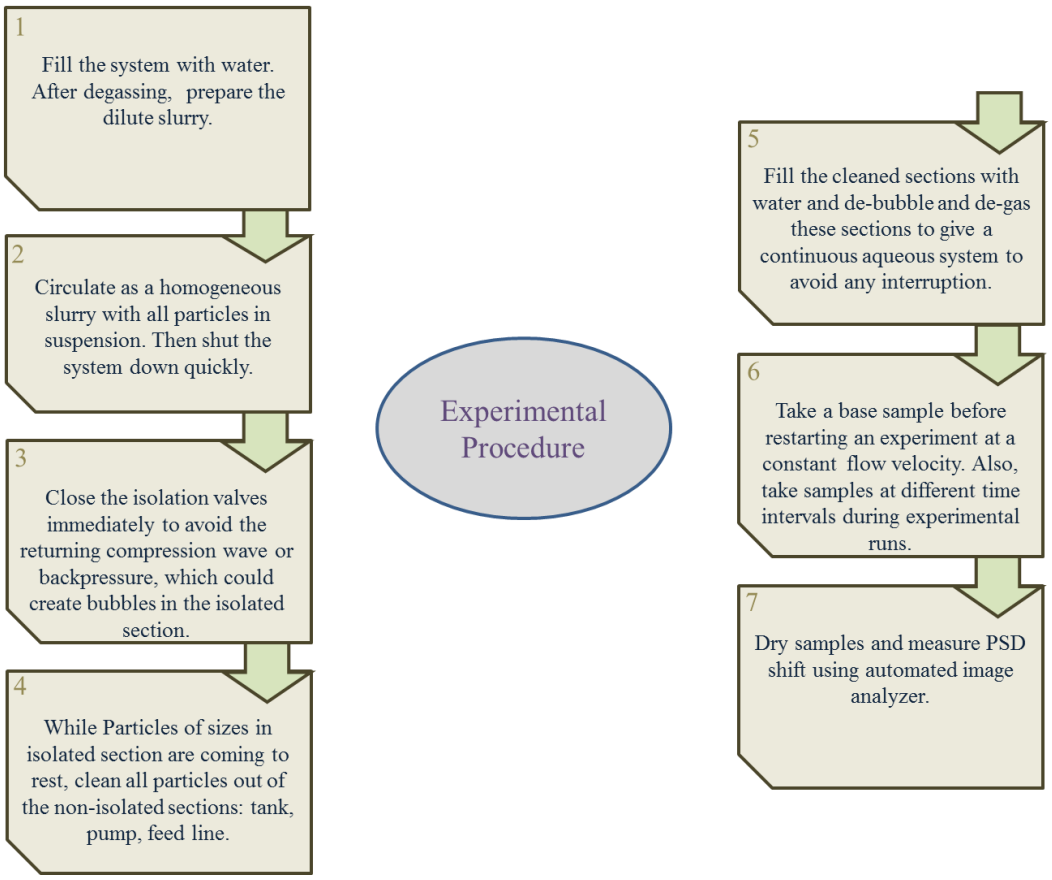

Figure 6.15 Summary of experimental procedure

Figure 6.16 illustrates schematically the sampling schedule of the experiment for 0.25 m/s flow velocity. The same procedure is repeated for each phase and for the velocities of 0.34 m/s and 0.39 m/s. The initial slurry flow was prepared at a high velocity of 1 m/s in order to ensure a homogeneous slurry. The slurry was left circulating for approximately 20 min and then the system was shut down for 2 days. After all of the particles had been deposited at the pipeline bottom, a baseline sample was taken before starting the experiments. Once the experiments

were started at the specified flow velocity, samples were taken at the time intervals shown in Figure 6.16.

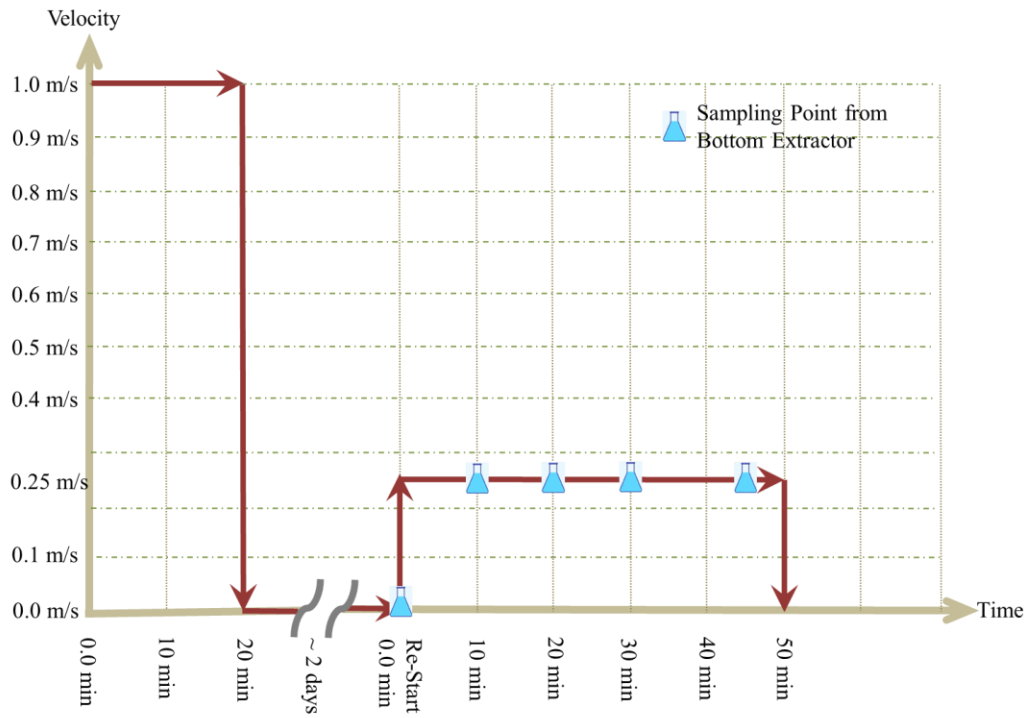

Figure 6.16 Schematic illustration of the experiment and sampling schedule

6.4 Analysis of Results

6.4.1 Phillips Domain

From the balance of forces acting on particles at 0.25 m/s (Figure 6.5), particles smaller than 40 μm have a strong attraction force such that the lifting forces cannot levitate the particles. The experiment was conducted to examine the effects of different forces and turbulent flow on particle detachment and removal from

the particle bed. Figures 6.17a–6.17d show the experimental PSD results for shifts in Phillips domain PSD following exposure to flow at an average velocity of 0.25 m/s for 10, 20, 30, and 45 min. The PSD in the deposit shifts towards smaller particles over time because the effective lifting force for this range of particles, which is an updraft under a burst, cannot overcome the attraction force.

The experimental results reveal that even the balance of forces suggests that particles larger than 40 μm should be removed; however, it appears that the magnitude of the attraction force for the 0.25 m/s velocity was greater than expected. Therefore, in these experiments, the concentration of particles smaller than approximately 45–49 μm is higher than the original concentration. The concentration of smaller particles increases with exposure to the flow. The coherent structures of a burst cycle near the wall in turbulent flow remove particles from the deposit bed. Theoretical calculations based on the force balance suggested that particles larger than 40 μm should be lifted (Figure 6.5). However, the experimental results show that the concentration of particles smaller than ~50 μm increases; in other words, only particles larger than ~50 μm are lifted. Hence, the burst activity takes particles larger than ~50 μm from the interface and over the burst activity (over the exposure to the turbulent flow) the concentration of larger particles decreases and the concentration of smaller particles increases accordingly.

Figure 6.17a shows the shift of the PSD toward smaller sizes compared to the original PSD for the Phillips domain sample collected following 10 min exposure

to flow at 0.25 m/s. The concentration of particles smaller than 45 µm increases and, hence, the concentration of particles larger than 45 µm decreases.

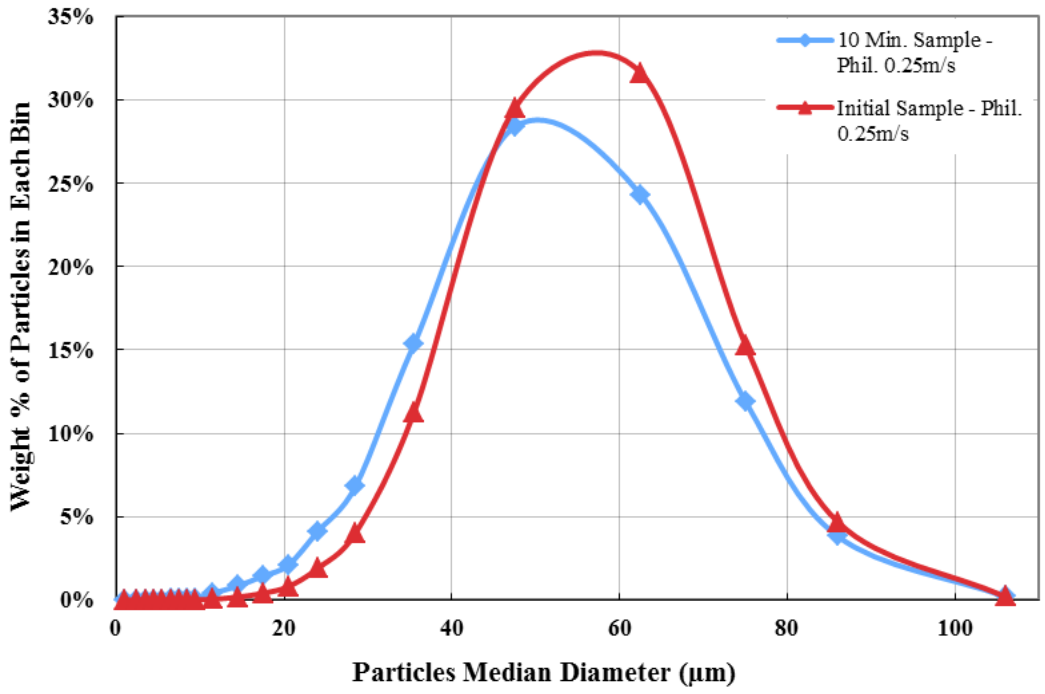

Figure 6.17a PSD of Phillips domain after 10 min flow at 0.25 m/s

Figure 6.17b depicts the PSD shift in the Phillips domain sample following 20 min exposure to flow at 0.25 m/s. The concentration of particles smaller than 49 µm increases and, consequently, the concentration of particles larger than 49 µm decreases.

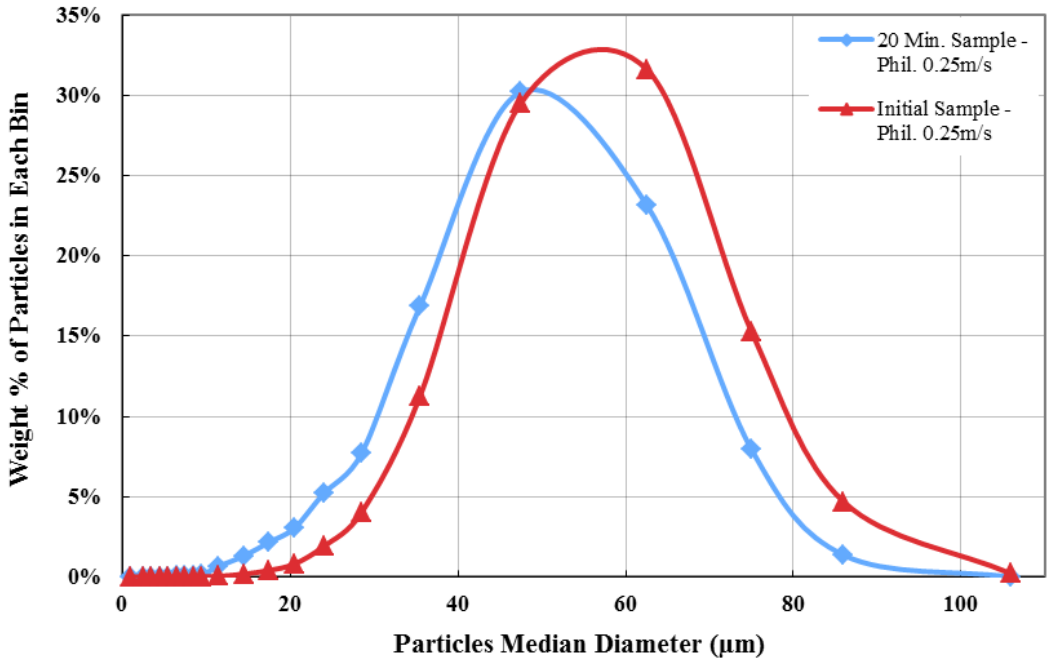

Figure 6.17b PSD of Phillips domain after 20 min flow at 0.25 m/s

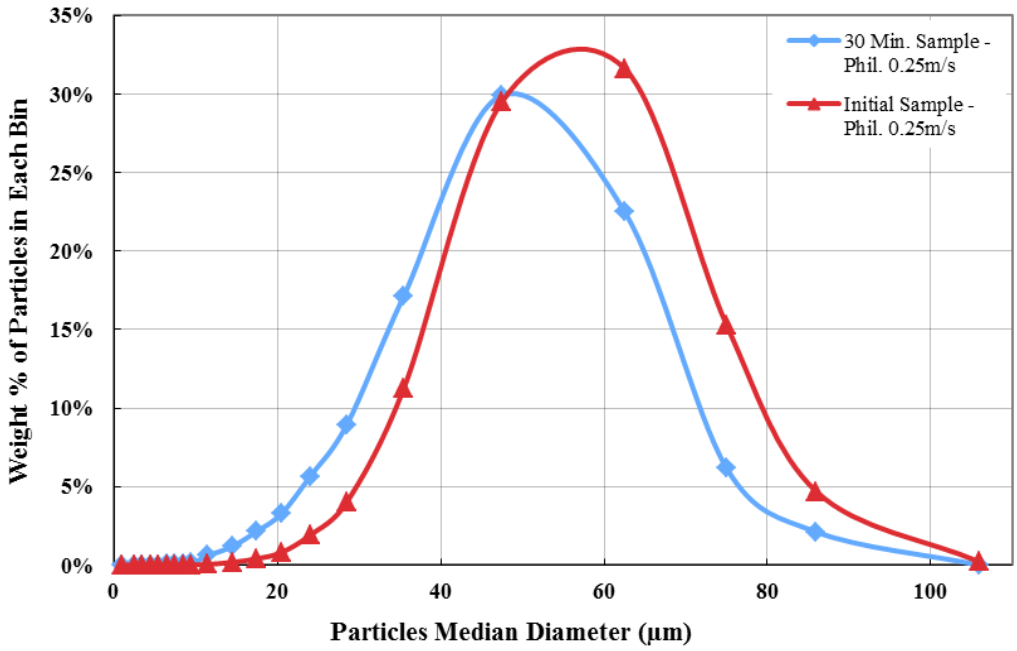

Figure 6.17c PSD of Phillips domain after 30 min flow at 0.25 m/s

The PSD shift for the Phillips domain sample collected following 30 min exposure to flow at 0.25 m/s is presented in the Figure 6.17c. The concentration of particles smaller than 48 µm increases and, consequently, the concentration of particles larger than 48 µm decreases.

The PSD shift in the Phillips domain sample following 45 min exposure to flow at 0.25 m/s is shown in Figure 6.17d. The similar to 10, 20, and 30 minutes experimental results concentration of particles smaller than 45 µm increases and, as a result, the concentration of particles larger than 45 µm decreases.

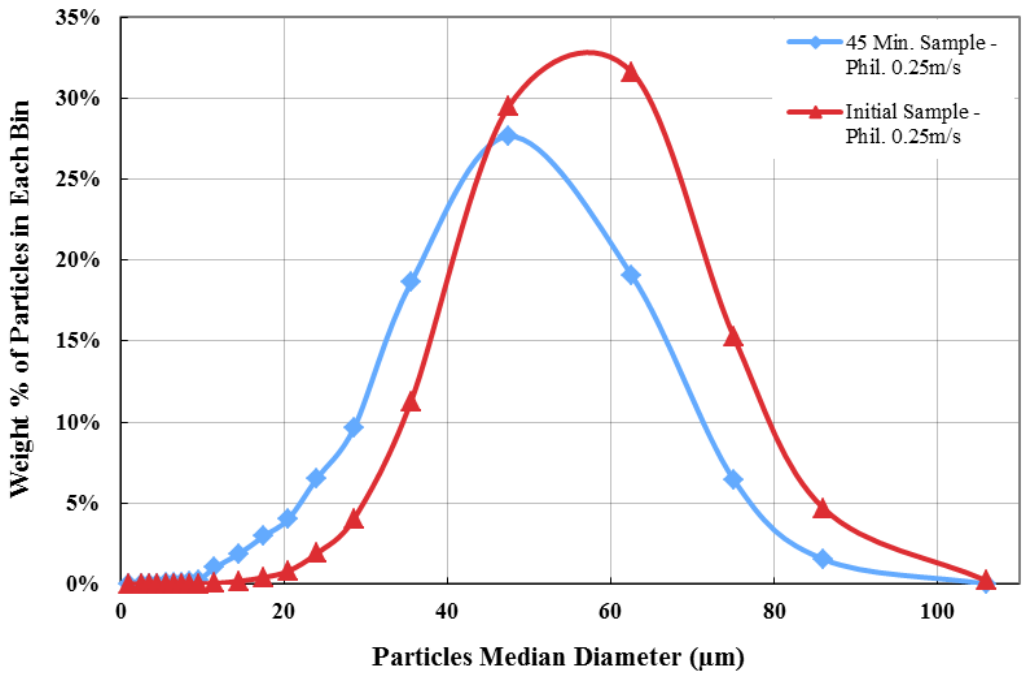

Figure 6.17d PSD of Phillips domain after 45 min flow at 0.25 m/s

The results of experiments conducted at 0.34 m/s velocity for the Phillips domain following exposure to the flow for specific periods are shown in Figures 6.18a–6.18d, along with the initial PSD of the deposit. Again, theoretical calculation based upon the force balances for the 0.34 m/s velocity (see Figure 6.6) indicates that particles larger than 25 μm are removed by updraft under a burst force. The experimental results demonstrate that the concentration of smaller particles increases from the original PSD. The burst activity carries away particles larger than around 31–37 μm and hence the concentration in this range decreases with time of exposure to the flow; accordingly, the percentage of smaller particles increases. The experimental results agree somewhat with the predictions from force balance analysis, except that the attraction force is stronger than calculated.

Figure 6.18a depicts shift of the PSD in the Phillips domain from that of the original deposit following 10 min exposure to flow at 0.34 m/s. The concentration of particles smaller than 37 μm increases while particles larger than 37 μm are lifted out of the bed.

The shift in the PSD following 20 min of exposure to flow at 0.34 m/s is illustrated in Figure 6.18b for the Phillips domain. The concentration of particles smaller than 31 μm increases and, hence, the concentration of the particles larger than 31 μm decreases.

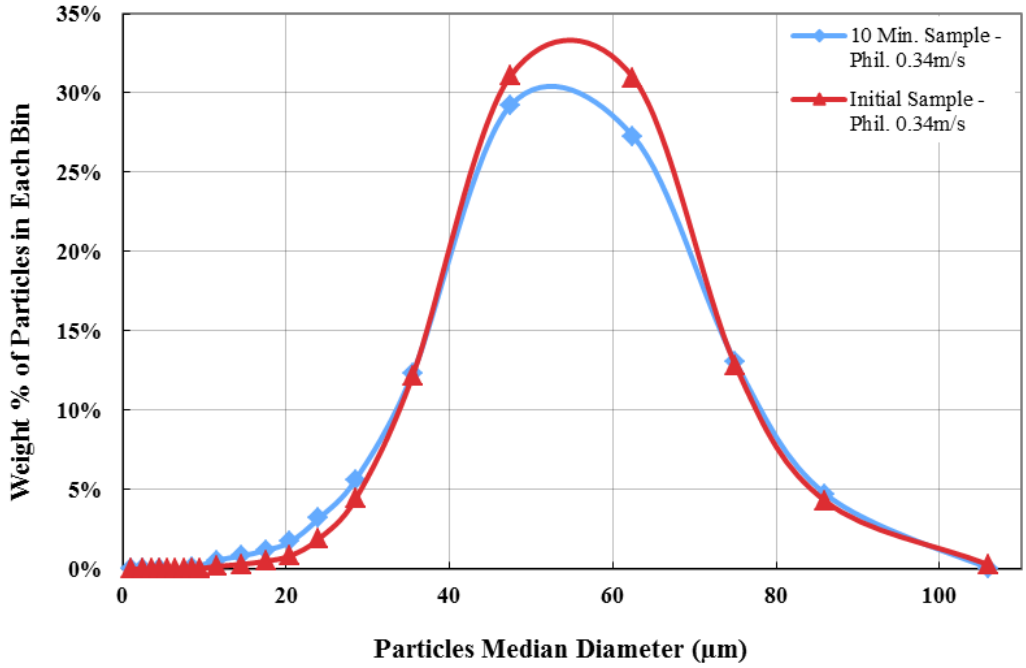

Figure 6.18a PSD of Phillips domain after 10 min flow at 0.34 m/s

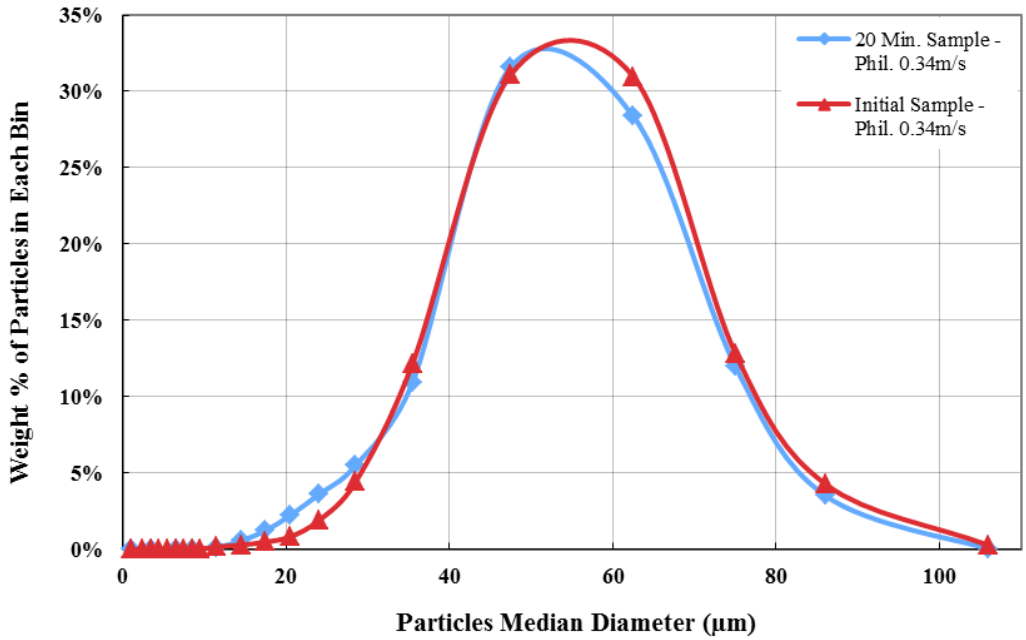

Figure 6.18b PSD of Phillips domain after 20 min flow at 0.34 m/s

The results for the sample from the Phillips domain 30 min after the start of the experiment for the 0.34 m/s velocity are shown in Figure 6.18c. The weight percentage of particles smaller than 32 µm goes up and, as a result, the percentage of particles larger than 32 µm decreases.

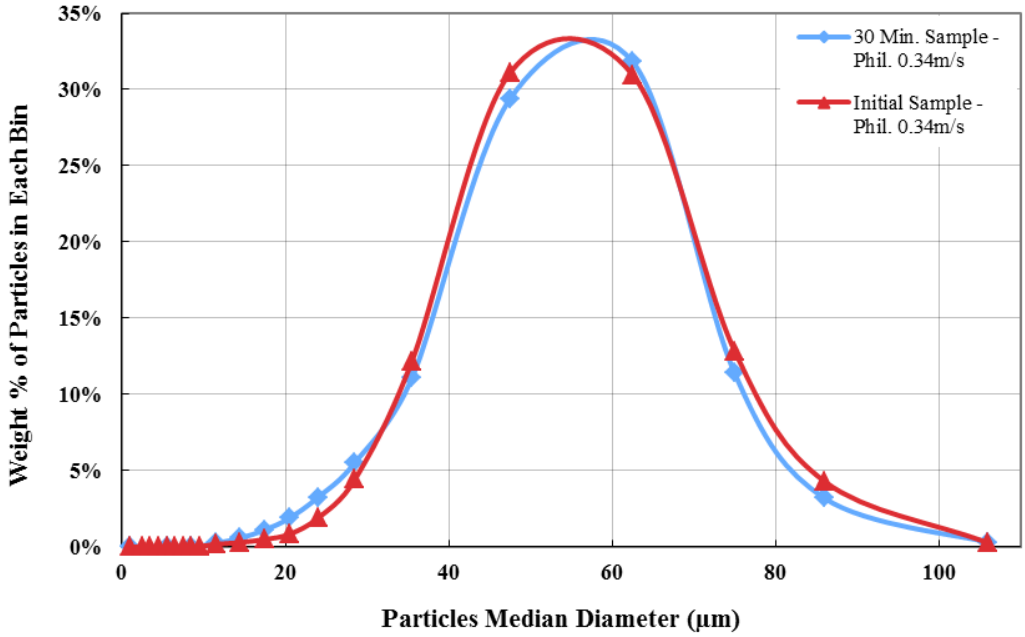

Figure 6.18c PSD of Phillips domain after 30 min flow at 0.34 m/s

Figure 6.18d shows the shift in PSD after 45 min exposure to flow at 0.34 m/s for the Phillips domain. The concentration of particles smaller than 31 µm increases and, consequently, the concentration of larger particles is reduced.

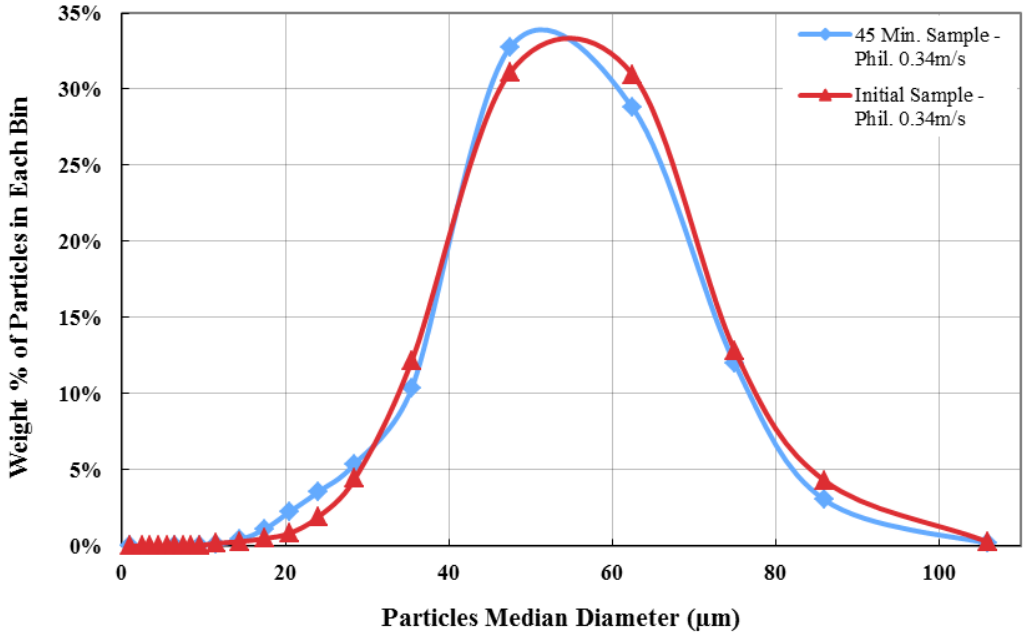

Figure 6.18d PSD of Phillips domain after 45 min flow at 0.34 m/s

The PSD analyses for the Phillips domain at 0.39 m/s are given in Figures 6.19a–6.19d. The force balance suggests that particles larger than 20 µm will be removed (see Figure 6.7). The experiment results show that the updraft under a burst force removes particles larger than around 32–37 µm. As the force balance indicates, particle removal by the lift force increases the concentration of particles larger than 32–37 µm in the deposit bed.

Figure 6.19a illustrates the PSD results for the sample collected after 10 min exposure to flow at 0.39 m/s for the Phillips domain. The weight percentage of particles up to 36 µm in diameter increases while the percentage of particles larger than 36 µm is reduced.

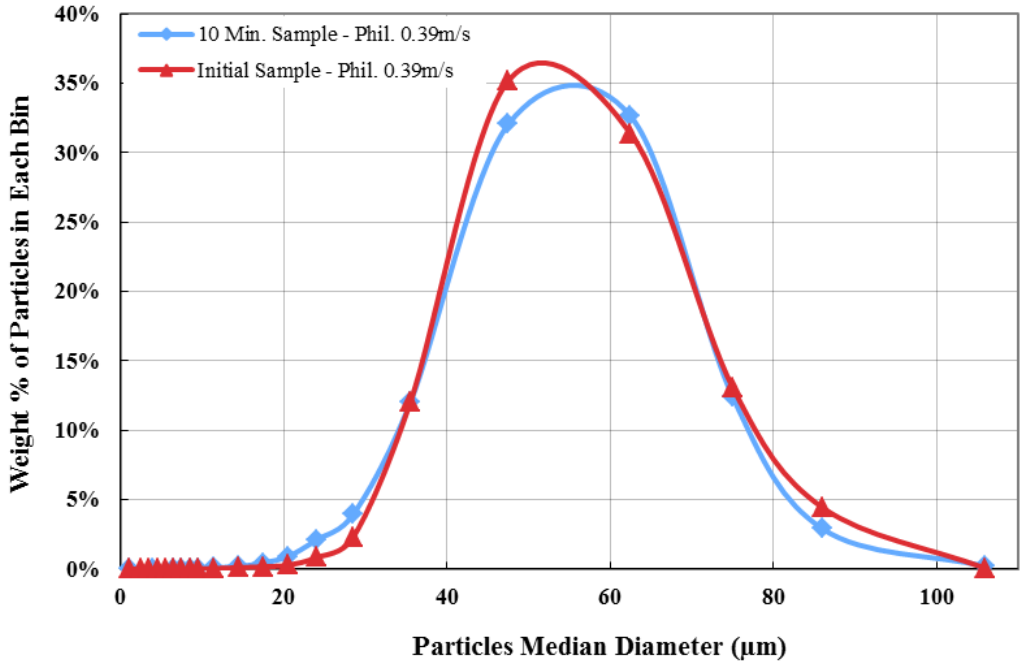

Figure 6.19a PSD of Phillips domain after 10 min flow at 0.39 m/s

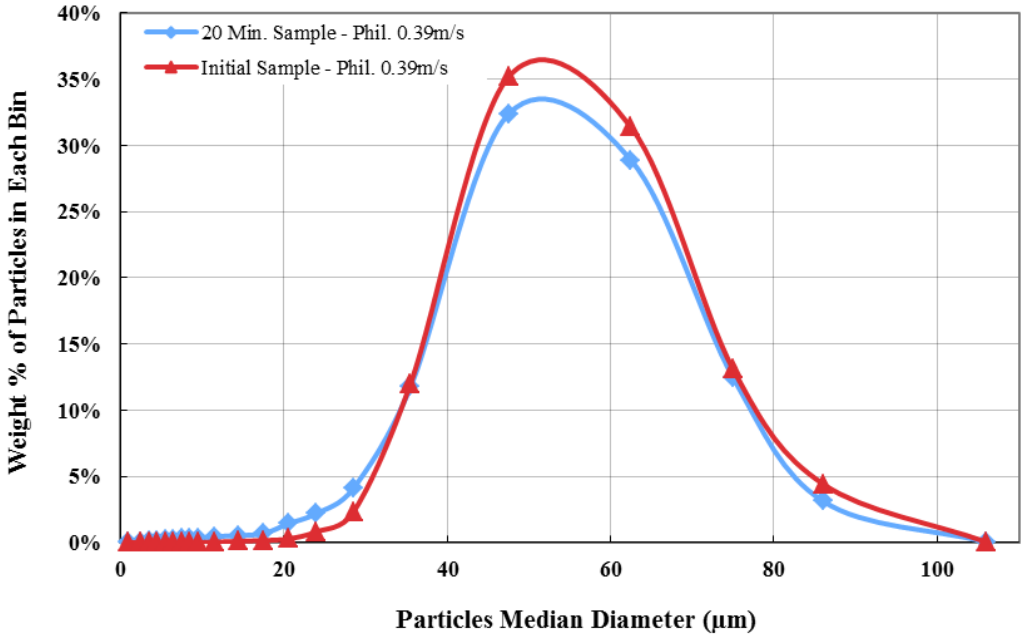

Figure 6.19b PSD of Phillips domain after 20 min flow at 0.39 m/s

The results for 20 min exposure to flow at 0.39 m/s for the Phillips domain are shown in Figure 6.19b. As expected, the concentration of particles smaller than 36 µm increases.

Figure 6.19c shows the results for the Phillips domain sample following 30 min exposure to flow at 0.39 m/s. The concentration of particles smaller than 37 µm increases and, hence, the concentration of larger particles is reduced.

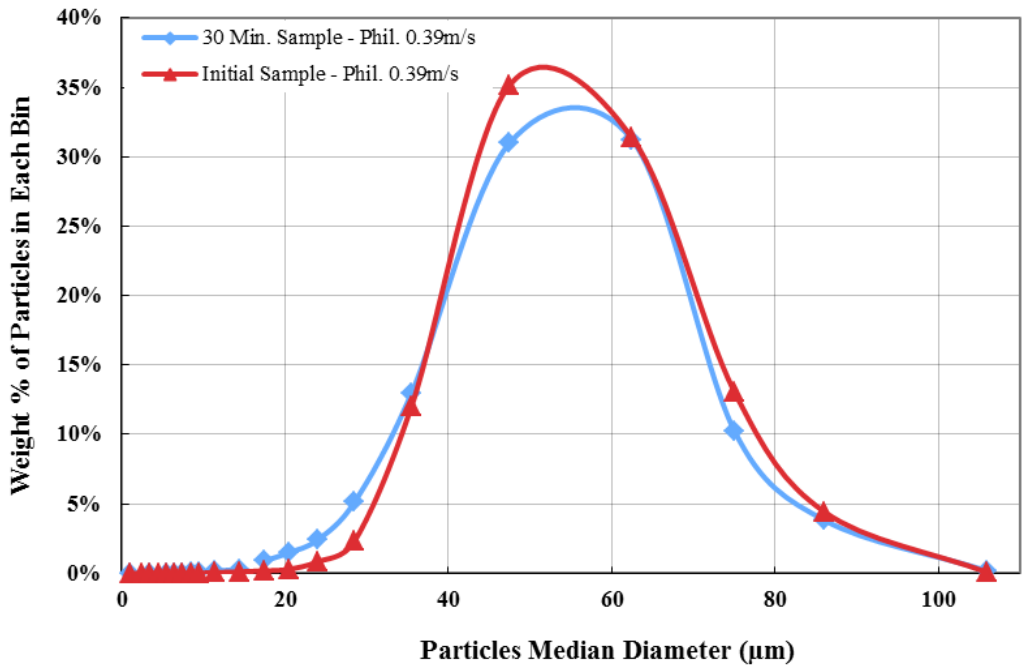

Figure 6.19c PSD of Phillips domain after 30 min flow at 0.39 m/s

The results for the Phillips domain sample following 45 min of exposure to flow at 0.39 m/s are given in Figure 6.19d. Again, because of the dominant attraction force, the concentration of particles smaller than 32 µm increases and, as a result, the concentration of particles larger than 32 µm is reduced.

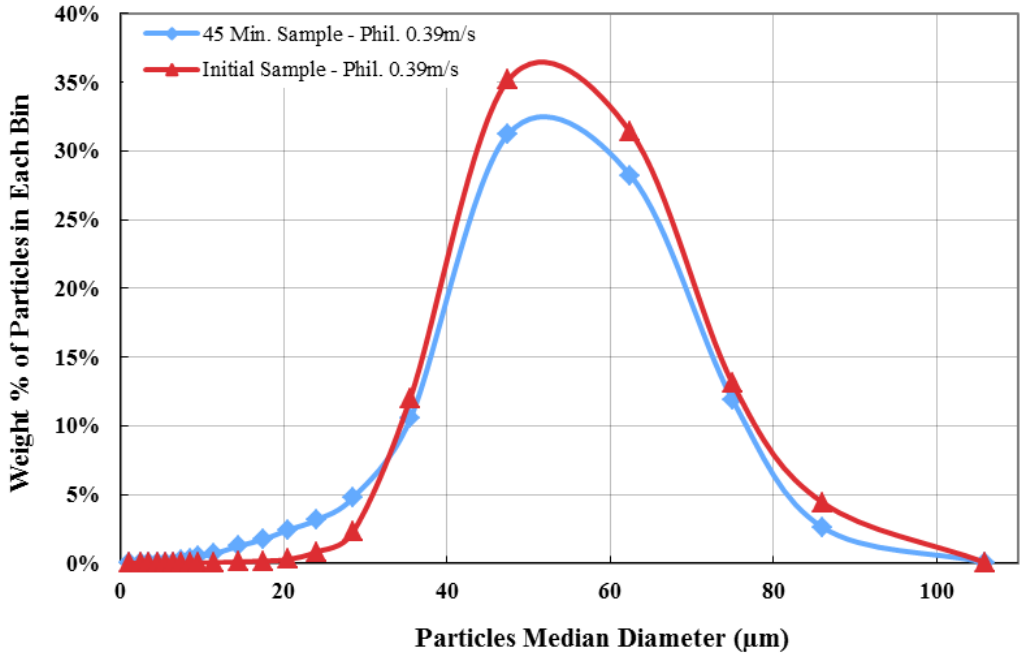

Figure 6.19d PSD of Phillips domain after 45 min flow at 0.39 m/s

The Phillips domain experimental results reveal that for increasing times of exposure to flow at the three velocities of 0.25, 0.34, and 0.39 m/s, the mass concentrations of fine particles in the deposits increase compared to the initial sample as coarser particles are selectively removed. In other words, the relative concentration of fine particles (the area between the PSD curves on the left side of the graphs) has an increasing trend with increased exposure to flow for the durations tested.

The reductions in the concentrations of larger particles compared to those in the initial sample (the area between the PSD curves on the right side of the graphs) increases with increasing duration of exposure to flow.

The effect of increasing velocity (below critical removal velocity) for the Phillips domain experiments is to shift the PSD towards smaller particle sizes as expected from the force balances of particles for different velocities. In the experiments at 0.25 m/s, particles larger than 45–49 μm are lifted; in the experiments at 0.34 m/s, particles larger than 31–37 μm are lifted; and in the experiments at 0.39 m/s, particles larger than 32–37 μm are lifted.

6.4.2 Intermediate Domain

For the intermediate domain, in which updraft under a burst is the force responsible for lifting the particles out of the deposit bed, experiments were carried out at three different velocities, 0.25 m/s, 0.34 m/s, and 0.39 m/s, the same as for the Phillips domain. For the 0.25 m/s flow velocity, the experimental results indicate that the concentration of particles smaller than 45–51 μm is increased (Figures 6.20a–6.20d). The lift force carries away particles up to ~ 120 μm in size; hence, their concentration in the deposit is reduced and the percentage of particles larger than ~ 120 μm is more or less the same as originally or slightly higher. The force balance, which is shown in Figure 6.5 for 0.25 m/s, is also applicable for this experiment and indicates that the lift force removes particles larger than 40 μm. The largest particles (>~ 120 μm) are probably carried away by sliding, rolling, or saltation due to the drag momentum at the surface rather than by removal into the main flow.

Figure 6.20a depicts the shift in PSD from the original PSD for the intermediate-domain experiments following 10 min exposure to flow at 0.25 m/s. There are

three regions in the intermediate experimental series (see Figure 6.29). The first region (see Figure 6.29 – Part 1) is the small-particles region (Phillips-dominated domain) and the concentration of these particles increases in this region due to strong attraction force. The second region (see Figure 6.29 – Part 2) is the dominated by the intermediate domain and the particles are lifted by updraft under a burst force, which reduces their concentration. The third region (see Figure 6.29 – Part 3) contains the larger particles, which are rolled or moved by saltation and their concentration is increased as the intermediate domain particles are lifted out of the bed. In the Phillips-dominated region, the mass concentration of particles up to 45 µm increases, accompanied by a reduction of particle concentrations in the size range from 45 to 108 µm and an increase in the concentration of particles larger than 108 µm.

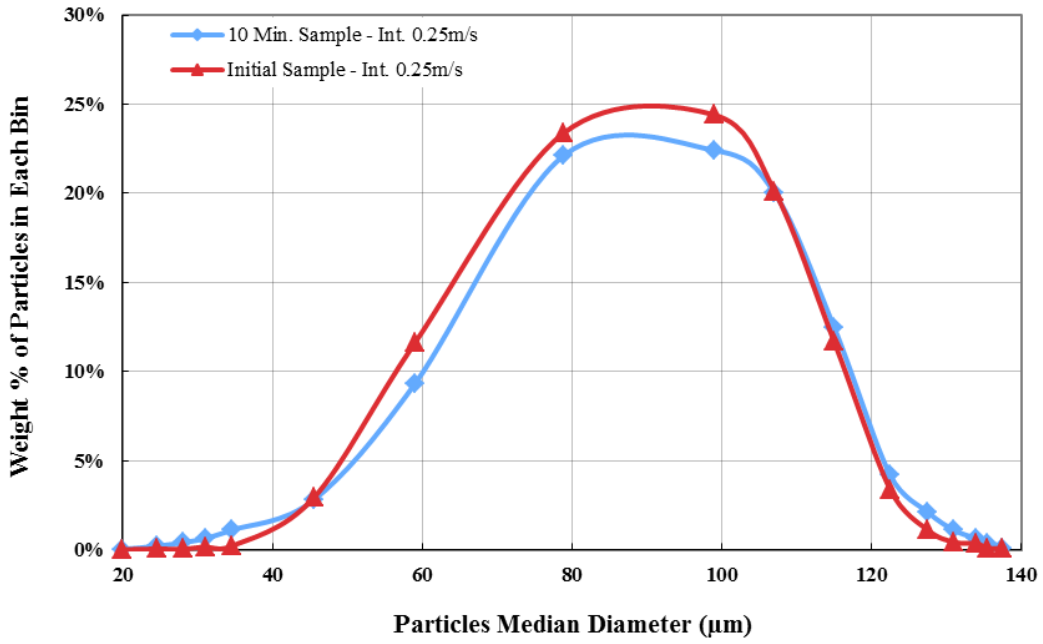

Figure 6.20a PSD of intermediate domain after 10 min flow at 0.25 m/s

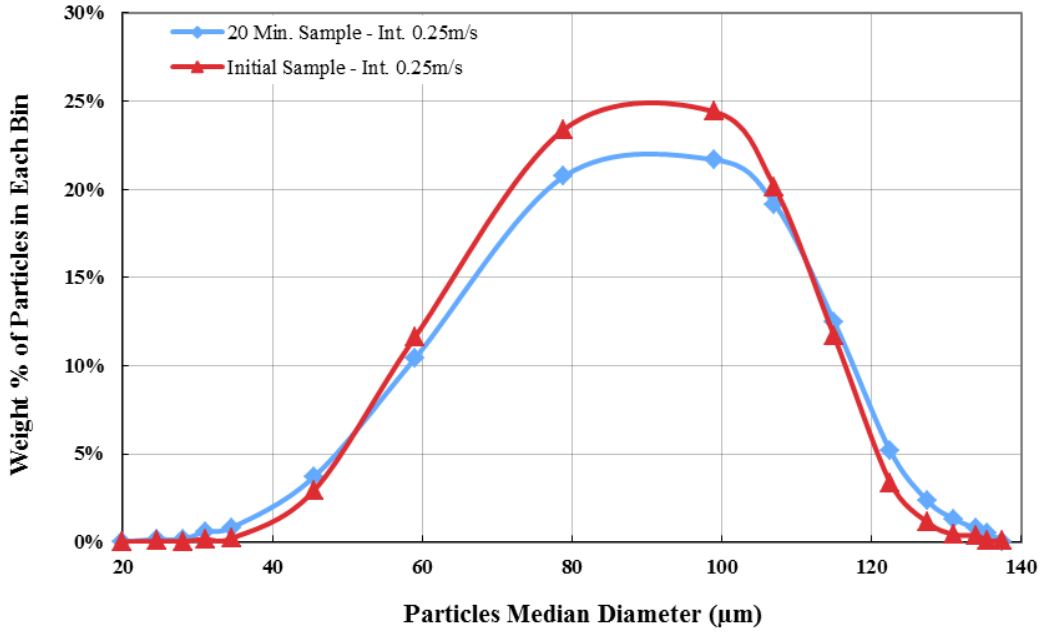

Figure 6.20b PSD of intermediate domain after 20 min flow at 0.25 m/s

The measured PSD of the intermediate-domain sample taken following 20 min exposure to flow at 0.25 m/s is shown in Figure 6.20b along with the PSD of the initial sample. The concentration of particles smaller than 51 µm increases, the concentration of particles in the second region from 51 to 112 µm is reduced, and, consequently, the concentration of particles larger than 112 µm increases.

Figure 6.20c presents the PSD results for intermediate-domain sample collected following 30 min exposure to flow at 0.25 m/s. The concentration of particles up to 51 µm in diameter increases, the concentration of particles from 51 to 122 µm in size is reduced, and, hence, the concentration of particles larger than 122 µm increases.

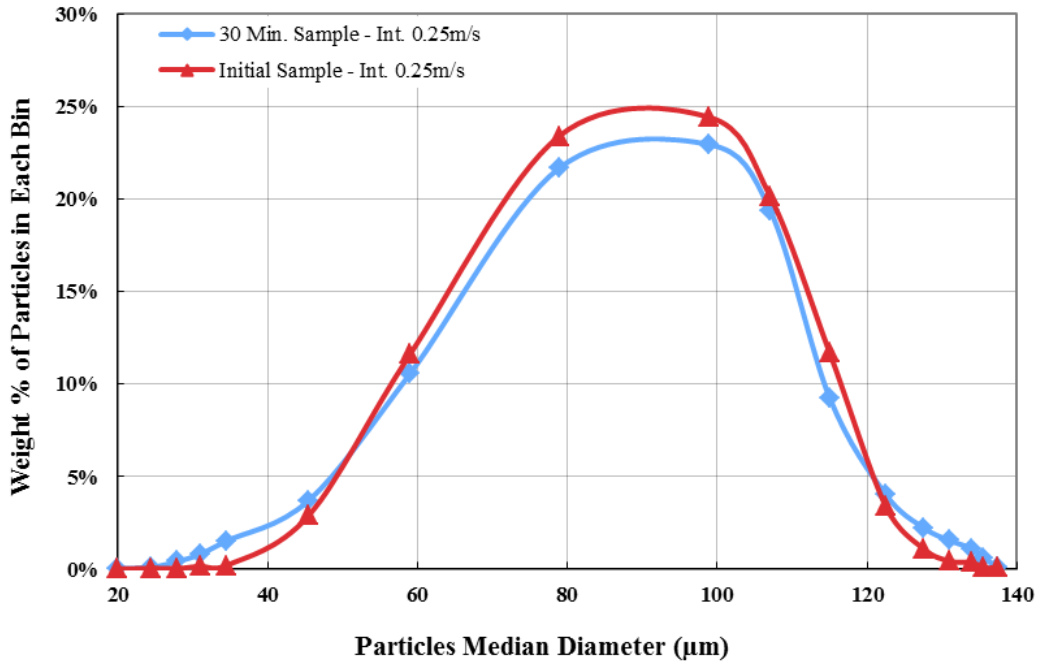

Figure 6.20c PSD of intermediate domain after 30 min flow at 0.25 m/s

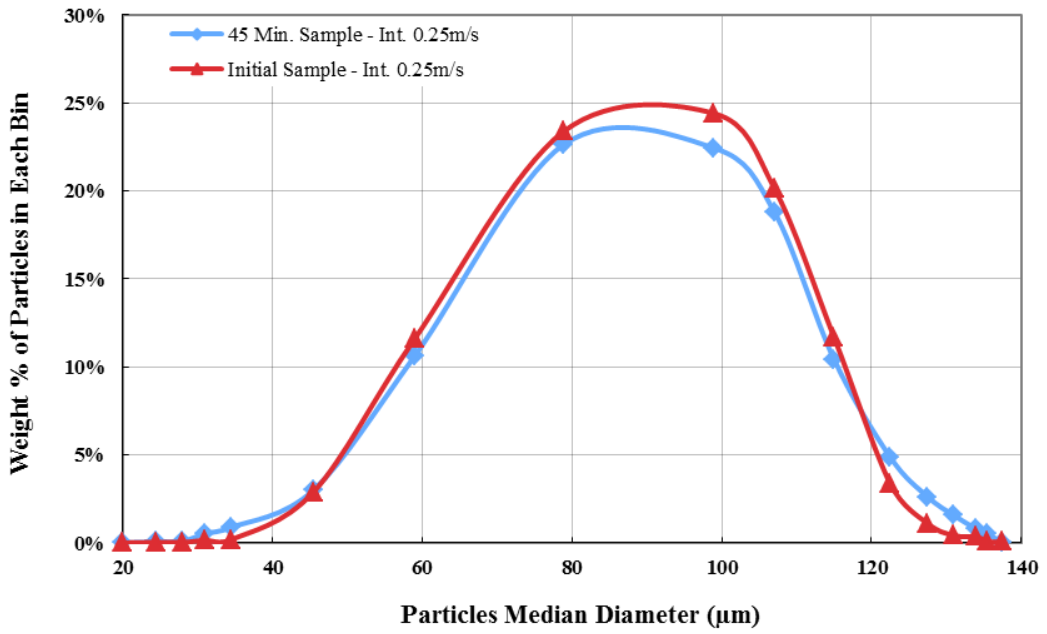

Figure 6.20d PSD of intermediate domain after 45 min flow at 0.25 m/s

Results for the intermediate-domain sample following 45 min exposure to flow at 0.25 m/s are shown in Figure 6.20d. The percentage of particles up to 48 µm in size increases, the percentage of particles from 48 to 119 µm in size decreases, while the percentage of particles larger than 119 µm increases.

The experimental PSDs for the intermediate domain and 0.34 m/s average flow velocity are shown in Figures 6.21a–6.21d, along with the initial PSD. The concentrations of particles in the smaller size ranges (up to ~ 42-44 µm) increase. The particle concentration remains the same for particles larger than ~101-109 µm. Again, for these size ranges, updraft under a burst is the effective upward force.

Figure 6.21a illustrates the results for the intermediate-domain sample following 10 min exposure to flow at 0.34 m/s. The concentration of particles smaller than 44 increases as the concentration of particles from 44 to 105 µm in size decreases, and the concentration of particles larger than 105 µm stays more-or-less the same.

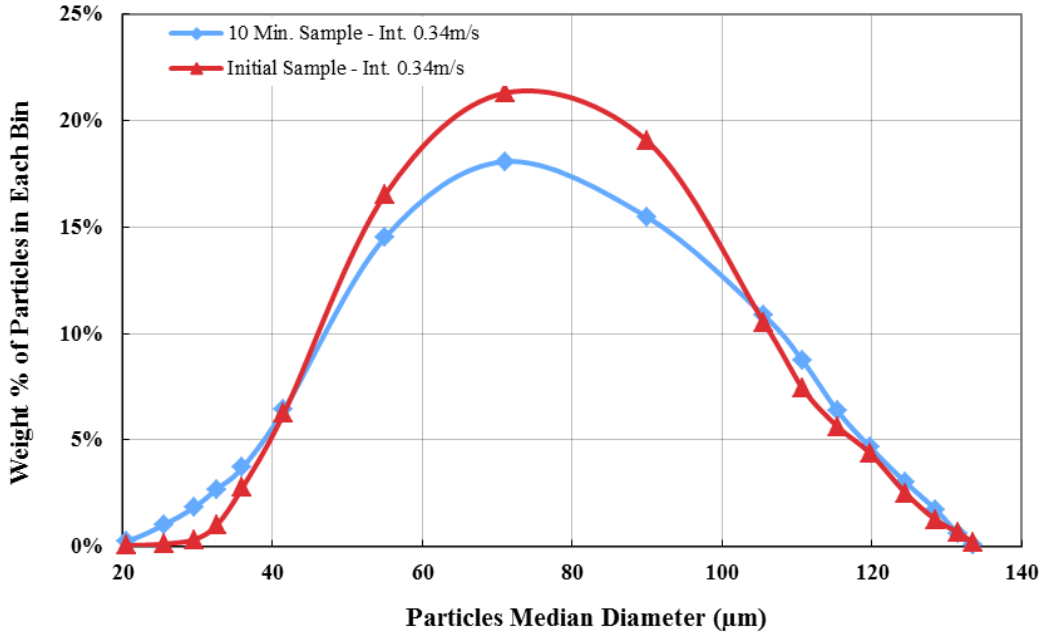

Figure 6.21a PSD of intermediate domain after 10 min flow at 0.34 m/s

Figure 6.21b depicts the PSD results for the intermediate-domain sample following 20 min exposure to flow at 0.34 m/s. As for the 10-min sample, the concentration of particles up to 44 µm in size increases, the concentration of particles from 44 to 105 µm decreases, and the concentration of particles larger than 105 µm remains the same.

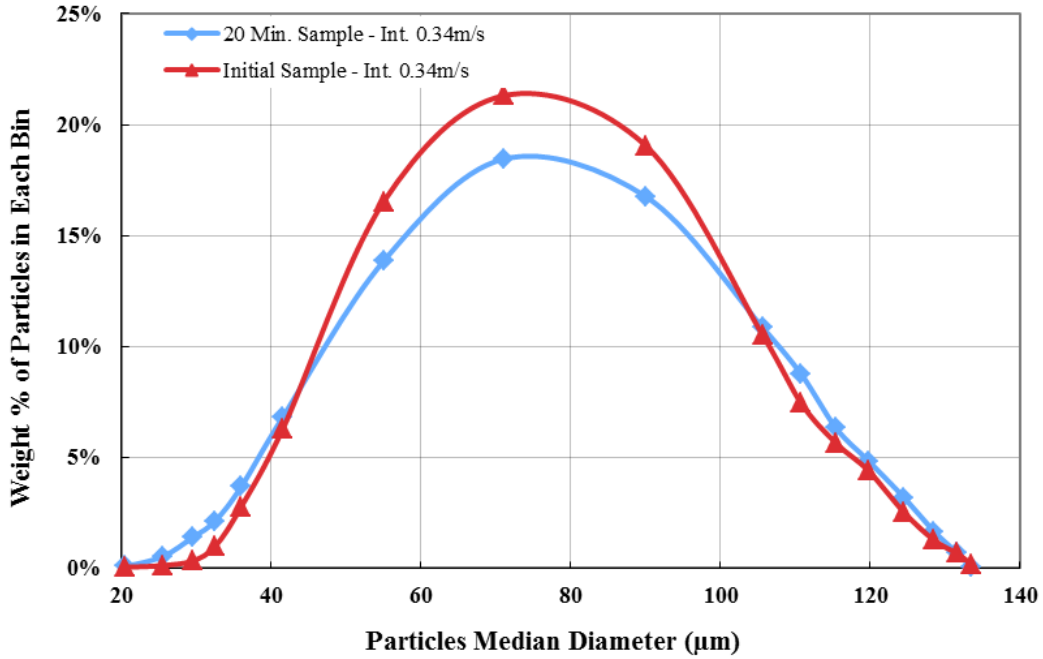

Figure 6.21b PSD of intermediate domain after 20 min flow at 0.34 m/s

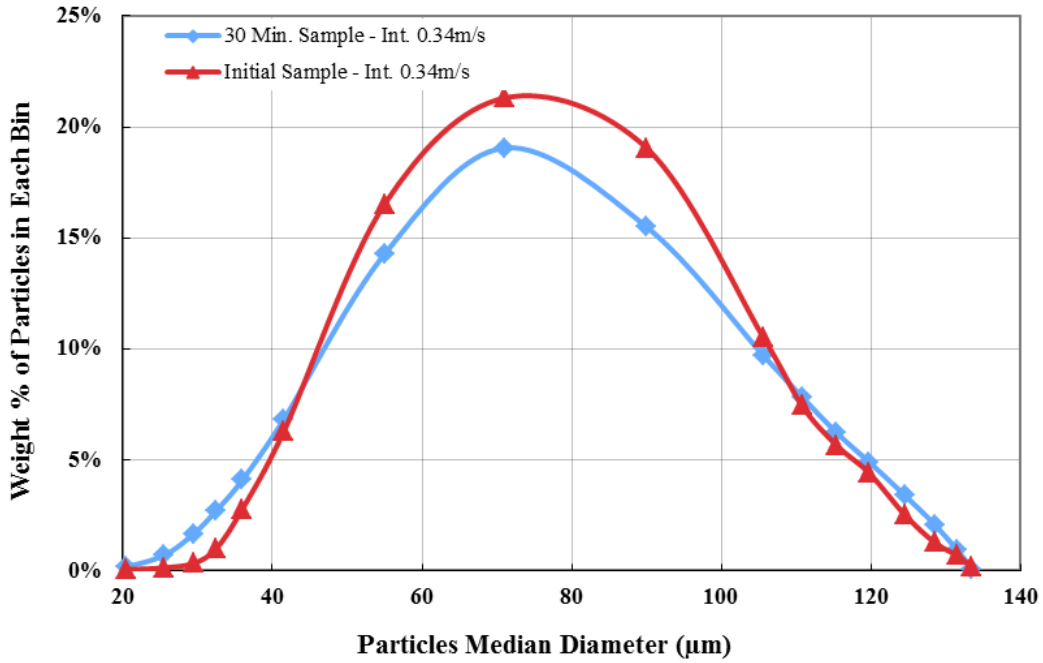

Figure 6.21c PSD of intermediate domain after 30 min flow at 0.34 m/s

The results for the intermediate-domain sample collected following 30 min exposure to flow at 0.34 m/s is presented in Figure 6.21c. The weight percentage of particles smaller than 44 µm increases, the percentage of particles from 44 to 109 µm decreases, and the percentage of particles larger than 109 µm stays the same.

The results for the intermediate domain sample collected following 45 min exposure to flow at 0.34 m/s is presented in Figure 6.21d. The weight percentage of particles smaller than 42 µm increases, while the percentage from 42 to 101 µm is reduced and the percentage of larger particles stays the same.

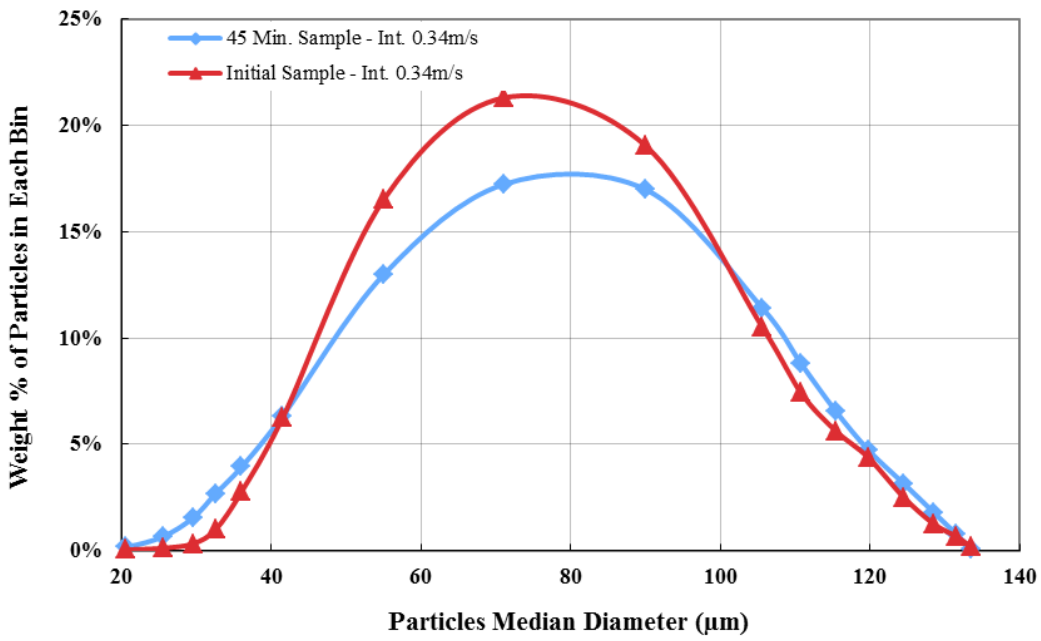

Figure 6.21d PSD of intermediate domain after 45 min flow at 0.34 m/s

The PSD results for the intermediate domain for various times of exposure to an average flow velocity of 0.39 m/s are shown in Figures 6.22a-6.22b. The initial PSDs range between 20 and 140 μm and, as Figure 6.7 suggests, the attraction force for particles up to 20 μm in size is stronger than the lifting force. For the rest of the particles the updraft under a burst force is the effective force for lifting the particles. The bursting of coherent structures near the interface, as low-speed currents are ejected out into the flow, removes particles from the deposit bed. From the experimental results, it appears that the bursting force is most effective for the smaller particles in the particle size interval in which particles (from 20 to 95-103 μm) are effectively removed.

Figure 6.22a depicts the results for of the intermediate-domain sample collected following 10 min exposure to flow at 0.39 m/s. The smaller particles up to 20 μm are not in the original PSD. The concentration of particles from 20 to 95 μm is reduced and, hence, the concentration of particles larger than 95 μm is increased in the bed.

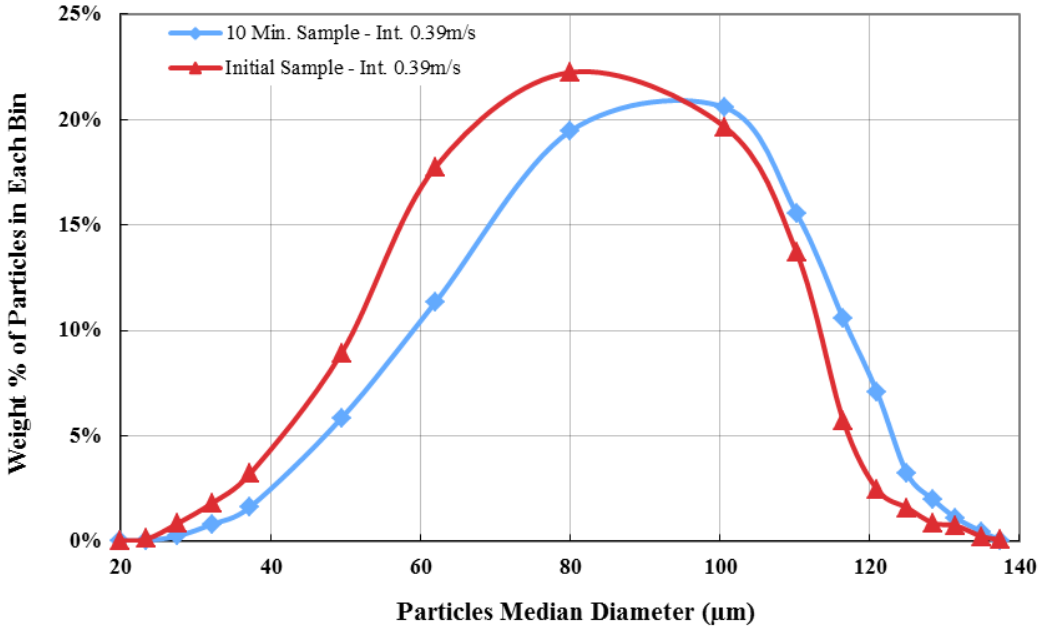

Figure 6.22a PSD of intermediate domain after 10 min flow at 0.39 m/s

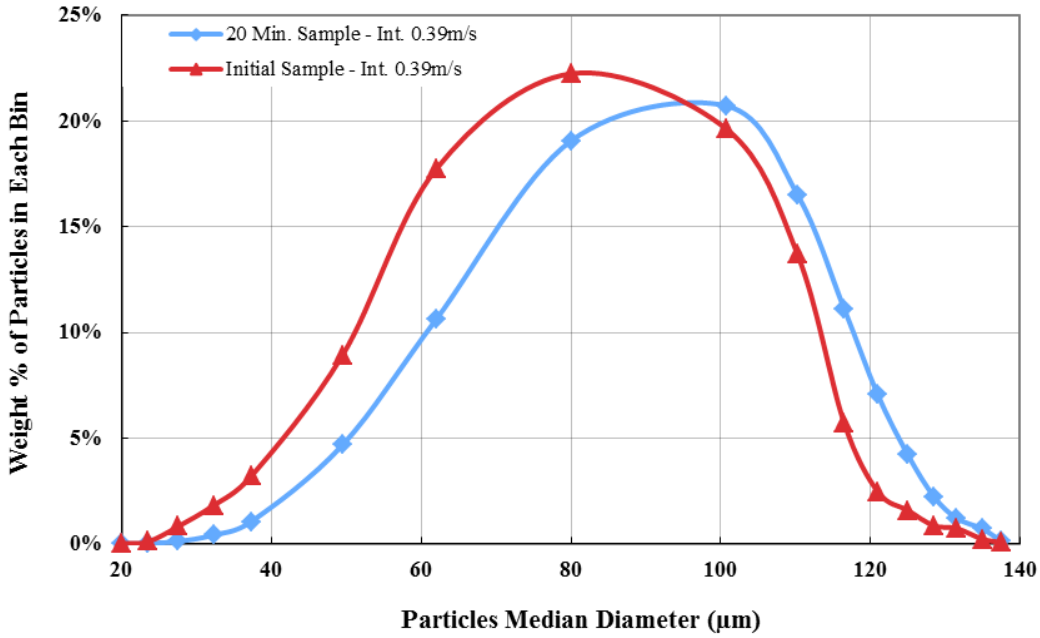

Figure 6.22b PSD of intermediate domain after 20 min flow at 0.39 m/s

The results for the intermediate domain sample following 20 min exposure to flow at 0.39 m/s is shown in Figure 6.22b. As with the sample for 10 min exposure, the concentration of particles from 20 to 95 µm in size decreases, while the concentration of particles larger than 95 µm increases.

Figure 6.22c shows PSD results for the intermediate-domain sample following 30 min exposure to flow at 0.39 m/s. The concentration of particles from 20 to 99 µm in size is reduced and, as a result, the concentration of particles larger than 99 µm increases.

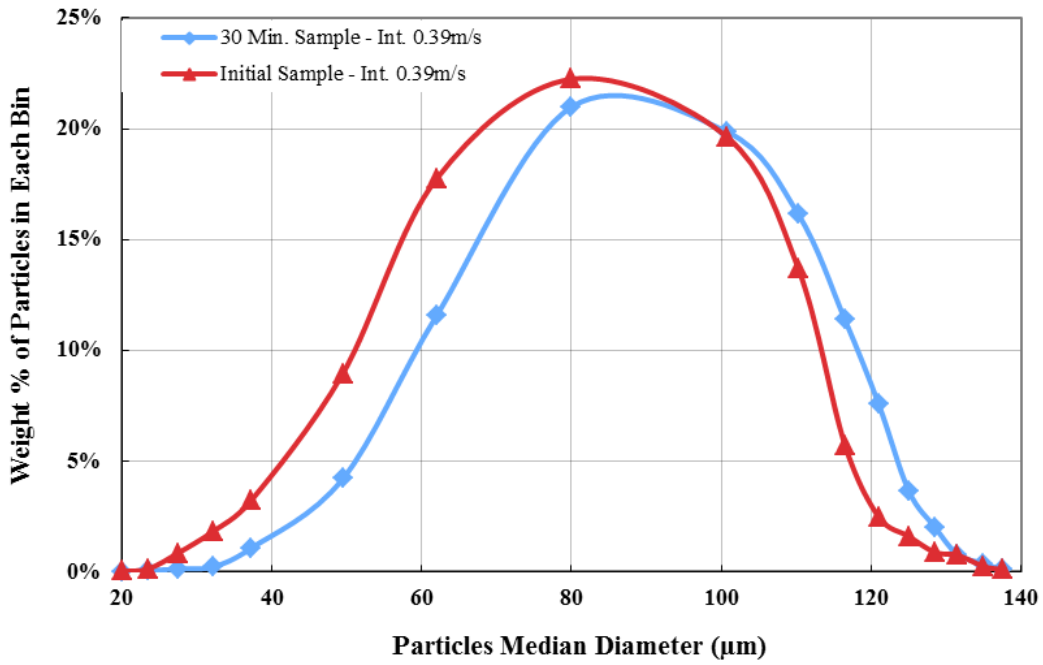

Figure 6.22c PSD of intermediate domain after 30 min flow at 0.39 m/s

The results for intermediate-domain sample following 45 min exposure to flow at 0.39 m/s is presented in Figure 6.22d. The concentration of particles from 20 to 103 µm in size decreases, while the concentration of particles larger than 103 µm increases.

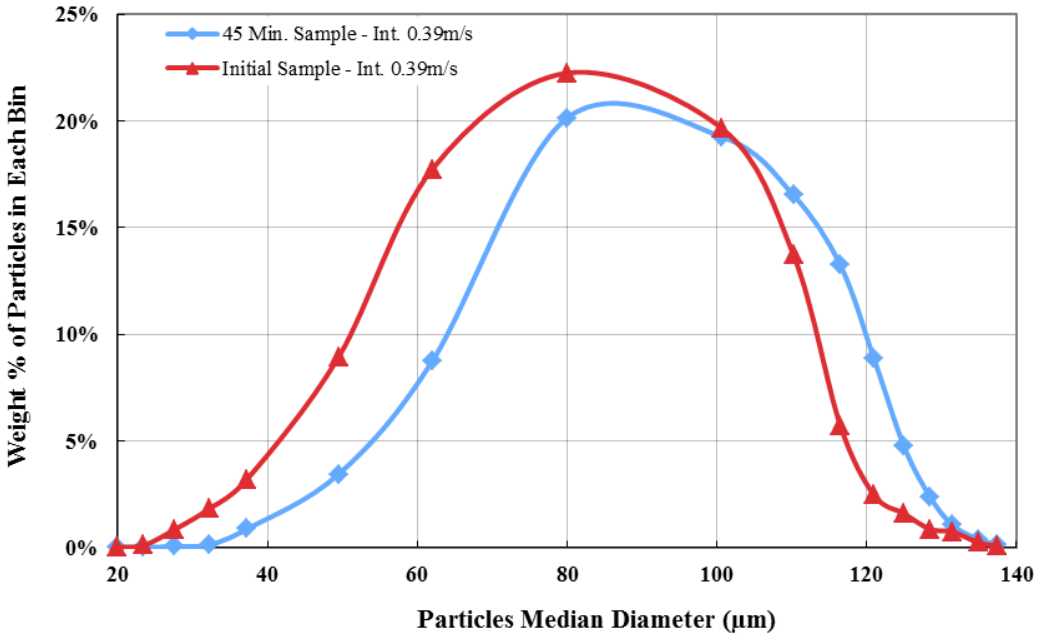

Figure 6.22d PSD of intermediate domain after 45 min flow at 0.39 m/s

The results of the intermediate-domain series of experiments indicate that, generally speaking, the longer the exposure to turbulent flow for the flow velocities of 0.25 and 0.34 m/s, the higher the concentration of fine particles. For the experiments at 0.39 m/s, there were no fine particles smaller than 20 µm in the initial PSD. As with the Phillips domain, the concentration of fine particles (occupying the area between the curves before they cross on the left side of the

graphs – see Figure 6.29, Part 1) is shifted towards higher concentrations from 10 to 20 min, from 20 to 30 min, and from 30 to 45 min (with increasing duration of exposure to flow).

For the intermediate-dominated region, (occupying the area between the curves to the right of where they first cross and up to where they cross for the second time – see Figure 6.29, Part 2), where the concentration of these particles is reduced due to removal to the bulk flow, mainly shifts toward lower concentrations from 10 to 20 min, 20 to 30 min, and from 30 to 45 min (with increasing duration of exposure to flow).

With increasing velocity (below the critical removal velocity), the series of intermediate domain experiments showed incremental shifts in the PSD to higher concentrations of smaller particles, as with the Phillips domain experiments. These results are in agreement with the theoretical calculations from the force balance. For the experiments at a flow velocity of 0.25 m/s, particles larger than 45–51 µm were removed; at 0.34 m/s, particles larger than 42–44 µm were removed; and at 0.39 m/s, the finer particles were not present in the original PSD.

6.4.3 Shields Domain

Figures 6.23a–6.23d, 6.24a–6.24d, and 6.25a–6.25d present the experimental results for flow velocities of 0.25 m/s, 0.34 m/s, and 0.39 m/s, respectively, for the Shields domain. The dominant lifting force for these particle sizes (larger than ~ 170 µm) is the hydrodynamic drag force. The drag force transports the particles

by rolling, sliding, and saltation at the interface in the flow direction rather than removing the particles from the bed. Because particles in this domain are not carried out, the PSD of the bed deposit after exposure to the flow is more or less unchanged.

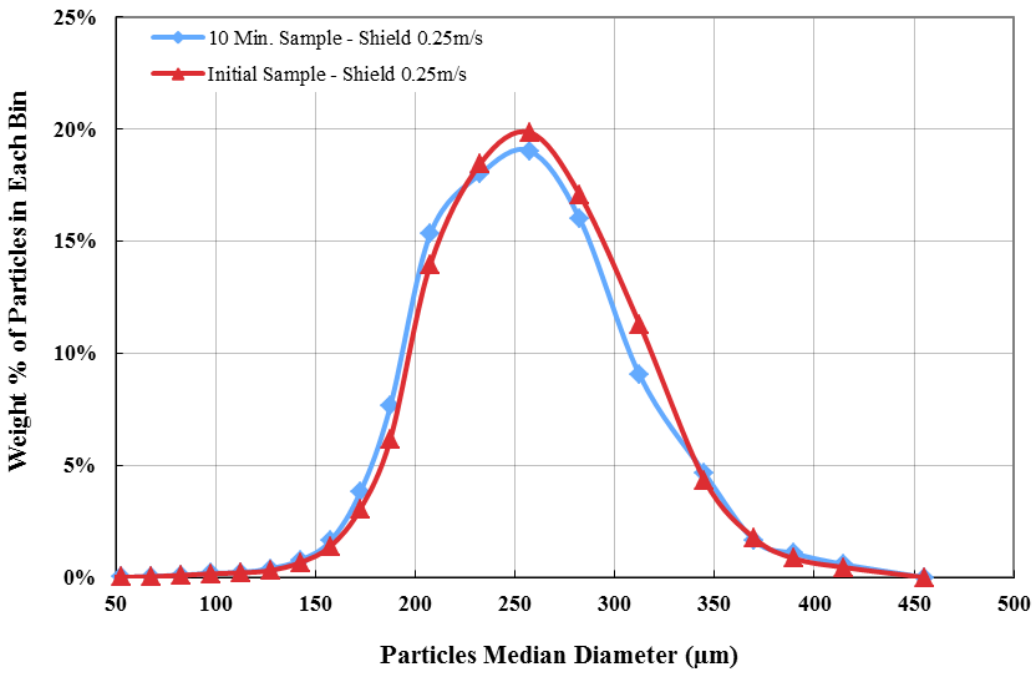

Figure 6.23a PSD of Shields domain after 10 min flow at 0.25 m/s

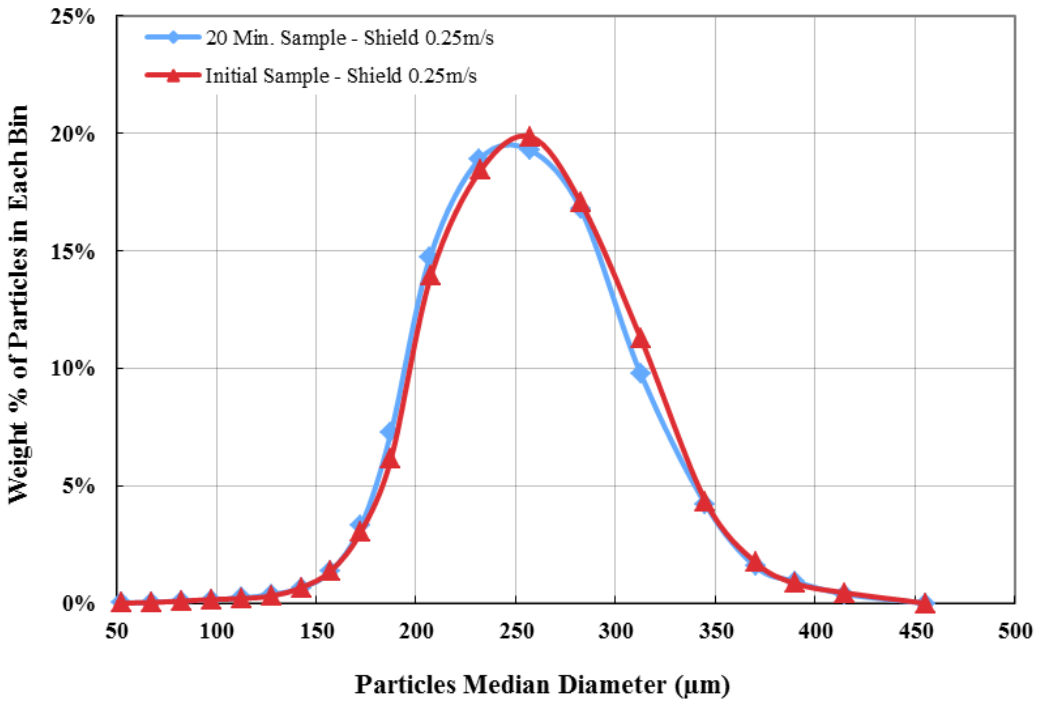

Figure 6.23b PSD of Shields domain after 20 min flow at 0.25 m/s

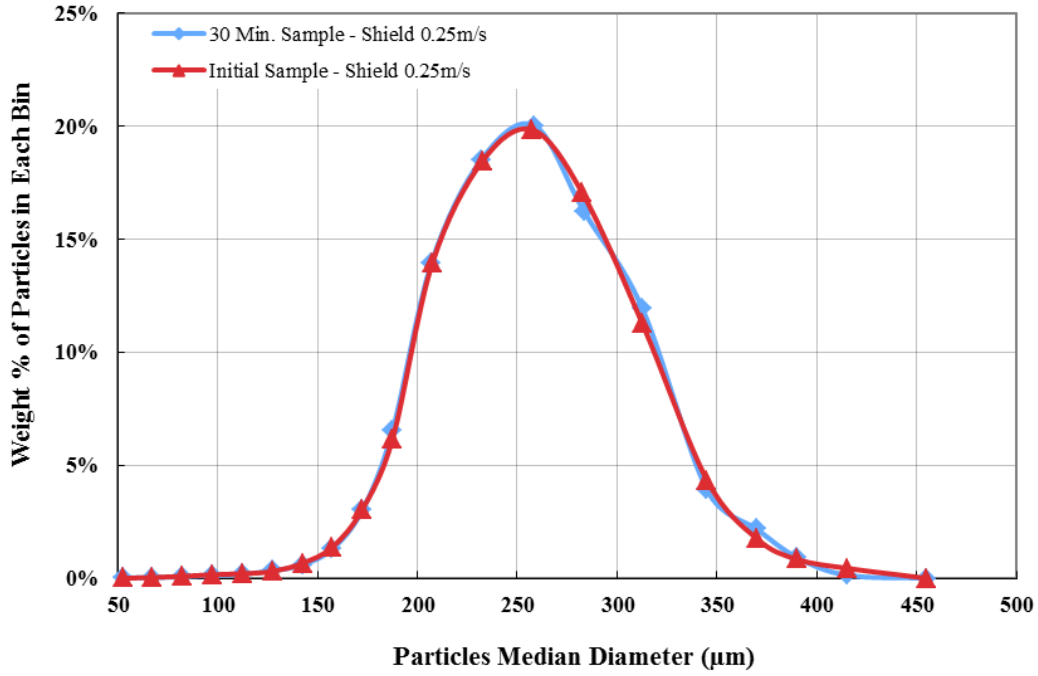

Figure 6.23c PSD of Shields domain after 30 min flow at 0.25 m/s

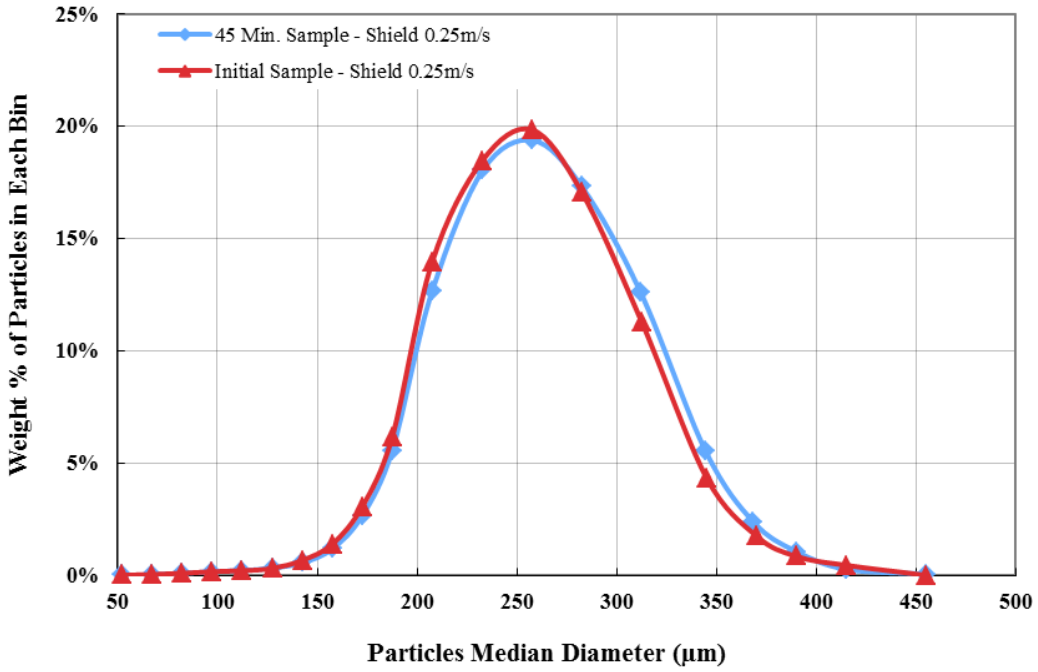

Figure 6.23d PSD of Shields domain after 45 min flow at 0.25 m/s

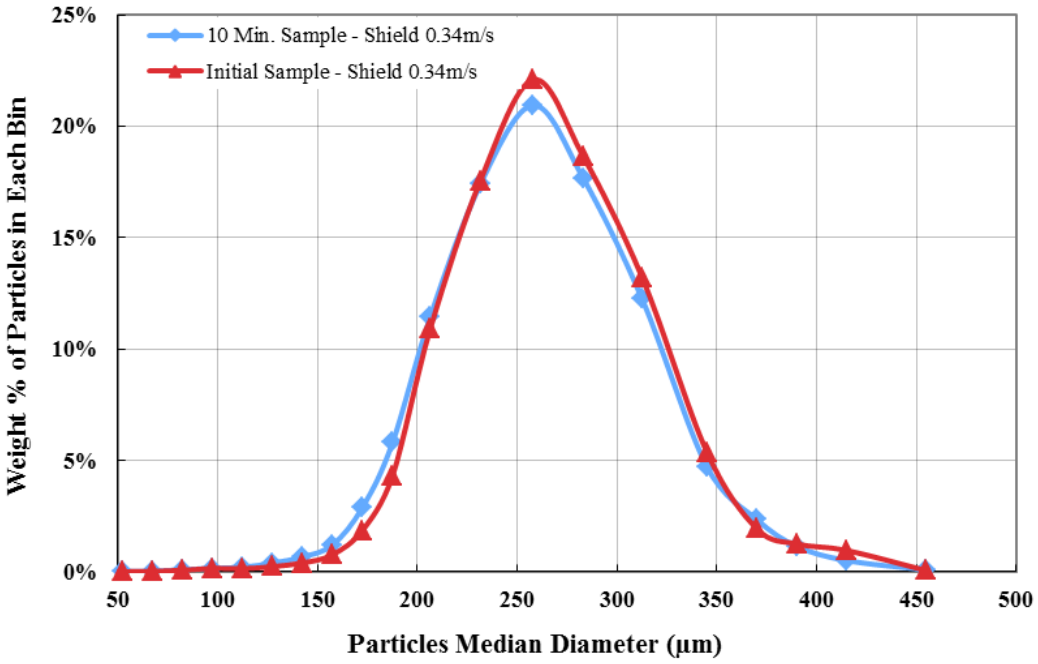

Figure 6.24a PSD of Shields domain after 10 min flow at 0.34 m/s

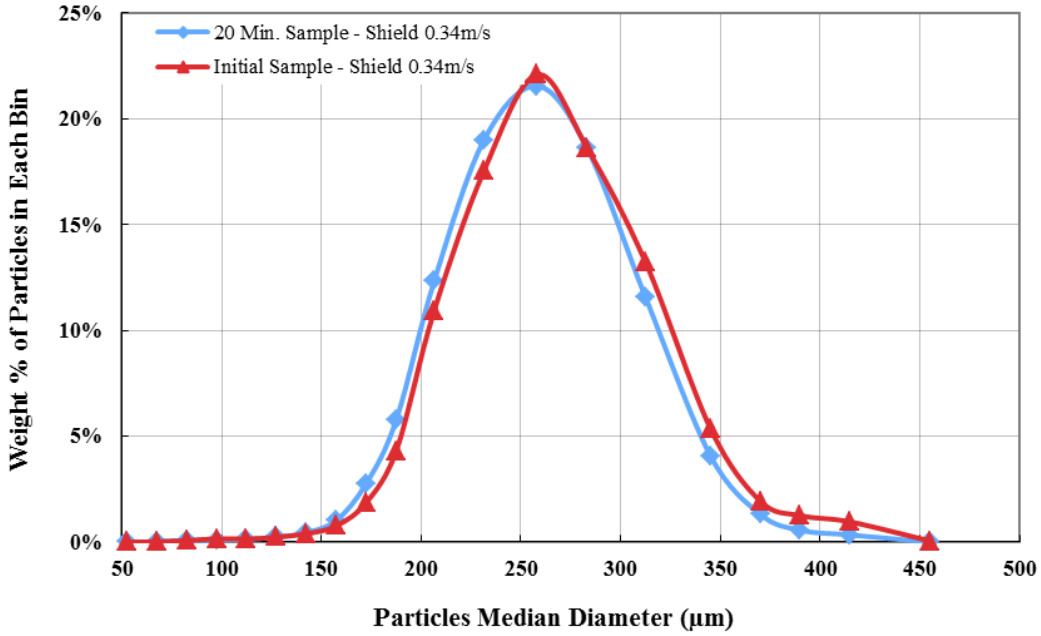

Figure 6.24b PSD of Shields domain after 20 min flow at 0.34 m/s

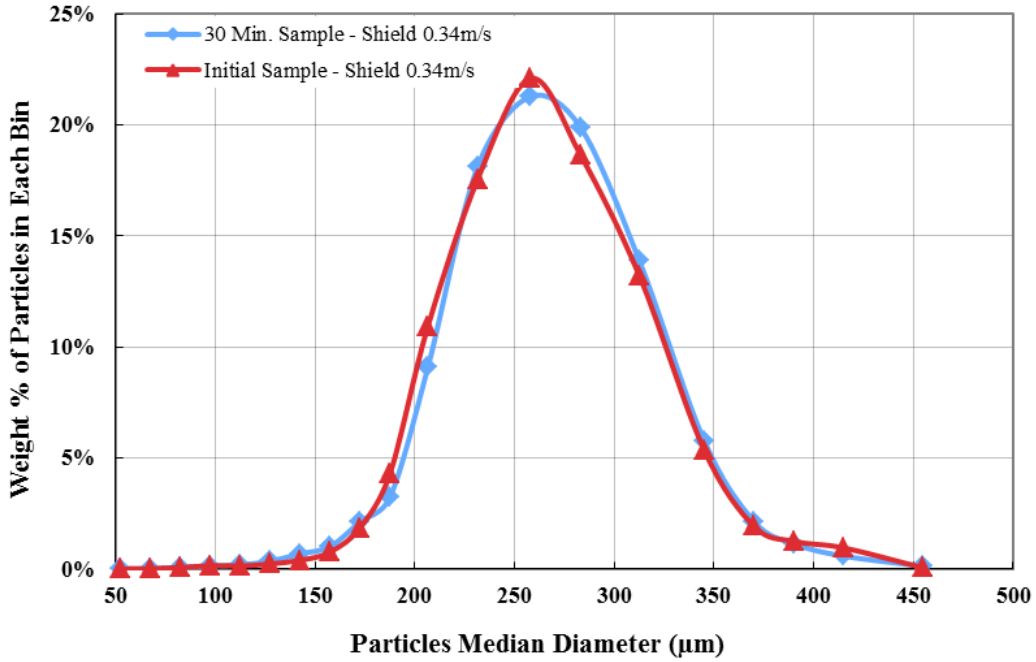

Figure 6.24c PSD of Shields domain after 30 min flow at 0.34 m/s

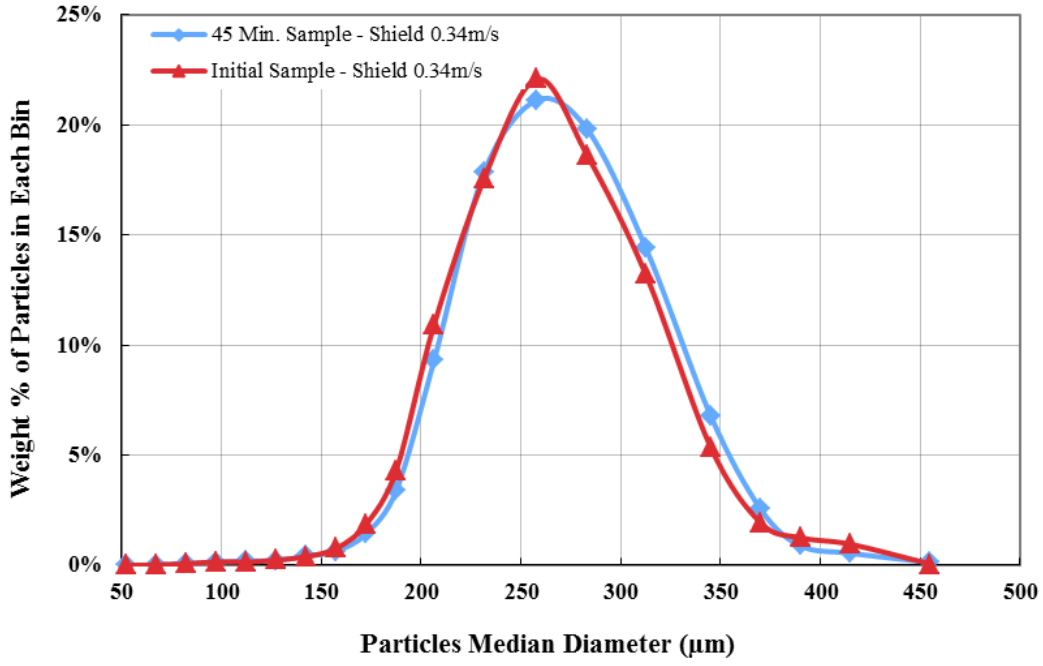

Figure 6.24d PSD of Shields domain after 45 min flow at 0.34 m/s

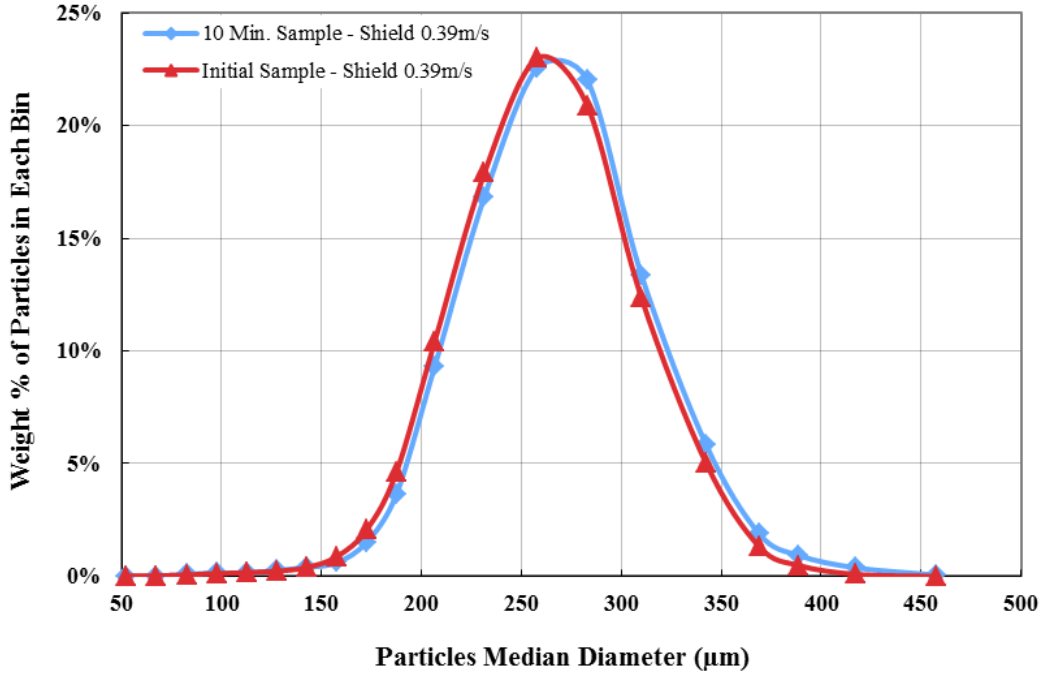

Figure 6.25a PSD of Shields domain after 10 min flow at 0.39 m/s

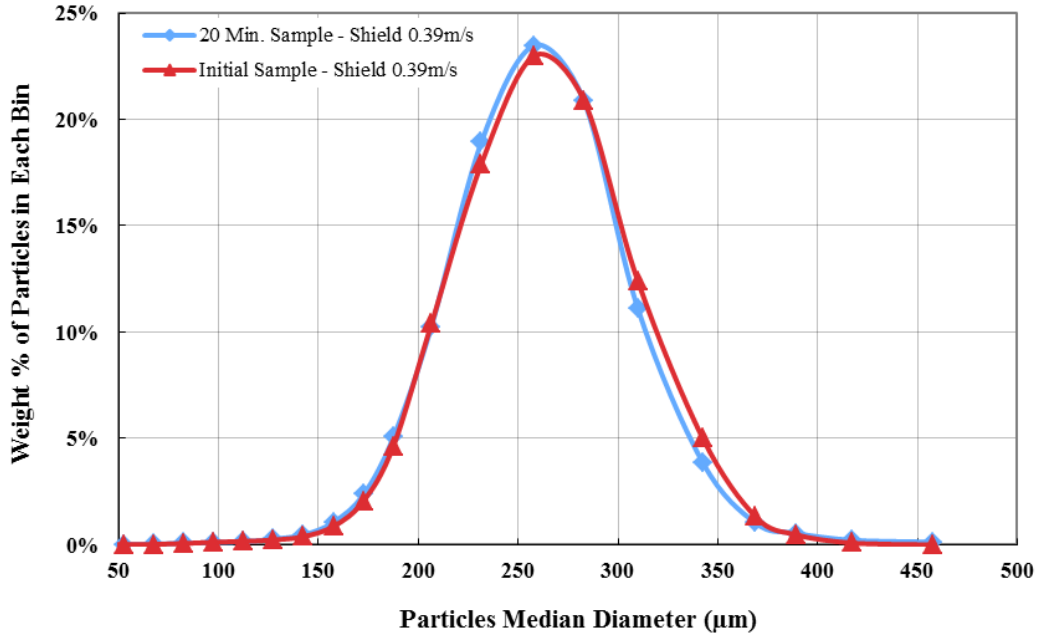

Figure 6.25b PSD of Shields domain after 20 min flow at 0.39 m/s

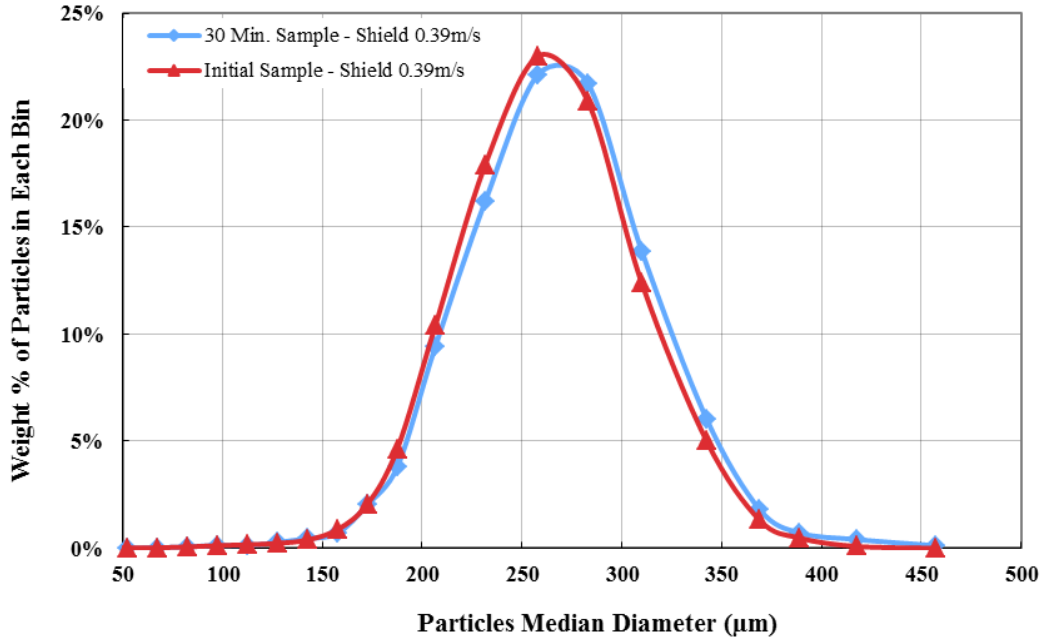

Figure 6.25c PSD of Shields domain after 30 min flow at 0.39 m/s

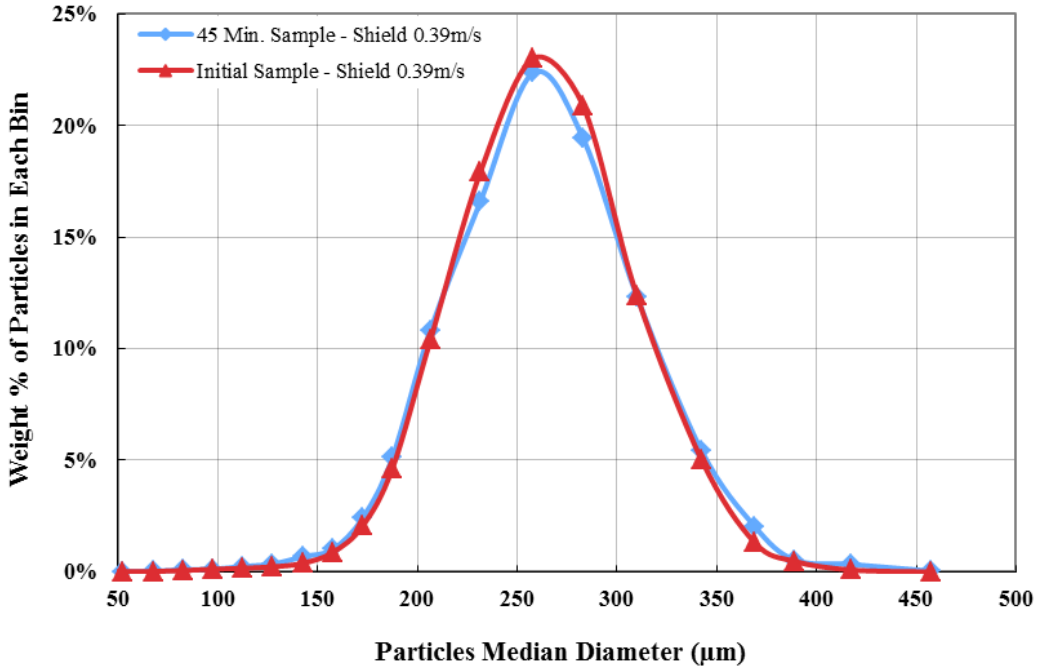

Figure 6.25d PSD of Shields domain after 45 min flow at 0.39 m/s

The results of Shields domain series of experiments for the original PSD show that, the concentration of particles for the three different velocities stays similar to the initial PSD, or unchanged. The main particle size fraction of the experimental series is > 150 µm and, from the theoretical calculations of the force balance, the lifting force for these particles is hydrodynamic drag force, which moves particles by rolling, sliding, and saltation. Therefore, the PSD following 10, 20, 30, and 45 min exposure to flow stays approximately the same as the original PSD.

With increasing velocity (below the critical removal velocity) of the results for the Shields domain experimental series demonstrate that, for the chosen original PSD,

the PSDs for the three velocities of 0.25, 0.34, and 0.39 m/s stay roughly the same.

6.4.4 Mixed Domain

The mixed-domain experiments were planned to measure the combined effects of the Phillips, intermediate, and Shields domains. Therefore, the original PSD was chosen to cover all domains. The experimental results for 0.25 m/s flow velocity demonstrate that the concentrations of particles 58–65 μm in size increase, while the concentrations of particles 156–189 μm in size decrease; consequently, the concentrations of larger particles increase. According to the force balance for this flow velocity (Figure 6.5), particles larger than 40 μm will be lifted and, for particle diameters up to approximately 160–170 μm the burst dynamics of coherent structures lift the particles. The larger particles are transported by hydrodynamic drag through rolling, sliding, and saltation (Figures 6.26a–6.26d).

Figure 6.26a depicts the PSD for the mixed experimental series following 10 min exposure to flow at 0.25 m/s. This series of experiments were conducted to investigate how particles interact when they are exposed to a broader range of particle sizes. In the Phillips-dominated region, the concentration of particles smaller than 65 μm increases. In the intermediate-dominated region, the mass concentration of particles from 65 to 156 μm is reduced. In the Shields-dominated region, consequently, the concentration of particles larger than 156 μm increases.

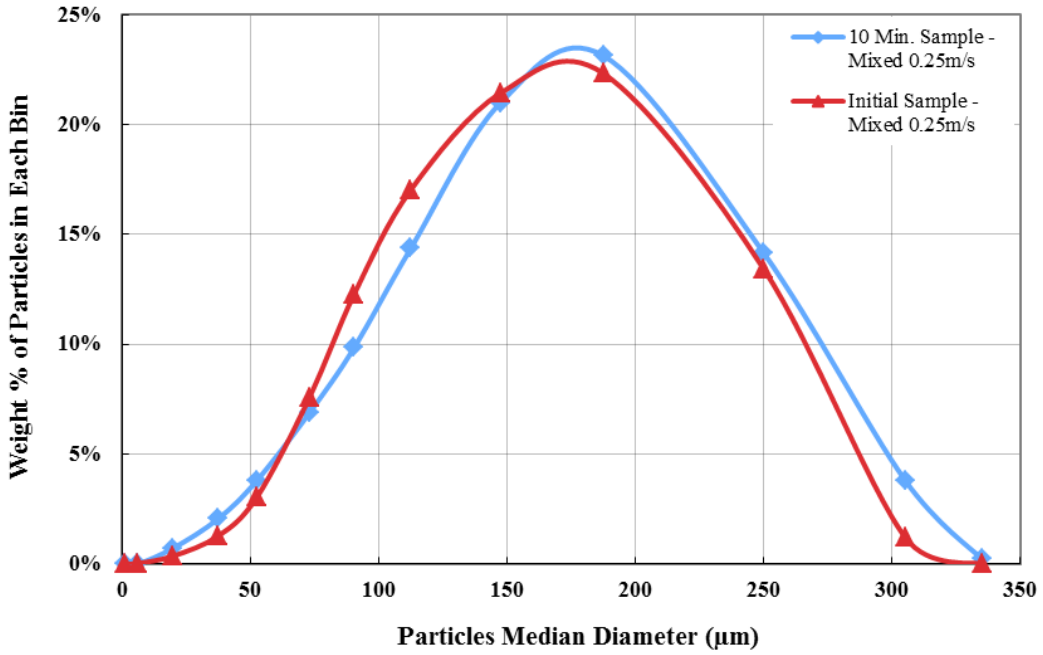

Figure 6.26a PSD of mixed domain after 10 min flow at 0.25 m/s

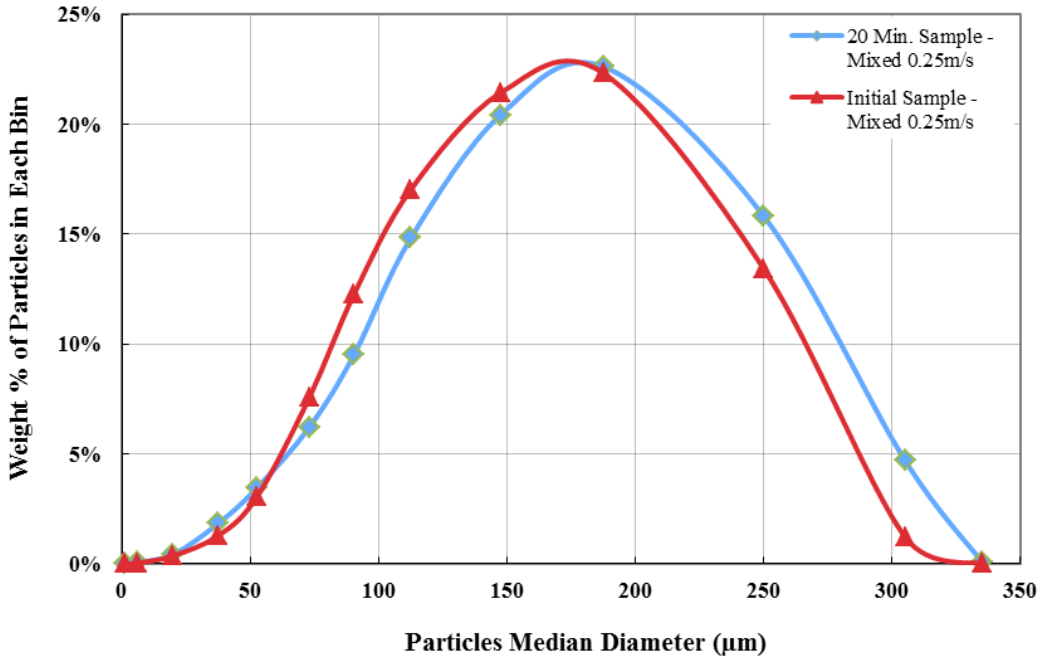

Figure 6.26b PSD of mixed domain after 20 min flow at 0.25 m/s

The experimental results for experiments with the mixed domain following 20 min exposure to flow at 0.25 m/s are shown in Figure 6.26b. In the first part, the concentration of particles up to 58 µm in size increases; in the second part, the concentration of particles from 58 to 179 µm decreases; and, hence, the concentration of particles larger than 179 µm increases.

Figure 6.26c illustrates PSD results following 30 min exposure to flow at 0.25 m/s. In the first part, the weight percentage of particles smaller than 58 µm increases, and in the second part, the percentage of particles from 58 to 177 µm in size is reduced. As a result, the weight percentage of particles larger than 177 µm increases.

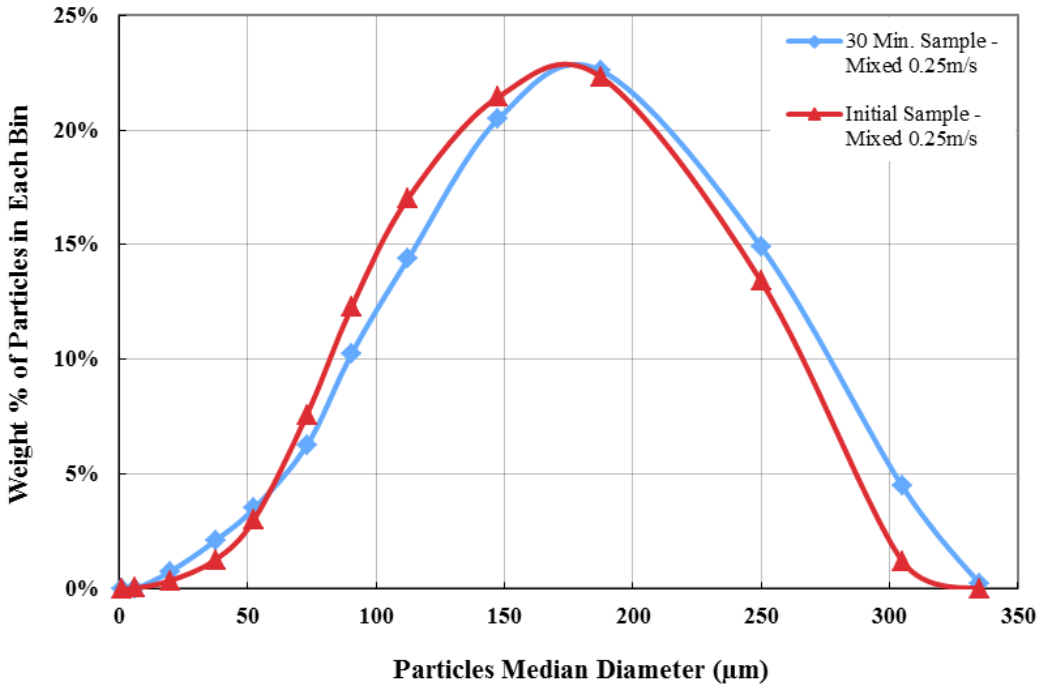

Figure 6.26c PSD of Mixed domain after 30 min flow at 0.25 m/s

The results for the mixed domain following 45 min exposure to flow at 0.25 m/s are presented in Figure 6.26d. In the first part, the percentage of particles smaller than 64 µm increases; in the second part, the concentration of particles from 64 to 189 µm in size is reduced and, hence, the percentage of particles larger than 189 µm increases.

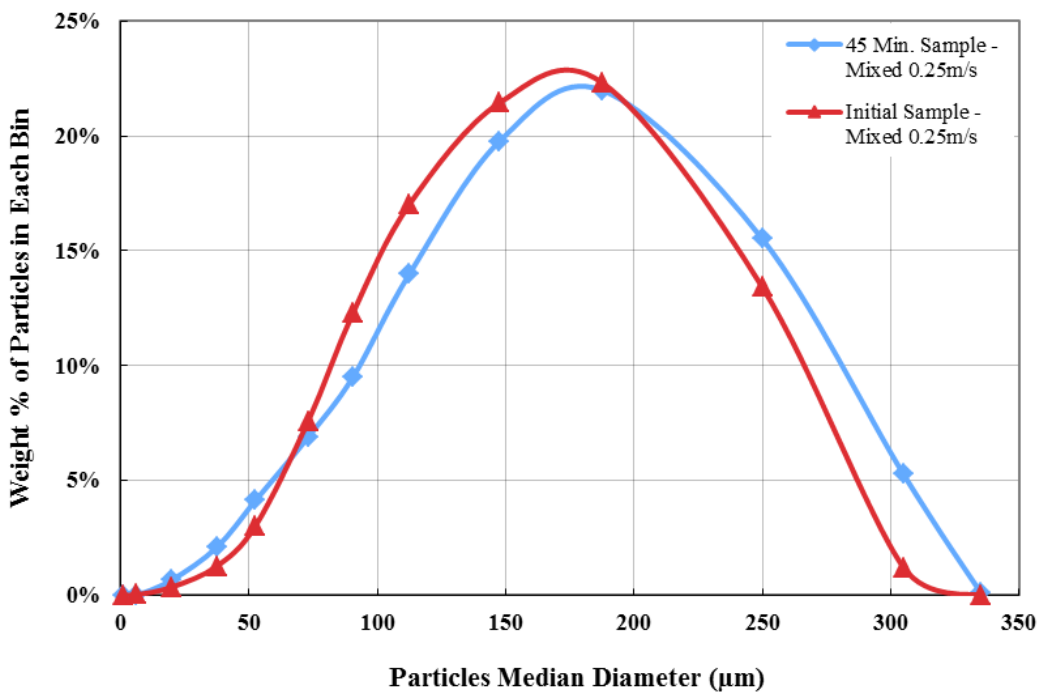

Figure 6.26d PSD of mixed domain after 45 min flow at 0.25 m/s

Figures 6.27a–6.27d present the PSD results for the mixed domain and a flow velocity of 0.34 m/s. The concentration of smaller particles (up to 52–58 µm) in the deposit bed increases with the duration of exposure to flow, and the updraft under a burst force removes particles up to 189–202 µm in size.

Figure 6.27a illustrates the results for the mixed domain following 10 min exposure to flow at 0.34 m/s. In the first part, the Phillips-dominated region, the concentration of particles smaller than 58 increases. In the second part, the intermediate-dominated region, the concentration of particles from 58 to 196 µm in size decreases. In the third part, the Shields-dominated region, therefore, the concentration of particles larger than 196 µm increases.

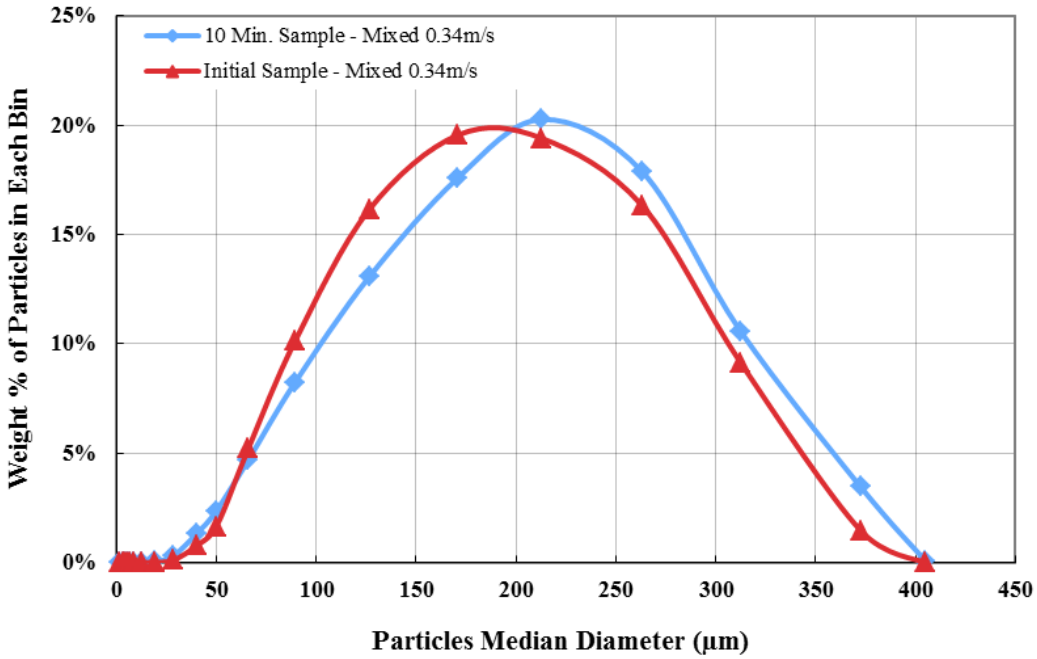

Figure 6.27a PSD of Mixed domain after 10 min flow at 0.34 m/s

The results for the mixed domain following 20 min exposure to flow at 0.34 m/s is shown in Figure 6.27b. In the first part, the concentration of particles smaller than 53 µm increases. In the second part, the concentration of particles from 53 to

195 µm in size is reduced and, consequently, in the third part, the concentration of particles larger than 195 µm increases.

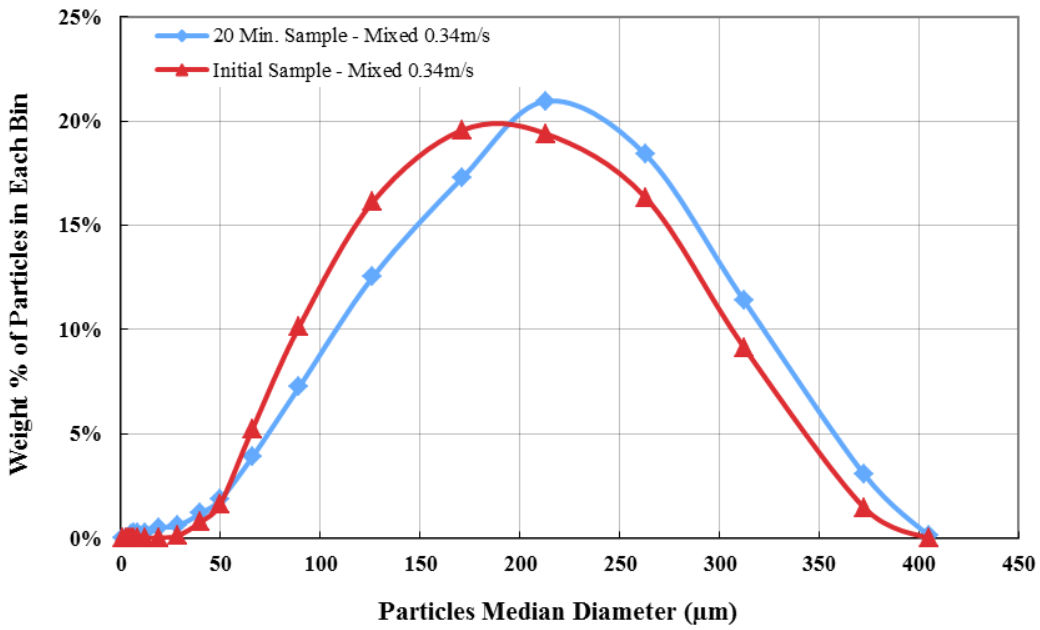

Figure 6.27b PSD of mixed domain after 20 min flow at 0.34 m/s

Figure 6.27c shows results for the mixed domain following 30 min exposure to flow at 0.34 m/s. In the first part, the concentration of particles up to 52 µm in size increases In the second part, the concentration of particles from 52 to 189 µm in size decreases and, as a result, the concentration of particles larger than 189 µm increases.

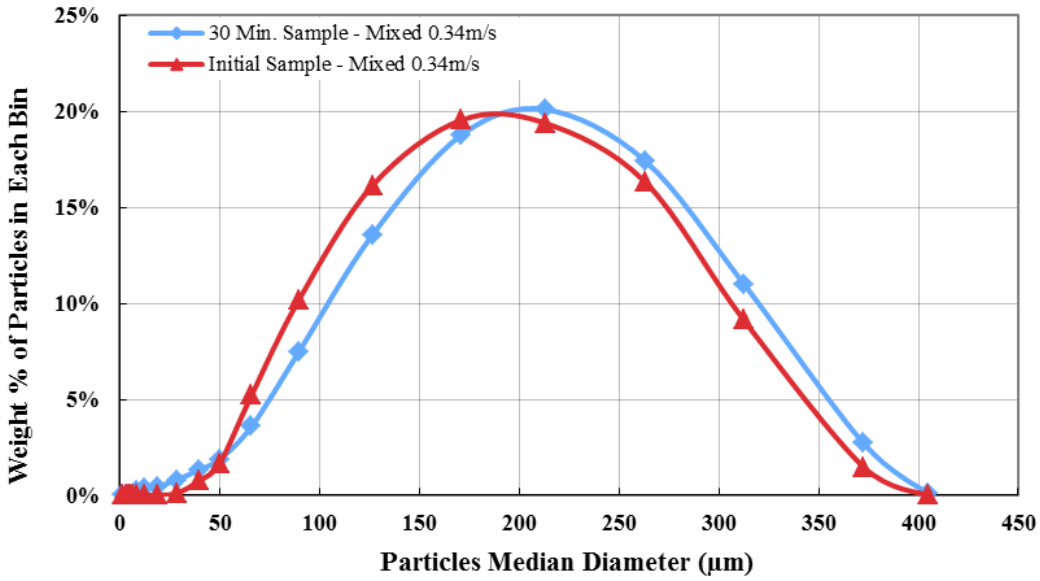

Figure 6.27c PSD of mixed domain after 30 min flow at 0.34 m/s

The results for the mixed domain following 45 min exposure to flow at 0.34 m/s are given in Figure 6.27d. In the first part, the percentage of particles up to 53 µm in size goes up. In the second part, the percentage of particles from 53 to 202 µm in size is reduced and, in the third part, consequently, the concentration of particles larger than 202 µm goes up.

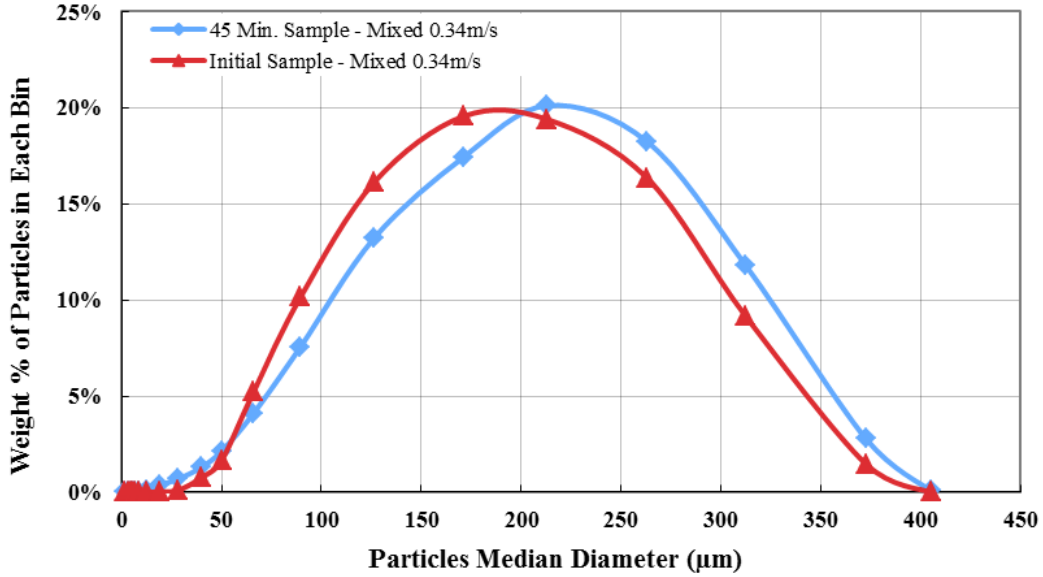

Figure 6.27d PSD of mixed domain after 45 min flow at 0.34 m/s

For the mixed-domain experiments at 0.39 m/s flow velocity, the mass concentration of particles up to 40-52 µm increases, and the mass concentration of particles from 40-52 µm to 182–213 µm in size decreases due to particle removal by burst activity; accordingly, the concentration of larger particles in the bed increases (Figure 6.28a–6.28d).

Figure 6.28a shows mixed-domain results following 10 min exposure to flow at 0.39 m/s. In the first part, the Phillips-dominated region, the concentration of particles up to 52 µm is slightly higher than in the initial PSD because of the low initial concentration of these particles. In the second part, the concentration of particles 52 to 182 µm in diameter is reduced. In the third part, the Shields-dominated region, the concentration of particles larger than 182 µm increases.

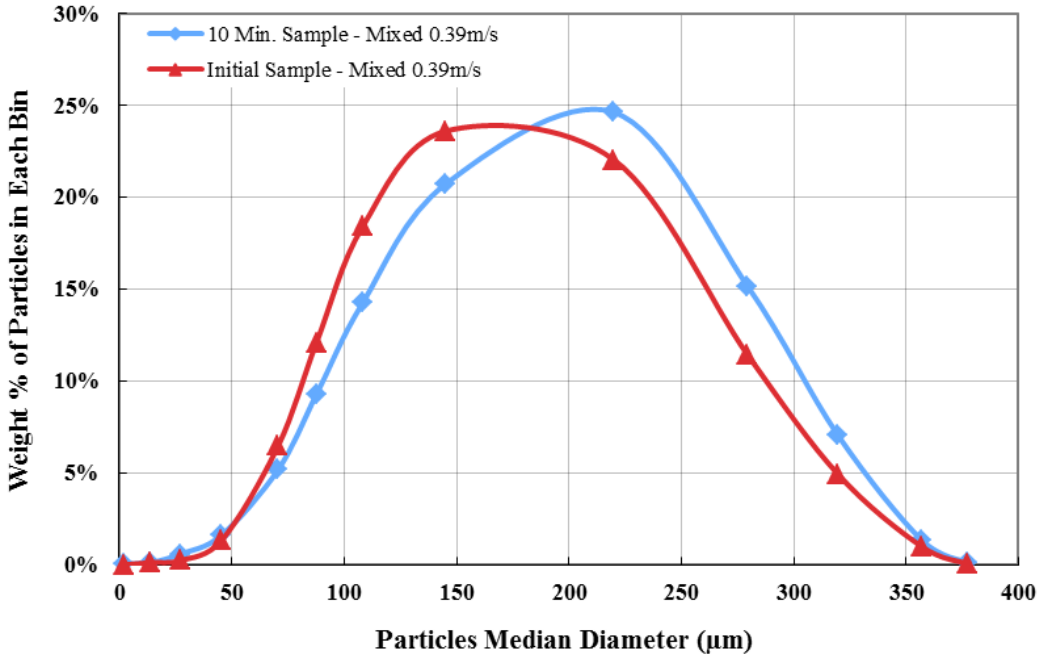

Figure 6.28a PSD of mixed domain after 10 min flow at 0.39 m/s

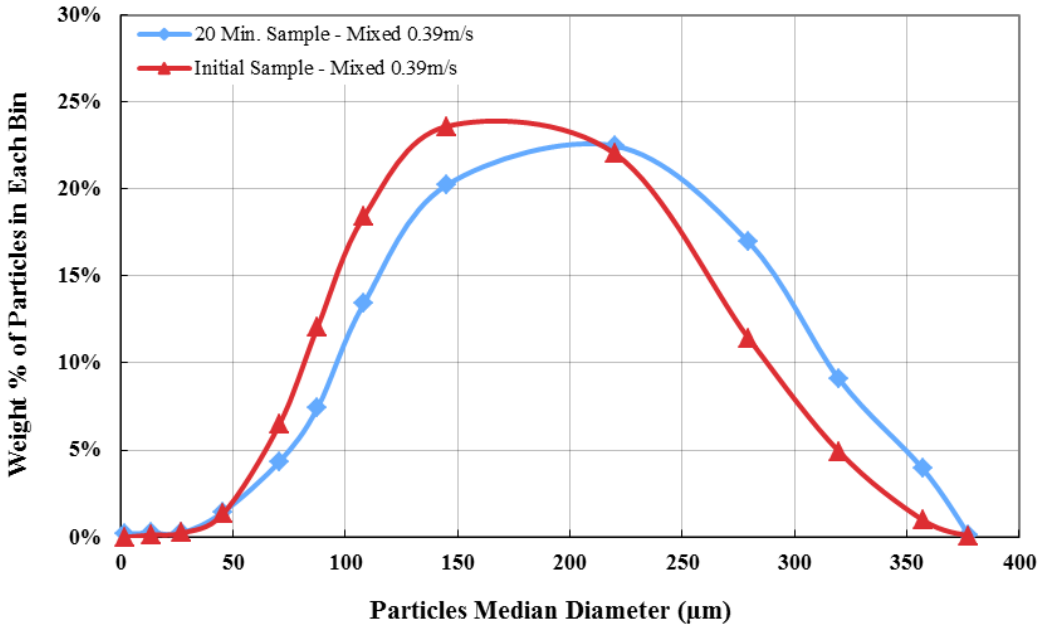

Figure 6.28b PSD of mixed domain after 20 min flow at 0.39 m/s

The results of mixed-domain experiments following 20 min exposure to flow at 0.39 m/s are presented in Figure 6.28b. In the first part, due to the initial low concentration of this fraction, the particle concentration for sizes up to 47 µm is more or less the same. In the second part, the concentration of particles from 47 to 213 µm in size is reduced and, as a result, the concentration of particles larger than 213 µm in the third part increases.

Figure 6.28c shows the mixed-domain results following 30 min exposure to flow at 0.39 m/s. Again, in the first part, due to the low initial concentration of particles up to 40 µm in size, the concentration of that fraction is slightly higher than in the initial PSD. In the second part, the concentration of particles from 40 to 197 µm in size decreases, while, in the third part, the concentration of particles larger than 197 µm consequently increases.

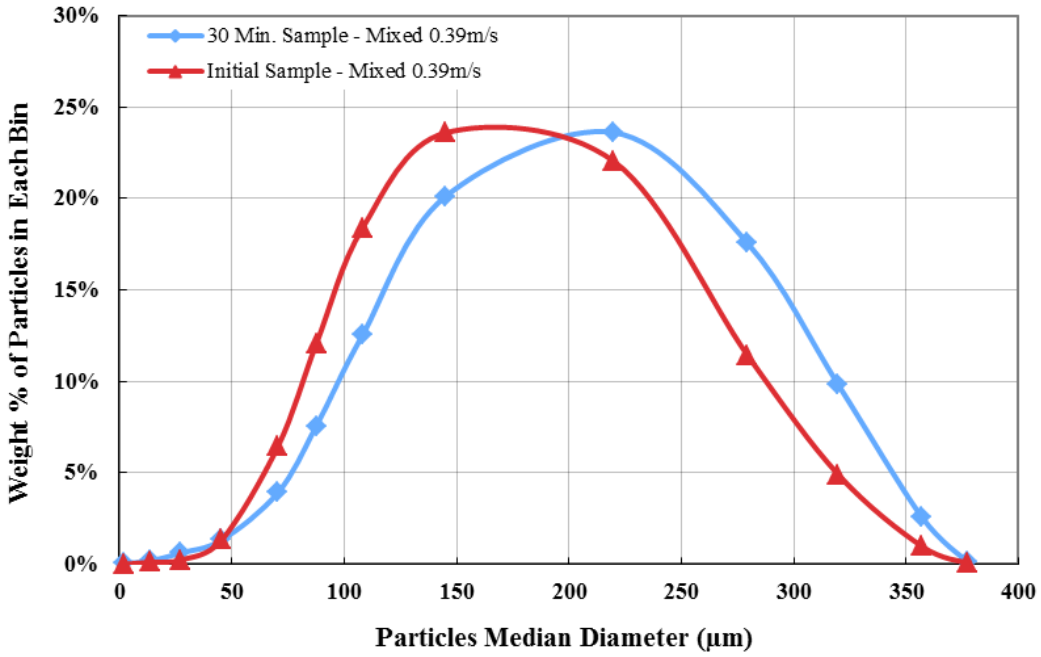

Figure 6.28c PSD of mixed domain after 30 min flow at 0.39 m/s

The results for the mixed domain following 45 min exposure to flow at 0.39 m/s is presented in Figure 6.28d. In the first part, the weight percentage of particles smaller than 43 µm goes up, In the second part, the percentage of particles from 43 to 184 µm in size is reduced. In the third part, therefore, the concentration of particles larger than 184 µm increases.

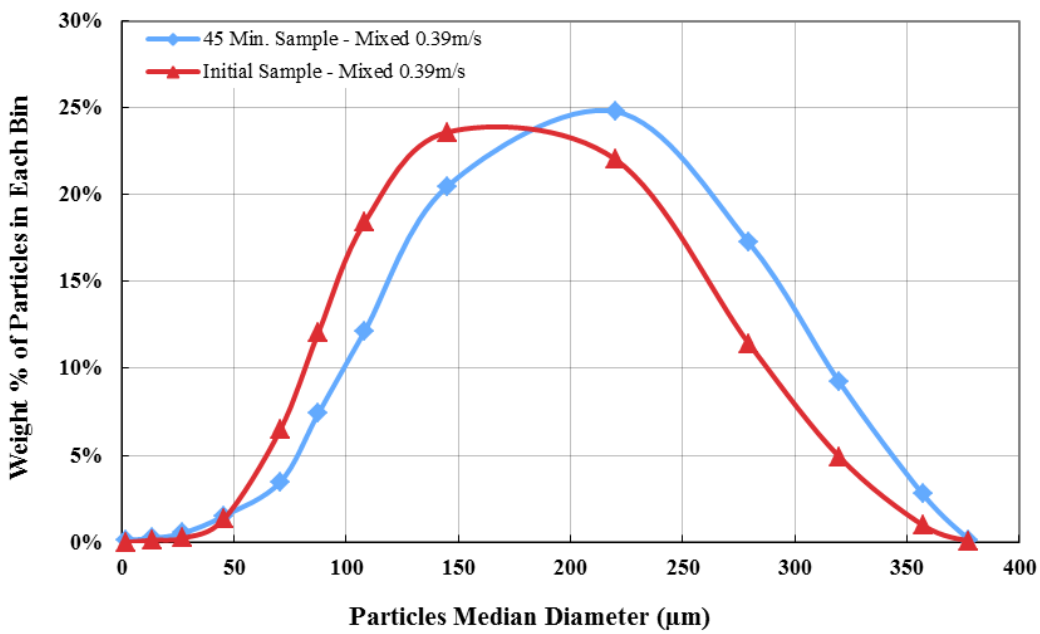

Figure 6.28d PSD of mixed domain after 45 min flow at 0.39 m/s

The mixed-domain (poly-dispersed particles) results, which confirm experimental results obtained with the Phillips, intermediate, and Shields domains together, show the general trend of incremental shifts in the concentration of fine particles with time of exposure to flow. As with the results for the Phillips and intermediate domains, the concentration of fine particles (occupying the area between the PSD

curves before they cross for the first time – see Figure 6.29, Part 1) shifts towards higher concentrations of smaller particles from 10 to 20 min, from 20 to 30 min, and from 30 to 45 min. For the second part, (occupying the area between the PSD curves from where they first cross to where they cross for the second time – see Figure 6.29, Part 2), the particle concentration is reduced due to removal to the bulk flow, and the PSD mainly shifts toward lower concentrations of these particles from 10 to 20 min, 20 to 30 min, and from 30 to 45 min. For the third part, (occupying the area between the PSD curves to the right of the second intersection of the curves, extending to the right side – see Figure 6.29, Part 3), it appears that the particle concentration increases with exposure time.

Increases in velocity (below the critical removal) for the mixed-domain experiments showed the same effects as for the Phillips and intermediate domains – the PSD shifts towards higher concentrations of smaller particles. For the 0.25 m/s experiments, particles larger than 58–65 µm are removed from the bed; for the 0.34 m/s experiments, particles larger than 52–58 µm are removed; and for the 0.39 m/s experiments, particles larger than 40–52 µm are removed.

6.5 Discussion: Experimental Results and Model Predictions

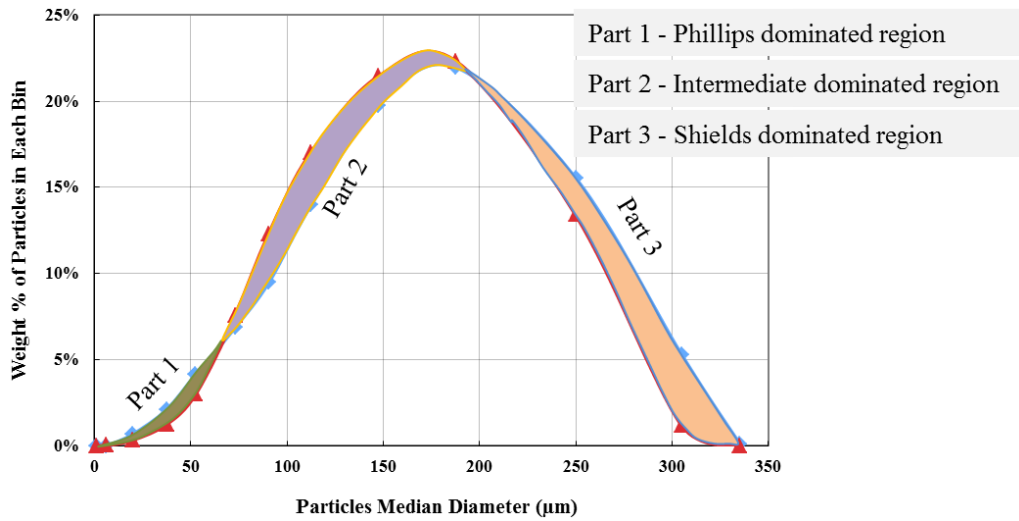

Figure 6.29 Division of the PSD curve into Phillips, intermediate, and Shields domains as used in Table 6.3

Table 6.3

PSD shift summary for different domains and three experimental velocities

Experimental flow velocity	Domain	Part 1 1st increased particle conc. range (µm)	Part 2 Reduced particle conc. range (µm)	Part 3 2nd increased particle conc. range (µm)
0.25 m/s	Phillips	45-49	45-49 → 110	N/A
	Intermediate	45-51	45-51 →108-122	108-122→140
	Shields	Same	Same	Same
	Mixed	58-65	58-65 →156-189	156-189→340
0.34 m/s	Phillips	31-37	31-37 → 110	N/A
	Intermediate	42-44	42-44 → 101-109	101-109→135
	Shields	Same	Same	Same
	Mixed	52-58	52-58 →189-202	189-202→400
0.39 m/s	Phillips	32-37	32-37 → 110	N/A
	Intermediate	N/A	20 → 95-103	95-103 →140
	Shields	Same	Same	Same
	Mixed	40-52	40-52→182-213	182-213→380

Particle removal in hydrotransport has received less attention than many other areas of research because of its complexity and the difficulty of analyzing and implementing all applicable conditions, especially when considering poly-dispersed rather than mono-disperse particles. The presence of a broad range of particles affects the interactions among them and alters the conditions; therefore, particle behaviors during experiments are not the same as for a monolayer of particles.

Table 6.3 summarizes experimental results for the twelve sets of experiments conducted, which cover four different particle size domains at bulk flow velocities of 0.25, 0.34, and 0.39 m/s, below the critical removal velocity. Essentially, particles are removed from the bed in turbulent flow in the viscous sublayer ($y^+ \leq 11$) through the generation of bursts [9], eruptions of slow-moving streaks near the wall into the fast-moving turbulent region.

The force balance for particle entrainment by the Phillips [8] and the Cleaver and Yates [9] burst models agrees well with the experimental results. The hypothesis effectively describes the particle removal behavior in the bed and explains the mechanism by which the PSD is altered.

The results obtained show that entrainment criteria for particle removal must be satisfied in order for particles to be lifted from the deposit bed. For example, the concentration of smaller particle sizes, influenced by interparticle attractive forces, increases in the bed, while larger particles that meet the entrainment criteria are removed.

The model suggests that for the 0.25 m/s velocity, particles smaller than 40 μm cannot be removed. However, for the Phillips domain at this velocity, with the original particle size ranges from 1 μm to 110 μm, and for the intermediate domain experiments with original size ranges from 20 μm to 140 μm, the concentration of smaller particles for sizes up to 45–49 μm and 45-51 μm increase in these domains, respectively (Table 6.3).

The experimental results show12–23% higher concentrations than predicted by the model for the Phillips domain at 0.25 m/s flow velocity. It may be that the model underestimates the attraction force. That also could be due to some error in experimental and particle size analysis procedures.

For the 0.34 m/s velocity, the original particle size ranges for the Phillips and intermediate domains are 1 μm to 110 μm and 20 μm to 140 μm, respectively, the same as for the experiment using a flow velocity of 0.25 m/s. The model prediction indicates that particles larger than 25 μm can be removed by the lift forces. The experiment results demonstrate that, for this velocity, the concentration of particles up to 31–37 μm in size increases for the Phillips domain and the concentration of particles up to 42–44μm increases for the intermediate domain. This introduces 24–48% more PSD shifting than the model prediction for the Phillips domain and 68–76% more for the intermediate domain.

For the Shields domain, the effective lifting force is hydrodynamic drag, which moves the particles by rolling, sliding, and saltation; therefore, the original PSD remains relatively unchanged, as expected.

For the mixed domain, which is the combination of the Phillips, intermediate, and Shields domains, the original particle size ranges are 0–340 μm, 0–400 μm, and 0–380 μm for velocities of 0.25 m/s, 0.34m/s, and 0.39 m/s, respectively. The results from the experiments show high concentrations of small particles for this domain. The smaller particle concentration for 0.25 m/s shows that the concentration of particles up to 58–65 μm in size rises and, for the 0.34 m/s, the concentration of particles up to 52–58 μm, and for the 0.39 m/s particles up to 40-52 in diameter increases. Image analysis of the smaller particles is challenging, and careful attention is needed in the analysis of the smaller size fractions. The microscope needs to be focused precisely on the smaller particles, on the one hand, but, at the same time, focusing on the smaller particles adds to the error associated with the analysis of a broad range of particle sizes using a single objective. The results for the mixed domain should be interpreted with extra caution to take into the account the error introduced by analyzing the broad range of particle sizes using only one objective.

The coherent structures, including burst and sweep events near the wall, account for 80% of the energy in turbulent fluctuations, and the burst activity accounts for most of the turbulent kinetic energy production in the boundary layer [33]. The coherent structures are streak-like structures near the wall in which slow-moving fluid is carried away to the main flow (burst or ejection) and high-speed fluid approaches the viscous sublayer outside the turbulent flow (sweep). The burst event lifts the particles in the portion of the deposit surface exposed to the turbulent burst [9] and the particles that are exposed to the sweep event are

brought back to the deposition surface. In this study, as explained earlier, particles were deposited onto the bottom of the pipe and the rest of the experimental rig was cleaned and filled with water; hence, particle deposition from the main flow to the surface during experiments is negligible. From the coherent structures (burst-sweep), only burst force caused by low-speed streaks near the wall removes particles from the deposit surface.

6.6 Conclusions

Experiments were designed to better understand and quantify the effect of the bursting process in lifting particles from the bed surface and resulting effects on the PSD in the deposit bed.

Force balance calculations were performed considering the bursting and drag forces as the effective lifting forces. Experiments were conducted for a broad range of particle sizes in order to verify the hydrotransport mechanism of the bed deposit. The experimental results indicate that, for particles up to ~170 μm in diameter, turbulent bursts lift the particles from the deposit bed. However, force balance describing particle motion suggests that, for particles with Reynolds number on the order of one, the burst and drag forces are comparable. By comparing the experimental results for this size range, it can be concluded that, for the effective burst force area, particles affected by the drag force may be moved by rolling, sliding, or saltation first, but the end result is that they are lifted by the turbulent burst events.

Due to the relatively high attraction force for particles smaller than 60 μm, their concentration in the deposit bed increases with exposure to the flow.

For the Phillips domain, longer exposure to the turbulent flow for the velocities 0.25, 0.34, and 0.39 m/s results in an increased concentration of fine particles in the deposit. The concentration of fine particles has an increasing trend from 10 to 20 min, from 20 to 30 min, and from 30 to 45 min at the three velocities.

Increasing the velocity (below the critical removal value) for the Phillips domain shifts particle removal towards smaller particle sizes as expected from the force balance of particles for different velocities. For a velocity of 0.25 m/s, particles larger than 45–49 µm are removed; for a velocity of 0.34 m/s, particles larger than 31–37 µm are removed; and for a velocity of 0.39 m/s, particles larger than 32–37 µm are removed.

The results of intermediate-domain experiments indicate that, the longer the exposure to the turbulent flow for the velocities of 0.25 and 0.34 m/s, the higher concentration of fine particles. As with the Phillips domain, the concentration shifts towards fine particles from 10 to 20 min, from 20 to 30 min, and from 30 to 45 min. For the second part, the intermediate-dominated region, where the concentration of particles is reduced due to removal to the bulk flow, the shift is mainly toward lower concentrations of particles from 10 to 20 min, from 20 to 30 min, and from30 to 45 min.

Increasing velocity (below the critical removal value) for the intermediate-domain experiments shows that, as with the Phillips-domain experiments, the concentration shifts incrementally towards smaller particles. These results are in agreement with the theoretical calculations from the force balance. For the 0.25 m/s velocity, particles larger than 45–51 µm were removed; for the 0.34 m/s velocity, particles larger than 42–44 µm were removed; and for the velocity of 0.39 m/s, the finer particles were not present in the original PSD.

The results of Shields-domain experiments show that the PSDs for the three different velocities remain similar to the initial PSD, or unchanged. The initial PSD of the experimental series are in the size range larger than ~ 150 µm and, from the theoretical calculations of the force balance, the lifting force for these particles is hydrodynamic drag force, which moves particles by rolling, sliding, and saltation. Therefore, the PSDs for exposure times of 10, 20, 30, and 45 min for the experiments conducted at three different velocities stay approximately the same the original PSD.

For velocity increases from 0.25 m/s to 0.34 m/s to 0.39 m/s (below the critical removal), the Shields domain experiments demonstrate that for the chosen original PSD, the PSDs stay roughly the same.

The mixed-domain (poly-dispersed particles) results, which are the confirmation experiments of the Phillips, intermediate, and Shields domains together, show the shift (increase) of the fine particle concentration with time. As with the Phillips and intermediate domains, the concentration of fine particles increases from 10 to 20 min, from 20 to 30 min, and from 30 to 45 min. The concentration of particles for the second part is reduced due to removal to the bulk flow, and mainly shifts toward lower concentration from 10 to 20 min, from 20 to 30 min, and from 30 to 45 min. For the third part, it appears that the concentration of particles increases with time.

Velocity increases (below the critical removal value) for the mixed domain showed that, as with the Phillips- and intermediate-domain experiments, the PSD

shifts towards smaller particles. For the 0.25 m/s velocity, particles larger than 58–65 µm are removed from the bed; for the 0.34 m/s velocity, particles larger than 52–58 µm are removed; and, for the 0.39 m/s velocity, particles larger than 40–52 are removed.

The experimental results satisfactorily support the hypothesis of particle removal from the deposit bed. In the mixed-domain experiment, with the coexistence of a broad range of particle sizes, it appears that the PSD shifts toward larger sizes than those for the Phillips and intermediate domains. For the mixed domain and a velocity of 0.25 m/s, the concentration of particles smaller than 58–65 µm increases. As with the Phillips domain, the concentration of particles smaller than 45–49 µm increases and, for the intermediate domain, the concentration of the 45–51 µm fraction increases. It appears that the PSD is broadened and that the attractive forces between the smaller particles increase. This observation might also be due to error in image analysis of the broad particle size range. Focusing on the wide range of sizes in the specimen using a single objective is problematic, as a single objective cannot focus precisely over the whole range of particle sizes.

6.7 References

[1] Shields, A., 1936, "Anwendung Der Ahnilchkeitsmechanik Und Der Turbulenzforschung Auf Die Geschiebebewegung Mitteilungen Der Preuss," Versuchsanst. F. Wasserbrau und Schiffbau, Berlin, Heft, 26 (see Yalin, M. S., 1977), pp. -.

[2] Yalin, M. S., 1977, *Mechanics of Sediment Transport*, Pergamon Press, Oxford; New York.

[3] Lick, W., Jin, L., and Gailani, J., 2004, "Initiation of Movement of Quartz Particles," Journal of Hydraulic Engineering, 130(8), pp. 755-761.

[4] Nalluri, C., Featherstone, R. E., Marriott, M., and Nalluri, C. C. E. H., 2009, *Nalluri & Featherstone's Civil Engineering Hydraulics : Essential Theory with Worked Examples*, Wiley-Blackwell, Oxford; Ames, Iowa.

[5] Bagnold, R. A., 2005, *The Physics of Blown Sand and Desert Dunes*, Dover Publications Inc., London.

[6] Bagnold, R. A., 1951, "The Movement of a Cohesionless Granular Bed by Fluid Flow over It," British Journal of Applied Physics, 2(2), pp. 29-34.

[7] Bagnold, R. A., 1960, "The Re-Entrainment of Settled Dust," International Journal of Air Pollution, 2(3), pp. 357-363.

[8] Phillips, M., 1980, "A Force Balance Model for Particle Entrainment into a Fluid Stream," Journal of Physics D: Applied Physics, 13(2), pp. 221.

[9] Cleaver, J. W., and Yates, B., 1973, "Mechanism of Detachment of Colloidal Particles from a Flat Substrate in a Turbulent Flow," Journal of Colloid and Interface Science, 44(3), pp. 464-474.

[10] Saffman, P. G., 1965, "The Lift on a Small Sphere in a Slow Shear Flow," Journal of Fluid Mechanics, 22(02), pp. 385-400.

[11] Kline, S. J., Reynolds, W. C., Schraub, F. A., and Runstadler, P. W., 1967, "The Structure of Turbulent Boundary Layers," Journal of Fluid Mechanics, 30(04), pp. 741-773.

[12] Corino, E. R., and Brodkey, R. S., 1969, "A Visual Investigation of the Wall Region in Turbulent Flow," Journal of Fluid Mechanics, 37(01), pp. 1-30.

[13] Kim, H. T., Kline, S. J., and Reynolds, W. C., 1971, "The Production of Turbulence near a Smooth Wall in a Turbulent Boundary Layer," Journal of Fluid Mechanics, 50(01), pp. 133-160.

[14] Morrison, W. R. B., Bullock, K. J., and Kronauer, R. E., 1971, "Experimental Evidence of Waves in the Sublayer," Journal of Fluid Mechanics, 47(04), pp. 639-656.

[15] Rao, K. N., Narasimha, R., and Narayanan, M. a. B., 1971, "The 'Bursting' Phenomenon in a Turbulent Boundary Layer," Journal of Fluid Mechanics, 48(02), pp. 339-352.

[16] Wallace, J. M., Eckelmann, H., and Brodkey, R. S., 1972, "The Wall Region in Turbulent Shear Flow," Journal of Fluid Mechanics, 54(01), pp. 39-48.

[17] Zeinali, H., Toma, P., and Kuru, E., 2012, "Effect of near-Wall Turbulence on Selective Removal of Particles from Sand Beds Deposited in Pipelines," Journal of Energy Resources Technology, 134(2), pp. 021003.

[18] Rabinovich, E., and Kalman, H., 2009, "Incipient Motion of Individual Particles in Horizontal Particle–Fluid Systems: B. Theoretical Analysis," Powder Technology, 192(3), pp. 326-338.

[19] Rabinovich, E., and Kalman, H., 2009, "Incipient Motion of Individual Particles in Horizontal Particle–Fluid Systems: A. Experimental Analysis," Powder Technology, 192(3), pp. 318-325.

[20] Rabinovich, E., and Kalman, H., 2009, "Pickup Velocity from Particle Deposits," Powder Technology, 194(1–2), pp. 51-57.

[21] Oroskar, A. R., and Turian, R. M., 1980, "The Critical Velocity in Pipeline Flow of Slurries," AIChE Journal, 26(4), pp. 550-558.

[22] Stevenson, P., Thorpe, R. B., and Davidson, J. F., 2002, "Incipient Motion of a Small Particle in the Viscous Boundary Layer at a Pipe Wall," Chemical Engineering Science, 57(21), pp. 4505-4520.

[23] Ramadan, A., Skalle, P., and Johansen, S. T., 2003, "A Mechanistic Model to Determine the Critical Flow Velocity Required to Initiate the Movement of Spherical Bed Particles in Inclined Channels," Chemical Engineering Science, 58(10), pp. 2153-2163.

[24] Rabinovich, E., and Kalman, H., 2008, "Generalized Master Curve for Threshold Superficial Velocities in Particle–Fluid Systems," Powder Technology, 183(2), pp. 304-313.

[25] Miedema, S. A., 2011, "Constructing the Shields Curve," ASME Conference Proceedings, 2011(44397), pp. 825-840.

[26] Papista, E., Dimitrakis, D., and Yiantsios, S. G., 2010, "Direct Numerical Simulation of Incipient Sediment Motion and Hydraulic Conveying," Industrial & Engineering Chemistry Research, 50(2), pp. 630-638.

[27] Newitt, D. M., Richardson, J. F., Abbott, M., and Turtle, R. B., 1955, "Hydraulic Conveying of Solids in Horizontal Pipes," Chemical Engineering Research and Design, 33a(-), pp. 93-113.

[28] Nino, Y., and Garcia, M., 1998, "Experiments on Saltation of Sand in Water," Journal of Hydraulic Engineering, 124(10), pp. 1014-1025.

[29] Albion, K., Briens, L., Briens, C., and Berruti, F., 2009, "Modelling of Oversized Material Flow through a Horizontal Hydrotransport Slurry Pipe to Optimize Its Acoustic Detection," Powder Technology, 194(1-2), pp. 18-32.

[30] Partheniades, E., 2009, *Cohesive Sediments in Open Channels - Properties, Transport, and Applications*, Elsevier,

[31] Robinson, S. K., 1991, "Coherent Motions in the Turbulent Boundary Layer," Annual Review of Fluid Mechanics, 23(1), pp. 601-639.

[32] Moody, L. F., 1944, "Friction Factors for Pipe Flow," Transactions of the ASME, 66(8), pp. 671–684.

[33] Lumley, J., and Blossey, P., 1998, "Control of Turbulence," Annual Review of Fluid Mechanics, 30(1), pp. 311-327.

7 Contributions of this Thesis

One of the main accomplishments of this experimental study was to design and build a slurry flow loop as a base platform for research on multiphase flow for the petroleum group at the University of Alberta. A horizontal transparent slurry flow loop with optical quality glass tubes was constructed to study slurry flow patterns and flow transitions from one pattern to another over a wide range of velocities, mostly below the critical deposition velocity. As in other similar projects, progressive modifications of the loop were implemented with improving understanding of loop operation as a result of initial experiments. Experiments with particles in the system are time-consuming; repeating the experiments after modifications to the system requires even more time. The findings from experimental observations are provided in the relevant chapters in this dissertation, followed by conclusions arising from the findings. This section concludes the research study by providing an overview of its contributions to the study and understanding of slurry transportation in pipelines.

The main focus of this research was on the slurry flow pattern characterized by lenticular deposits (LDs). LDs form at low slurry concentrations and low transportation velocities. It is significant that the friction force does not apply for dilute slurry; therefore, in the force balance, friction force effects can be neglected. Natural LDs are formed and transported at the bottom of pipelines carrying a broad range of PSDs (from 1 to 500 μm, in the range of oil sands PSDs). The experiments were repeated using a narrow PSD and a broad PSD,

both comprising polydisperse particle mixtures. The original method of extraction from the bed was designed to extract the samples from the bed for analysis of PSD shifts. The extracted samples were analyzed by an automated image analyzer to assess the effect of turbulent flow at the bed interface on the mass exchange between the bed and the bulk flow. The near-wall turbulent activities (burst-sweep) were quantified for frequency and intensity near the bed at the viscous sublayer to explain the lifting of particles into the core flow.

From the experiments with bed transport in an LD flow pattern at constant velocity, it was observed that the propagation rate of the LDs at the bottom of pipe is higher for particles in the Shields domain ($d_p > 170$ µm), followed by the intermediate domain, and then the Phillips domain ($d_p < 60$ µm). This behavior is due to relatively strong attraction force (van der Waals forces) in the smaller particle size ranges.

The dynamic exchange of solid particulates between deposit, moving bed, and co-currently fluidized slurry includes continuous entrainment (due to turbulent bursting) and deposition (due to the sweep character of turbulence) of solid particles. Two distinct mechanisms of removal separately favor the selective removal of larger particles of the population in the size range from submicrometer to approximately 60 µm (Phillips domain). This is reversed for particle sizes from approximately 170 µm up to the maximum particle size in this experiment, 500 µm (Shields domain) – the smaller particles are lifted in this range. Particles of sizes between these ranges (intermediate domain) are exposed to more-or-less

equal lifting forces and particles are evenly removed. The results from the experiments are in good agreement with the hypothesis. The concentrations of fine and large particles over the exposure of slurry flow to the turbulent flow are increased, while the concentration of the particles lifted by the turbulent “updraft under a burst” force is reduced.

Natural phenomena seek out the most stable situation. The results of frictional pressure drop measurements from the slurry pattern transition revealed that, when two patterns could co-exist at constant velocity, the continuous bed gradually re-forms to an LD slurry flow pattern. Pressure drop measurements during the transition between patterns revealed a 6–8% reduction in frictional pressure drop. Repetition of the experiment confirmed this result, leading to the conclusion that the presence of LDs represents a more stable form of slurry transportation than the presence of a continuous bed.

With the aid of the nonintrusive 2D PIV technique, the coherent structures adjacent to the pipe wall (burst-sweep) for LD, continuous bed, and water-only flows were quantified for their occurrence and intensity. All bed forms are created naturally as the bed morphology influences the enhancement or suppression the turbulent intensity and frequency near the wall. The findings reveal that the frequency and turbulent kinetic energy (TKE) are the lowest for the LD case. This also explains the reduction of pressure drop in the transition from a continuous bed to LDs. As the TKE is lower in LD flow, LDs are a more stable form than a continuous bed.

7.1 Limitations of the Current Study and Recommendations for Future Work

The experiments in this study were completed in a pipeline system; such systems are commonly utilized in petroleum production, oil sands transportation, ore industry, and many other applications. Drilling includes inner pipe and annulus sections, in which drilled cuttings, are transported through the annulus. The results obtained in this study demonstrate the characteristics of the near-wall turbulent flow region as seen in both pipeline and wellbore annulus systems. However, separate experiments should be conducted to verify the applicability of the results of this study for the annulus system to enable comparison of the results and improve understanding of the effects of the annular geometry. In addition, the effect of rheology on selective particle removal needs to be investigated.

In the particle size distribution (PSD) shift experiments, all efforts were made to obtain reliable and precise results. A further experimental program could be conducted to further validate the experimental results and confirm the theoretical hypotheses. For example, for the conducted experiments, the force balance (see Figures 6.5-6.7) suggests that particles smaller than 40 µm for the 0.25-m/s flow velocity, 25 µm for the 0.34-m/s flow velocity, and 20 µm for 0.39-m/s flow velocity are not removed from the bed because the lifting forces cannot overcome the strong downward attraction force. Experiments similar to those in this study for particles smaller than 40 µm for the 0.25 m/s, 25µm for the 0.34 m/s, and 20 µm for 0.39 m/s flow velocities could be conducted. After sufficient exposure to

turbulent flow, samples from these experiments could be analyzed for PSD and compared to the initial PSD for further validation of the hypotheses.

Nonintrusive techniques open new horizons in research. PIV is a relatively new technology for use in fluid dynamics research. In this study, replacing the normal lens with the micro lens improved the data resolution considerably. The highest resolution is possible with PIV; however, special care should be taken to maximize the signal-to-noise ratio and obtain reliable data. A few modifications could be applied to obtain more reliable and higher-resolution data from PIV. Modifications could include use of a camera with higher resolution, a lens with better field of view and focus, and an increase of visible seeding in the images captured by PIV. The importance of higher-resolution data from PIV is that the results from PIV would then be comparable with data from direct numerical simulation (DNS).

Considering the computational limits of DNS and the fact that only low-velocity flows can be computed, the greatest advantage of the improved PIV method over DNS is that the highest Reynolds numbers can be examined. This opens a new avenue to better understand transport phenomena, transport mechanisms, and turbulence effects.